UNIVERSITY OF OTTAWA

DOCTOR OF PHILOSOPHY THESIS

QUANTUM EFFECTS IN STRONG FIELD PHYSICS

Author:

Neda Boroumand

Supervisor:

Thomas Brabec

Thesis submitted in partial fulfillment of the requirements for the Doctorate of Philosophy in Physics

Department of Physics
Faculty of Science
University of Ottawa

To the memory of my mother,

whose resilience, bravery, and wisdom have left an everlasting impact on me.

Abstract

When matter is exposed to strong fields, electrons are ionized and a number of processes such as high harmonic generation (HHG), above threshold ionization (ATI), non-sequential ionization happen. These processes are usually investigated semiclassically, i.e. matter is treated by quantum mechanics, and radiation is treated classically. In particular HHG which is the generation of ultrashort coherent extreme ultraviolet (XUV) pulses, has enabled a wealth of novel ultrashort spectroscopic methods in atomic, molecular, and condensed matter physics. Further, ionization has applications in micro-machining.

Strong field physics continues to have numerous open questions. As an illustration, the mechanisms underlying dominant HHG pathways in solids remain insufficiently understood. It is not clear which mechanism dominates HHG in various materials. Possible pathways are the interband and intraband contributions. Furthermore, many of these processes in strong field physics have been described by single active electron (SAE) approximation. This approach relies on the assumption that the interaction between a single electron and the intense laser field dominates all other interactions. However, this is clearly not the case especially in solids where interactions with the lattice and other electrons can be important. In addition, quantum optical aspects of strong field physics have generated increasing interest, yet they remain partially explored. This chapter involves treating electromagnetic fields using the formalism of second quantization. Quantum optical properties, such as squeezing, entanglement and the negativity of the Wigner function, are of fundamental importance for the field of quantum information and quantum computation.

The central theme of my thesis is the development of quantum optical and statistical theoretical frameworks for describing intense laser field processes such as ionization and HHG in atomic and molecular gases and in solids.

The second chapter focuses on gaining a detailed understanding of the mathematical

steps involved in the Keldysh theory of ionization to establish a solid theoretical foundation. Through this analysis we identified an additional factor of two compared to Keldysh's original derivation of atomic ionization rates.

The third chapter addresses the inadequately understood mechanisms that govern dominant high harmonic generation (HHG) pathways in solids. One approach to clarify these mechanisms involves introducing real (resonant) and virtual processes. We developed the strong field adiabatic following (SFAF) formalism which is based on Dyson expansion using the von-Neumann equation of density matrix. Using SFAF a diagnostic method is obtained to separate virtual and resonant channels. Through this separation, and by comparing with experimental results, we identified the need to incorporate many-body effects.

The fourth chapter explores the fact that a solid is a complex many body system in which the SAE approximation is very crude. The electron interacts with holes, other electrons, collective excitations such as plasmons, and phonons. Our work is based on the idea that all theses effects can be treated as a quantum statistical heat bath of bosonic harmonic oscillators. We apply this to our SFAF formalism. In the ionization case, this work has settled a long standing issue which is the fact that simple phenomenological approaches such as the relaxation time approximation T_2 result in nonphysical enhancement of ionization.

In chapter five, we have investigated ways to transfer quantum optical properties on the otherwise classical high harmonic radiation. The goal is to use HHG to scale quantum sources to smaller wavelengths. Quantum properties can be imprinted by perturbing HHG with a quantum field, such as bright squeezed vacuum (BSV). In this chapter the theory of quantum sideband high harmonic generation (QSHHG) in atoms and solids is derived to find ways by which to transfer quantum properties from the perturbative BSV to the harmonic sideband. The theoretical framework is a quantum generalization of the semi-classical Lewenstein model of HHG. It gives closed-form solutions for the HHG and QSHHG wavefunctions. Knowing the wavefunction, we can identify the quantum properties of QSHHG. The additional photons absorbed and emitted from the quantum perturbation, here BSV, create entanglement between individual harmonic sidebands and between the harmonic sidebands and the BSV. We show how this entanglement can be used to create a variety of non-classical states commonly used in quantum information science, such as high purity single photon states, Schrödinger cat states, and photon added squeezed vacuum states. Some of these non-Gaussian states with negative Wigner

functions have been shown to provide a quantum computational advantage over their Gaussian counterparts. Additionally, they play a significant role in quantum metrology, enhancing precision measurements beyond classical limits. This chapter has opened a path to quantum engineering of HHG.

Acknowledgments

I would like to thank my supervisor Prof. Brabec for making this thesis possible.

Furthermore, I would like to express my sincere gratitude to Prof. Giulio Vampa for his endless patience and guidance through the last stages of my Ph.D. His mentorship and wealth of knowledge have been instrumental in shaping my understanding and approach throughout this journey. I am truly grateful for his support and encouragement.

Additionally, I would like to express my sincere gratitude to Prof. Robert W. Boyd for their exceptional guidance and the invaluable knowledge imparted through their nonlinear optics course. Beyond academics, their manner and kindness toward students have had a lasting impact on me, inspiring both my learning and personal growth.

I would also like to express my sincere appreciation to members at NRC including Prof. André Staudte, Dr. David Purschke, Dr. Shima Gholam Mirzaeimoghadar, Dr. Nida Haram, Pooya Ghavami. Especially, I am deeply grateful to Prof. André Staudte, Dr. David Purschke, and Dr. Shima Gholam Mirzaeimoghadar for their generosity, guidance, and support. They listened to me when I needed it most and offered invaluable help throughout my journey. Not only are they exceptionally intelligent, but I have also come to know them as truly kind and compassionate individuals. I would like to extend my gratitude to David for patiently answering all my questions. I truly appreciate his generosity in sharing his expertise.

I would also like to express my deepest gratitude to my friend and colleague, Dr. Soheil Zibod, for his unwavering support throughout this journey.

Finally, I would like to express my most profound appreciation to my parents, my sister, Homa, and my partner, Renato, for their unwavering support, encouragement, and unconditional love throughout this entire journey.

List of Publications, Contributions

N. Boroumand, A. Thorpe, A. M. Parks, and T. Brabec,"Keldysh ionization theory of atoms: mathematical details" Journal of Physics B: Atomic, Molecular and Optical Physics 55, 213001 (2022).

Contribution: The calculations and writing of the paper were done by me and A. T. and T. B.

A. Thorpe*, **N. Boroumand***, A. M. Parks, E. Goulielmakis, and T. Brabec,"High harmonic generation in solids: Real versus virtual transition channels, " Phys. Rev. B 107, 075135 (2023).

Contribution: First co-author
Theory was developed by T. B. , A. T. and me, and the paper was written by all authors.

S. Lemieux, S. A. Jalil, D. N. Purschke, **N. Boroumand**, T. J. Hammond, D. Villeneuve, A. Naumov, T. Brabec, and G. Vampa,"Photon bunching in high-harmonic emission controlled by quantum light, " Nature Photonics 10.1038/s41566-025- 01673-6 (2025).

Contribution: I participated in the experiment and in writing the paper, and developed the theory together with T. B. and G. V.

N. Boroumand, A. Thorpe, G. Bart, A. Parks, M. Toutounji, G. Vampa, T. Brabec, and L. Wang, Strong field physics in open quantum systems (2025), arXiv:2502.10240.
Contributions: The idea came from Prof. Brabec when I joined his group (2020).
Prof. Brabec and I developed the theory (2021-2022).
I gave my OCIP (Ottawa Carleton Institute for Physics) talk in spring (2022).
https://ocip.ca/calendar-events/seminars/22/ocip-graduate-student-symposium-spring-2022-

session-3
L. W., the new postdoc of Prof. Brabec, (fall 2024-winter 2025) wrote the manuscript (changed my previous notes i.e. changing from atomic units to SI, changing notations) and generated the figures.

N. Boroumand, A. Thorpe, G. Bart, L. Wang, D. N.Purschke, G. Vampa, and T. Brabec, Quantum engineering of high harmonic generation (2025), arXiv:2505.22536

Contribution: I developed the theory together with T. B., and all authors contributed in writing of the paper

A. Thorpe, **N. Boroumand**, G. Bart, L. Wang, G. Vampa, and T. Brabec, A unified perspective of high-harmonic generation in gases and solids (In Preparation)

Contribution: I contributed to the development of the theory.

Contents

List of Figures

List of Abbreviations

ATI: Above Thershold Ionization
BCH : Baker-Campbell-Hausdorff
BSV : Bright Squeezed Vacuum
CF : Correlation Function
DFG : Difference Frequency Generation
FT : Fourier Transform
FVB : Frozen Valence Band
HBT : Hanbury-Brown-Twiss
HHG : High Harmonic Generation
NZ : Nakajima-Zwanzig
QSHHG : Quantum Sideband High Harmonic Generation
SAE : Single Active Electron
SD : Spectral Density
SFAF : Strong Field Adiabatic Following
SFG : Sum Frequency Generation
WF : Wigner Function
XUV: Extreme Ultraviolet

Chapter 1

Introduction

1.1 Strong field physics

Following the development of the theory of stimulated emission [6], laser science has seen significant progress ranging from the realization of visible light sources [7] to the generation of extremely short (on the order of femtoseconds, 10^{-15}s) and highly intense pulses [8]. The high field intensity achieved enabled the ability to probe and alter the properties of matter. This is known as the field of nonlinear optics where the field is strong enough to induce nonlinear responses in matter [9, 10]. Initially, the intensity of strong laser fields was on the order of $\approx 10^8$ W/cm^2, placing them within the perturbative regime, such as in the first nonlinear optics experiment, the discovery of second harmonic generation by Franken et al. [11]. In that experiment, they used a ruby laser on a quartz plate. Perturbative nonlinear optics is where the field is strong but still not comparable with the binding forces that electrons experience in the matter. The theory of this regime is successfully described by the perturbative theory of quantum mechanics. The polarization, therefore, is written as a power series in the field as follows [10]

$$\mathbf{P}(t) = \epsilon_0 \left[\chi^{(1)}\mathbf{E}(t) + \chi^{(2)}\mathbf{E}^2(t) + \chi^{(3)}\mathbf{E}^3(t) + ...\right]. \tag{1.1}$$

There are two main conditions where the above expansion diverges [10]; first, when the material is resonantly excited, and second in the regime of extreme nonlinear optics. In these two cases other methods need to be used.

First, when the material is resonantly excited, there is a large population transfer to the excited states. As a result, perturbation techniques must be abandoned. In the cases where only two main levels remain, the problem can be solved exactly. It is called the Rabi

model when the external field is considered classically and the Jaynes-Cummings model when the external field is treated quantum mechanically. The Jaynes-Cummings model using quantum mechanics includes processes that have no classical counterparts such as spontaneous emission [4].

The second case where Eq. (1.1) becomes invalid belongs to the regime of extreme nonlinear optics. Extreme nonlinear optics emerges when the external field is of the order of the atomic field strength of electrons in matter which is of the order of 1 at.u (atomic unit). The main difference between perturbative nonlinear optics and extreme nonlinear optics is that in the perturbative regime, where Eq. (1.1) is valid, the probability of the emission of the *n*th harmonic decreases rapidly as n increases. However, in the extreme nonlinear optics a plateau region with higher harmonics and with a different cut-off shape can be observed experimentally. This was first studied in the gaseous phase and plasma media [12, 13]. Two principal processes are investigated in this regime: ionization, which initiates all strong field experiments, and high harmonic generation (HHG), involving the production of higher order harmonics of light. Ionization has practical applications in laser machining and material modification [14, 15], while HHG is used in time resolved spectroscopy of solids [15] and phase transitions and topological effects [15]. HHG in particular in solids is used in probing material properties such as the crystal momentum dependent bandgap [16, 17, 18, 19, 20], Berry phase [21, 22], and valence potential [23]. HHG also creates a source of extreme ultraviolet emission (EUV), which has enabled groundbreaking advances in attosecond science [24].

I will now go to a more detailed description of: **ionization in atomic media**, **ionization in solids**, and then **HHG in gases or atomic systems**, and finally **HHG in solids**.

- First, **ionization in atoms** is the process through which a bound electron is brought up into the continuum. Electrons experience a potential that is the combination of the atomic core Coulomb potential and the electric field of the laser. A quantitative description of ionization was given by Keldysh where a so-called Keldysh parameter γ was introduced [25, 1]. When $\gamma << 1$, tunnel ionization prevails, and when $\gamma >> 1$ multiphoton ionization is dominant, see Fig. (1.1). The multi-photon limit of ionization describes the dominant mechanism as being the simultaneous absorption of multiple photons to free a bound electron [1], whereas tunneling is the electron passing through the potential barrier to continuum [1]. For an intuitive

overview of tunnel ionization and multiphoton ionization see reference [26]. The parameter γ can be understood by this relation $\gamma = \sqrt{\frac{I_p}{2U_p}}$ where I_p is the ionization potential and U_p is the ponderomotive energy, which is defined as the energy of free electrons in the electromagnetic field when cycle averaged. Using Keldysh parameter, we see that ionization in a low-intensity laser field has a multiphoton nature, whereas in a stronger laser field it acquires the character of tunneling [1]. A schematic of different ionization channels is shown in Fig. (1.1).

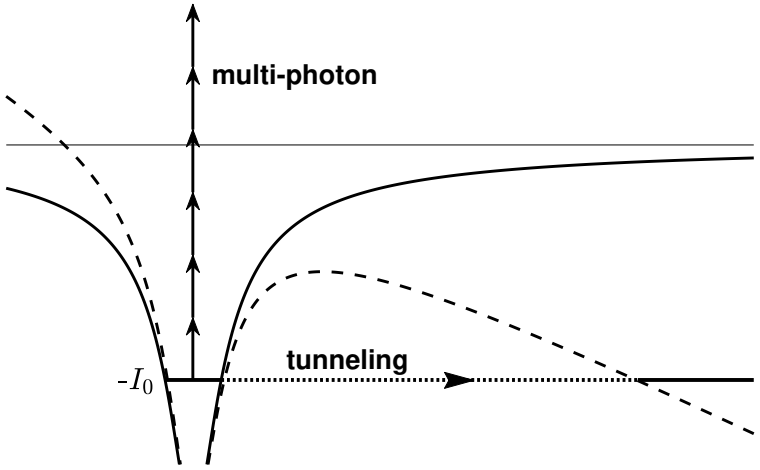

Figure 1.1: Schematic of multi-photon and tunnel ionization; Coulomb potential (full line); Coulomb potential plus laser field (dashed line). [1]

- Second, **ionization in solids** can be described as the electron population in the valence band being brought up into the conduction band. Similar to the atomic case, Keldysh theory [25] was the main approach for describing ionization in solids when under-resonantly excited. One can subdivide solids into semiconductors and dielectrics. Ionization experiments in semiconductors [27] are in agreement with Keldysh theory or the frozen valence band (FVB) approximation [28] (Keldysh used FVB approximation). The FVB approximation is where the population in the valence band is frozen and the dynamics of this band do not affect the ionization. One important point to note is that FVB approximation does not conserve the populations, so it is only applicable at very small ionization levels [25]. In dielectrics [29], on the other hand, ionization rates do not follow the Keldysh theory or the FVB approximation. It was shown that this difference between semiconductors and dielectrics could be due to dynamical Stark shift which is more pronounced in

dielectrics [30, 5].

- Third, **HHG in gases** can be described by the three-step model [31] as follows:

  1. **Ionization**: The laser field causes the electrons to tunnel to the continuum by tilting of the Coulomb potential and lowering of the tunneling barrier.
  2. **Acceleration**: The electrons in the next step accelerate within the laser field.
  3. **Recombination**: The electrons recombine with the parent ion when the electric field direction reverses. The electrons, then, emit the additional energy in the form of high harmonics of the laser light.

A schematic of three-step model can be found in Fig. (1.2).

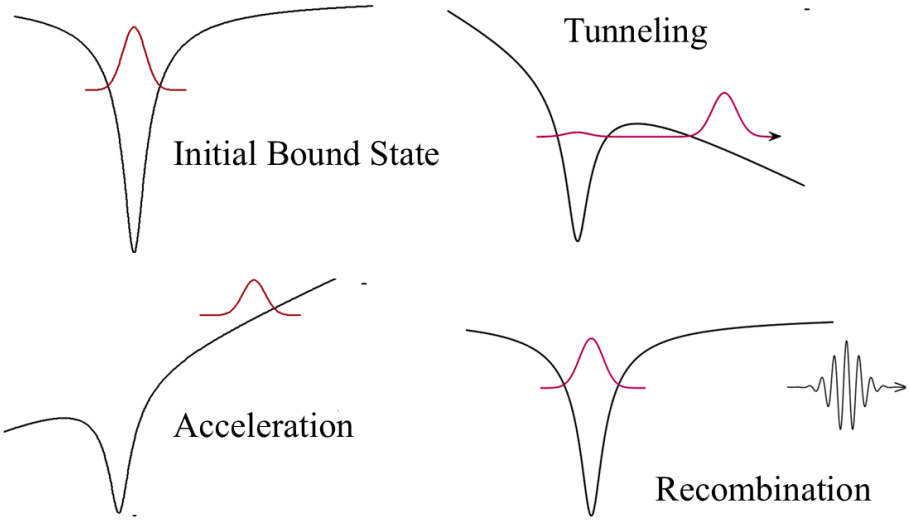

Figure 1.2: Three Step Model

While the first and third steps can be described quantum mechanically the second step description can remain classical. The semiclassical description of three step model was pioneered by Lewenstein et al. [28].
Here, I provide a more detailed description of the propagation (or acceleration) step of the three step model in the semiclassical approach. As mentioned before, this step description remains classical. Atomic units are used throughout the calculation, and the Coulomb potential is considered to be zero in this step, which is a reasonable

approximation. An electron is born at time t_b in the first step. We assume light is monochromatic and linearly polarized for simplicity. Therefore, the field is given by $\mathbf{F} = F_0 \cos(\omega_0 t)\hat{x}$. As a result, the momentum can be obtained by integrating the acceleration calculated using Newton's law. We have [2]

$$\mathbf{p} = \hat{x} \int_{t_b}^{t} F_0 \cos(\omega_0 \tau) d\tau = -\frac{F_0}{\omega_0} \left[\sin(\omega_0 t) - \sin(\omega_0 t_b)\right] \hat{x} + \mathbf{v}_0. \tag{1.2}$$

The three step model assumes that the electron tunnels with nearly zero initial velocity. Therefore, $\mathbf{v}_0 \approx 0$ in Eq. (1.2). Note that the vector notation can be dropped for simplicity. Integration of Eq. (1.2) will give us the position of the electron as a function of time. We have [2]

$$x(t, t_b) = \int_{t_b}^{t} p = \frac{F_0}{\omega_0^2} \left[\cos(\omega_0 t) - \cos(\omega_0 t_b) + \sin(\omega_0 t_b)(t - t_b)\right]. \tag{1.3}$$

Electrons born at $t_b = 0$, which corresponds to the peak of the electric field, will re-encounter the parent ion after each cycle. At $t_b = 0$, the last term in the LHS of Eq. (1.3) vanishes and the remaining terms scales $\propto \sin^2(\frac{\omega_0 t}{2})$. While the $\sin^2$ term effectively halves the period of the oscillation, the factor of 2 in the denominator doubles it, restoring the original periodicity. The electrons born at $t_b > 0$, on the other hand, will re-encounter the parent ion earlier in the cycle. After electron recombines with the parent ion, it releases its kinetic energy as a harmonic photon. One can, thus, express it in mathematical form as

$$n\hbar\omega_0 = T + I_p, \tag{1.4}$$

where I_p is the ionization potential, and T is the kinetic energy. Using Eq. (1.2) we find that T is given by

$$T = 2U_p \left[\sin(\omega_0 t) - \sin(\omega_0 t_b)\right]^2, \tag{1.5}$$

where U_P is the ponderomotive energy. It is found numerically, using Eq. (1.5), that the harmonic photon peaks at energy [2]

$$\hbar\omega_{max} = 3.17U_p + I_p. \tag{1.6}$$

The equation above suggests that there should be continuous bandwidth of emitted photons. However, only odd harmonics are generated, which can be explained by the interference of emitted photons in successive half-cycles. For the dipole moment we have $d(t + \frac{\pi}{\omega_0}) = -d(t)$. Therefore, for the nth harmonic the sum of polarization of successive half-cycles can be written as [2]

$$d(t)e^{in\omega_0 t} + d(t + \frac{\pi}{\omega_0})e^{in\omega_0(t+\frac{\pi}{\omega_0})} = d(t)e^{in\omega_0}\left[1 - e^{in\pi}\right], \tag{1.7}$$

which clearly shows constructive interference for odd harmonic number and destructive for the even ones. Fig. (1.3) shows that due to symmetrical path reasons only odd harmonics appear [2].

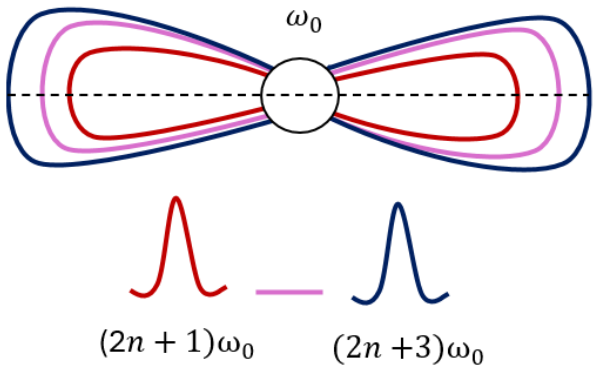

Figure 1.3: Due to symmetry reasons only odd harmonics appear. See Eq. (1.7) [2]

- Finally, the first demonstration of **HHG in solids** was done in semiconductors under intense mid-IR pulses irradiation [32]. HHG research in solids can be distinguished by material and laser wavelength. As HHG experiments take place in the under-resonant limit, the driving laser wavelength has to be chosen smaller than the bandgap. As a result, smaller minimum bandgap energies require longer wavelength driving lasers. Therefore, we have far-IR semiconductors [20, 33, 34, 35], mid-IR semiconductors [32, 36, 37, 38, 39, 40, 41, 42], and near-IR dielectrics [17, 18, 23]. The difference between dielectrics and semiconductor is in the bigger bandgap in dielectrics and the applicability of higher intensity lasers due to higher damage threshold [5]. Dielectrics and semiconductors differ in terms of which channel dominates the HHG response. It is shown that this difference between semiconductors and dielectrics could be due to dynamical Stark shift and their

importance in the dielectrics case [30, 5].
HHG in solids can still be described by the three-step model similar to the atomic case. Fig. (1.4) presents a schematic of the HHG process in momentum space for both atoms and solids.

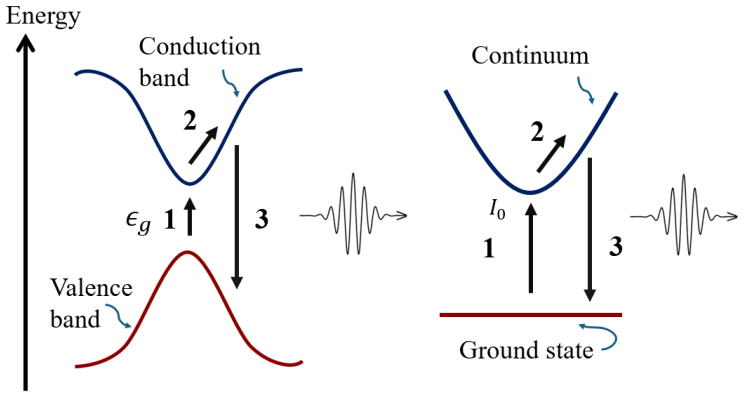

Figure 1.4: Three step model in momentum space for atoms and bulk solids, right and left respectively

Using the semiconductor Bloch equations, theoretical investigations into the propagation or acceleration step of HHG in solids have revealed two dominant mechanisms: **interband** and **intraband** currents. Single active electron (SAE) approximation in semiconductor Bloch equations (SBEs) and in the length gauge [43, 5], is the widely used approach that offers a decomposition of the induced current into intraband and interband contributions. SAE approximation relies on the assumption that the interaction between a single electron and the intense laser field dominates all other interactions.
The starting point is that HHG spectrum in total is determined by the absolute square of the Fourier transform (FT) of the expectation value of the current, $|\mathrm{FT}\{\langle \mathbf{j} \rangle(t)\}|^2$, with the expectation value of current, in the density matrix formalism, being

$$\langle \mathbf{j} \rangle = \int_{\overline{\mathrm{BZ}}} d^3K \mathrm{Tr}\left[\mathbf{j}\rho\right]_{\mathbf{K}} . \tag{1.8}$$

ρ is the density matrix, and $\overline{\mathrm{BZ}}$ is the Brillouin zone in the shifted momentum frame defined as $\overline{\mathrm{BZ}} = \mathrm{BZ} - \mathbf{A}(t)$. In the density matrix formalism, the analysis starts from

the von Neumann (one-body semiconductor Bloch) equation for density matrix ρ,

$$i\partial_t \rho(\mathbf{K}, t) = [H(\mathbf{K}_t, t), \rho(\mathbf{K}, t)], \tag{1.9}$$

derived in the moving crystal momentum frame $\mathbf{K}_t = \mathbf{K} + \mathbf{A}(t)$, with crystal momentum $\mathbf{K}$ defined in the shifted first Brillouin zone, $\overline{\mathrm{BZ}} = \mathrm{BZ} - \mathbf{A}(t)$. The vector potential is $\mathbf{A}(t)$ and the electric field $\mathbf{F}(t) = -\partial_t \mathbf{A}(t)$. The elements of the current operator are given by $j_{vc}(\mathbf{K}_t) = -i\langle v(\mathbf{K}_t)|\nabla_{\mathrm{x}}|c(\mathbf{K}_t)\rangle$, where $|v(\mathbf{K}_t)\rangle$ and $|c(\mathbf{K}_t)\rangle$ are valence and conduction band, respectively. To further proceed, the diagonal elements can be associated with the band velocity, while the off-diagonal elements relate to the derivative of dipole moment elements. We have

$$\begin{aligned} \mathbf{v_i}(\mathbf{K_t}) = j_{ii}(\mathbf{K}_t) &= -i\langle i|\nabla_{\mathbf{x}}|i\rangle = \nabla_{\mathbf{k}} E_i, \\ j_{il}(\mathbf{K}_t) &= -i\langle i|\nabla_{\mathbf{x}}|l\rangle = -\frac{d}{dt}\mathbf{d}_{il}(\mathbf{K}_t). \end{aligned} \tag{1.10}$$

$\mathbf{v}_i$ is the velocity of the band i, and E_i is the respective band energy. Using Eq.(1.8) and the fact that the total population is conserved; meaning the sum of the valence and conduction band populations equals one, $\rho_{vv} = 1 - \rho_{cc}$, we reach to the definitions of interband and intraband currents. Note that in doing so, the term

$$\int_{\overline{\mathrm{BZ}}} d^3K\, j_{vv}(\mathbf{K}_t) \tag{1.11}$$

is zero since the band velocity is the gradient of the band energy, and an integral of the gradient of any function that is periodic with the (Brillouin zone) BZ is zero [44]. In sum, we have:

1. **Interband HHG**: It is due to polarization build up between the valence and conduction band. It dominates in semiconductors and it can be described by a three-step process similar to atomic and molecular cases [36, 38, 45, 46, 47, 48, 49, 50]. See Fig. (1.4). The interband HHG can be calculated mathematically by inserting Eq. (1.8) into Eq. (1.10)

$$\langle \mathbf{j}_{er} \rangle \approx \frac{d}{dt} \int_{\overline{\mathrm{BZ}}} d^3K\, \mathbf{p}(\mathbf{K}, t), \tag{1.12}$$

where the $\mathbf{p}$ represents the polarization. For more detailed description of the

Eq. (1.12) see chapter (3).

2. **Intraband HHG**: It is due to the nonlinearity of the band velocity, see Fig. (1.4). It dominates in dielectrics [17, 18]. The intraband HHG can be calculated mathematically by the relation

$$\langle \mathbf{j}_{ra} \rangle \approx \int_{\overline{\mathrm{BZ}}} d^3K \, \mathbf{v}(\mathbf{K}_t) n_c(\mathbf{K}, t), \tag{1.13}$$

where the bandgap velocity is defined as the difference between the conduction band and the valence band velocities, $\mathbf{v}(\mathbf{K}) = \mathbf{v}_c(\mathbf{K}) - \mathbf{v}_v(\mathbf{K})$, and $n_c(t) = \int_{\overline{\mathrm{BZ}}} d^3K \, n_c(\mathbf{K}, t)$ is the conduction band population. For more detailed description of the Eq. (1.13) see chapter (3).

Having reviewed the key components across the four categories, **ionization in atomic media**, **ionization in solids**, **HHG in gases or atomic systems**, and **HHG in solids**, I present here a topic related to controlling HHG, whose underlying concepts will be applied in Chapter (5), when quantum sidebands are generated.

- **Achieving control over HHG, one possible way: two color HHG**

Due to interference, only odd harmonics are generated in centrosymmetric media, as discussed here[2], see Eq. (1.7), and Fig. (1.3). There is growing interest in achieving greater control over the high harmonic generation (HHG) process, particularly in enhancing conversion efficiency [51, 36]. Two-color high harmonic generation enables sub-cycle control of the generating electric field [51, 36]. Notably, this configuration causes consecutive half-cycles to differ rather than simply mirror each other in sign, see Fig. (1.5). This breakdown of inversion symmetry in the electric field has been exploited in various applications, for instance in the generation of both even and odd harmonics with enhanced conversion efficiency [51, 52, 36]. For more details related to generation of even harmonics see tutorial [2]. Eq. (1.7) can be written in a crude way to account for the second harmonic light added as a perturbation as follows [51, 36, 2]

$$d_F(t) e^{in\omega_0 t + i\sigma(t,\phi)} + d_F\left(t + \frac{\pi}{\omega_0}\right) e^{in\omega_0(t+\frac{\pi}{\omega_0}) + i\sigma(t+\frac{\pi}{\omega_0},\phi)} = d_F(t) e^{in\omega_0} \left[e^{i\sigma(t,\phi)} - e^{in\pi} e^{-i\sigma(t,\phi)} \right], \tag{1.14}$$

where we have used the fact that $\sigma(t + \frac{\pi}{\omega_0}, \phi) = -\sigma(t, \phi)$, σ is the time-dependent and ϕ-dependent phase added in the this unbalanced interferometer. ϕ is the phase difference between the second harmonic perturbation and the fundamental laser field. d_F is the

dipole moment due to the fundamental laser field as it is the strongest contribution. Eq. (1.14) leads to [2]

$$\begin{aligned} &2d_F(t)e^{in\omega_0 t}\cos(\sigma(t,\phi)), \quad \text{odd n case} \\ &2d_F(t)e^{in\omega_0 t}\sin(\sigma(t,\phi)), \quad \text{even n case} \end{aligned} \tag{1.15}$$

As can be seen in Eq. (1.15) the intensity of the even and odd harmonics depend on $I_{2n} \propto |\sin(\sigma(t,\phi))|^2$, and $I_{2n+1} \propto |\cos(\sigma(t,\phi))|^2$, respectively. Therefore, by modifying the relative intensity and phase of the second harmonic and the fundamental, one can modulate both even and odd harmonics.

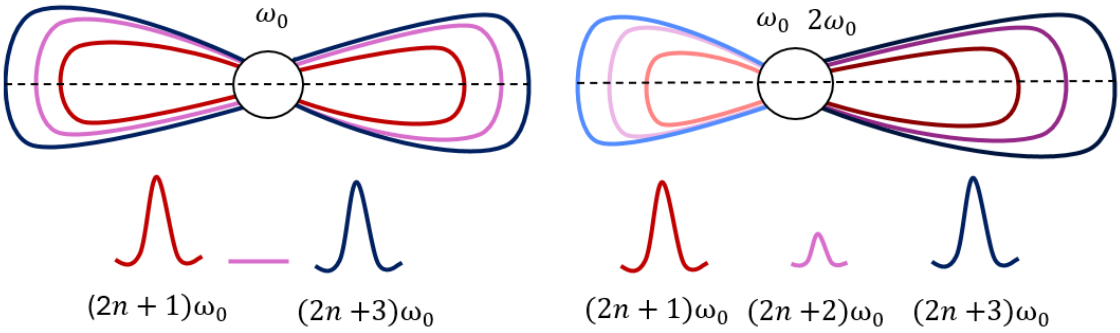

Figure 1.5: Two-color HHG breaks down the symmetry and enables the generation of even harmonic. See Eqs. (1.14, 1.15) [2].

1.2 Open quantum systems

In the previous section, HHG in solids was explained using the SAE approximation which is frequently used. But this is a strong approximation. In fact, in solids many body effects include electron-electron collisions, interactions between electrons and collective excitations such as plasmons and excitons, as well as electron-phonon interactions. Modeling the dynamical evolution of electrons in the presence of these effects remains a significant theoretical challenge. Therefore, we have chosen an avenue in which bosonic interactions are treated as a heat bath, see chapter (4). This does not apply to electron-electron collisions which are fermionic in nature. Developing a fermionic heat bath will be subject to future research.

To support the reader's understanding, this section provides a summary of the foundational

concepts of how to treat matter in a heat bath. This is required for understanding chapter (4).

- **Closed and open quantum systems**: Realistic physical systems are in contact with their environment, and any quantum system that interacts with its environment is called an open quantum system [53]. The reason why closed quantum systems are not realistic is that firstly, there is no such condition to prepare a perfectly closed system, and secondly one always needs to do measurements on the system in study. The measurement process in itself creates a flow of information to and from the system [53]. In contrast to closed quantum systems where evolution can be described by unitary time evolution, deriving a mathematical description of the dynamics of open quantum systems is a complicated task. The interaction between the system of interest and the environment introduces some correlations, and the evolution of the system can not be described by local unitary operators anymore [54, 3, 53, 55, 56]. A brief general mathematical formulation for open and closed quantum systems is given below.

  An equation of motion for a closed system is encoded by the Schrödinger equation given below [57]

  $$i\hbar\frac{\partial}{\partial t}|\psi(t)\rangle = \hat{H}|\psi(t)\rangle. \tag{1.16}$$

  Note that Eq. (1.16) is linear and deterministic. That means if we know the state $|\psi(t_0)\rangle$, later time states like $|\psi(t)\rangle$ can be predicted by Eq. (1.16). The time evolution of $|\psi\rangle$ can be described by a unitary time evolution operator as follows

  $$|\psi(t)\rangle = \hat{U}(t,t_0)|\psi(t_0))\rangle, \tag{1.17}$$

  where the unitary operator $\hat{U}(t,t_0)$ is defined as $\hat{U}(t,t_0) = e^{-\frac{i}{\hbar}\hat{H}(t-t_0)}$ [57].

  On the other hand, the equation of motion for the density operator, $\rho = |\psi\rangle\langle\psi|$, is given by the Liouville-von Neumann equation [3]

  $$i\hbar\frac{\partial}{\partial t}\hat{\rho}(t) = [\hat{H},\hat{\rho}(t)]. \tag{1.18}$$

  Similar to the Schrödinger equation the evolution of the Liouville-von Neumann equation can be written as

  $$\hat{\rho}(t) = \hat{U}(t,t_0)\,\hat{\rho}(t_0)\,\hat{U}^{\dagger}(t,t_0) = \mathcal{U}(t,t_0)\,\hat{\rho}(t_0), \tag{1.19}$$

where $\mathcal{U}(t,t_0) = e^{-\frac{i}{\hbar}\mathcal{L}(t-t_0)}$ is the time evolution superoperator with $\mathcal{L}$ being the Liouville superoperator [3].

Density operator formalism given in Eqs. (1.18, 1.19), is suitable for the description of quantum systems whose state is not known completely, or for the description of subsystems of a composite quantum system. [3, 55]

In an open quantum system, one has a system of interest, S, that interacts with an environment (called a heat bath when we have a reservoir in thermal equilibrium at temperature T), B. The total Hamiltonian is written as the sum of the system and environment Hamiltonians, plus an interaction part that is responsible for the correlations (entanglement) and the reason why the evolution cannot be written using local unitary operators anymore.

$$\hat{H}_{total} = \hat{H}_S \otimes \hat{I}_B + \hat{I}_S \otimes \hat{H}_B + \hat{H}_I. \tag{1.20}$$

Knowing the formulation for the density operator, one can start formulating an

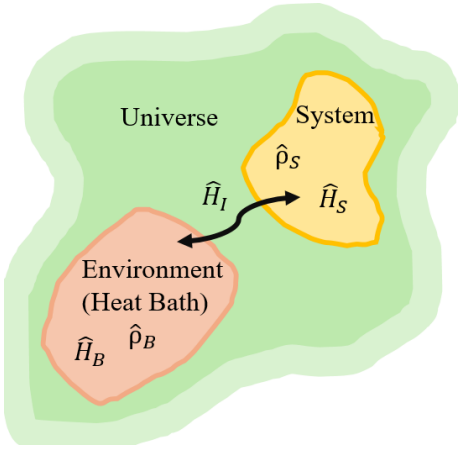

Figure 1.6: A quantum system in contact with its environment. The total Hamiltonian is $\hat{H}_{total} = \hat{H}_S \otimes \hat{I}_B + \hat{I}_S \otimes \hat{H}_B + \hat{H}_I$.

equation of motion for an open quantum system. The goal is to derive an equation of motion for the reduced density operator, obtained by taking the trace of the total density operator with respect to all heat bath degrees of freedom.

$$\hat{\rho}_s(t,t_0) = \mathrm{tr}_{bath}\left\{\hat{\rho}_{total}(t,t_0)\right\}. \tag{1.21}$$

If the heat bath bases that are used in tracing over the total density operator in

Eq. (1.21) are time-independent, one can bring the time derivative inside the trace. Using the Liouville von Neumann equation, Eq. (1.18) one can write

$$\begin{aligned}\frac{\partial}{\partial t}\hat{\rho}_s(t,t_0) &= \mathrm{tr}_{bath}\left\{\frac{\partial}{\partial t}\hat{\rho}_{total}(t,t_0)\right\}\\ &= -\frac{i}{\hbar}\mathrm{tr}_{bath}\Big\{\left[\hat{H}_S\otimes\hat{I}_B+\hat{I}_S\otimes\hat{H}_B+\hat{H}_{SB},\ \hat{\rho}_{total}(t,t_0)\right]\Big\}.\end{aligned} \tag{1.22}$$

Further simplifying Eq. (1.22) is possible by using the fact the H_S is not affected by tracing over the heat bath degrees of freedom. Thus, we have

$$\frac{\partial}{\partial t}\hat{\rho}_s(t,t_0) = -\frac{i}{\hbar}\left[\hat{H}_S,\ \hat{\rho}_s(t,t_0)\right] - \frac{i}{\hbar}\mathrm{tr}_{bath}\Big\{\left[\hat{I}_S\otimes\hat{H}_B+\hat{H}_{SB},\ \hat{\rho}_{total}(t,t_0)\right\}\Big]. \tag{1.23}$$

Since H_B acts only in the state space of the heat bath, we can use the cyclic properties of the trace in the first part of the second term of RHS part. Then, we remain with

$$\frac{\partial}{\partial t}\hat{\rho}_s(t,t_0) = -\frac{i}{\hbar}\left[\hat{H}_S,\ \hat{\rho}_s(t,t_0)\right] - \frac{i}{\hbar}\mathrm{tr}_{bath}\Big\{\left[\hat{H}_{SB},\ \hat{\rho}_{total}(t,t_0)\right]\Big\}. \tag{1.24}$$

Eq. (1.24) is not closed in $\hat{\rho}_S$ yet since it contains $\hat{\rho}_{total}(t,t_0)$ in the second term of the RHS of the equation. One, therefore, needs to use approximation methods to develop a closed form formalism for the reduced density operator which is called a master equation [3].

- **Markovian and non-Markovian regimes**: A number of different methods and approximations exist to obtain the equation of motion for the reduced density matrix. As discussed, Eq. (1.24) is the starting point to obtain such equations. There are two main categories of equations: Markovian or time-convolutionless type of equations, and non-Markovian type of equations. The characteristic feature of non-Markovianity is the memory effects. In a non-Markovian regime, the determination of $\hat{\rho}(t)$ requires knowledge about $\hat{\rho}(t-\tau)$ or the density operator at earlier times while in a Markovian regime equations are time local. One can do a Markov approximation to achieve a Markovian master equation from a non-Markovian one by assuming that $\hat{\rho}(t)$ does not change much in time τ_{memory}, the characteristic time of memory effects, so $\hat{\rho}(t-\tau)$ can be approximated by $\hat{\rho}(t)$. There have been many efforts to mathematically define these memory effects referred to as quantum non-Markovianity. For a review please refer to this paper [58]. In what follows, important equations of Markovian and non-Markovian types are briefly discussed.

– **Nakajima-Zwanzig (NZ) master equations**: NZ equations are generally of the non-Markovian type and are based on a projection superoperator. Their advantage lies in the fact that the perturbation series can be summed exactly, eliminating the need to limit the analysis to second order approximations which are valid only for weak-system-bath coupling. They can be written in the interaction picture as [3]

$$\frac{\partial}{\partial t}\hat{\rho}_S^{(I)}(t) = -\frac{i}{\hbar}\mathrm{tr}_{bath}\left\{\mathcal{L}_{SB}^{(I)}(t)\hat{B}\right\}\hat{\rho_S}^{(I)}(t) - \frac{1}{\hbar}\int_{-\infty}^{t} d\tau\ \mathrm{tr}_{bath}\left\{\mathcal{L}_{SB}^{(I)}(t)\mathcal{S}_{\mathscr{L}}(t,\tau)\mathscr{L}\mathcal{L}_{SB}^{(I)}(\tau)\hat{B}\right\}\hat{\rho_S}^{(I)}(\tau). \quad (1.25)$$

$\mathscr{L}$ is the orthogonal superoperator to the projection superoperator that is defined as

$$\mathscr{P}... = 1 - \mathscr{L}... = \hat{B}\,\mathrm{tr}_{bath}\{...\}. \quad (1.26)$$

$\hat{B}$ is the equilibrium density operator of the heat bath. $\mathcal{L}_{SB}^{(I)}$ and $\mathcal{S}_{\mathscr{L}}(t,\tau)$ are given by the following

$$\mathcal{L}_{SB}^{(I)}... = \left[\hat{H}_{SB}^{(I)},\ ...\right], \quad (1.27)$$

$$\mathcal{S}_{\mathscr{L}}(t,\tau) = \hat{T}\exp\left\{-i\int_{-\infty}^{t} d\tau\mathscr{L}\mathcal{L}_{SB}^{(I)}(\tau)\right\}. \quad (1.28)$$

By expanding $\mathcal{S}_{\mathscr{L}}(t,\tau)$ into the Dyson series, for example, one can include as many orders of the perturbation series in $\hat{H}_{SB}$ as needed in Eq. (1.25).

– **Redfield and Lindblad master equations** : In the category of time-convolution-free or Markovian equations of motion, two important types of equations are the Redfield [59] and Lindblad [60] types. Where the system-bath coupling is weak, second order perturbation theory in addition to a Markov approximation lead to Redfield type of master equations. The problem with the Redfield type of equation is that it does not obey the positivity condition for the density matrix, and can result in negative populations. These types of equations usually need more approximations such as the Rotating Wave Approximation (RWA) and the secular approximation, where the population (diagonals) and coherences (off diagonals) are decoupled from each other. Accounting for these approximations leads to the second group or the Lindblad master equations. Lindblad type of equations, on the contrary, obey the positivity condition

[3, 53].

The Lindblad equation [60] is written as

$$\frac{\partial}{\partial t}\hat{\rho}_S(t) = \mathcal{L}\hat{\rho}_S(t). \tag{1.29}$$

The most general form of the superoperator $\mathcal{L}$ can be written as follows [60, 3, 53]

$$\mathcal{L}\hat{\rho}_S(t) = -\frac{i}{\hbar}\left[\hat{H},\ \hat{\rho}_s(t)\right] + \sum_m \gamma_m \left(\hat{A}_m \rho_S(t) \hat{A}_m^\dagger - \frac{1}{2}\left[\hat{A}_m^\dagger \hat{A}_m,\ \hat{\rho}_S(t)\right]_+\right). \tag{1.30}$$

m is the state of the system. In the case of two level atom m can be 1 and 2. $\hat{A}_m$ is called the Lindblad operator and for the case of pure dephasing is $\hat{A}_m = |m\rangle\langle m|$. γ_m is the relaxation rate. If one wants to consider decay for the case of two level system for example, $\hat{A}$ would be $\hat{\sigma}_-$, the lowering operator. Since there is no decay defined for the ground state to lower states, one obtains for $\mathcal{L}$ for the case of the two level system

$$\mathcal{L}\hat{\rho}_S(t) = -\frac{i}{\hbar}\left[\hat{H},\ \hat{\rho}_s(t)\right] + \Gamma\left(\hat{\sigma}_-\hat{\rho}_S(t)\hat{\sigma}_+ - \frac{1}{2}\left[\hat{\sigma}_-\hat{\sigma}_+,\ \hat{\rho}_S(t)\right]_+\right). \tag{1.31}$$

Redfield [59] and Lindblad equations can be connected in the following way. The Redfield equation is given as follows

$$\frac{\partial}{\partial t}\hat{\rho}_S(t) = -\frac{i}{\hbar}\left[\hat{H},\ \hat{\rho}_s(t)\right] - \frac{1}{\hbar^2}\sum_u \left[\hat{K}_u,\ \hat{\Lambda}_u\hat{\rho}_s(t) - \hat{\rho}_s(t)\hat{\Lambda}_u^+\right]. \tag{1.32}$$

$\hat{K}_u$ is the system part of the interaction Hamiltonian. Suppose $\hat{H}_{SB}$ can be factorized in the system part and bath part; then, we have

$$\hat{H}_{SB} = \sum_u \hat{K}_u \hat{E}_u, \tag{1.33}$$

here u accounts for the different contributions for a specific model, and $\hat{E}_u$ is the heat bath part of the interaction Hamiltonian. $\hat{\Lambda}_u$ is defined as

$$\hat{\Lambda}_u = \sum_\nu \int_0^\infty d\tau C_{u\nu}(\tau)\hat{K}_\nu^{(I)}(-\tau). \tag{1.34}$$

where C_{uv} is the correlation function. $\hat{K}_v^{(I)}$ is the system part of the interaction Hamiltonian in the interaction picture defined as

$$\hat{K}_v^{(I)}(-\tau) = e^{-\frac{i}{\hbar}\hat{H}_s\tau}\hat{K}_v e^{+\frac{i}{\hbar}\hat{H}_s\tau}. \tag{1.35}$$

Further approximations to Eq. (1.32) such as the Rotating Wave Approximation (RWA) and secular approximation turn it to the Lindblad type of equations, Eq. (1.30) [59, 3, 53].

- **Spin-boson model**: Here, we bring a formalism to model system environment coupling which is called spin-boson model. It allows for a very efficient and closed form solution. We will use it in chapter (4). The Hamiltonian is given by

$$\hat{H} = \frac{\varepsilon}{2}\hat{\sigma}_z + \frac{1}{2}\Omega(t)\hat{\sigma}_x + \sum_q \omega_q \hat{b}_q^\dagger \hat{b}_q + \hat{\sigma}_z \sum_q g_q \left(\hat{b}_q + \hat{b}_q^\dagger\right). \tag{1.36}$$

We have $\hat{\sigma}_z = \hat{a}_2^\dagger \hat{a}_2 - \hat{a}_1^\dagger \hat{a}_1$ and $\hat{\sigma}_x = \hat{a}_2^\dagger \hat{a}_2 + \hat{a}_1^\dagger \hat{a}_1$. g_q is the coupling between the bath mode q and the two-level system. spin-boson model [61], Eq. (1.36), is one of the fundamental models suitable for describing many physical systems. It describes a coupling between a two-level system and an environment of harmonic oscillators. The coupling Hamiltonian between the two-level system and the environment is given by a linear combination of the Pauli matrices, here $\hat{\sigma}_z$, and the position operator of the environment, $\hat{b}_q + \hat{b}_q^\dagger$, with some coupling coefficients, g_q [54, 3, 53, 56, 61].

- **Properties of the environment**: In previous sections , a starting point to write a quantum master equation was presented, see Eq. (1.24). Since the environment was considered as a system with many degrees of freedom, acquiring the dynamics of the total density operator was impossible and not considered. Thus, averaging over the degrees of freedom of the environment was done. Thus, the use of the formulations of quantum statistics is appropriate[1]. Looking at Eq. (1.24), besides the fact that one does need to determine the bases over which the trace is taken, a mathematical way to formulate the environment properties is required as well. This mathematical formulation that includes the coupling strength information is given through the spectral density or similarly the correlation function of the environment. In the

[1] A point to note here is that a quantum system can be coupled to a microscopic environment with a few degrees of freedom, and one can still call that irrelevant part an environment, but this is not the case in this thesis. In this thesis an environment consists of many degrees of freedom.

following, using quantum statistics, the determination of the density operator of the heat bath, an important type of environment, is given. The correlation function and spectral density are defined, afterwards. In the end, several types of important spectral densities are presented.

– **Density operator of the environment (Heat bath)**: In most cases, the environment in contact with the system is in thermal equilibrium, kept at a fixed temperature T. This is called a heat bath for the system. The statistical operator of the heat bath using quantum statistical theory is given by the canonical ensemble [62]. Thus, the density operator of the heat bath, the operator $\hat{B}$, is given by

$$\hat{B} = \frac{e^{-\hat{H}_0\beta}}{\mathrm{tr}_{bath}\left\{e^{-\hat{H}_0\beta}\right\}}, \tag{1.37}$$

where $\beta = \frac{1}{k_b T}$, k_b is the Boltzmann constant. In the instance of phonons, where the harmonic approximation can be made, the heat bath Hamiltonian, $\hat{H}_0$, is defined as $\hat{H}_0 = \sum_q \omega_q \left(\hat{b}_q^\dagger \hat{b}_q + \frac{1}{2}\right)$. Summation is made over all modes q. The denominator in Eq. (1.37) is called the partition function, Z [62]. We have

$$\begin{aligned} Z =& \mathrm{tr}_{bath}\left\{e^{-\beta\sum_q \omega_q\left(b_q^\dagger b_q+\frac{1}{2}\right)}\right\} = \prod_{q=q_1}^{q_n}\sum_{n_q=0}^{\infty}\langle n_q|e^{-\beta\omega_q\left(n_q+\frac{1}{2}\right)}|n_q\rangle \\ =& \prod_{q=q_1}^{q_n}\frac{e^{-\beta\omega_q/2}}{1-e^{-\beta\omega_q}} = \prod_{q=q_1}^{q_n}\frac{\sqrt{z_q}}{1-z_q}, \end{aligned} \tag{1.38}$$

where $z_q = e^{-\beta\omega_q}$, and we have used the relation $\sum_{n=0}^{\infty} e^{-nx} = \frac{1}{1-e^{-x}}$ [4].

– **The environment correlation function**: In writing a master equation, terms involving the average over the products of heat bath operator part of $\hat{H}_{SB}$ at different times are encountered, see Eq. (1.33). The environment correlation function is usually defined as the following [3]

$$\begin{aligned} \hat{H}_{SB} &= \sum_u \hat{K}_u \hat{E}_u, \\ C_{uv}(t-t') &= \langle \hat{E}_u(t)\hat{E}_v(t')\rangle_e - \langle \hat{E}_u\rangle_e\langle \hat{E}_v\rangle_e, \end{aligned} \tag{1.39}$$

where u and v account for different contributions in a model.$\hat{K}_u$ is the system

part of the interaction Hamiltonian, and $\hat{E}_u$ is the heatbath part of the interaction Hamiltonian. $\langle ... \rangle_e$ means averaging with respect to the environment. In the density operator formalism, we have $\langle \hat{A} \rangle_e = \mathrm{tr}\left\{\hat{\rho}_e \hat{A}\right\}$. If u and v are chosen to be the same one reaches the environment autocorrelation function. It is useful to define $\tau_c = 2\pi/\omega_c$ the time at which the correlation function decays to zero, ω_c is the cutoff frequency. For the harmonic oscillator heat bath, the correlation function can be calculated through the given spectral density [3]. In other words, calculating the correlation function requires knowledge of the spectral density [3].

– **The environment spectral density**: Spectral density sometimes referred to as the Fourier transform of the correlation function, in the general form, is defined as [3]

$$J(\omega) = \sum_q \frac{g_q^2}{\omega_q^2} \delta(\omega - \omega_q). \tag{1.40}$$

where g_q is related to the coupling strength to the mode q. The correlation function of the heat bath of bosonic harmonic oscillator is given as follows [3]

$$C(t) = \int_0^\infty d\omega \left(\cos(\omega t) \coth\left(\frac{\beta\omega}{2}\right) - i \sin(\omega t) \right) J(\omega). \tag{1.41}$$

Eq. (1.41) is calculated for the bosonic heatbath. We have

$$\hat{E}_u \propto \sum_q \frac{g_q}{\omega_q} \hat{x}_E, \tag{1.42}$$

where $\hat{x}_E$ is the position operator of the environment.
In the case of many modes we define $\sum_q \frac{g_q^2}{\omega_q^2} \to \int_0^\infty J(\omega) d\omega$. Depending on the problem at hand, one might choose different forms of spectral densities. Some important types are given below. Once the spectral density is defined, the correlation function of the heat bath can be calculated using Eq. (1.41)[2].
In the high-temperature limit, Eq. (1.41) simplifies to

$$C(t) = \left(\frac{2}{\beta} + i\partial_t\right) \int_0^\infty d\omega \frac{1}{\omega} \cos(\omega t) J(\omega). \tag{1.43}$$

[2]In literature, there are two ways to define spectral density. We pulled ω^2 inside the definition of the spectral density Eq. (1.40). Thus, Eq.(1.41) does not have the factor ω^2, when comparing with reference [3].

Eq. (1.43) shows that the real part of the correlation function is temperature dependent while the imaginary part is independent of temperature. At the room temperature we have $\beta \approx 10^3$, in atomic units.

There are three most commonly used types of spectral densities as follow:

* **Ohmic spectral density**: Ohmic spectral density is defined as the following

$$J(\omega) = j_o \frac{\omega}{\omega_c^2} e^{-\frac{\omega}{\omega_c}}. \tag{1.44}$$

The correlation function in the limit of high temperature for the Ohmic spectral density using Eq. (1.43) would be

$$C(t) = \left(\frac{2}{\beta} + i\partial_t\right) \frac{j_o}{\omega_c} \frac{1}{1+\omega_c^2 t^2}. \tag{1.45}$$

* **Debye spectral density**: Debye spectral density is defined as the following

$$J(\omega) = j_d \frac{\omega}{\omega^2 + \omega_d^2}. \tag{1.46}$$

The correlation function in the limit of high temperature for the Debye spectral density using Eq. (1.43) would be

$$C(t) = \left(\frac{2}{\beta} + i\partial_t\right) \frac{\pi}{\omega_d} e^{-\omega_d |t|}. \tag{1.47}$$

* **Gaussian spectral density**: Gaussian spectral density is defined as the following

$$J(\omega) = j_g \frac{\omega}{\omega_g^2} e^{-\frac{\omega^2}{\omega_g^2}}. \tag{1.48}$$

The correlation function in the limit of high temperature for the Gaussian spectral density using Eq. (1.43) would be

$$C(t) = \left(\frac{2}{\beta} + i\partial_t\right) \frac{j_g \sqrt{\pi}}{2\omega_g} e^{-\frac{t^2\omega_g^2}{4}}. \tag{1.49}$$

- **The studies of the breakdown of the single active electron (SAE) approximation in solids, the need to add dephasing effects to both ionization and HHG theories in the solid cases**:

In modeling ionization and HHG accurately one should consider dephasing effects, particularly in solid cases. HHG has applications in both spectroscopy [63] and microscopy [64] while ionization plays a crucial role in micromachining [14]. Accordingly, a deeper understanding of dephasing effects in both HHG and ionization is crucial for advancing these areas. Dephasing refers to the loss of phase coherence resulting from the interaction between an electron and its environment. In light–matter interactions, the relaxation time approximation T_2 is the most commonly used model to describe this process [65, 45]. This relaxation time approximation leads to non-physical, overestimation of ionization and HHG currents [5, 66]. As stated before, the SAE approximation in semiconductor Bloch equations (SBEs), and in the length gauge [43] is the widely used approach that offers a decomposition of the induced current into intraband and interband contributions. SAE approximation relies on the assumption that the interaction between a single electron and the intense laser field dominates all other interactions. However, this is clearly not the case, especially in solids, where additional interactions are also of great importance [66]. The electron interacts with holes, other electrons, and collective excitations such as plasmons and phonons. These interactions induce dephasing in the oscillatory part of mathematical formulations that can suppress specific ionization and HHG channels [5, 66]. Dephasing in open quantum systems is treated as a quantum statistical heat bath of bosonic harmonic oscillators [3, 53, 61]. Following that one can borrow this idea in strong field physics [66]. See Fig. (1.7). We used the popular spin boson model and we integrated into the semiconductor Bloch equations governing intense laser solid-state physics [66]. The spin boson model is a popular model used to describe dephasing effects [61, 67, 68, 69]. Although the model was firstly used in the area of condensed matter [70, 61], it found usage in areas such as chemical reactions [71], light harvesting complexes [72], and trapped ions [73] later. For strong coupling regimes, where the system and environment are coupled strongly one can use polaron transformation of spin boson model [74, 75, 76, 77]. Some of these studies use variational polaron transformation [75] while other studies even add time dependent variational methods to address relevant non equilibrium problems; therefore, upgrading the previous method [77]. Besides, in the continuum limit, spectral density is often used to avoid material dependent many body calculations [78]. In the case of phonons as an illustration, several studies have investigated the use of different spectral densities [79, 80].

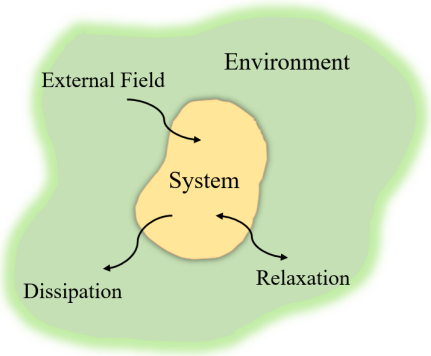

Figure 1.7: A quantum system in contact with its environment. The information is exchanged by relaxation and dissipation. A driving external field is also present [3].

1.3 Quantum optics

While strong field physics has been treated with classical electromagnetic fields so far, recently quantum properties of strong field physics have become of interest. We give here a brief introduction to quantum optics strong field physics and the most important elements of quantum optics.

- **Quantization of a single mode field**: Here, I follow the derivation given in Gerry and Knight's book [4], and briefly discuss the important parts. Starting from the question of confining a single mode, linearly polarized (in the x direction) radiation into a 1D cavity (along z direction with length L). Using Maxwell's equations and the necessary boundary conditions, one can obtain the following results for the electric and magnetic field [4]

$$\mathbf{F}(z,t) = \hat{x}\left(\frac{2\omega_n^2}{V\epsilon_0}\right)^{\frac{1}{2}} q(t)\sin(kx),$$
$$\mathbf{B}(z,t) = \hat{y}\left(\frac{\mu_0\epsilon_0}{k}\right)\left(\frac{2\omega_n^2}{V\epsilon_0}\right)^{\frac{1}{2}} \dot{q}(t)\cos(kx). \tag{1.50}$$

V later denotes the quantization volume, which corresponds to the cavity volume. ω_n are the allowed frequencies, $\omega_n = cn\pi/L$. Here q will act as a canonical position

and $\dot{q}$ as a canonical momentum. For a single mode field the energy is given by [4]

$$E = \frac{1}{2}\int dV \left[\epsilon_0 \mathbf{F}^2 + \frac{1}{\mu_0}\mathbf{B}^2\right]. \tag{1.51}$$

By using Eqs. (1.50), it is very easily verified that the energy can be written in the form of a harmonic oscillator Hamiltonian for $m = 1$. Therefore, we have $H = \frac{1}{2}(p^2 + \omega^2 q^2)$ [4].

- **Quadrature operators and phase space representation**: It is convenient to define two operators that are related to the position and momentum operators (from quantization of the harmonic oscillator equations obtained from Maxwell's equations) but are scaled to be dimensionless. We have

$$\begin{aligned} \hat{\mathbf{x}}_1 &= \frac{1}{2}(\hat{a} + \hat{a}^\dagger) = \sqrt{\frac{\omega}{2\hbar}}\hat{q} \qquad \text{(X quadrature)}, \\ \hat{\mathbf{x}}_2 &= \frac{1}{2i}(\hat{a} - \hat{a}^\dagger) = \frac{\hat{p}}{\sqrt{2\hbar\omega}} \qquad \text{(P quadrature)}. \end{aligned} \tag{1.52}$$

X and P quadratures are associated with the field amplitudes oscillating $\pi/2$ out of phase, and together they are the foundation of a phase-space representation similar to the classical case [4]. Note that in contrast to classical phase space representation where the state can be localized, here there is uncertainty due to the commutation relations between quadratures [57]. See Fig. (1.8). Three main quasi-probability distributions are commonly used throughout the literature: the P distribution, the Q distribution, and the Wigner function [4]. Here, we only use the Wigner function which is therefore explained in further detail below.

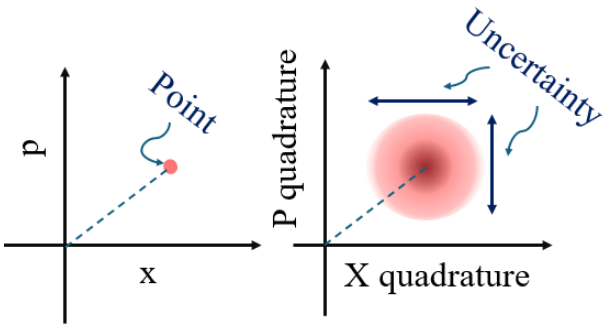

Figure 1.8: Phase-space representation of classical (left) and quantum (right) harmonic oscillator.

- **Wigner distribution function**: As mentioned before, among three mostly used quasi probability distributions, here in this thesis, we use the Wigner function. Therefore, I present the necessary information in this section. Wigner function is defined in one of the following forms as [4]

$$W(p,q) = \frac{1}{2\pi\hbar}\int_{-\infty}^{\infty} \psi^*\left(q-\frac{1}{2}\xi\right)\psi\left(q+\frac{1}{2}\xi\right)e^{ip\xi/\hbar}d\xi,$$
$$W(q,p) = \frac{1}{2\pi\hbar}\int_{-\infty}^{\infty} \langle q+\frac{1}{2}\xi|\rho|q-\frac{1}{2}\xi\rangle e^{ip\xi/\hbar}d\xi. \tag{1.53}$$

Eqs. (1.53) are in the wavefunction or density matrix representation, depending on the problem. Note that the wavefunction ψ or the density matrix ρ can be written in the phase space representation which is what is given in Eq. (1.53). Using the definition of Delta function, δ, one can easily verify the following relations. We have

$$\int_{-\infty}^{\infty} W(q,p)dp = |\psi(q)|^2,$$
$$\int_{-\infty}^{\infty} W(q,p)dq = |\phi(p)|^2. \tag{1.54}$$

Eqs. (1.54) are giving the probability density for q and p, respectively [4, 81]. The projection of the time-evolving Wigner function onto the $\hat{\mathbf{x}}_1$ quadrature yields its expectation value as a function of time. This is proportional to the expectation value of the electric field. It can be readily shown that the time evolution of a coherent state of light manifests as a mere clockwise rotation in phase space [4]. In Fig. (1.9)

the Wigner function of coherent state of light as well as vacuum state are shown. As can be seen, coherent light corresponds to a displaced vacuum state in phase space, whose time evolution is represented by a clockwise rotation, as illustrated by the arrow.

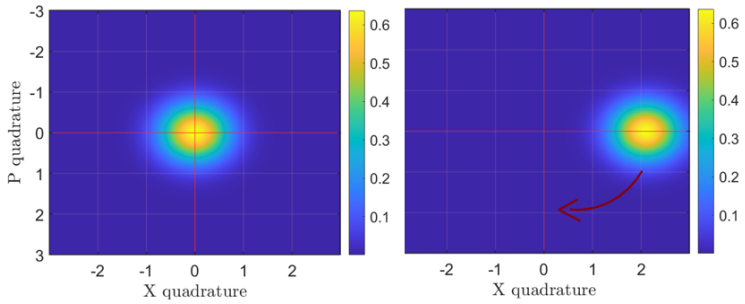

Figure 1.9: The Wigner functions for vacuum (left) and coherent (right) state of light are plotted. Coherent light corresponds to a displaced vacuum state in phase space, whose time evolution is represented by a clockwise rotation, as illustrated by the arrow.

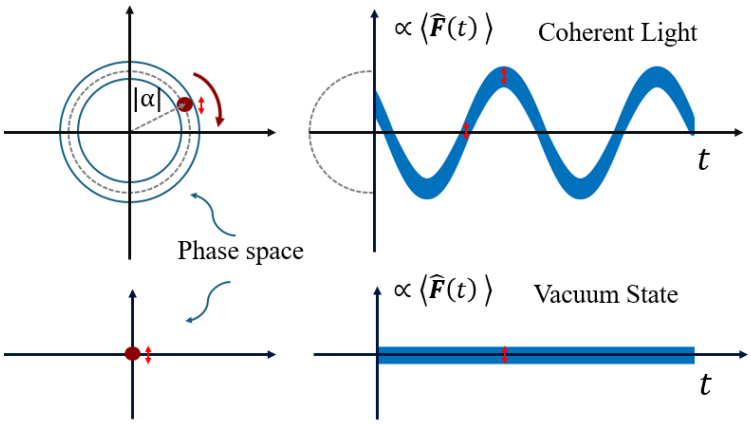

Figure 1.10: Time evolution of the Wigner functions of coherent and vacuum states in phase space are illustrated. The projection along the quadrature is proportional to the expectation value of the field [4].

The Wigner function is one theoretical tool to characterize the nature of non classical light states. Another important indicator of non-classicality is the quantum second order correlation function which is discussed below.

- **Quantum second order correlation function, $g^{(2)}(\tau)$:** The idea of $g^{(2)}(\tau)$ was pioneered by the Hanbury Brown and Twiss (HBT) experiment [82]. They developed

a correlation function based on intensity rather than the field [82, 4]. A simplified schematic of the HBT setup is given in Fig. (1.11). The setup measures a delayed coincidence rate, where the delay is shown by τ. The two arms are considered to have equal size. In general, they can vary and one can obtain the generalized space-dependent $g^{(2)}$ instead [4].

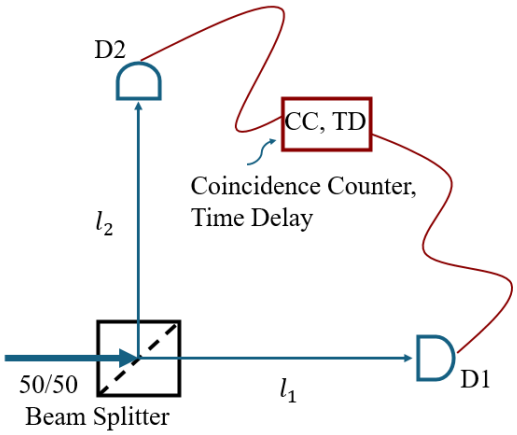

Figure 1.11: Schematic of HBT experiment [4]

The classical second order correlation function is calculated through [4]

$$\gamma^{(2)}(\tau) = \frac{\langle I(t+\tau)I(t)\rangle}{\langle I(t)\rangle^2}. \tag{1.55}$$

It can be shown that it can only get values between 1 to ∞, and $\gamma^{(2)}(\tau) < \gamma^{(2)}(0)$, meaning that the correlation drops as delay increases. Rewriting everything in terms of operators, one obtains the quantum second-order correlation function, defined as [4, 83]

$$g^{(2)}(\tau) = \frac{\langle \hat{\mathbf{F}}(t)^{(-)}\hat{\mathbf{F}}(t+\tau)^{(-)}\hat{\mathbf{F}}(t)^{(+)}\hat{\mathbf{F}}(t+\tau)^{(+)}\rangle}{\langle \hat{\mathbf{F}}(t)^{(-)}\hat{\mathbf{F}}(t)^{(+)}\rangle\langle \hat{\mathbf{F}}(t+\tau)^{(-)}\hat{\mathbf{F}}(t+\tau)^{(+)}\rangle}, \tag{1.56}$$

where $\hat{\mathbf{F}}^{(+)}$ is the positive frequency components of the field. For a single mode field one obtains the simplified relation as follows [4]

$$g^{(2)}(\tau) = g^{(2)}(0) = \frac{\langle \hat{a}^\dagger \hat{a}^\dagger \hat{a}\hat{a}\rangle}{\langle \hat{a}^\dagger \hat{a}\rangle} = 1 + \frac{\langle (\Delta\hat{n})^2\rangle - \langle \hat{n}\rangle}{\langle \hat{n}^2\rangle}. \tag{1.57}$$

- **Photon number statistics**: Knowledge about $g^{(2)}$ provides insight into photon

number statistics. There are three main categories of statistical distribution here [4].

1. **Poissonian statistics**: Poissonian distribution is generally given by the following formula

$$P(m) = \frac{\overline{m}^m e^{-\overline{m}}}{m!}, \tag{1.58}$$

where m is the number of photons in this context, and $\overline{m}$ is the photon number average. The main property of this distribution is that the mean and variance are equal, and it corresponds to states having $g^{(2)} = 1$. Note that the more the mean value, $\overline{m}$, deviates from zero the more the discrete shape is similar to the continuous normal distribution. See Fig. (1.12) for three different valuse of $\overline{m}$.

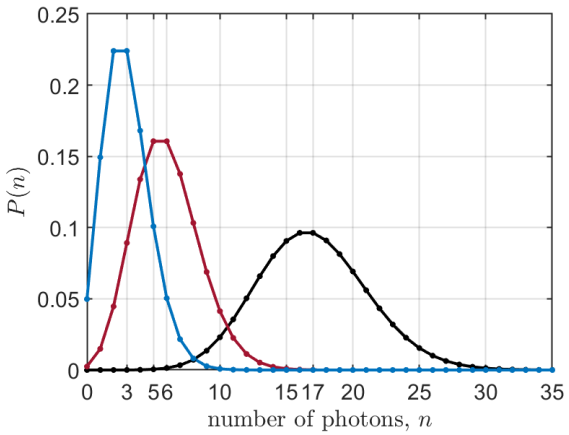

Figure 1.12: Three differennt Poissonian distributions with mean photon numbers, 3 (blue), 6 (red), 17 (black)

2. **Super-Poissonian statistics**: In this case, variance > mean. It corresponds to light having $g^{(2)} > 1$ [4].
3. **Sub-Poissonian statistics**: In this case, variance < mean. It corresponds to light having $g^{(2)} < 1$. (This alone demonstrates non-classical behavior, whereas super-Poissonian statistics may or may not have quantum properties.) [4]

Below is a simple schematic illustrating the deviation from a Poissonian distribution toward sub-Poissonian and super-Poissonian statistics, highlighting the distinctions between them [4].

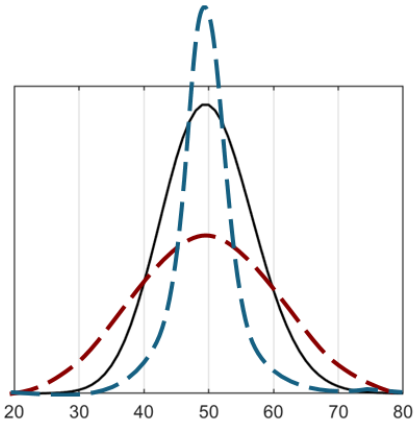

Figure 1.13: Qualitative, Poissonian distribution (black), Super-Poissonian (red), and Sub-Poissonian (blue) is plotted for the same average photon number of 50; Y-axis is the probability.

- **Photon bunching and photon anti-bunching**: Photon bunching and anti-bunching are additional key characteristics of light. Photon bunching is when photons arrive in pairs that mathematically translates to $g^{(2)}(\tau) < g^{(2)}(0)$. This property in itself is not an indication of quantum light. In the case of anti-bunching, we observe $g^{(2)}(\tau) > g^{(2)}(0)$, which serves as a clear signature of nonclassical light. Random light states satisfy the relation $g^{(2)}(\tau) = g^{(2)}(0)$, making $g^{(2)}$ to be independent of delay time. Note that photon bunching, and anti-bunching are characteristics of multimode field. For the single mode field $g^{(2)}$ is independent of delay time. A qualitative schematic illustrating the distinctions among these three cases is shown in Fig. (1.14). For a big enough (τ), $g^{(2)}(\tau)$ in all three cases approaches 1. The red dots in the bottom plot shows perfectly anti-bunched light having zero variance in photon number. Note that anti-bunched and sub-Poissonian light, as well as bunched and super-Poissonian light, are often confused but are not equivalent and exchangeable [4].

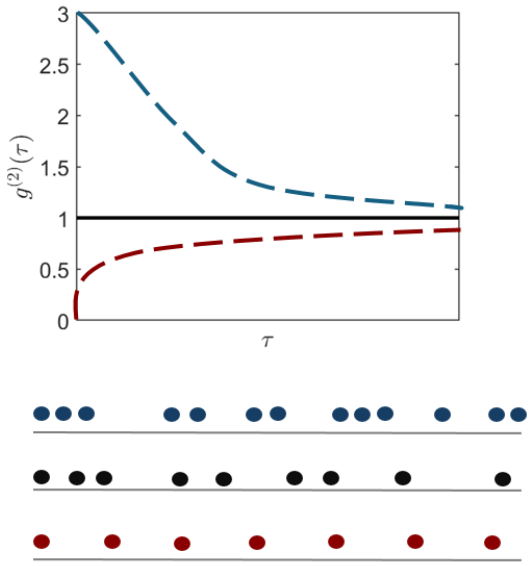

Figure 1.14: Top: Photon bunched light (blue), Random light (black), and Photon anti-bunched light (red) is illustrated, qualitatively. Note, that the top plot shows one hypothetical example; as we noted anti-bunched photons can also have $g^{(2)} > 1$. Bottom: Photon bunching: photons arrive in pairs, Random light: photons are arriving totally independent of each other, Photon anti-bunching: the illustrated case shows nearly zero variance in photon number corresponding to the perfectly anti-bunched light [4].

- **Selected quantum states of light: Squeezed Light, Cat States, Photon-added Squeezed Vacuum**:

  1. **Squeezed light**: While a full explanation of everything could easily fill an entire chapter, in this section I highlight only the most significant parts. When discussing squeezing, one may refer to either quadrature squeezing or amplitude (number) squeezing, both of which are subcategories of displaced-squeezed states. Accordingly, it is natural to begin with the squeezed vacuum (quadrature squeezed), and then, displaced squeezed vacuum states. For a review on squeezed light generation please refer to this paper [84]. Also note that recently bright squeezed vacuum (BSV), squeezed vacuum with high mean photon number, has gained interest [85, 86, 87].

     Squeezed vacuum light:

     In order to generate squeezed vacuum, one the main approach is using the process of parametric down conversion (a $\chi^{(2)}$ process) [84]. The nonlinear

part of the Hamiltonian is given by

$$\hat{H}_{nl} = i\hbar\chi^{(2)}\left(\hat{a}_S^2\hat{a}_P^\dagger - \hat{a}_S^{\dagger 2}\hat{a}_P\right), \tag{1.59}$$

where the subscripts S and P correspond to squeezed and pump photons. If we assume pump is a strong coherent light one can replace $\hat{a}_P, \hat{a}_P^\dagger$ with $\alpha_P e^{i\omega_P t}$ and $\alpha_P^* e^{-i\omega_P t}$. The time evolution of the Hamiltonian, as a result, gives rise to the famous squeezing operator defined as follows [4]

$$\hat{S}(\xi) = e^{\frac{1}{2}(\xi^*\hat{a}^2 - \xi\hat{a}^{\dagger 2})}, \tag{1.60}$$

where $\xi = re^{i\theta}$, r is the squeezing parameter and θ shows the rotated angle. In order to evaluate properties of squeezed light it is very helpful to use the Bogoliubov transformation as follows

$$\begin{aligned}\hat{S}^\dagger(\xi)\hat{a}^\dagger\hat{S}(\xi) &= \hat{a}^\dagger\cosh(r) - \hat{a}\sinh(r)e^{-i\theta}, \\ \hat{S}^\dagger(\xi)\hat{a}\hat{S}(\xi) &= \hat{a}\cosh(r) - \hat{a}^\dagger\sinh(r)e^{i\theta}.\end{aligned} \tag{1.61}$$

Using the above relations to calculate the quadrature variances, for $\theta = 0$ we obtain

$$\begin{aligned}\langle(\Delta\hat{X})^2\rangle &= \frac{1}{4}e^{-2r} \\ \langle(\Delta\hat{P})^2\rangle &= \frac{1}{4}e^{2r}.\end{aligned} \tag{1.62}$$

Above equations demonstrates squeezing in the X quadrature, indicating a reduction in quantum noise below the vacuum level which is a quantum property. A schematic of squeezed vacuum light is demonstrated in Fig. (1.15). In Fig. (1.16), time evolution of the Wigner function is plotted. The projection of the Wigner function on the quadrature axis is proportional to the expectation value of the field.

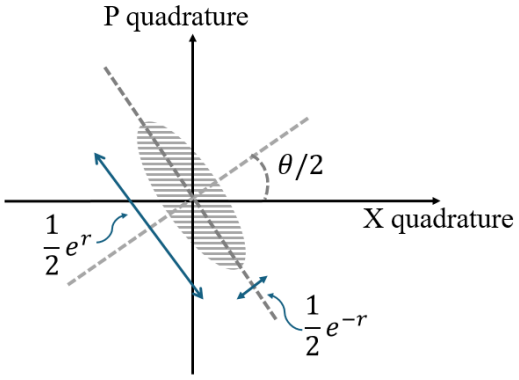

Figure 1.15: Phase space representation of squeezed vacuum state for squeezing parameter r, and angle θ [4]

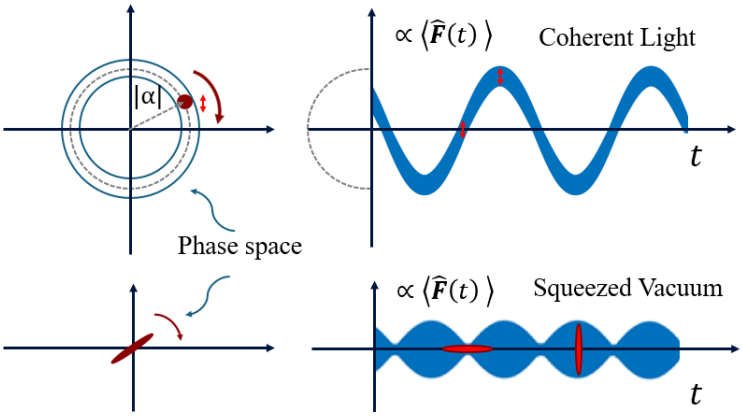

Figure 1.16: Time evolution of the Wigner functions of coherent and squeezed vacuum states in phase space are illustrated. The projection along the quadrature is proportional to the expectation value of the field [4].

Displaced squeezed light:

A more general form of squeezing can be obtained by applying the displacement operator on squeezed vacuum state [4]. One gets

$$|\alpha, \xi\rangle = \hat{D}(\alpha)\hat{S}(\xi)|0\rangle. \tag{1.63}$$

A schematic of the displaced squeezed state is illustrated in Fig. (1.17).

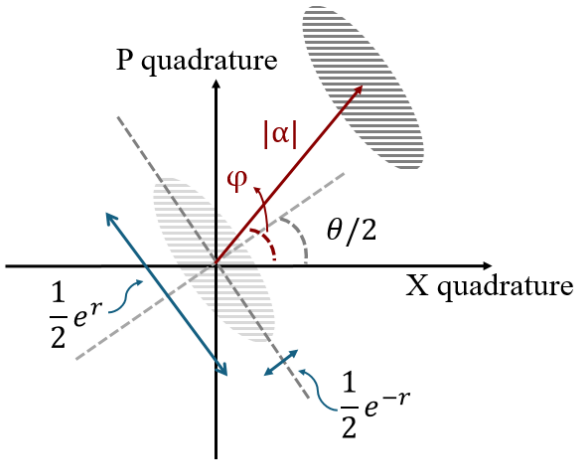

Figure 1.17: Displaced squeezed state phase space representation for squeezing parameter r, and angle θ is illustrated; φ is the phase of the displacement operator related to the coherent state [4].

It can be shown that depending on the angles θ, and φ one can switch between generating quadrature squeezed (super-Poissonian) or amplitude squeezed (Sub-Poissonian) states of light [4]. See Fig. (1.18).

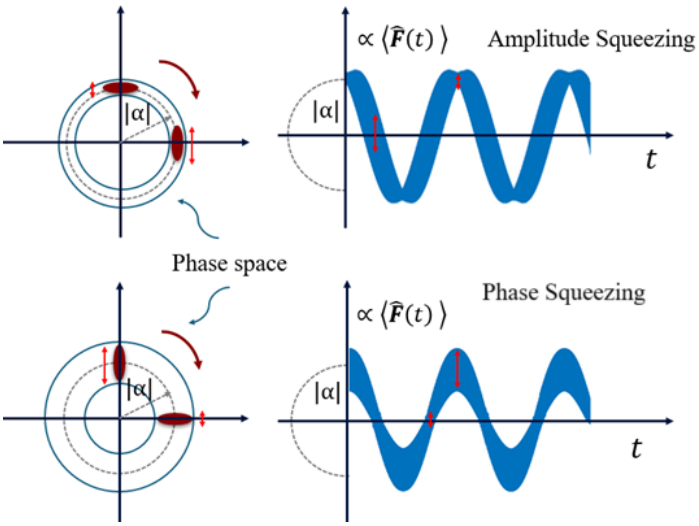

Figure 1.18: Time evolution of the Wigner functions of two displaced squeezed states in phase are illustrated; one of them leads to amplitude squeezing while the other corresponds to phase squeezing. The projection along the quadrature is proportional the expectation value of the field [4].

2. **Cat states**: Cat states are defined as the superposition of two coherent states

with equal amplitude but with a phase difference of π [4]. We have

$$|\psi\rangle = \frac{1}{\sqrt{2}}\left[1 + e^{-2\alpha^2}\cos(\phi)\right]\left(|\alpha\rangle + e^{i\phi}|-\alpha\rangle\right). \tag{1.64}$$

Depending on ϕ, there are three important cases [4].

(a) **Even cat states**: when $\phi = 0$, we generate even cat states. Only even number of photons are occupied which is the result of interference. $g^{(2)}$ calculation shows super-Poissonain statistics for even cat states for small values of α. As α grows, $g^{(2)} \to 1$. Regarding quadrature squeezing, one finds that for small values of α, squeezing occurs in one of the field quadratures [88, 4].

(b) **Odd cat states**: when $\phi = \pi$, we generate odd cat states. Only odd number of photons are occupied which is the result of interference. $g^{(2)}$ calculation shows sub-Poissonain statistics for odd cat states from small values of α. As α grows, $g^{(2)} \to 1$. No quadrature squeezing can be found here for odd cat states [88, 4].

(c) **Yurke-Stoler states**: when $\phi = \pi/2$, Yurke-Stoler states are generated. In this case, $g^{(2)} = 1$ for all values of α. Regarding quadrature squeezing, one finds that for small values of α, squeezing occurs in one of the field quadratures [89, 4].

Wigner distribution functions for even and odd cat states are given in Fig. (1.19). Cat states are produced by different methods such as using a Kerr nonlinear medium; for a review see [90]. They have applications in metrology and quantum information [91].

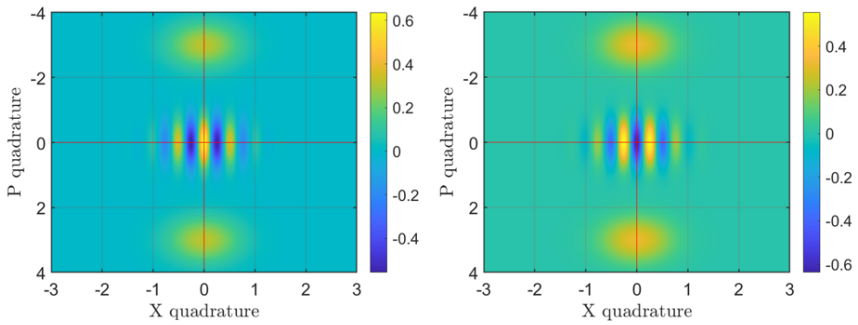

Figure 1.19: Wigner distribution functions for even (left) and odd (right) cat states are illustrated; the fringe frequency is proportional to the value of α

3. **Photon-added squeezed vacuum**: m-Photon-added squeezed vacuum is generated through [92]

$$\hat{a}^{\dagger m}\hat{S}(\xi)|0\rangle \tag{1.65}$$

Wigner function of photon added squeezed states can be obtained via the same procedure as the photon subtracted squeezed vacuum states in this work [93], where we can replace the $|1\rangle\langle 1|$ state to $|m\rangle\langle n|$ and use the linearity property of the Wigner function [93]. The Wigner function for $|m\rangle\langle n|$ is given explicitly in terms of associated Laguerre polynomials [94]. It can be seen that the Wigner function of one-photon added squeezed vacuum state is the same as that of a squeezed one-photon state as well as one-photon subtracted squeezed vacuum state [93]. The three states can be represented by the following equations

$$\begin{aligned}
&\hat{a}^{\dagger}\hat{S}(\xi)|0\rangle = \hat{S}(\xi)\hat{S}^{\dagger}(\xi)\hat{a}^{\dagger}\hat{S}(\xi)|0\rangle, \\
&\hat{a}\hat{S}(\xi)|0\rangle = \hat{S}(\xi)\hat{S}^{\dagger}(\xi)\hat{a}\hat{S}(\xi)|0\rangle, \\
&\hat{S}(\xi)\hat{a}^{\dagger}|0\rangle.
\end{aligned} \tag{1.66}$$

If one uses the Bogoliubov transformations given below

$$\begin{aligned}
\hat{S}^{\dagger}(\xi)\hat{a}^{\dagger}\hat{S}(\xi) &= \hat{a}^{\dagger}\cosh(r) - \hat{a}\sinh(r)e^{-i\theta}, \\
\hat{S}^{\dagger}(\xi)\hat{a}\hat{S}(\xi) &= \hat{a}\cosh(r) - \hat{a}^{\dagger}\sinh(r)e^{i\theta},
\end{aligned} \tag{1.67}$$

the above statements can be easily verified.

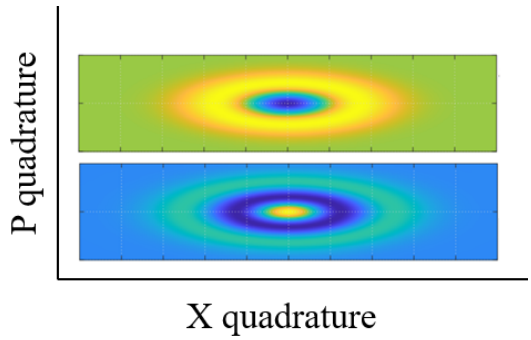

Figure 1.20: Qualitative Wigner distribution functions in phase space for squeezed one-photon sate (top), squeezed two-photon state, with the same squeezing parameters are plotted. Yellowish hues correspond to positive values, whereas bluish tones indicate negative ones.

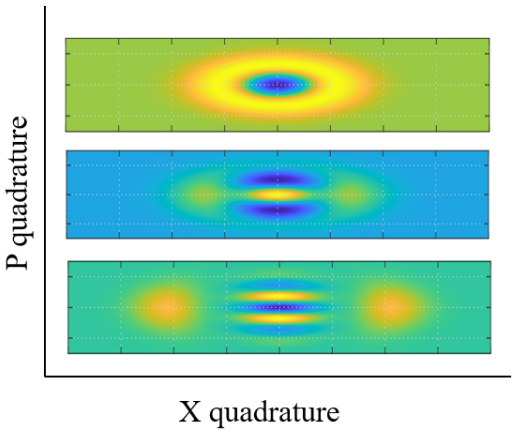

Figure 1.21: Qualitative Wigner distribution functions in phase space for one-photon added squeezed state (top), two-photon added squeezed state (middle), and five-photon added squeezed state (bottom), with the same squeezing parameters are plotted. Yellowish hues correspond to positive values, whereas bluish tones indicate negative ones.

- **Search for quantumness in strong field processes, treating the field in the second quantization formalism in HHG calculations and the usage of quantum light studies** :

Only recently has HHG been analyzed from a quantum optical perspective. By describing the harmonic emission process with quantum optical operators and modeling the intense laser field classically, it has been demonstrated that the photon statistics of high harmonic (HH) radiation can be modified under certain conditions [95, 96, 97], such as by accounting

for the electron dynamics between bound states. HHG has also been described in two-level atoms using quantum optical models [98, 99] and has been shown both theoretically and experimentally to induce non-classical Schrödinger cat states in the intense laser modes [100, 101, 102, 103]. Additional intriguing predictions from theory include light-electron entanglement during above threshold ionization [104], entangled x-ray photon pair generation through HHG from pair production [105], and entanglement between harmonics in intense laser driven atoms, when a resonance lies close to a harmonic [106]. In the limit of strong field driving, when the atomic ground state gets depleted, the quantum state of the driving field and harmonics become entangled and squeezed [107, 97]. Furthermore, theoretical and experimental investigations have started to look into the modification of strong field physics in the case where the intense laser field is replaced by a BSV beam. Full quantum optical calculations have predicted substantial deviations from the semi-classical three-step model, the most notable of which are harmonics beyond the semi-classical cutoff, higher damage thresholds, and the photon statistics of the BSV influencing the emitted electrons [108, 109, 110, 111, 97]. Developing quantum sources at shorter wavelengths is a desirable goal, because of the higher information density and lower noise of detectors. The required intensity for extending HHG into the XUV range presents a challenge, if the only driving field is intended to be quantum mechanical. Ideally, this is used for applications in quantum information science [104]. These have been the guiding principles behind a recent experiment: perturbing regular HHG with a BSV to produce quantum sideband high harmonics (QSHH) that exhibit super-Poissonian photon-bunching statistics [112, 113]. See chapter (5) [97].

1.4 Thesis layout

The thesis is organized as follows.

- **Chapter (2)**: Reviews the derivation of the Keldysh ionization theory, and it is based on the publication [1]. In particular, we give a detailed account of the analytic continuation of the integration contour into the complex domain, a key piece of Keldysh's analysis. Another central point, that is presented in detail is how to evaluate a saddle point integral in the presence of a singularity. We also obtained a factor of 2 relative to Keldysh's original derivation in the atomic ionization rates. This creates the foundation for understanding strong field processes and acquiring the necessary theoretical tools.

- **Chapter (3)**: The strong field adiabatic following (SFAF) formalism that yields a closed-form solution for modeling strong field processes in solids is developed. This chapter is based on the publication [5]. This chapter answers the question related to uncertainties about which mechanism should be dominant. To further investigate the problem the division of channels into resonant (real) and non-resonant (virtual) was done by our model. The contribution of virtual channels in HHG has been disregarded so far in contrast to their importance in perturbative nonlinear optics [10, 5]. Finally, in chapter (3) we show evidence of the need to add many-body effects to our model which will be the discussion of chapter (4).

- **Chapter (4)**: It is based on publication [66]. It explores the necessity of incorporating many body effects into numerical simulations to achieve clean and high contrast spectra that align with experimental results [45]. Besides, noise can also play a role in ionization alone [65]. Strong laser matter interactions are typically modeled as closed quantum systems using the single active electron (SAE) approximation. While this approach is widely applied in gaseous media, it can also be extended to solids with additional caution since it is very complex to account for all of the interactions in them. In nonliner optics often many body effects are described by interaction with a heat bath model in an open quantum system [3]. We have followed this idea and generalized it to strong field physics [66].

- **Chapter (5)**: It is based on publications [113, 97]. The generation and control of quantum HHG is investigated. In order to investigate quantumness in HHG, the electromagnetic field is treated in second quantization. These quantum optical properties, such as squeezing, entanglement, negative Wigner functions are of fundamental importance for the field of quantum information and quantum computation [114, 104]. In this chapter, the theory of quantum sideband high harmonic generation (QSHHG), the quantum even harmonics, in atoms and solids is derived to find ways by which to give quantum properties from the perturbative bright squeezed vacuum (BSV) light to the harmonic sideband. The theoretical framework is a quantum generalization of the semi classical Lewenstein model of HHG. It gives closed form solutions for the wavefunctions of HHG and QSHHG. Knowing the wavefunction, we can identify the quantum properties of QSHHG. The additional photons absorbed and emitted from the quantum perturbation, here BSV, create entanglement between individual harmonic sidebands and between the harmonic sidebands and the BSV.

We show how this entanglement can be used to create a variety of non-classical states commonly used in quantum information science [114, 104], such as high purity single photon states, Schrödinger cat states, and photon added squeezed vacuum states. Some of these non-Gaussian states with negative Wigner functions have been shown to provide a quantum computational advantage over their Gaussian counterparts [114]. Additionally, they play a significant role in quantum metrology, enhancing precision measurements beyond classical limits [114]. In sum, quantum properties of our quantum light, here BSV, can be transferred to QSHHG, which will open a path towards engineering the quantum properties of ultrashort XUV high harmonics [97].

- **Chapter (6)**: This chapter presents the final conclusions of the study and outlines potential directions for future work.

Chapter 2

Mathematical Details: Keldysh Ionization Theory

This chapter is based on the publication [1], and it overlaps with its text with the permission of the journal-copyright by the Journal of Physics B: Atomic, Molecular and Optical Physics.

2.1 Introduction

Optical field ionization of atomic systems has two limiting cases. Tunnel ionization, or the quasi-static limit, occurs when the field remains frozen during the ionization process [115, 116]; when the field varies substantially, multi-photon ionization dominates, see Fig. 2.1.

Keldysh developed a seminal theory of optical field ionization that comprises both limiting cases, the tunneling, and the multi-photon limit [25]. Dominance of the two ionization mechanisms is determined by the Keldysh parameter

$$\gamma = \frac{\omega\sqrt{2I_0}}{F}. \tag{2.1}$$

Here, ω is the laser circular frequency, F is the laser electric field strength, and I_0 is the ionization potential. Tunnel ionization dominates for $\gamma \ll 1$, whereas multi-photon ionization is dominant for $\gamma \gg 1$. For an intuitive overview of these regimes see, [26], and for an overview of other regimes, see [117].

Keldysh's work [25] along with similar work by Faisal [118] and Reiss [119] are sometimes referred together as KFR theory [120], here we focus on Keldysh's formulation.

Keldysh's work is based on the strong field approximation; the wave function is represented as a superposition of an s-bound state ($l, m = 0$) and the non-relativistic, laser dressed free electron wavefunction in dipole approximation. As a result, the effect of the far-range Coulomb potential on the continuum electron and on ionization is neglected. Therefore, in the low frequency limit $\omega \to 0$, the Keldysh ionization rate does not go over into the (static) tunnel ionization rate [115, 116], as it should. Whereas Keldysh gave a simple Coulomb correction factor, a more sophisticated correction was developed subsequently in the PPT (Perelomov-Popov-Terent'ev) approach [121], where also ionization rates for $l, m \neq 0$ [121, 122] were derived (for a comprehensive review of this 'imaginary-time' method, see [123]). Further, for high Rydberg states with large n the original approach becomes inaccurate and corrections have to be added [124]. For detailed reviews of optical field ionization of atomic systems, see [117, 125, 126, 127, 128]. Recently, some technical issues with regard to employing saddle point integration versus residue theory in Keldysh's ionization theory were discussed [124, 129] and the original approach was confirmed. For reviews, see [126, 128].

The Keldysh approach to ionization has remained relevant to date. Although it is being widely used, its mathematical methods and intricacies are not easily accessible. This is unfortunate, as the methodology is of relevance for current research in strong field physics including, for example, attosecond science [130, 131, 132]. Other subsequently explored phenomena include above-threshold ionization (ATI) [133, 134] and more complicated ionization pathways like non-sequential double ionization [135]. For summaries of other applications involving strong field physics, including those involving novel molecular and solid state systems see [117].

This work does not contain new results. It started as a comprehensive exam question, driven by the authors' desire to understand the mathematical details of Keldysh's derivation of strong field ionization in atoms [25]. Our efforts are complementary to previous work exploring details of Keldysh ionization theory in atoms [129, 124, 128]. Our tutorial is presented in the hope that it will be of use for a wider audience in the fields of strong laser field physics and attosecond science and will entail an even deeper appreciation of Keldysh's brilliant work.

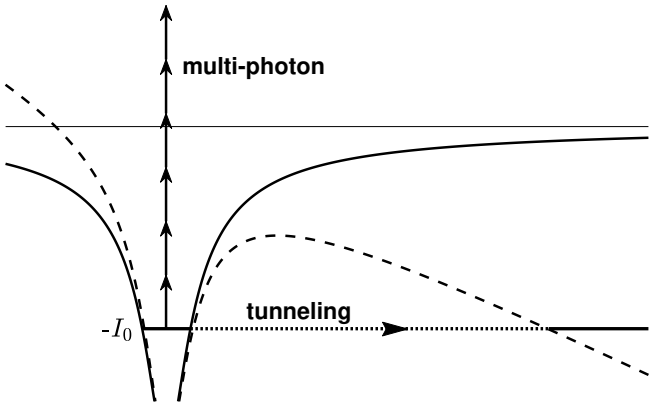

Figure 2.1: Schematic of multi-photon and tunnel ionization. Continuum threshold (thin line); Coulomb potential (full line); Coulomb potential plus laser field (dashed line) [1].

2.2 Closed form solution of the transition rate

We have adopted most of Keldysh's notation. Atomic units are used to keep the notation simpler. Following the more modern literature [28], $\mathbf{P}$ is used as canonical momentum instead of $\mathbf{p}$ in Keldysh. For the same reason we have reserved S for the classical action and use T instead of S in (16) and (18) of [25]. Finally, we use t instead of T as a time variable.

The derivation of the Keldysh ionization rate for the ground state ($n = 1$, $l = 0$) of a hydrogen atom starts from the Schrödinger equation. The laser electric field is accounted for in dipole approximation and in length gauge,

$$i\partial_t \Psi(\mathbf{x}, t) = \left(H_0 - \mathbf{x}\mathbf{F}(t)\right) \Psi(\mathbf{x}, t), \tag{2.2}$$

where Ψ is the wavefunction, $H_0 = -(1/2)\boldsymbol{\nabla}^2 - \sqrt{2I_0}/|\mathbf{x}|$ is the field free Hamiltonian, $\mathbf{F}(t) = \mathbf{F}\cos(\omega t)$ is the laser electric field, and $|\mathbf{F}| = F$.

Eq. (2.2) is solved by utilizing the strong field approximation; the ansatz

$$\Psi(\mathbf{x}, t) = a(t)e^{iI_0 t}\,|0\rangle + \int d^3p\, b(\mathbf{p}, t)\,|\mathbf{p}\rangle \tag{2.3}$$

consists of a ground state part fulfilling the time independent Schrödinger equation, $H_0\,|0\rangle = -I_0\,|0\rangle$ with ground state energy $-I_0$ and wavefunction $|0\rangle = 1/\sqrt{\pi a_0^3}\exp(-|\mathbf{x}|/a_0)$.

Here, $a_0 = 1/\sqrt{2I_0}$ is the atomic radius, with $a_0 = 1$ for a hydrogen ground state ($I_0 = 1/2$). The ground state probability amplitude $a(t) \approx 1$ is assumed to remain frozen which is a good approximation as long as ionization is weak. The second part of Eq. (2.3) is an expansion of the continuum wavefunction in terms of plane waves $|\mathbf{p}\rangle = 1/(2\pi)^{3/2} \exp(i\mathbf{px})$ with mechanical momentum $\mathbf{p}$; $b(\mathbf{p}, t)$ represents the continuum electron probability amplitude.

The strong field ansatz Eq. (2.3) introduces three approximations: First, excited bound states are neglected. Second, loss of ground state population due to ionization is disregarded. Third, the effect of the Coulomb potential on the continuum part of the electron wavefunction is not accounted for.

Inserting ansatz Eq. (2.3) into Eq. (2.2), utilizing the Schrödinger equation for the ground state, neglecting the Coulomb interaction for the free electron part, and applying $\langle \mathbf{p}' |$ to the resulting equation yields

$$i\partial_t b(\mathbf{p}, t) = \left(\frac{\mathbf{p}^2}{2} - i\mathbf{F}(t)\boldsymbol{\nabla}_{\mathbf{p}}\right) b(\mathbf{p}, t) - \mathbf{V}_0(\mathbf{p}) \cos(\omega t) e^{iI_0 t}. \tag{2.4}$$

Here, we have relabelled $\mathbf{p}' \to \mathbf{p}$ for notational convenience, and inserted the definition of $\mathbf{F}(t)$. Further, $\mathbf{V}_0(\mathbf{p}) = \mathbf{F} \langle \mathbf{p} | \, \mathbf{x} \, | 0 \rangle$ is the potential energy associated with the laser driven transition from ground state to continuum. Following [136] one obtains

$$V_0(\mathbf{p}) = -i \frac{2^{7/2} (2I_0)^{5/4}}{\pi} \frac{\mathbf{Fp}}{(p^2 + 2I_0)^3}. \tag{2.5}$$

The dipole term differs by a factor $(2\pi)^{3/2}$ from Keldysh due to the normalized definition of the plane wave states.

Integration of Eq. (2.4) is performed by transforming into a moving momentum frame $\mathbf{P} = \mathbf{p} + \mathbf{A}(t)$, where $\mathbf{P}$ is the canonical momentum and $\mathbf{A}(t) = -(\mathbf{F}/\omega) \sin(\omega t)$ is the vector potential defined by $-\partial_t \mathbf{A}(t) = \mathbf{F}(t)$. The equation of motion in the transformed frame is

$$i\partial_t b(\mathbf{P}, t) = \frac{1}{2} \mathbf{P}_t^2 \, b(\mathbf{P}, t) - V_0(\mathbf{P}_t) \cos(\omega t) e^{iI_0 t}, \tag{2.6}$$

where $\mathbf{P}_t = \mathbf{P} - \mathbf{A}(t)$. Integration of Eq. (2.6) results in

$$b(\mathbf{P}, t) = i \int_0^t dt' \, V_0(\mathbf{P}_{t'}) \cos(\omega t') \, e^{-\frac{i}{2} \int_{t'}^t \mathbf{P}_\tau^2 d\tau + iI_0 t'}. \tag{2.7}$$

The ionization rate is determined by $w_0 = \int d^3P \partial_t |b(\mathbf{P},t)|^2$; inserting Eq. (2.7) we find

$$w_0 = \lim_{t\to\infty} \int d^3P\, V_0^*(\mathbf{P}_t) \cos\omega t \int_0^t dt'\, V_0(\mathbf{P}_{t'}) \cos\omega t' \times \exp\left(-i\int_{t'}^t I_0 + \frac{1}{2}\mathbf{P}_\tau^2 d\tau\right) + c.c., \tag{2.8}$$

where the rules of scattering theory are applied; the perturbation is switched on at time zero and the scattered state is analyzed at $t \to \infty$, where a steady state ionization rate has been reached [137]. We proceed by inserting the definition of $\mathbf{F}(t)$ and $\mathbf{A}(t)$ in Eq. (2.8) and obtain

$$w_0 = 2\lim_{t\to\infty} \mathrm{Re} \int d^3P \int_0^t dt' \cos(\omega t)\cos(\omega t') V_0^*\left(\mathbf{P} + \frac{\mathbf{F}}{\omega}\sin(\omega t)\right) V_0\left(\mathbf{P} + \frac{\mathbf{F}}{\omega}\sin(\omega t')\right) \times \exp\left(-i\int_{t'}^t I_0 + \frac{1}{2}\left(\mathbf{P} + \frac{\mathbf{F}}{\omega}\sin(\omega\tau)\right)^2 d\tau\right), \tag{2.9}$$

in agreement with (8) in Keldysh [25], but with an extra factor of 2 that is missing in Keldysh's manuscript. The prefactor $1/(2\pi)^3$ in Keldysh is contained here in the two dipole moments. The symbol Re represents the real part.

Next, a Fourier expansion of the integrand is performed. To that end we reexpress the ionization rate as

$$w_0 = 2\lim_{t\to\infty} \mathrm{Re} \int d^3P \cos(\omega t) L^*(\mathbf{P},t) \int_0^t \cos(\omega t') L(\mathbf{P},t') dt'$$
$$L(\mathbf{P},t) = V_0\left(\mathbf{P}_t\right) \exp\left(i\int_0^t I_0 + \frac{1}{2}\mathbf{P}_\tau^2\, d\tau\right). \tag{2.10}$$

The Fourier series expansion of $L(\mathbf{P},t)$ and the corresponding coefficients L_n are given by

$$L(\mathbf{P},t) = \sum_{n=-\infty}^{\infty} L_n(\mathbf{P}) \exp\left(i\Omega_n t\right) \tag{2.11}$$

$$L_n(\mathbf{P}) = \frac{\omega}{2\pi}\int_0^{T_0} L(\mathbf{P},t)\, \exp\left(-i\Omega_n t\right) dt \tag{2.12}$$

with $\Omega_n = \left(\tilde{I}_0 + \mathbf{P}^2/2 - n\omega\right)$, $\tilde{I}_0 = I_0 + \mathbf{F}^2/(4\omega^2)$, and $T_0 = 2\pi/\omega$ the optical cycle. The first two terms in Ω_n are the non-sinusoidal contributions of the exponent in Eqs. (2.9),

(2.10) which have been separated out.

The time integral in Eq. (2.10) is performed by using Eq. (2.11) and by replacing cos with exponentials resulting in frequencies $\Omega_{n\pm1}$. The summation index is redefined so that $\Omega_{n\pm1} \to \Omega_n$. The ionization rate contains a double sum coming from the expansion of $L(\mathbf{P},t)$ and $L^*(\mathbf{P},t)$. Only terms with the same index fulfill energy conservation and result in ionization. All other terms are of virtual nature and do not contribute to net (cycle-averaged) ionization. Their neglect eliminates one of the sums. The resulting integral is divergent in the limit $t \to \infty$ and must be modified to be well defined,

$$w_0 = \frac{1}{2}\mathrm{Re}\int_{-\infty}^{\infty} d^3P \sum_{n=-\infty}^{\infty} \left|L_{n+1}(\mathbf{P}) + L_{n-1}(\mathbf{P})\right|^2 \lim_{\varepsilon\to 0^+}\lim_{t\to\infty}\int_0^t e^{-(i\Omega_n+\varepsilon)(t-t')}dt'. \tag{2.13}$$

The time integral for $t \to \infty$ becomes

$$\lim_{\varepsilon\to 0^+}\int_0^\infty e^{-(i\Omega_n+\varepsilon)\tau}d\tau = \lim_{\varepsilon\to 0^+}\frac{-i}{\Omega_n - i\varepsilon} = \pi\delta(\Omega_n) - i\mathrm{P}\frac{1}{\Omega_n} \tag{2.14}$$

with P denoting Cauchy's principal value [138, 139] which gives an imaginary contribution in Eq. (2.13) that drops out. Further, in the last equality of Eq. (2.14) the Sokhotski-Plemelj theorem is used [139].

The δ-function in Eq. (2.14) in combination with the definition of L_n, Eq. (2.12), yields the relation

$$L_{n\pm1}(\mathbf{P}) = \frac{\omega}{2\pi}\int_0^{T_0} L(\mathbf{P},t)\,\exp(\pm i\omega t)\,dt. \tag{2.15}$$

Use of relations Eq. (2.14) and Eq. (2.15) in Eq. (2.13) results in

$$\begin{aligned} w_0 &= 2\pi\int_{-\infty}^{\infty} d^3P\,|L(\mathbf{P})|^2 \sum_{n=-\infty}^{\infty}\delta(\Omega_n), \\ L(\mathbf{P}) &= \frac{1}{2\pi}\int_0^{2\pi} L(\mathbf{P},x)\cos(x)dx, \end{aligned} \tag{2.16}$$

in agreement with (14) of [25]; the variable transformation $x = \omega\tau$ was used and $L(\mathbf{P},x)$ is defined in Eq. (2.10). As the Fourier transform is periodic, integration over any 2π interval can be used.

The second part of Eq. (2.16) is rewritten with the help of variable transformations

$\sin(x) = u$, so that $\cos(x)dx = du$, and $dx = du/\cos(x) = du/\sqrt{(1-u^2)}$. We obtain

$$L(\mathbf{P}) = \frac{1}{2\pi} \oint V_0 \left(\mathbf{P} + \frac{\mathbf{F}}{\omega} u\right) \exp\left(\frac{i}{\omega} S(u)\right) du \tag{2.17a}$$

$$S(u) = \int_0^u \left[I_0 + \frac{1}{2}\left(\mathbf{P} + \frac{\mathbf{F}}{\omega} v\right)^2\right] \frac{dv}{\sqrt{1-v^2}} \tag{2.17b}$$

which agrees with (15) of Keldysh [25]. The above variable transformation is not bijective, i.e. for a given value of u, x is not single valued. This problem can be dealt with in two ways. First, the integration path in Eq. (2.16) can be split in intervals for which the exponent is single valued. Alternatively, the integral can be analytically continued into the complex domain, where with the help of a branch cut the exponent is made single valued, see the dogbone contour in Fig. 2.2. We follow Keldysh and continue the contour into the complex plane, and deform it in a way that it passes through the saddle points, see Fig. 2.2, which yield the dominant contribution to the ionization rate. This is discussed next.

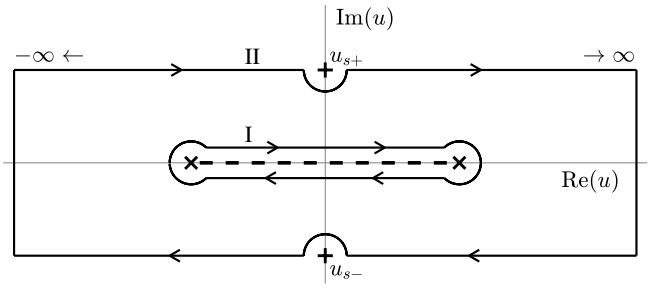

Figure 2.2: Integration contour in Eq. (2.17a). The branch points (x) of the square root in Eq. (2.17b) at ± 1 are connected by a branch cut (dashed line); it cannot be crossed to keep the square root single valued. As such, the dogbone contour (I) around the the branch cut is chosen. It can be further deformed into any contour obtainable without crossing a singularity. Contour (II) runs through the saddle points $u_{s\pm}$ (+) which yield the dominant contributions to integral Eq. (2.17a). It is extended to $\pm\infty$, where the integrals along the vertical paths closing the contour are negligible. As the dipole moment V_0 in the pre-exponent has a singularity at $u_{s\pm}$, the contour needs to be run around $u_{s\pm}$ without crossing it [1].

2.3 Saddle point integration of transition rate

The exponent of the integral in Eq. (2.17) is rapidly oscillating which is why it can be calculated by using the saddle point method [138]. We expand the phase to second order

about the saddle points $u_{s\pm}$, $S(u) \approx S(u_{s\pm}) + S'(u_{s\pm})\delta u + (1/2)S''(u_{s\pm})\delta u^2$ with prime and double prime indicating first and second derivatives and $\delta u = (u - u_{s\pm})$. The main contribution to the integral comes from the saddle points at which $S'(u_{s\pm}) = 0$,

$$S'(u) = \left[I_0 + \tfrac{1}{2}\left(P_z + \tfrac{F}{\omega}u \right)^2 + \tfrac{1}{2}P_\perp^2 \right] \tfrac{1}{\sqrt{1-u^2}}, \tag{2.18a}$$

$$I_0 + \tfrac{1}{2}\left(P_z + \tfrac{F}{\omega}u_{s\pm} \right)^2 + \tfrac{1}{2}P_\perp^2 = 0. \tag{2.18b}$$

Here, we have assumed $\mathbf{F} = F\hat{\mathbf{z}}$, and have introduced the longitudinal and transverse momenta P_z and $\mathbf{P}_\perp = (P_x, P_y)$; further, $P_\perp^2 = P_x^2 + P_y^2$ and $P^2 = P_z^2 + P_\perp^2$. From Eq. (2.18b) we obtain $(P_z + \frac{F}{\omega}u_{s\pm}) = \pm i\sqrt{2I_0 + P_\perp^2}$; the $\pm$ sign represents saddle points for the positive and negative laser half cycle. The second derivative is found to be

$$S''(u) = \frac{F}{\omega}\frac{P_z + \frac{F}{\omega}u}{\sqrt{1-u^2}} + S'(u)\frac{u}{1-u^2}, \tag{2.19a}$$

$$S''(u_{s\pm}) = \pm i\frac{F}{\omega}\frac{\sqrt{2I_0}}{\sqrt{1-u_{s\pm}^2}}. \tag{2.19b}$$

After saddle point integration, $S''(u_{s\pm})$ will end up as pre-exponential. We only carry along exponential transverse momentum dependence, which is why $P_\perp^2$ has been neglected in the numerator of Eq. (2.19b). As a result, the phase $S(u)$ is approximated as

$$S(u) \approx S(u_{s\pm}) \pm i\frac{F}{2\omega}\frac{\sqrt{2I_0}}{\sqrt{1-u_{s\pm}^2}}\delta u^2. \tag{2.20}$$

The rules of saddle point integration dictate that the integration contour is deformed to pass through $u_{s\pm}$ and that δu is chosen along the path of steepest descent. We make the ansatz $\delta u = u - u_{s\pm} = se^{i\varphi}$ and insert it in Eq. (2.20). Further, $1/\sqrt{1-u_{s\pm}^2}$ is split into amplitude and phase term $\pm\exp(i\zeta)$ with phase ζ defined in the positive imaginary half plane. The two saddle points are mirror points in the positive and negative imaginary half

plane for which the phase differs by π, This yields

$$\frac{i}{\omega}S = \frac{i}{\omega}S(u_{s\pm}) \mp \eta s^2 e^{2i\varphi}\left(\pm e^{i\zeta}\right), \tag{2.21a}$$

$$\eta = \frac{F\sqrt{2I_0}}{2\omega^2}\left|\frac{1}{\sqrt{1-u_{s\pm}^2}}\right|. \tag{2.21b}$$

The signs in Eq. (2.21a) cancel so that each saddle point gives the same contribution in the second term. The path of steepest descent is determined by $\varphi = -\zeta/2$. With this choice the last term in Eq. (2.21a) results in a Gaussian decay (steepest descent) in Eq. (2.17). Further, as the saddle point is dominantly imaginary, see Eq. (2.29) further down, $\zeta \approx 0$ and the path of steepest descent is close to parallel to the real axis. Finally, as the Gaussian expansion in the integrand decays quickly, the integral is extended to $\pm\infty$, where the vertical parts of the closed contour integral have no contribution, see Fig. 2.2.

Inserting the above in Eq. (2.17a) one arrives at

$$L(\mathbf{P}) = \frac{1}{2\pi}\sum_{u_{s\pm}}\int_{\mp\infty}^{\pm\infty} V_0\left(\mathbf{P}+\frac{\mathbf{F}}{\omega}u_{s\pm}\right) e^{\frac{i}{\omega}S(u_{s\pm})-\eta s^2} e^{-i\frac{\zeta}{2}} ds, \tag{2.22}$$

where the different signs of the integration limits represent the integrals through $u_{s\pm}$, respectively; see Fig. 2.2.

Following the rules of saddle point integration, pre-exponential factors are to be evaluated at the saddle points. However, the dipole moment V_0 in Eq. (2.22) has a singularity at $u_{s\pm}$. As such, we need to replace $u_{s\pm} \to u_{s\pm} + \delta u$ in the denominator of V_0,

$$V_0\left(\mathbf{P}+\frac{\mathbf{F}}{\omega}u_{s\pm}\right) \to -i\frac{2^{1/2}(2I_0)^{5/4}F(P_z+\frac{F}{\omega}u_{s\pm})}{\pi\left(I_0+\frac{1}{2}\left(P_z+\frac{F}{\omega}(u_{s\pm}+\delta u)\right)^2+\frac{1}{2}P_\perp^2\right)^3} = \frac{\mu}{\delta u^3} \tag{2.23}$$

with $\mu = i2^{3/2}I_0 a_0^{3/2}\omega^3/\pi F^2$. Here, we have expanded the denominator to first order with regard to δu and have utilized the saddle point condition Eq. (2.18b). Further, as Eq. (2.23) contributes to the pre-exponent, we set $P_\perp^2 \approx 0$.

With the help of Eq. (2.23), the integral in Eq. (2.22) can be recast into

$$L(\mathbf{P}) = \frac{1}{2\pi}\sum_{u_{s\pm}} e^{\frac{i}{\omega}S(u_{s\pm})}\int_{\mp\infty}^{\pm\infty}\frac{\mu}{s^3}e^{-\eta s^2}e^{i\zeta}ds. \tag{2.24}$$

In order to evaluate the integral in Eq. (2.24), its path needs to be deformed around the singularity without crossing it, see Fig. 2.2. This results in splitting the integral into a principal value (PV) integral and an integral that runs counterclockwise along an infinitesimal half circle around the saddle point $s = 0$,

$$\int_{-\infty}^{+\infty} \frac{\mu}{s^3} e^{-\eta s^2} e^{i\zeta} ds = \fint \frac{\mu}{s^3} e^{-\eta s^2} e^{i\zeta} ds + \oint \frac{\mu}{s^3} e^{-\eta s^2} e^{i\zeta} ds, \tag{2.25}$$

where the first term on the right hand side of Eq. (2.25), the principal value integral, is zero since the integrand is odd about $s = 0$. In Eq. (2.25) only the integral around u_{s+} is displayed. The other integral proceeds counterclockwise along an upper half circle. We proceed with the u_{s+} integral. Evaluation of the u_{s-} integral proceeds similarly and gives the same result.

The counterclockwise lower half circle integral around u_{s+} is obtained by performing a Laurent expansion of the integrand,

$$\begin{aligned} \oint \frac{\mu}{s^3} e^{-\eta s^2} e^{i\zeta} ds &= \oint \frac{\mu}{s^3} (1 - \eta s^2 + \frac{1}{2}\eta^2 s^4 - ...) e^{i\zeta} ds \\ &= \lim_{\varepsilon \to 0} \int_{\pi}^{2\pi} \left(\frac{\mu}{\varepsilon^3 e^{3i\vartheta}} - \frac{\eta\mu}{\varepsilon e^{i\vartheta}} + \frac{\eta^2 \mu}{2} \varepsilon e^{i\vartheta} - ... \right) i\varepsilon e^{i\vartheta} d\vartheta e^{i\zeta}. \end{aligned} \tag{2.26}$$

To evaluate the half circle integral a change of variables $s = \varepsilon e^{i\vartheta}$ has been introduced. In evaluating the $d\vartheta$ integral, only the second term (residue) in the brackets gives a non-zero result. Therefore, Eq. (2.26) becomes

$$\oint \frac{\mu}{s^3} e^{-\eta s^2} e^{i\zeta} ds = -i\eta\mu\pi e^{i\zeta}. \tag{2.27}$$

Inserting Eq. (2.27) into Eq. (2.24) yields

$$L(\mathbf{p}) = \frac{I_0 \omega}{\pi F} \sqrt{\frac{a_0}{2}} \sum_{u_{s\pm}} \left| \frac{1}{\sqrt{1 - u_{s\pm}^2}} \right| e^{\frac{i}{\omega} S(u_{s\pm})}, \tag{2.28}$$

which for each of the saddle points agrees with the last equation of the left column on p. 1309 in Keldysh [25] divided by $(2\pi)^{3/2}$. The difference comes again from the normalized plane waves but disappears in w_0 in Eq. (2.8). Note that we have dropped constant complex phase factors $(-ie^{i\zeta})$ in the pre-exponential as they drop out of $|L(\mathbf{P})|^2$ in the

ionization rate.

To completely determine Eq. (2.28), $S(u_{s\pm})$ still needs to be worked out. This is done by solving Eq. (2.18b) for $u_{s\pm}$

$$u_{s\pm} = -P_z\frac{\omega}{F} \pm i\frac{\omega}{F}\sqrt{2I_0 + P_\perp^2} \approx \pm i\gamma - P_z\frac{\gamma}{\sqrt{2I_0}} \pm i\frac{\gamma}{4I_0}P_\perp^2 = \pm i\gamma + \Delta_\pm \tag{2.29}$$

with the Keldysh parameter γ defined in Eq. (2.1). Here, only terms of order $P_\perp^2$ have been kept, as dominant contributions to ionization come from small $P^2 \ll 2I_0$ [128]. As a result, also $|\Delta_\pm|/\gamma \ll 1$.

Let us digress to interpret the meanings of the saddle points $u_{s\pm} = \pm i\gamma + \Delta_\pm$. For only this discussion, given that $|\Delta_\pm|/\gamma \ll 1$, consider $u_{s\pm} \approx \pm i\gamma$. Given that the variable u is related to time through $u = \sin(\omega t)$, the equivalent time saddle points are given by

$$t_{s+} \approx \frac{i}{\omega}\sinh^{-1}(\gamma), \tag{2.30a}$$

$$t_{s-} \approx \frac{\pi}{\omega} + \frac{i}{\omega}\sinh^{-1}(\gamma). \tag{2.30b}$$

They reflect the dominant times at which electrons are born in the continuum that result in the same final state [122]. The complex nature of these times reflects the quantum mechanical nature of tunneling. The imaginary parts are necessary for describing the trajectories of photoelectrons as they result in exponential decay of $\exp(iS/\omega)$, and thus, the ionization rate. The real parts coincide with the peaks of the laser field, separated by a half-cycle π/ω, when the probability of ionization is most likely. Complex time points have also been notably used in a later work involving semiclassical analysis by PPT [121, 123].

Returning to the current problem, Eq. (2.29) is inserted in Eq. (2.17b); then, following the analytic continuation procedure of Eq. (2.48) and Eq. (2.49) are used to determine $S(u_{s+})$ and $S(u_{s-})$, respectively. This is followed by a Taylor expansion with respect to $\Delta_\pm$ so that,

$$S(u_{s\pm}) \approx S(\pm i\gamma) + \Delta_\pm S'(\pm i\gamma) + \frac{\Delta_\pm^2}{2}S''(\pm i\gamma) = S(\pm i\gamma) - \frac{i}{2}\frac{\gamma}{\sqrt{1+\gamma^2}}P_z^2. \tag{2.31}$$

The last line has been obtained after some calculations with the help of Eq. (2.18a) and Eq. (2.19a). Finally, in calculating the second term in the last line, only terms up to second

order in momentum have been kept.

Using an integral of the form of Eq. (2.48) for $S(i\gamma)$ and of the form of Eq. (2.49) for $S(-i\gamma)$ in Eq. (2.31) yields

$$\begin{aligned}\frac{i}{\omega}S(u_{sj}) = &-\frac{\tilde{I}_0}{\omega}\left[\sinh^{-1}(\gamma) - \frac{\gamma\sqrt{1+\gamma^2}}{1+2\gamma^2}\right] \\ &-\frac{1}{2\omega}\left[\sinh^{-1}(\gamma) - \frac{\gamma}{\sqrt{1+\gamma^2}}\right]P_z^2 - \frac{1}{2\omega}\sinh^{-1}(\gamma)P_\perp^2 \\ &-j\frac{iP_zF}{\omega^2}\sqrt{1+\gamma^2} + \frac{i}{\omega}\left(\tilde{I}_0 + \frac{P^2}{2}\right)\pi\delta_{j,-},\end{aligned} \tag{2.32}$$

where $j = +,-$ corresponds to the sign in the subscript of $u_{s\pm}$; further, $\delta_{j=-,-} = 1$ and $\delta_{j=+,-} = 0$. See the continuation section for more details on the analytic continuation procedure leading to the sign conventions and the presence of the final term for u_{s-} which is equivalent to $in\pi$ through the δ-function relation $\delta(\Omega_n)$.

To obtain the ionization rate, Eq. (2.32) is inserted into Eq. (2.16),

$$\begin{aligned}w_0 = &\frac{I_0 a_0 \gamma^2}{\pi(1+\gamma^2)}\exp\left(-\frac{2\tilde{I}_0}{\omega}\left[\sinh^{-1}(\gamma) - \frac{\gamma\sqrt{1+\gamma^2}}{1+2\gamma^2}\right]\right) \\ &\times 2\pi\sum_{n=-\infty}^{\infty}\int_0^\infty dP\,P^2\int_{-1}^{1}dx\,\delta\left(\tilde{I}_0 + \frac{P^2}{2} - n\omega\right) \\ &\times\exp\left(-\frac{1}{\omega}\sinh^{-1}(\gamma)P^2 + \frac{1}{\omega}\frac{\gamma}{\sqrt{1+\gamma^2}}P^2x^2\right).\end{aligned} \tag{2.33}$$

In arriving at this result, interference terms between the two saddle point contributions to $|L(\mathbf{P})|^2$ have been dropped. It has been demonstrated numerically in [128] that their contribution to the net ionization rate is small. Nevertheless, if one wishes to study the differential ionization rate with respect to θ, the angle of the projection of $\mathbf{P}$ onto $\mathbf{F}$, these terms cannot be neglected [128]. They manifest as oscillations with θ in said differential ionization rate (see for example figure 3 of [128]), and if they are neglected, the differential ionization rate appears more or less as the average of these oscillations. The papers [122, 140] explain these oscillations as results of interference of partial electron waves and, further, the paper [122], indicates that they are emitted in adjacent half cycles. We would like to note that in the tunneling limit, electrons with opposite drift momenta are generated which do not interfere. Nevertheless, it is important to note that ionization

is analysed in the steady state limit corresponding to observation time in the limit $t \to \infty$ and so the oscillations from the interference terms cannot be interpreted as instantaneous phenomena. Non-interference terms from both saddle points, in the positive and the negative complex half plane, yield the same contribution to w_0 and give an additional factor of 2 compared to Keldysh from hereon [128].

Here we have introduced spherical variables for $\mathbf{P}$ with $P_z = P\cos(\theta)$ and use the transformation $\cos(\theta) = -x$. The integral over dP is performed using the δ-function. Then, using the variable transformation $y = x[2\gamma(n - \tilde{I}_0/\omega)/\sqrt{1+\gamma^2}]^{1/2}$, the resulting integral over dy gives the Dawson function $\Phi(z) = \int_0^z e^{y^2-z^2} dy$. This results in

$$\begin{aligned} w_0 =& \frac{2\sqrt{2I_0\omega}\gamma^{3/2}}{(1+\gamma^2)^{3/4}} \exp\left(-\frac{2\tilde{I}_0}{\omega}\left[\sinh^{-1}(\gamma) - \frac{\gamma\sqrt{1+\gamma^2}}{1+2\gamma^2}\right]\right) \\ &\times \sum_{n=\bar{n}}^{\infty} \exp\left(-2\left(\sinh^{-1}\gamma - \frac{\gamma}{\sqrt{1+\gamma^2}}\right)\left(n - \frac{\tilde{I}_0}{\omega}\right)\right) \\ &\times \Phi\left(\left\{\frac{2\gamma}{\sqrt{1+\gamma^2}}\left(n - \frac{\tilde{I}_0}{\omega}\right)\right\}^{1/2}\right). \end{aligned} \tag{2.34}$$

The sum in Eq. (2.34) does not start at $n = -\infty$, but at $\bar{n} = \langle \tilde{I}_0/\omega + 1 \rangle$ corresponding to the lowest number of photons to reach the continuum, see Fig. 2.3. Here, $\langle\rangle$ denotes the integer part of a real number. For convenience, the summation index is shifted, $n \to n + \bar{n}$, so that summation runs from $n = 0$ to ∞.

With this final change we arrive at Keldysh's Eqs. (16)-(18) for the ionization rate [25] with an additional factor of 2,

$$w_0 = 2\sqrt{2I_0}\sqrt{\omega}\left(\frac{\gamma}{\sqrt{1+\gamma^2}}\right)^{\frac{3}{2}} T\left(\gamma, \frac{\tilde{I}_0}{\omega}\right) \times \exp\left\{-\frac{2\tilde{I}_0}{\omega}\left[\sinh^{-1}(\gamma) - \gamma\frac{\sqrt{1+\gamma^2}}{1+2\gamma^2}\right]\right\} \tag{2.35}$$

Note that (16) in the original paper has ω instead of $\sqrt{\omega}$ found here. Dimensional analysis

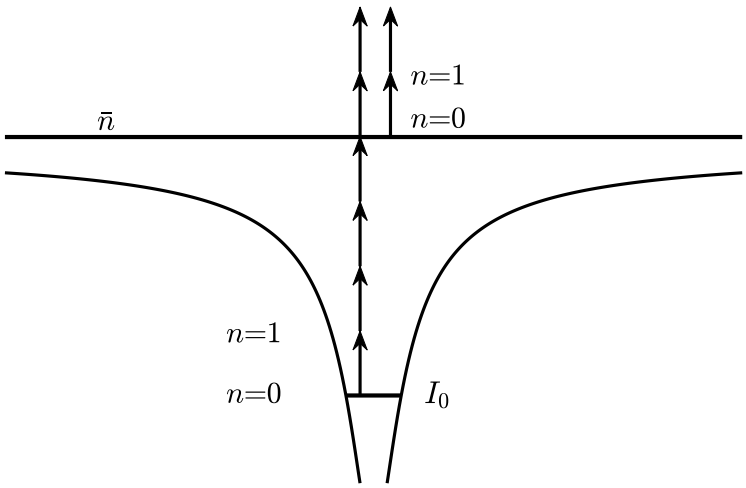

Figure 2.3: The redefinition of n. Original n gives electron energy relative to $-I_0$ as $-I_0 + n\omega$ ($n = 0, \cdots, \infty$). Redefined $n + \bar{n}$ ($n = 0, \cdots, \infty$) counts number of photons relative to threshold ionization energy in continuum, $\bar{n} = \langle \tilde{I}_0/\omega + 1 \rangle$ [1].

suggests $\sqrt{\omega}$ to be correct, as it yields units 1/time. Further, T is defined as

$$T(\gamma, x) = \sum_{n=0}^{\infty} \exp\left\{-2\left[<x+1> -x+n\right]\left(\sinh^{-1}\gamma - \frac{\gamma}{\sqrt{1+\gamma^2}}\right)\right\} \times \Phi\left\{\left[\frac{2\gamma}{\sqrt{1+\gamma^2}}(<x+1> -x+n)\right]^{1/2}\right\}. \tag{2.36}$$

The ionization rate Eq. (2.35) contains tunnel ionization and multi-photon ionization as two limiting cases for $\gamma \ll 1$ and for $\gamma \gg 1$.

2.4 Tunneling limit

In the limit $\gamma \ll 1$, tunneling is the dominant ionization mechanism derived in the following from Eq. (2.35) and Eq. (2.36). We start with T. For $\gamma \to 0$

$$\sinh^{-1}(\gamma) - \frac{\gamma}{\sqrt{1+\gamma^2}} \approx \frac{\gamma^3}{3}, \tag{2.37}$$

Inserting in T yields

$$T(\gamma, x) = \sum_{n=0}^{\infty} \exp\Big(-\frac{2}{3}\gamma^3 \left[< x+1 > -x + n\right]\Big) \times \Phi\Big(\sqrt{2\gamma \left[< x+1 > -x + n\right]}\Big), \tag{2.38}$$

To get a rough idea of the main contribution (maximum) of T, we need to approximate $\Phi(x) \approx x$ $(x < 1)$ with a rising function, as the exponential is continuously decreasing with growing x. Then, from $dT_n/dn = 0$ we find large $n \approx \gamma^{-3}$. This justifies setting $< x+1 > -x \approx 0$ in Eq. (2.38). Further, it allows us to change summation into integration. Expansion of the Dawson function for large values gives to lowest order $\Phi(x) \approx 1/(2x)$. As a result, Eq. (2.38) becomes

$$T(\gamma, x) = \int_0^{\infty} \exp\left(-\frac{2}{3}\gamma^3 n\right) \frac{1}{2\sqrt{2n\gamma}} dn = \frac{\sqrt{3\pi}}{4\gamma^2}. \tag{2.39}$$

Using Eq. (2.39), $\tilde{I}_0 = (1 + 1/2\gamma^2) I_0$ and the Taylor expansion of the exponent,

$$\left(1 + \frac{1}{2\gamma^2}\right)\left[\sinh^{-1}(\gamma) - \gamma\frac{\sqrt{1+\gamma^2}}{1+2\gamma^2}\right] \approx \frac{2\gamma}{3} - \frac{\gamma^3}{15}, \tag{2.40}$$

in Eq. (2.35), yields

$$w_0 = \frac{\sqrt{6\pi}}{2}\sqrt{\frac{I_0\omega}{\gamma}} \exp\left(-\frac{4}{3}\frac{I_0\gamma}{\omega}\left[1 - \frac{1}{10}\gamma^2\right]\right). \tag{2.41}$$

which, up to a factor of 2 coming from two saddle points, becomes equivalent to (20) in Keldysh [25], once γ from Eq. (2.1) is inserted.

The tunneling limit can be interpreted by noting that, as Keldysh did [25], the Keldysh parameter can be written as $\gamma = \omega/\omega_t$, where $\omega_t = F/\sqrt{2I_0}$ is the tunneling frequency. This can also be reframed in terms of a time relative to the laser half-cycle by multiplying the top and bottom by π, so that $\gamma = T_t/(T_0/2)$, where $T_t = \pi\sqrt{2I_0}/F$. As can be seen, Coulomb barrier suppression due to a strong laser field relative to $\sqrt{2I_0}$ reduces the time T_t so that an electron is able to tunnel more quickly. If the laser half-cycle $T_0/2$ is long relative to T_t, then the electron has sufficient time to pass through the suppressed Coulomb barrier during each laser half-cycle.

As is mentioned in Keldysh's original work [25], this equation fails in the static limit as $\omega \to 0$. This is because the effect of the Coulomb field is ignored for the ionized electron. Keldysh's paper does include a correction factor, apparently derived quasiclassically for the general ionization rate in (1) there [25]. However, better articulation of a quasiclassically obtained correction factor is explored by PPT [121]. However, it should be stressed that the results of PPT are not exact and continued research on improving the Coulomb correction is needed [128].

2.5 Multi-photon limit

In the opposite limit of multi-photon ionization $\gamma >> 1$ so that $\sinh^{-1}(\gamma) \approx \ln 2\gamma$. Further, we use the identity $\exp(a \ln \gamma) = \gamma^a$ and set $n = 0$ in the sum in Eq. (2.36), as multi-photon ionization is dominant for small n. With these approximations we reach

$$T(\gamma, x) = \left(\frac{1}{4\gamma^2}\right)^{<x+1>-x} \exp\left(2\left(< x+1 > -x\right)\right) \times \Phi\left\{\left(2(< x+1 > -x)\right)^{1/2}\right\}. \quad (2.42)$$

Inserting Eq. (2.42) into Eq. (2.35) and expanding the exponent gives

$$w_0 = 2\sqrt{2I_0\omega}\left(\frac{1}{4\gamma^2}\right)^{\langle \tilde{I}_0/\omega+1\rangle} \exp\left(2\left\langle \frac{\tilde{I}_0}{\omega}+1\right\rangle - \frac{\tilde{I}_0}{\omega}\right) \times \Phi\left\{\left[2\left\langle \frac{\tilde{I}_0}{\omega}+1\right\rangle - 2\frac{\tilde{I}_0}{\omega}\right]^{1/2}\right\}, \quad (2.43)$$

in agreement with (21) of [25] up to a factor of 2.

The multi-photon limit of ionization describes the dominant mechanism as being the simultaneous absorption of multiple photons to free a bound electron. While tunneling is an inherently quantum mechanical process, the tutorial [126] describes multi-photon ionization as a 'nearly classical' mechanism where a laser field 'shakes' the Coulomb potential walls such that an electron contained within eventually has enough energy to pass over the potential.

Although Keldysh presented an important preliminary formulation of multi-photon ionization, it has been criticized as being too idealistic for describing actual atoms [126, 124, 141, 142]. The multi-photon limit has been considered as a limit where perturbation theory can be applied, but is considered to be of too low order to be valid [126]. The model's neglect of excited states between the ground state and the continuum, that are

considered to be highly relevant, has also been criticized [124, 141]. The goal of this work was to make the derivation of Keldysh ionization theory more accessible by adding more details so that only simple few-line manipulations are left between equations. We hope that the more detailed exposition of the mathematical methods and tools used in Keldysh's work will benefit the research community.

2.6 Analytic continuation of Eq. (2.16)

The analytical continuation of Eq. (2.16) into the complex plane, leading to (2.17), is derived in more detail. We start from $L(\mathbf{P}, x)$ of Eq. (2.16). The exponent of $L(\mathbf{P}, x)$, as defined in Eq. (2.10), is expressed as

$$\begin{aligned} S &= \int_0^x I_0 + \frac{1}{2}\left(\mathbf{P} + \frac{\mathbf{F}}{\omega}\sin(\tau)\right)^2 d\tau \\ \frac{S}{\omega} &= \int_0^x (n - c_2) + c_1 \sin(\tau) + 2c_2 \sin^2(\tau)\, d\tau \\ &= nx - c_1 \cos(x) - \frac{c_2}{2}\sin(2x) \\ &= n \sin^{-1}(u) - c_1\sqrt{1-u^2} - c_2 u\sqrt{1-u^2}, \end{aligned} \tag{2.44}$$

where $\sin^{-1} = \arcsin$. Further, we have used the δ-function in Eq. (2.16) in going from line 1 to 2, $c_1 = (\mathbf{PF})/\omega^2$, and $c_2 = F^2/(4\omega^3)$. Moreover, the constant terms in the third line arising from the lower integration limit are not shown, as they drop out in $|L(\mathbf{P})|^2$ in Eq. (2.16). Finally, in the last line we have used the transformation $\sin(x) = u$. The integral as a function of u must be treated with some care, as for every value u two values of x exist. This can be remedied by splitting the integration path into segments over which u is single valued [129].

The integral in Eq. (2.16), and therewith the integral Eq. (2.44), run from 0 to 2π. The integration points $x = 0, \pi/2, 3\pi/2, 2\pi$ correspond to $u = 0, 1, -1, 0$ in the transformed u-domain. The goal is to define the functions $\sin^{-1}(u)$, $\sqrt{1-u^2}$, and $u\sqrt{1-u^2}$ in a way that they are single valued over the whole integration path, i.e. have a unique x-value for each value of u. We discuss $\sin^{-1}(u)$ in more detail and then give the results for the other two functions. The principal branch of $\sin^{-1}(u)$, where it is single valued, ranges from $-\pi/2 \leq x \leq \pi/2$. To keep $\sin^{-1}(u)$ single valued and to make it cover the whole original x-domain of $[0, 2\pi]$, the integration path in Eq. (2.16) is split into segments,

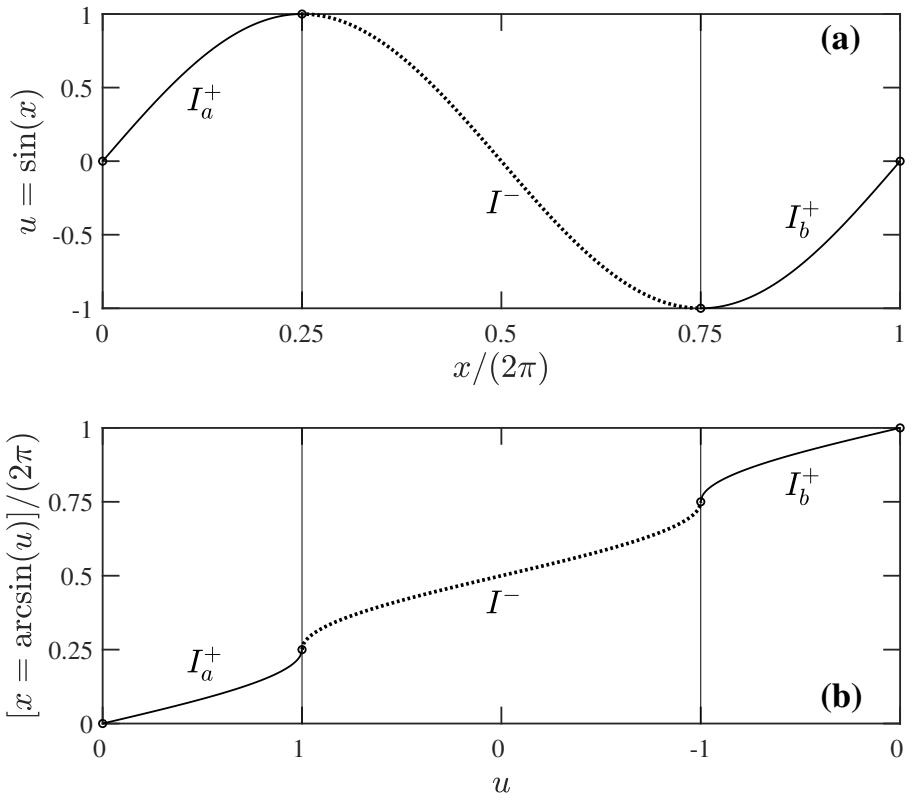

Figure 2.4: (a,b) show transformation $u = \sin(x)$ (a) and its inverse $x = \arcsin(u)$ (b), with $\sin^{-1}$ defined in the text so that it recovers the full range of the x-domain, see x-range plotted along y-axis of (b). The points $x = 0, \pi/2, 3\pi/2, 2\pi$ correspond to $u = 0, 1, -1, 0$ (open circles in (a,b)). The thin lines show the boundaries of integration segments I_a^+ (full line), I^- (dotted line), and I_b^+ (full line) defined in the text [1].

each lying within a particular single-valued branch. In segment I_a^+, $0 \le x \le \pi/2$, we have $x = \sin^{-1}(u)$. Segment I^- occupies the next branch, $\pi/2 \le x \le 3\pi/2$ for which $x = \pi - \sin^{-1}(u)$. Finally, the last segment I_b^+ runs from $3\pi/2 \le x \le 2\pi$ with $x = 2\pi + \sin^{-1}(u)$. The transformation $u = \sin(x)$ and its inverse are plotted in Fig. 2.4(a,b). We see from Fig. 2.4(b) that the above definition of $\sin^{-1}$ is single valued and recovers the whole range from 0 to 2π (the x-axis in Fig. 2.4(a).

Similarly, to make the remaining functions $g(u) = \sqrt{1-u^2}, u\sqrt{1-u^2}$ in Eq. (2.44) single valued, they need to be defined in I_a^+, I^-, I_b^+ as $g(u), -g(u), g(u)$, respectively. The functions $g(u)$ change sign in I^-.

As a result, Eq. (2.16) can be written as

$$L(\mathbf{P}) = \frac{1}{2\pi}\int_0^1 V_0\, e^{i\left[n\sin^{-1}(u)-c_1\sqrt{1-u^2}-c_2u\sqrt{1-u^2}\right]}du + \frac{1}{2\pi}\int_1^{-1} V_0\, e^{i\left[n\left(\pi-\sin^{-1}(u)\right)+c_1\sqrt{1-u^2}+c_2u\sqrt{1-u^2}\right]}du$$
$$+ \frac{1}{2\pi}\int_{-1}^{0} V_0\, e^{i\left[n\left(2\pi+\sin^{-1}(u)\right)-c_1\sqrt{1-u^2}-c_2u\sqrt{1-u^2}\right]}du, \tag{2.45}$$

where $V_0 = V_0(\mathbf{P} + \mathbf{F}u/\omega)$. The three integrals correspond to segments I_a^+, I^-, I_b^+, respectively. So far, we have shown how to remedy the multi-valuedness of the transformation $u = \sin(x)$ in the real domain.

The same procedure can be done very elegantly by continuing integral Eq. (2.16) into the complex domain, see Fig. 2.5. The variable transformation $x = \sin(u)$, used to go from Eq. Eq. (2.16) to (2.17), introduces multi-valuedness that needs to be resolved by an appropriate definition of the integration contour. The factor $1/\sqrt{1-v^2}$ in Eq. (2.17b) is multi-valued and has branch points at $v = \pm 1$. We introduce a branch cut between -1 and 1 to make the function single-valued. Points v infinitesimally above and below the branch cut are denoted by $v^\pm = v \pm i\varepsilon$.

The branch cut is defined by setting $v + 1 = r_2\exp(i\varphi_2)$ and $v - 1 = r_1\exp(i\varphi_1)$ with $0 \le \varphi_1, \varphi_2 < 2\pi$ which results in $\sqrt{1-v^2} = \sqrt{r_1 r_2}\exp(i\varphi)$ with $\varphi = (\varphi_1 + \varphi_2 - \pi)/2$. As $\varphi_1 \approx \pi, \pi$ and $\varphi_2 = 0, 2\pi$ we find $\varphi = 0, \pi$ for v on I^+ and I^-, respectively. As a result, $\lim_{\varepsilon\to 0}\sqrt{1-v_\pm^2} \to \pm\sqrt{1-v^2}$. This agrees with the $\pm$ difference between the square root evaluated on I^+ and I^-, respectively, obtained before in the real domain. As a result, we find that the $\pm$ difference can be realized by choosing I^+ and I^- to be located above and below the real axis, respectively. We connect I^+ and I^- by infinitesimal circles ($C_{\pm 1}$) around $v = \pm 1$ which yields the dog bone contour in Fig. 2.5. As such, the requirement of a single valued integrand has defined the integration contour of the integral

$$L(\mathbf{P}) = \frac{1}{2\pi}\oint V_0\left(\mathbf{P} + \frac{\mathbf{F}}{\omega}u\right) e^{i\frac{S(u)}{\omega}}du$$
$$\frac{S(u)}{\omega} = \int_0^u \frac{(n-c_2) + c_1 v + 2c_2 v^2}{\sqrt{1-v^2}}dv \tag{2.46}$$

in the complex plane. The integral defining $S(u)$ on the real axis is

$$\int_0^u \frac{2c_2v^2 + c_1 v + (n-c_2)}{\sqrt{1-v^2}}dv = n\sin^{-1}(u) - (c_1 + c_2 u)\sqrt{1-u^2}. \tag{2.47}$$

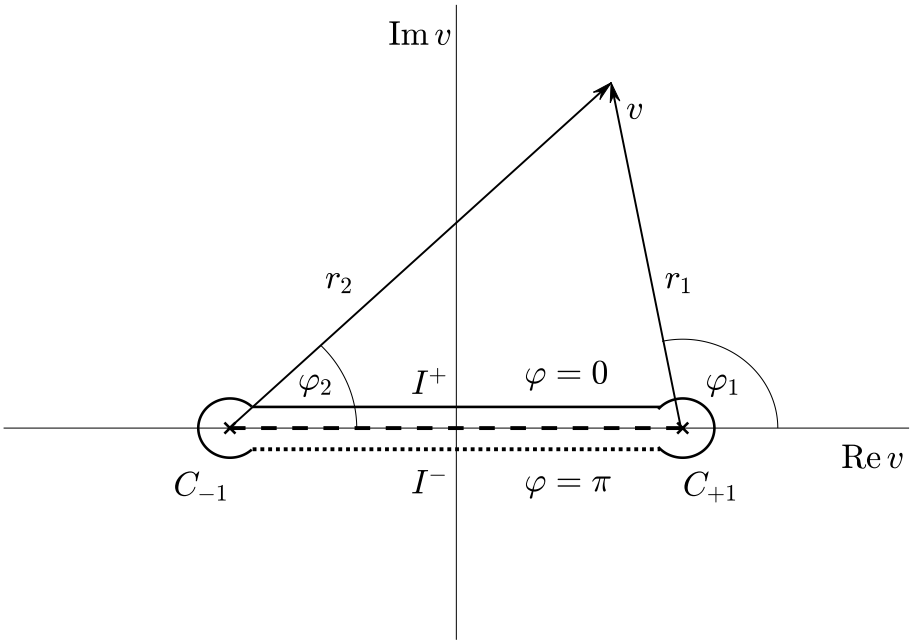

Figure 2.5: Closed integration contour in Eq. (2.17); branch points are at $-1, 1$ (cross), and the branch cut (dashed line) runs between -1 and 1; I^+ (full) and I^+ (dotted) run along $\pm i\varepsilon$; $C_{\pm 1}$ are circular integrals around ± 1. Arrows represent the complex numbers $v \pm 1$ in polar form, see text; φ represents the phase of $\sqrt{1-v^2}$ [1].

What remains to be done is to evaluate integral Eq. (2.47) on the complex integration contour and to show that the result agrees with the integrals in Eq. (2.45). The integral along the dogbone contour consists of an integral along I_a^+ from $0^+ \to 1^+$, a circular integral along C_{+1}, an integral along I^- from $1^- \to -1^-$, another circular integral along C_{-1}, and finally an integral I_b^+ from $-1^+ \to 0^+$. The two circular integrals drop out, as they scale $\propto \lim_{\varepsilon\to 0} \sqrt{(\varepsilon)} = 0$. We denote $S_{I_a^+}(u^+)$, $S_{I^-}(u^-)$, and $S_{I_b^+}(u^+)$, as the integrals for which u lies in the intervals of I_a^+, I^-, I_b^+, respectively. With the help of Eq. (2.47) we obtain

$$\begin{aligned}\frac{S_{I_a^+}(u^+)}{\omega} &= \int_0^{u^+} \frac{(n-c_2) + c_1 v + 2c_2 v^2}{\sqrt{1-v^2}} dv \\ &= n \sin^{-1}(u) - (c_1 + c_2 u)\sqrt{1-u^2}, \end{aligned} \tag{2.48}$$

$$\begin{aligned}\frac{S_{I^-}(u^-)}{\omega} =& \frac{S_{I_a^+}(1^+)}{\omega} + \int_{1^-}^{u^-} \frac{(n-c_2)+c_1 v+2c_2 v^2}{-\sqrt{1-v^2}} dv \\ =& n\left(\pi - \sin^{-1}(u)\right) + (c_1+c_2 u)\sqrt{1-u^2}, \end{aligned} \tag{2.49}$$

where $S_{I_a^+}(1^+)/\omega = n\pi/2$, and

$$\begin{aligned}\frac{S_{I_b^+}(u^+)}{\omega} =& \frac{S_{I^-}(-1^-)}{\omega} + \int_{-1^+}^{u^+} \frac{(n-c_2)+c_1 v+2c_2 v^2}{\sqrt{1-v^2}} dv \\ =& n\left(2\pi + \sin^{-1}(u)\right) - \left(c_1+c_2 u\right)\sqrt{1-u^2} \end{aligned} \tag{2.50}$$

with $S_{I^-}(-1^-)/\omega = 3n\pi/2$. The classical actions in all three segments agree with the phase terms in Eq. (2.45) which shows that the treatments in the real and complex domains are consistent.

Chapter 3

Strong Field Adiabatic Following Formalism

This chapter is based on the paper [5], and it overlaps with its text with the permission of the journal (Physical Review B)-copyright by the American Physical Society.

3.1 Introduction

In this chapter, a closed-form formalism for modeling high harmonic generation in solids is derived which is called strong field adiabatic following (SFAF) formalism. Using SFAF the separation into resonant and virtual processes is presented. This chapter is about finding the dominant contribution to HHG. To further investigate the problem the division of channels into resonant (real) and non-resonant (virtual) was done by our model. The contribution of virtual channels in HHG has been disregarded so far in contrast to their importance in perturbative nonlinear optics [10, 5]. Recent experiments have shown virtual processes importance in below-minimum band gap harmonics [143]. Besides, light-field control of real and virtual charge carriers have been recently demonstrated [144]. We developed the strong field adiabatic following (SFAF) approach which is built on the adiabatic following approximation of perturbative nonlinear optics [10]. It is suitable for mid-IR and far-IR semiconductors, as well as near-IR dielectric experiments where the bandgap energy defines the fastest time parameter. The regular adiabatic following approximation only accounts for virtual transitions. In strong field processes, both virtual and real (resonant) processes are important. Both of these processes can be captured by our SFAF approach [5]. Virtual processes in strong field experiments gain importance especially in near-IR dielectric experiments due to dynamical Stark shift. Why are they

so important in dielectrics? The reason is the larger dipole moments of dielectrics and at the same time the applicability of higher intensities due to higher damage thresholds in them [17]. A schematic of resonant (real) and non-resonant (virtual) processes and their difference in extreme and perturbative nonlinear optics can be found in Fig. (3.1). Real transition is bridged by 4 photons, ensuring energy conservation. Virtual transitions, on the other hand, do not fulfill energy conservation and return to the ground state after the laser pulse. In perturbative nonlinear optics, only the lowest-order absorption channel (fuller arrows) dominates, making virtual (left) and real (right) transitions distinguishable. In extreme nonlinear optics, a large number of higher-order, net-zero-photon processes (blue arrows) become important as well, complicating the separation [5].

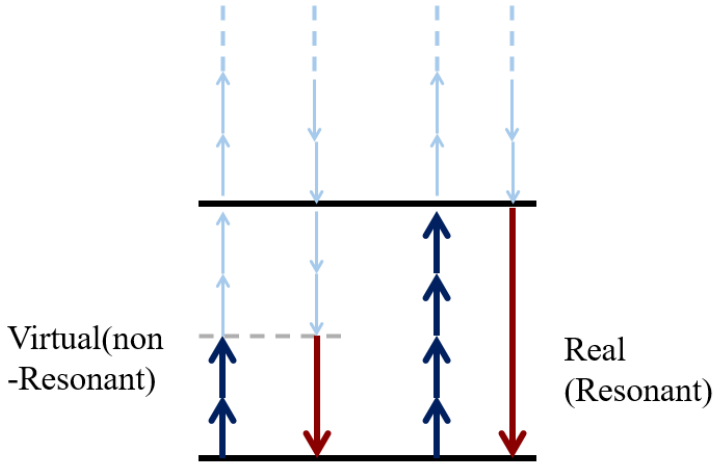

Figure 3.1: Real (resonant) versus virtual (non-resonant) processes [5].

Finally, in this chapter we show evidence of the need to add many-body effects to our model which will be the discussion of chapter (4).

3.2 Strong field adiabatic following (SFAF) formalism

Our analysis starts from the von Neumann (one-body semiconductor Bloch) equation for density matrix ρ, [5]

$$i\partial_t \rho(\mathbf{K}, t) = [H(\mathbf{K}_t, t), \rho(\mathbf{K}, t)], \tag{3.1}$$

derived in the moving crystal momentum frame $\mathbf{K}_t = \mathbf{K} + \mathbf{A}(t)$, with crystal momentum $\mathbf{K}$ defined in the shifted first Brillouin zone, $\overline{\mathrm{BZ}} = \mathrm{BZ} - \mathbf{A}(t)$. The vector potential is $\mathbf{A}(t)$ and the electric field $\mathbf{F}(t) = -\partial_t \mathbf{A}(t)$. The Hamilton operator H is given by

$$H(\mathbf{K}_t, t) = \frac{1}{2}\begin{bmatrix} \varepsilon(\mathbf{K}_t) & \Omega(\mathbf{K}_t, t) \\ \Omega(\mathbf{K}_t, t) & -\varepsilon(\mathbf{K}_t) \end{bmatrix} \tag{3.2}$$

with $\Omega(\mathbf{K}_t, t) = 2\mathbf{F}(t)\mathbf{d}_{vc}(\mathbf{K}_t)$ the Rabi frequency and $\mathbf{d}_{vc}$ the transition dipole element between valence and conduction band. We consider only inversion symmetric materials with purely real or imaginary transition dipole. The bandgap $\varepsilon(\mathbf{K}) = E_c(\mathbf{K}) - E_v(\mathbf{K})$ is the difference between conduction and valence energy bands. The density operator and Hamiltonian are defined with respect to the Bloch basis functions $|v\rangle(\mathbf{K}_t)$, $|c\rangle(\mathbf{K}_t)$, for valence and conduction band, respectively; e.g. H_{11} refers to basis $|c\rangle\langle c|$.

In the limit of laser frequency much smaller than the minimum bandgap, the electron dynamics follows dominantly the laser field and the adiabatic following approximation can be used.
This is done by first diagonalizing the Hamiltonian (3.2),

$$\widetilde{H}(\mathbf{K}_t, t) = V^+ H V = \frac{1}{2}\begin{bmatrix} \lambda(\mathbf{K}_t, t) & 0 \\ 0 & -\lambda(\mathbf{K}_t, t) \end{bmatrix}, \tag{3.3}$$

with $\lambda(\mathbf{K}_t, t) = \sqrt{\varepsilon^2(\mathbf{K}_t) + \left|\Omega(\mathbf{K}_t, t)\right|^2}$ and unitary matrix

$$V(\mathbf{K}_t, t) = \frac{1}{\sqrt{2}}\begin{bmatrix} \frac{\sqrt{\lambda+\varepsilon}}{\sqrt{\lambda}} & -\frac{\Omega}{\sqrt{\lambda}\sqrt{\lambda+\varepsilon}} \\ \frac{\Omega}{\sqrt{\lambda}\sqrt{\lambda+\varepsilon}} & \frac{\sqrt{\lambda+\varepsilon}}{\sqrt{\lambda}} \end{bmatrix}. \tag{3.4}$$

Multiplying the von Neumann equation with V^+, V from the left and right, inserting $VV^+ = \mathbb{1}$ and defining $\tilde{\rho} = V^+ \rho V$ yields the transformed equation

$$i\partial_t \tilde{\rho} = [\widetilde{H}, \tilde{\rho}] + i(\partial_t V^+) V \tilde{\rho} + i\tilde{\rho} V^+ (\partial_t V). \tag{3.5}$$

The above equation is still exact. We start to integrate the above equation. We use the

Ansatz

$$\tilde{\rho}(t) = e^{-i\int_{-\infty}^{t}\widetilde{H}(\mathbf{K}_\tau,\tau)d\tau}\tilde{\rho}'(t)e^{i\int_{-\infty}^{t}\widetilde{H}(\mathbf{K}_\tau,\tau)d\tau} \tag{3.6}$$

in Eq. (3.5). We have

$$\begin{aligned} &ie^{-i\int_{-\infty}^{t}\widetilde{H}(\mathbf{K}_\tau,\tau)d\tau}\partial_t\tilde{\rho}'e^{i\int_{-\infty}^{t}\widetilde{H}(\mathbf{K}_\tau,\tau)d\tau} + e^{-i\int_{-\infty}^{t}\widetilde{H}(\mathbf{K}_\tau,\tau)d\tau}\cancel{[\widetilde{H},\tilde{\rho}']}e^{-i\int_{-\infty}^{t}\widetilde{H}(\mathbf{K}_\tau,\tau)d\tau} = \\ &e^{-i\int_{-\infty}^{t}\widetilde{H}(\mathbf{K}_\tau,\tau)d\tau}\cancel{[\widetilde{H},\tilde{\rho}']}e^{-i\int_{-\infty}^{t}\widetilde{H}(\mathbf{K}_\tau,\tau)d\tau} + i(\partial_t V^+)Ve^{-i\int_{-\infty}^{t}\widetilde{H}(\mathbf{K}_\tau,\tau)d\tau}\tilde{\rho}'(t)e^{i\int_{-\infty}^{t}\widetilde{H}(\mathbf{K}_\tau,\tau)d\tau} + \\ &ie^{-i\int_{-\infty}^{t}\widetilde{H}(\mathbf{K}_\tau,\tau)d\tau}\tilde{\rho}'(t)e^{i\int_{-\infty}^{t}\widetilde{H}(\mathbf{K}_\tau,\tau)d\tau}V^+(\partial_t V) \end{aligned} \tag{3.7}$$

Two terms cancel and by multiplying the Eq. (3.7) by $e^{i\int_{-\infty}^{t}\widetilde{H}(\mathbf{K}_\tau,\tau)d\tau}$, and $e^{-i\int_{-\infty}^{t}\widetilde{H}(\mathbf{K}_\tau,\tau)d\tau}$ from left and right respectively, we reach

$$\partial_t\tilde{\rho}'(t) = \tilde{W}\tilde{\rho}'(t) + \tilde{\rho}'(t)\tilde{W} \tag{3.8}$$

where

$$\tilde{W}(\mathbf{K},t) = e^{i\int_{-\infty}^{t}d\tau\widetilde{H}(\mathbf{K}_\tau)}(\partial_t V^+(\mathbf{K}_t))V(\mathbf{K}_t)e^{-i\int_{-\infty}^{t}d\tau\widetilde{H}(\mathbf{K}_\tau)}. \tag{3.9}$$

Eq. (3.8) can be solved. We have

$$\tilde{\rho}'(t) = \left(\hat{T}e^{\int_{-\infty}^{t}d\tau\tilde{W}(\mathbf{K},\tau)}\right)\tilde{\rho}'(t=-\infty)\left(\hat{T}e^{\int_{-\infty}^{t}d\tau\tilde{W}(\mathbf{K},\tau)}\right)^+ \tag{3.10}$$

Based on Eq. (3.6) $\tilde{\rho}'(t=-\infty) = \tilde{\rho}(t=-\infty)$. Therefore, after some mathematical steps, we get the following unitary transformation for $\rho(\mathbf{K},t)$

$$\begin{aligned} \rho(\mathbf{K},t) &= X^+(\mathbf{K},t)\rho(\mathbf{K},t=-\infty)X(\mathbf{K},t) \\ X(\mathbf{K},t) &= \left(\hat{T}e^{\int_{-\infty}^{t}d\tau\tilde{W}(\mathbf{K},\tau)}\right)^+ e^{i\int_{-\infty}^{t}d\tau\widetilde{H}(\mathbf{K}_\tau)}V^+(\mathbf{K}_t) \\ \tilde{W}(\mathbf{K},t) &= e^{i\int_{-\infty}^{t}d\tau\widetilde{H}(\mathbf{K}_\tau)}(\partial_t V^+(\mathbf{K}_t))V(\mathbf{K}_t)e^{-i\int_{-\infty}^{t}d\tau\widetilde{H}(\mathbf{K}_\tau)}. \end{aligned} \tag{3.11}$$

We omit the explicit time dependence in V, V^+, $\widetilde{H}$, Ω, and λ from Eq. (3.11) from now on. Here, $X(\mathbf{K},t)$ and $W(\mathbf{K},t)$ are matrix operators introduced to simplify the presentation of Eq. (3.11), and $\hat{T}$ refers to the time ordering operator, which numerically is evaluated as $\hat{T}e^{\int_{-\infty}^{t}d\tau W(\mathbf{K},\tau)} = \Pi_{j=0}^{n}e^{W(\mathbf{K},t_j)d\tau}$ on a time window between t_0 and t_n with step size $d\tau \to 0$ small enough to converge. The time ordered operator can be expanded into a Dyson series

[57]. We keep terms up to second order. It yields

$$\hat{T}e^{\int_{-\infty}^{t}d\tau W(\mathbf{K},\tau)} \approx 1+\int_{-\infty}^{t}dt'\,W(\mathbf{K},t')+\int_{-\infty}^{t}dt'\,W(\mathbf{K},t')\int_{-\infty}^{t'}dt''\,W(\mathbf{K},t''). \tag{3.12}$$

Putting the Dyson expanded time ordering operator Eq. (3.12) in Eq. (3.11), after some mathematical steps one gets

$$\begin{aligned}\rho(t) = V(t)\left\{1+\int_{-\infty}^{t}W(t,t')dt'+\int_{-\infty}^{t}W(t,t')dt'\int_{-\infty}^{t'}W(t,t'')dt\varepsilon+...\right\}V^{+}(t)\rho_0 V(t)\\ \left\{1+\int_{-\infty}^{t}W^{+}(t,t')dt'+\int_{-\infty}^{t}\left(\int_{-\infty}^{t'}W^{+}(t,t'')dt\varepsilon\right)W^{+}(t,t')dt'\right\}V^{+}(t),\end{aligned} \tag{3.13}$$

where we have substituted $\rho_0 = Ve^{-i\int_{-\infty}^{t}\tilde{H}}\rho(t=-\infty)e^{i\int_{-\infty}^{t}\tilde{H}}V^{+}$ which is the zeroth order contribution. Note that the $\mathbf{K}$ dependence is omitted here for simplicity. We define $W(t,t')$ to be

$$W(t,t') = e^{-i\int_{-\infty}^{t}\tilde{H}dt''}\tilde{W}(t')e^{i\int_{-\infty}^{t}\tilde{H}dt''} = e^{-i\int_{t'}^{t}\tilde{H}dt''}\left\{\partial_{t'}V^{+}(t')\right\}V(t')e^{i\int_{t'}^{t}\tilde{H}dt''}. \tag{3.14}$$

Note that $\tilde{W}(t)$ is given in Eq. (3.9). To further simplify we define $\tilde{\rho}_0 = V^{+}\rho_0 V$; therefore, Eq. (3.13) yields

$$\begin{aligned}\tilde{\rho}(t) = \tilde{\rho}_0+\int_{-\infty}^{t}W(t,t')dt'\times\tilde{\rho}_0+\int_{-\infty}^{t}W(t,t')dt'\int_{-\infty}^{t'}W(t,t'')dt''\times\tilde{\rho}_0\\ +\tilde{\rho}_0\times\int_{-\infty}^{t}W^{+}(t,t')dt'+\tilde{\rho}_0\times\int_{-\infty}^{t}\left(\int_{-\infty}^{t'}W^{+}(t,t'')dt''\right)W^{+}(t,t')dt'\\ +\int_{-\infty}^{t}W(t,t')dt'\times\tilde{\rho}_0\times\int_{-\infty}^{t}W^{+}(t,t')dt',\end{aligned} \tag{3.15}$$

In Eq. (3.14), we have $\partial_{t'}V^{+}(t')$ which contains the derivative of the field. Therefore, one can expect to get the conventional adiabatic following approximation given in nonlinear books from the zeroth order [10].

After calculating matrix $W(t,t')$ in Eq. (3.14) and its integral, we reach the following

contributions.

$$\rho_0(\mathbf{K},t) = \frac{1}{2}\begin{bmatrix} \frac{\lambda-\varepsilon}{\lambda} & -\frac{\Omega}{\lambda} \\ -\frac{\Omega}{\lambda} & \frac{\lambda+\varepsilon}{\lambda} \end{bmatrix}_{\mathbf{K}_t} \tag{3.16a}$$

$$\rho_1(\mathbf{K},t) = \begin{bmatrix} \frac{\Omega}{2\lambda}\mathrm{Re}[u_{12}] & -\frac{\epsilon}{\lambda}\mathrm{Re}[u_{12}] - i\mathrm{Im}[u_{12}] \\ \frac{\epsilon}{\lambda}\mathrm{Re}[u_{12}] + i\mathrm{Im}[u_{12}] & -\frac{\Omega}{2\lambda}\mathrm{Re}[u_{12}] \end{bmatrix}_{\mathbf{K},t} \tag{3.16b}$$

$$\rho_2(\mathbf{K},t) = \begin{bmatrix} \frac{\varepsilon}{\lambda}|u_{12}|^2 & \frac{\Omega}{\lambda}|u_{12}|^2 \\ \frac{\Omega}{\lambda}|u_{12}|^2 & -\frac{\varepsilon}{\lambda}|u_{12}|^2 \end{bmatrix}_{\mathbf{K},t}, \tag{3.16c}$$

where we have

$$\mathrm{u}_{12}(t) = -\frac{1}{2}\frac{\Omega}{\lambda} + \frac{i}{2}\int_{-\infty}^{t} \Omega e^{-i\int_{t'}^{t}\lambda d\tau} dt'. \tag{3.17}$$

Finally, in the limit of intense laser fields, the dynamics is dominated by the exponent in u_{12}. As a result, pre-exponential factors of order $(|\Omega|/\varepsilon)$ and higher are of secondary significance and are neglected [5]. This results in

$$\rho(\mathbf{K},t) \approx \begin{bmatrix} 0 & 0 \\ 0 & 1 \end{bmatrix} + \begin{bmatrix} 0 & -\mathfrak{u} \\ -\mathfrak{u}^* & 0 \end{bmatrix}_{\mathbf{K},t} + \begin{bmatrix} |\mathfrak{u}|^2 & 0 \\ 0 & -|\mathfrak{u}|^2 \end{bmatrix}_{\mathbf{K},t} \quad \text{with}$$

$$\mathfrak{u}(\mathbf{K},t) = \frac{i}{2}\int_{-\infty}^{t} dt' \Omega(\mathbf{K}_{t'}) e^{-i\int_{t'}^{t}\lambda(\mathbf{K}_\tau)d\tau}. \tag{3.18}$$

3.3 HHG using SFAF formalism

The current expectation value can be decomposed into contributions coming from the various density matrix expansion orders, $\langle \mathbf{j} \rangle = \sum_{j=0}^{2} \langle \mathbf{j}_j \rangle$, where $\langle \mathbf{j}_j \rangle = \int_{\overline{\mathrm{BZ}}} d^3K \, \mathrm{Tr}[\overline{\rho}_j(\mathbf{K},t)\mathbf{j}(\mathbf{K}_t)]$. We only get HHG contributions from $\langle \mathbf{j}_1 \rangle$ and $\langle \mathbf{j}_2 \rangle$. Replacing $\langle \mathbf{j}_1 \rangle \to \langle \mathbf{j}_{er} \rangle$ and $\langle \mathbf{j}_2 \rangle \to \langle \mathbf{j}_{ra} \rangle$ we obtain interband and intraband current

$$\langle \mathbf{j}_{er} \rangle \approx -\frac{d}{dt}\int_{\overline{\mathrm{BZ}}} d^3K \, \mathbf{d}(\mathbf{K}_t)\, \mathfrak{u}(\mathbf{K},t) + \mathrm{c.c.}, \tag{3.19a}$$

$$\langle \mathbf{j}_{ra} \rangle \approx \int_{\overline{\mathrm{BZ}}} d^3K \, \mathbf{v}(\mathbf{K}_t) n_c(\mathbf{K},t). \tag{3.19b}$$

Here, $n_c(\mathbf{K},t) = |\mathfrak{u}(\mathbf{K},t)|^2$ and $n_c(t) = \int_{\mathrm{BZ}} d^3K\, n_c(\mathbf{K},t)$ is the conduction band population. In the limit of small Rabi frequency, $\lambda \to \varepsilon$ in the exponent of Eq. (3.18), Eqs. (3.19) go over into the FVB solution [25, 45, 30]. The main difference between the SFAF and FVB solution is the dynamic Stark shift. In the following, a comparison of SFAF and FVB approximation is shown.

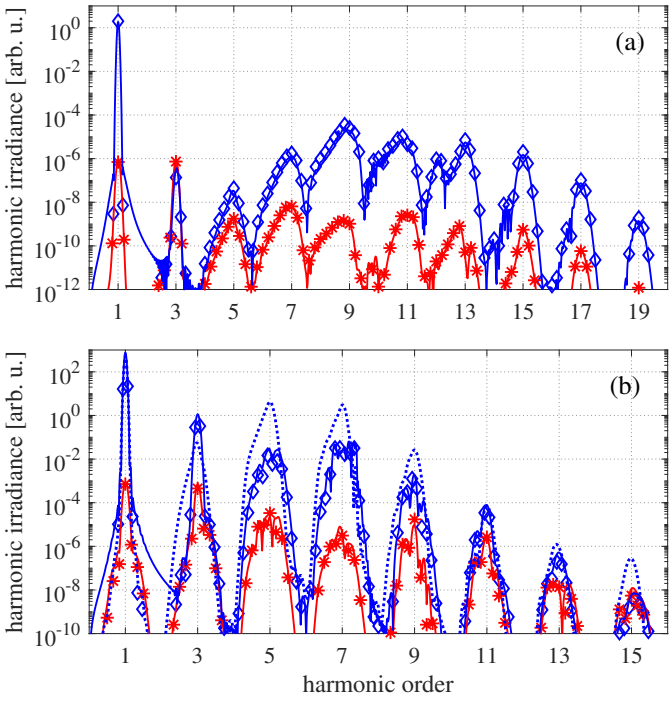

Figure 3.2: (a,b) Interband (blue full line) and intraband (full red line) HHG as obtained from the numerical solution of Eq. (3.1) are compared to interband (blue diamond) and intraband (red asterisk) HHG from SFAF Eqs. (3.19). Dotted line in (b) represents FVB solution ($\lambda \to \varepsilon$) in Eq. (3.18). (a) Model semiconductor: $E_g = 0.129$, $\Delta_1 = 0.17$, $d_0 = 3.64$, $a = 5.3$; mid-ir laser: $F_0 = 0.002$ (1.2×10^{11}W/cm^2), $\omega_0 = 0.015$ (3.04μm), $\tau_0 = 6T_0$. (b) Model dielectric: $E_g = 0.32$, $\Delta_1 = 0.06$, $\Delta_2 = -0.0035$, $\Delta_3 = -0.001$, $\Delta_4 = -0.0007$, $d_0 = 6.5$, and $a = 9.45$; near-ir laser: $F_0 = 0.012$ (4.3×10^{12}W/cm^2), $\omega_0 = 0.06$ (0.76μm), $\tau_0 = 6T_0$ [5].

In Fig. (3.2) interband HHG (blue line) and intraband HHG (red line), as determined by a numerical solution of Eq. (3.1) for model semiconductor (a) and dielectric (b), are compared to harmonics obtained from currents (3.19a) (blue diamonds) and (3.19b) (red asterisks). The blue dotted line in (b) represents FVB interband HHG. Note that the FVB interband currents are not shown in (a), as it is the same as the exact numerical solution. Interband HHG is dominant over the whole spectrum in (a). The important thing to note

is a difference of up to two orders between the SFAF and FVB results for interband HHG. FVB intraband HHG is not shown but displays similar disagreement. Therefore, we can conclude a greater importance of the dynamical Stark shift in dielectrics in comparison to semiconductors. The greater importance of the dynamic Stark effect in dielectrics can be due to larger dipole moments or due to higher applicable intensities because of higher damage thresholds [17]. We also see that for higher harmonics, $N \geq 15$, the intensities of inter- and intraband contributions become comparable in Fig. (3.2b) [5].

3.4 Separation of real and virtual transitions using SFAF formalism

Based on Eqs. (3.19) we can develop a method to separate virtual and real transitions. This is done by first splitting Eq. (3.18) into a probability amplitude of ionization, $\mathfrak{v}$, and into an exponent that is responsible for interband HHG,

$$\begin{aligned}\mathfrak{u}(\mathbf{K},t) &= e^{-i\int_{-\infty}^{t} d\tau\, \lambda(\mathbf{K}_\tau)}\mathfrak{v}(\mathbf{K},t)\\ \mathfrak{v}(\mathbf{K},t) &= \frac{i}{2}\int_{-\infty}^{t} dt' \Omega^*(\mathbf{K}_{t'}) e^{i\int_{-\infty}^{t'} \lambda(\mathbf{K}_\tau) d\tau}.\end{aligned} \tag{3.20}$$

Then, $\mathfrak{v} = \mathfrak{v}_r + \mathfrak{v}_{nr}$ and consequently, $\mathfrak{u} = \mathfrak{u}_r + \mathfrak{u}_{nr}$ are split into resonant and non-resonant parts based on the following . Resonant transitions are expected to exhibit a steady increase of n_c over time, while non-resonant transitions are oscillatory and the population returns to the valence band after the laser pulse.

Therefore, we define a resonant filter as $G_r(\omega) = 1$ for $-\omega_0/2 \leq \omega \leq \omega_0/2$ and $G_r(\omega) = 0$ elsewhere. The nonresonant filter is $G_{nr}(\omega) = 1 - G_r(\omega)$. Therefore, the resonant (non-sinusoidal) and nonresonant (sinusoidal) transition probability amplitudes are given by

$$\mathfrak{v}_i(\mathbf{K},t) = \mathrm{FT}^{-1}\left[G_i(\omega)\tilde{\mathfrak{v}}(\mathbf{K},\omega)\right], \tag{3.21}$$

for $i = r, nr$, respectively. Here, FT^{-1} represents the inverse Fourier transform and $\tilde{\mathfrak{v}}$ is the Fourier transform of $\mathfrak{v}$.

For the intraband current we have $n_c = |\mathfrak{v}|^2 = n_c^r + n_c^{nr}$. Therefore, $n_c^i(t) = \int_{\mathrm{BZ}} d^3K\, n_c^i(\mathbf{K},t)$

$(i = r, nr)$,

$$n_c^r(\mathbf{K}, t) = |\mathfrak{v}_r(\mathbf{K}, t)|^2 \tag{3.22}$$

$$n_c^{nr}(\mathbf{K}, t) = |\mathfrak{v}_{nr}(\mathbf{K}, t)|^2 + \left[\mathfrak{v}_{nr}(\mathbf{K}, t)\mathfrak{v}_r^*(\mathbf{K}, t) + \text{c.c.}\right]. \tag{3.23}$$

The various processes contained in the transition probability amplitude $\mathfrak{v}$ are pictured in the schematic in Fig. (3.3). Real (resonant) transitions require energy conservation of the combined system of electron-hole pair and driving laser. It means that for a given number of photons real transitions are the ones that occur at sharp K-values at which bandgap (black line) and the absorbed photon energy are the same (full circles). In other words, a resonant transition occurs when the exponent in $\mathfrak{v}$ becomes zero which is a steady growth of the conduction band probability amplitude. The shaded area is for a finite pulse and explains the choice of G_r above. Note that the population from real transitions remains after the laser pulse. On the other hand, virtual transitions (empty circles) reflect the distortion of the valence band due to the laser. The exponential in $\mathfrak{v}$ is rapidly oscillating and its integral is zero which results in a temporary, oscillating population of conduction band states. The virtual population disappears after the laser pulse. Separating real from virtual absorption channels would not be possible without having the closed-form expression for the transition probability amplitude $\mathfrak{v}$, Eq. (3.20). The above discussion shows why real and virtual channels are difficult to disentangle in intense laser fields. In fact, many channels consisting of photons with varying energies contribute to each real and virtual transition.

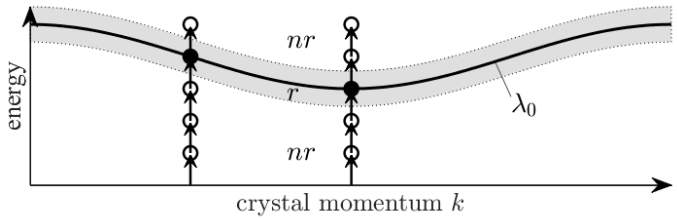

Figure 3.3: Real (resonant) versus virtual (non-resonant) processes in solids for a finite pulse. For a finite pulse a band of photon energies exists which extends the range of allowed resonant channels in the vicinity of the sharp K-values (shaded area) [5]

3.5 Resonant and non-resonant interband and intraband currents

Now, the resonant and non-resonant interband and intraband currents are defined as follows

$$\langle \mathbf{j}^i_{er} \rangle \approx -\frac{d}{dt} \int_{\overline{\mathrm{BZ}}} d^3K \, \mathbf{d}(\mathbf{K}_t) \, \mathfrak{u}_i(\mathbf{K}, t) + \text{c.c.}, \tag{3.24}$$

$$\langle \mathbf{j}^i_{ra} \rangle \approx \int_{\overline{\mathrm{BZ}}} d^3K \mathbf{v}(\mathbf{K}_t) n^i_c(\mathbf{K}, t) \;\; (i = r, nr). \tag{3.25}$$

We separate the resonant and non-resonant parts in semiconductor and dielectric cases.

3.5.1 Semiconductor case

Intraband current is only comparable to interband current until the third harmonic. Therefore, we only split the interband current into the resonant and non-resonant parts. See Fig. (3.4), note that the markers were chosen to reflect the relation between HHG currents. Interband HHG: j_{er}(diamonds) = j^r_{er}(triangle up) + j^{nr}_{er}(triangle down); triangle up and down combine to a diamond, see Fig. (3.2). Looking at Fig (3.4) we see that for N=1,3 the most contribution is coming from the non-resonant parts. For N=5, they are comparable. Note that the first above bandgap harmonic is N=9, and we see that the contribution is coming from the resonant part in agreement with the theory [45, 46, 47, 48, 50] and experiment [36, 38] .

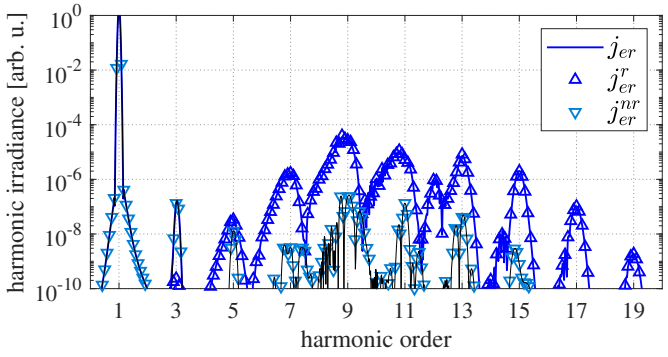

Figure 3.4: Model semiconductor with same parameters as in Fig. 3.2(a); HHG from j_{er} (full blue line), j^r_{er} (blue triangles up), and j^{nr}_{er} (blue triangles down, different shade of blue for visibility; thin black line is a guide to the eye) is compared. Symbols are plotted with lower resolution [5].

3.5.2 Dielectric case

In the dielectric case, if one refers back to the Fig. (3.2b), the intraband current becomes relevant as well as the interband current for higher order harmonics. Therefore, we split the intraband current into resonant and non-resonant parts. In doing so, looking at Eq. (3.25) we see that n_c^i $(i = r, nr)$, the populations, are needed for the calculation. n_c^r (red crosses) and n_c^{nr} (red plus) are plotted in Fig. 3.5(a,b), respectively. The parameters are the same as in Fig. 3.2(b) except for $F_0 = 0.02$ and a shorter pulse duration $\tau = 3T_0$ usually used in high-intensity experiments. As expected, we see a steady growth in the population for the resonant case. The non-resonant population is oscillatory in nature and goes to zero after the laser pulse [5].

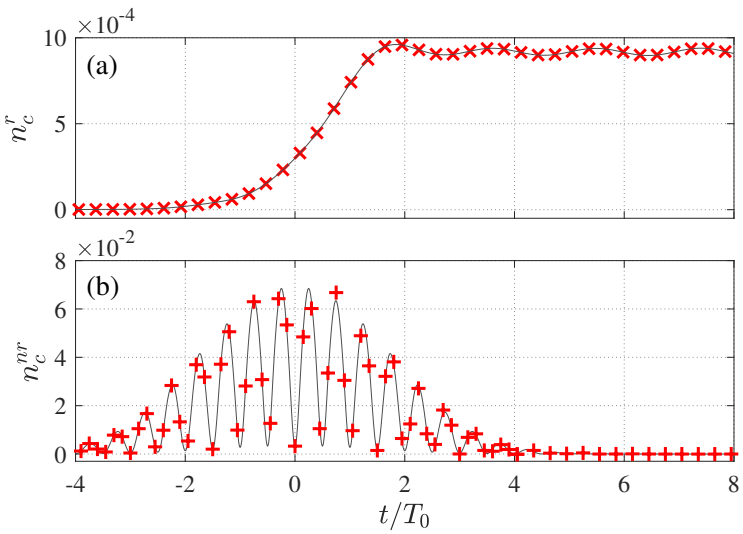

Figure 3.5: (a,b) Conduction band population time evolution for the model dielectric; parameters are the same as in Fig. 3.2(b) except for $\tau_0 = 3T_0$ and $F_0 = 0.02$. (a) n_c^r (Eq. (3.22), red cross); (b) n_c^{nr} (Eq. (3.23), red plus); thin black lines are guides to the eye [5].

As for the calculation of HHG, we plot the harmonic fluence by integrating harmonic signals over the frequency interval $|\omega - N\omega_0| < (\omega_0/2)$. See Fig. (3.6) for $F_0 = 0.005$ (a,b) and for $F_0 = 0.012$ (c,d) the other parameters are the same as in Fig. 3.5. Sub-plots (a,c) and (b,d) show interband and intraband currents, respectively. Note that the first above minimum bandgap is N=7. In the lower field for (a,b) we see that only the interband current is relevant. For higher field, (c,d) the interband resonant is the dominant contribution as expected. We also see the non-resonant intraband becomes comparable to the resonant interband at higher harmonics $N \geq 11$. The most important point is that the resonant

intraband is the weakest of all contributions. This explains why HHG from j^r_{ra} could not be observed in the numerical analysis of the semiconductor Bloch equations [17, 18]. It also shows that virtual transitions are more important in dielectrics due to dynamical Stark shift that increases the effective minimum bandgap and as a result, weakens resonant transitions [30]. The last point is that HHG in dielectrics can be modeled by [17, 19, 23]

$$j^x_{ra} = c|\mathrm{FT}[v(A(t))]|^2, \tag{3.26}$$

c is a constant, and it is in the order of $n_c^2(t \to \infty)$. It is clear that it can be obtained from Eq. (3.25) by assuming that the conduction band population is delta-function like around $K = 0$. It is shown by the green line in Fig. (3.6). The j^r_{ra} and j^x_{ra} overlap in the two cases. The problem here is that the amount is negligible to other contributions. One possibility can be dephasing. Dephasing can happen through two mechanisms, propagation, and microscopic scattering. This was the motivation to add heatbath to the formalism which is the topic of the next chapter.

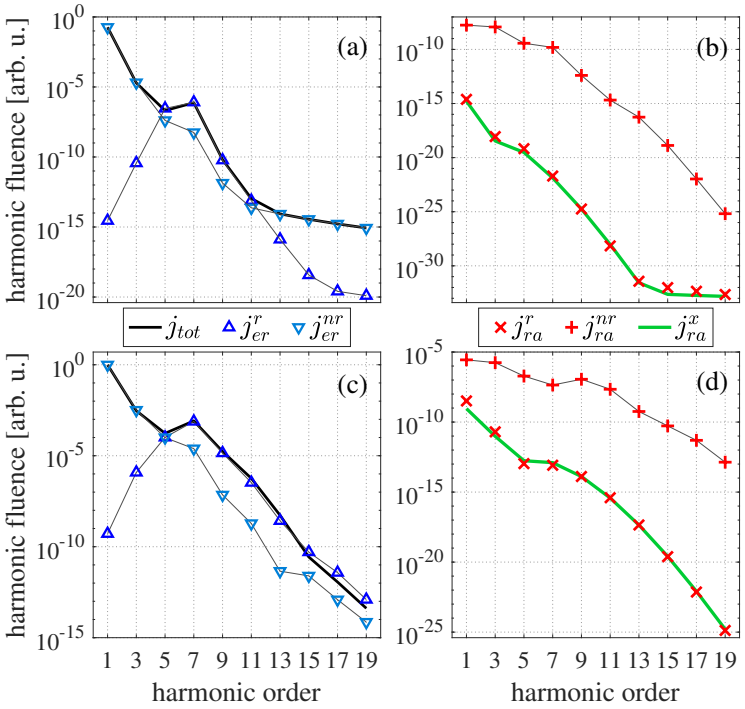

Figure 3.6: same parameters as in Fig. 3.5 except for $F_0 = 0.005$ (a,b) and $F_0 = 0.012$ (c,d). Thin gray lines serve as guide to the eye. (a,c) HHG from interband currents j^r_{er} (blue triangles up), and j^{nr}_{er} (blue triangles down), HHG from total current (black full line). (b,d) HHG from intraband currents j^r_{ra} (red crosses), j^{nr}_{ra} (red pluses), j^x_{ra}, see text (green full lines)[5].

Finally, in terms of physics, this chapter has confirmed the dominance of the interband recollision model in mid-IR semiconductor experiments. In near-IR dielectrics, due to stronger dipole moments and higher damage thresholds, the dynamic Stark shift becomes more pronounced and suppresses optical field ionization. As a result, real and virtual HHG channels can become comparable.

HHG in near-IR driven dielectrics can be explained in terms of simple classical model derived from the intraband current. This is starkly different to the interband recollision mechanism found in mid-IR semiconductors. The physical mechanisms responsible for this difference have remained a mystery to date. Neither numerical ab-initio calculations nor simple models have been able to explain it.

We have identified the resonant intraband current to be the weakest of all contributions in contradiction to experiments. Interband HHG depends on the accumulation of a quantum phase during the laser driven evolution of electron-hole pairs. By contrast, intraband HHG depends only on the band velocity and not on phase terms. As such, one possibility to explain the apparent contradiction between theory and experiment is that dephasing suppresses the other HHG channels and makes intraband HHG dominant. This reveals the first evidence that collisional many-body processes going beyond one-electron-hole and mean-field approaches might be important. The method developed here lays the necessary theoretical foundation to further pursue the above ideas.

Chapter 4

Heat Bath Noise Perturbation in Strong Field Physics

This chapter is based on this publication [66]. It is reprinted with the permission of Reports on Progress in Physics-Copyright by the Journal.

Contribution: I together with Thomas Brabec developed the theory (2021-2022). Lu Wang wrote the paper and generated the figures (2025).

4.1 Strong field physics in open quantum systems

In chapter (3), a closed-form formalism for modeling high harmonic generation in solids was derived; comparing it to experiments identifies the importance of often neglected processes, such as dephasing of the strong field dynamics from coupling to the many-body environment of solids. At the moment there is no good method beyond the relaxation time approximation to deal with noise in strong field processes. Relaxation time approximation leads to unphysical excitation to the excited states [5]. In this chapter, we are going to derive a mathematical formalism for such dephasing processes. We will use the popular spin-boson model. The idea is to develop a generic model that treats the long-wavelength aspects of all noise sources and allows a closed form formulation of the equations. The main advantage is that field and noise are expanded in the same way, meaning that, for example, in the second order perturbation we have all the field and noise terms in there. The only things that are missing are higher orders. For more introductory material please refer to the open quantum systems section in the introduction chapter.

OPEN ACCESS
IOP Publishing

Letters
Reports on Progress in Physics

Rep. Prog. Phys. **88** (2025) 070501 (8pp)
https://doi.org/10.1088/1361-6633/adeebb

Letter

Strong field physics in open quantum systems

Neda Boroumand[1], Adam Thorpe[1], Graeme Bart[1], Andrew M Parks[2], Mohamad Toutounji[3], Giulio Vampa[4], Thomas Brabec[1,*] and Lu Wang (汪璐)[1,*]

[1] Department of Physics, University of Ottawa, Ottawa, Ontario K1N 6N5, Canada
[2] Wyant College of Optical Sciences, University of Arizona, Tucson, AZ, United States of America
[3] College of Science, Department of Chemistry, UAE University, Al-Ain, United Arab Emirates
[4] Joint Attosecond Science Laboratory, National Research Council of Canada and University of Ottawa, 100 Sussex Drive, Ottawa, Ontario K1A 0R6, Canada

E-mail: [redacted]

Received 21 March 2025, revised 29 June 2025
Accepted for publication 11 July 2025
Published 18 July 2025

Corresponding editor: Dr Paul Mabey

Abstract

Dephasing is the loss of phase coherence due to the interaction of an electron with the environment. The most common approach to model dephasing in light–matter interaction is the relaxation time approximation. Surprisingly, its use in intense laser physics results in a pronounced failure, because ionization is highly overestimated. Here, this shortcoming is corrected by developing a strong field model in which the many-body environment is represented by a heat bath. Our model reveals that ionization enhancement and suppression by several orders of magnitude are still possible, however only in more extreme parameter regimes. Our approach allows the integration of many-body physics into intense laser dynamics with minimal computational and mathematical complexity, thus facilitating the identification of novel effects in strong-field physics and attosecond science.

Supplementary material for this article is available online

Keywords: strong field physics, relaxation time approximation, quantum optics, open quantum system

* Authors to whom any correspondence should be addressed.

Rep. Prog. Phys. **88** (2025) 070501 Letters

1. Introduction

Strong laser-matter interaction is commonly modeled as a closed quantum system with a single active electron [1, 2]. While this assumption is well justified for atomic gases, its validity is not so clear for denser materials, such as liquids and solids. A full many-body treatment of the non-perturbative dynamics of all electrons and nuclei is prohibitively difficult. Therefore, it is more practical to model dense materials as a single active electron within an open quantum system, where many-body effects are accounted for by interactions with the environment [3–5]. Due to its simplicity, the environment in intense laser-driven solids is mostly modeled in the relaxation time approximation [6, 7], where the effect of many-body dynamics is replaced by a dephasing time T_2 [8–10]. Here, the relaxation time approximation only refers to the dephasing term T_2, not the energy relaxation time T_1. In particular, the T_2 represents a constant decay of the dynamics of off-diagonal density matrix elements (ρ_{ij}, $i \neq j$) i.e. loss of coherence. Note that dephasing is also commonly referred to by Γ [11]. In our case $\Gamma = 1/T_2$. For dielectrics, the T_2 is typically around a few femtoseconds [6, 12, 13].

However, a simple calculation for an under-resonantly driven two-level system reveals questionable features of the relaxation time approximation in accurately predicting ionization [14]. Following the conventional optical ionization theory, we refer to ionization as the laser-induced excitation of an electron from the valence $|0\rangle$ to the conduction $|1\rangle$ band. In figure 1(a) the ionization dynamics with dephasing described via the relaxation time approximation (yellow $\sim 10^{-1}\%$) and without dephasing (blue $\sim 10^{-8}\%$) are compared. It can be seen that the relaxation time approximation predicts $10^{-1}\%$ ionization under a very moderate electric field strength $E_0 = 5 \times 10^8\,\mathrm{V\,m^{-1}}$.

This is clearly unphysical because laser damage of semiconductors (ZnO, for example) occurs around $5 \times 10^9\,\mathrm{V\,m^{-1}}$. This leads to laser induced free carrier density $\sim 10^{22}\,\mathrm{cm^{-3}}$ [15, 16], equivalent to $\sim 5\%$ ionization based on the atomic density $\sim 2 \times 10^{23}\,\mathrm{cm^{-3}}$ [17]. For weak electric field $5 \times 10^8\,\mathrm{V\,m^{-1}}$, the expected free carrier density is $\sim 10^{16}\,\mathrm{cm^{-3}}$ corresponding to ionization $\sim 10^{-6}\%$ [18]. By comparing $\sim 10^{-6}\%$ to the yellow curve in figure 1(a) ($\sim 10^{-1}\%$), we can see that the relaxation time approximation overestimates the ionization by five orders of magnitude.

Many attempts have been made to mitigate the overestimation of ionization [12, 13, 19–21]. However, the underlying issue is still not resolved. Dephasing typically refers to the loss of coherence between two energy levels and is generally considered separate from excitation or transition processes. However, our results indicate that when the phase relationship between the laser field and the two-level system is disrupted, virtually excited electrons are prevented from returning to the ground state. This leads to a real transition i.e. a change in population distribution in the two-level system after the laser pulse is gone. We refer to the resulting ionization enhancement as *dephasing ionization*. The apparent shortcomings of the relaxation time approximation leave a gap between more complex and computationally demanding many-body approaches and oversimplified dephasing models commonly used in intense light–matter interaction.

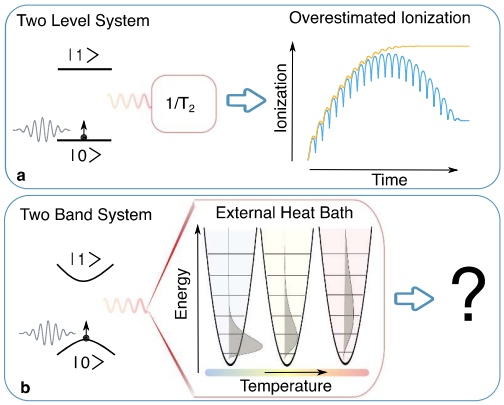

Figure 1. Illustration of under-resonantly driven, open two-level/band systems. Panel (a) presents the two-level system (band gap $E_g = 3.51$ eV) described by the relaxation time approximation. On the right-hand side, ionization with ($T_2 = 6$ fs, yellow curve) and without dephasing ($T_2 = \infty$, blue curve) is compared. A moderate electric field strength $E_0 = 5 \times 10^8\,\mathrm{V\,m^{-1}}$ with photon energy ~ 0.39 eV ($\lambda_0 = 3.2\,\mu$m) is chosen (see supplement figure S5 for details). Panel (b) shows the two-band system coupled to a heat bath described via the spin-boson model. The heat bath is modeled using boson harmonic oscillator modes. As the temperature rises, boson modes with higher energies are engaged (gray curves).

Furthermore, ionization is the first step in all strong field processes, such as material machining [22–24], petahertz electronics [25, 26], electron acceleration from nano emitters [27], and high-harmonic generations [2, 28]. Due to the importance of ionization, a deeper understanding of dephasing ionization is essential.

As such, a more sophisticated model is needed that ideally maintains most of the simplicity and wide applicability of the relaxation time approximation. We borrow inspiration from the field of open quantum systems and adopt one of its key achievements, the spin-boson model, which typically serves as a minimal model to describe the quantum dynamics of an electron under the influence of the environment [29–31]. Here, the spin-boson model is integrated into the semiconductor Bloch equations governing intense laser solid-state physics. The electron dynamics is represented by a single electron–hole, two-band model which is linearly coupled to its environment via bosonic harmonic oscillator modes, see figure 1(b). The so-called strong field spin-boson (SFSB) model allows for a closed-form solution of the electron dynamics in an environment and in the presence of an intense laser. We refer to the environment as a heat bath in the rest of the paper.

The SFSB model fixes the pathological ionization behavior displayed by the relaxation time approximation. Nevertheless, numerical analysis of the SFSB equation reveals that ionization enhancement of up to a few orders

Rep. Prog. Phys. **88** (2025) 070501 Letters

of magnitude is still possible, but only at high temperatures. Interestingly, in the opposite low-temperature limit the heat bath can suppress ionization by up to a few orders of magnitude, which we term as *dephasing suppressed ionization*. This occurs when the electron and heat bath interact strongly.

The SFSB model provides a distinctive approach to uncovering the physics of complex many-body systems with minimal computational and mathematical complexity. The predictive power of the SFSB approach can be progressively refined through either more detailed models or by fine-tuning the heat bath response through comparison with experiments. We anticipate that the SFSB framework will facilitate the discovery of new phenomena in strong-field physics and attosecond science.

2. Theory

Our analysis starts with a single electron two-band system coupled to a bosonic heat bath via a linear interaction term, [32, 33]

$$H = -\frac{1}{2}\mathcal{E}\left(\boldsymbol{K}_t,t\right)\sigma_z + \frac{1}{2}\hbar\Omega\left(\boldsymbol{K}_t,t\right)\sigma_x + \sum_q \hbar\omega_q b_q^\dagger b_q + \sigma_z\sum_q g_q\left(b_q + b_q^\dagger\right). \tag{1}$$

Here, $\mathbf{E}(t)$ is the laser electric field, the vector potential is defined by $-\partial_t\mathbf{A} = \mathbf{E}$, and $\boldsymbol{K}_t = \boldsymbol{K} + e\boldsymbol{A}(t)/\hbar$. The canonical momentum $\boldsymbol{K}$ belongs to the shifted Brillouin zone $\overline{\mathrm{BZ}}$. Further, $\Omega(\boldsymbol{K}_t,t) = (2e/\hbar)\mathbf{d}(\boldsymbol{K}_t,t)\mathbf{E}(t)$ is a generalized Rabi frequency, $e>0$ is the elementary charge and $\hbar$ is the reduced Planck constant; $\mathbf{d}(\boldsymbol{K}_t,t)$ and $\mathcal{E}(\boldsymbol{K}_t,t)$ represent transition dipole and bandgap between conduction $|1\rangle$ and valence $|0\rangle$ band, respectively. The time dependence of these quantities arises from the moving momentum frame. The Pauli matrices are denoted by σ_j $(j = x,y,z)$. Finally, ω_q, $\hat{b}_q^\dagger$, $\hat{b}_q$, and g_q are the harmonic oscillator frequency, creation, and annihilation operators, and the coupling coefficient of a mode with momentum $\mathbf{q}$, respectively. In particular, the work [34] suggests that the coupling strength g_q is proportional probability distributions of the bosonic environment of mode q. This coupling term proportional to g_q in equation (1) is a generic form and is valid for strong field interactions of electron-plasmon [35], electron-phonon [36], and electron-exciton. Besides, g_q can be directly calculated via the ab-initio method, which corresponds to the scattering matrix element between the initial and the final state [34–36]. Here we refer to the interactions between the electron (in the two-band system) and the exciton or plasma as collective electron interactions.

The coupling term between the heat bath and the two-band system appears exclusively in the diagonal terms of the Hamiltonian. Thus, it accounts only for dephasing, and not directly for heat-bath driven transitions between bands, i.e the off-diagonal terms. Nevertheless, due to the coupling of laser and heat bath driven dynamics [6, 37], dephasing does influence the overall ionization. In the high-temperature limit, multi-boson transitions between valence and conduction band could become relevant but are ignored here.

The Hamiltonian shown in equation (1) can be further simplified. First, we perform a polaron transformation that diagonalizes the laser-free Hamiltonian [38]. This is followed by a change to the interaction picture, which results in

$$H_I = -\frac{\mathcal{E}\left(\boldsymbol{K}_t,t\right)}{2}\sigma_z + \frac{1}{2}\hbar\Omega\left(\boldsymbol{K}_t,t\right)\left(\sigma_+ D^{\dagger^2} + \sigma_- D^2\right). \tag{2}$$

For a detailed derivation, see supplementary material, section I. Here, $\sigma_+ = (\sigma_x + i\sigma_y)/2$ and $\sigma_- = (\sigma_x - i\sigma_y)/2$. The interactions with laser and heat bath are now described by a single term, with the shift operator defined as $D(t) = \exp\left\{-\sum_q g_q\left[b_q^\dagger(t) - b_q(t)\right]/(h\omega_q)\right\}$.

The evolution of the density matrix is determined by the integration of the Liouville–Von Neumann equation with the Hamiltonian shown in equation (2). Initially, the valence band is fully occupied, the conduction band is empty, and the heat bath is in thermal equilibrium. A closed-form solution is obtained by using a Dyson expansion up to the second order. As we are only interested in the two-band system dynamics, the heat bath degrees of freedom are traced out (see supplementary material sections II and III for details) [9, 32, 33, 39–46]. We found that the dominant contribution to ionization is contained in the second order expansion term [44] from which the conduction band population follows as

$$n_c\left(\boldsymbol{K},t\right) = \frac{1}{2}\mathrm{Re}\left\{\int_{-\infty}^{t}\int_{-\infty}^{t_1}\Omega^*\left(\boldsymbol{K}_{t_1},t_1\right)\Omega\left(\boldsymbol{K}_{t_2},t_2\right) \times \exp\left[iS(t_1,t_2) + C(t_1-t_2)\right]dt_1dt_2\right\}, \tag{3}$$

$$n_c(t) = \int_{\overline{\mathrm{BZ}}} n_c\left(\boldsymbol{K},t\right)d\boldsymbol{K}, \tag{4}$$

where the action $S(t_1,t_2) = \int_{t_2}^{t_1} d\tau\,\mathcal{E}_s(\boldsymbol{K}_\tau,\tau)/\hbar$, and $\mathcal{E}_s(\boldsymbol{K}_\tau,\tau) = \sqrt{\mathcal{E}(\boldsymbol{K}_\tau,\tau)^2 + |\hbar\Omega(\boldsymbol{K}_\tau,\tau)|^2}$ is the bandgap shifted by the dynamic Stark effect [44, 47, 48]. As equation (3) suggests, all the environment (heat bath) influences are exclusively included by the correlation function $C(t_1-t_2)$. Typically, the correlation function indicates that the future evolution of the system depends not only on its instantaneous state but also on its past history [4, 49]. Specifically, the correlation function is defined as:

$$C(t_1-t_2) \approx \int_{-\infty}^{\infty} J(\omega)\left\{i\sin\left[\omega\left(t_1-t_2\right)\right] - \left\{1-\cos\left[\omega\left(t_1-t_2\right)\right]\right\}\coth\left(\frac{\hbar\omega}{2k_BT}\right)\right\}d\omega, \tag{5}$$

where k_B is the Boltzmann constant. The temperature T dependence in equation (5) is contained only in the coth term. The g_q coefficient in equations (1) and (2) are replaced by a spectral density $J(\omega)$ through a transition from discrete to continuous modes. The spectral density depends on two parameters: coupling strength j_o, and cutoff frequency ω_c. There exists a wealth of different models for the spectral density $J(\omega)$, such as the Debye [43], Ohmic [9], Under-Damped

Rep. Prog. Phys. **88** (2025) 070501 Letters

Brownian [33, 45], Gaussian [46], and Shifted-Gaussian models, the definition of which can be found in the supplementary material, section IV.

The relaxation time approximation is recovered for the Debye bath in the high T-limit, $C(t_1 - t_2) \to -(t_1 - t_2)/T_2$ with $T_2 = \hbar/(2\pi k_B T j_o)$, as outlined in the supplementary material, section IV.A. By contrast, the high T-limits of the other heat bath models do not exhibit a linear time dependence in the exponent.

In the context of strong laser solid material interaction, the temperature T refers to the local electron or ion temperature. Our approach presents an approximation, as the system, its dependence on laser pulse duration, is not always in thermal equilibrium. This process is typically analyzed via the well-established two-temperature model [50–52], where the laser first heats the electrons, and the absorbed energy of the electrons is subsequently transferred to the lattice, increasing its temperature. Material damage or melting is typically determined by the lattice temperature. For dielectrics, damage occurs around a few thousand K, even though the electron temperature can be much higher, reaching up to 10^5 K [50–52]. While our approach can be extended to describe non-equilibrium heat baths, this would go beyond the limit of an initial investigation.

The cutoff frequency ω_c falls within the terahertz to the far-infrared range for phonons, and spans the far-infrared to the mid-infrared range for collective electronic excitations, such as excitons and plasmons. The coupling strength j_o is a dimensionless parameter ranging from 10^{-3} to multiples of unity [32, 33, 53–56]. For phonons, $j_o < 1$ in III–V semiconductors, whereas $j_o > 1$ in more polar II–VI compounds [3]. Strong electron-phonon coupling $j_o > 1$ typically occurs in very polar materials [55, 57] such as bi-layer graphene [58], single-layer InSe [59] and superconductors [60, 61]. For collective electronic excitations, the coupling strength depends on the electron density [35]. For electron densities above 10^{20} cm^{-3} and for $\hbar\omega_c \sim 1$ eV the plasmon coupling strength can become comparable to and even exceed the phonon coupling strength.

3. Results

We have selected zinc oxide (ZnO), a representative and widely studied semiconductor. The crystal momentum $\boldsymbol{k}$ dependence in the entire 3D Brillouin zone is considered for the two-band system. Material parameters are derived from *ab initio* calculations [62–64] (see supplementary material section V, table I). We find that both 3D and 1D calculations along the Γ-M direction yield similar results in terms of relative heat bath-induced ionization changes, both quantitatively and qualitatively (see supplementary material figure S4). Therefore, for computational efficiency, we focus on the 1D Brillouin zone along the Γ-M direction throughout the following calculations.

A driving laser with the center wavelength $\lambda_0 = 3.2\,\mu$m is selected. The center frequency is defined as $\omega_0 = 2\pi c/\lambda_0 \approx 2\pi \times 10^{14}$ Hz ($\hbar\omega_0 \sim 0.39$ eV) with c the vacuum light velocity. The energy of the laser photons is much lower than the resonance energy of ZnO (with a band gap of $\mathcal{E}_g = 3.51$ eV), meaning that at least 9 photons are required to excite an electron from the valence band to the conduction band. We choose a linearly polarized electric field defined as $\mathbf{E} = E_x = E_0 \exp\left(-t^2/\tau^2\right)\cos(\omega_0 t)$, where $\tau = 20$ fs. The electric field strength $E_0 = 1.5 \times 10^9\,\mathrm{V\,m^{-1}}$ is well below the single pulse damage threshold of ZnO [65]. These parameter values are used throughout the paper unless otherwise stated.

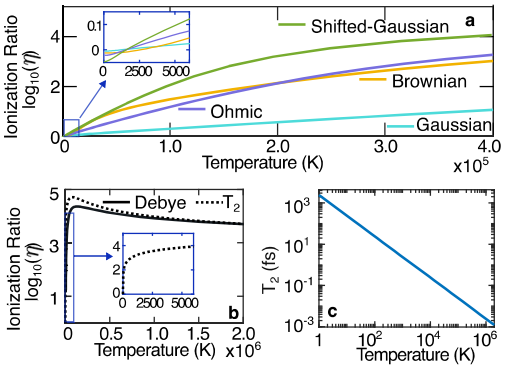

Figure 2. Panel (a) presents the ionization ratio versus temperature T for various heat baths. Panel (b) shows the ionization ratio for the Debye heat bath and relaxation time approximation versus T. The insets in (a) and (b) show details in the low T regime. The relaxation time $T_2 = \hbar/(2\pi k_B T j_o)$ obtained from the Debye spectral density, is plotted in (c) as a function of T. The heat bath parameters are $\omega_c = 0.1\omega_0$, $j_o = 0.1$.

The change of ionization due to the heat bath is characterized by calculating the ionization ratio with and without the heat bath,

$$\eta = \left.\frac{n_c\left(j_o \neq 0\right)}{n_c\left(j_o = 0\right)}\right|_{t=\infty}, \tag{6}$$

where $n_c(t)$ is defined in equation (4).

In figure 2(a), the ionization ratio $\log_{10}(\eta)$ is plotted versus T for Ohmic, Under-Damped Brownian, Gaussian, and Shift-Gaussian spectral densities, all of which follow a similar trend and yield comparable results. Thus, without loss of generality, we have chosen the Ohmic spectral density throughout the entire numerical analysis. The ionization ratio is plotted in $\log_{10}$ scale, where the positive (negative) numbers of $\log_{10}(\eta)$ correspond to the order of magnitude of enhancement (suppression) of ionization. Figure 2(b) shows that the Debye spectral density converges to the relaxation time approximation at very high temperatures. The temperature dependence of T_2, obtained from the Debye spectral density in the high T limit above, is presented in figure 2(c). Both Debye and relaxation time approximation show an unrealistic rise of η at low T and therefore do not represent realistic heat bath models. This is to be expected, due to the unphysically long high-frequency tail of the Debye spectral density [57, 66]. Finally, by comparing the zoomed-in sections of figures 2(a) and (b), one can see that the relaxation time approximation substantially overestimates

Rep. Prog. Phys. **88** (2025) 070501 Letters

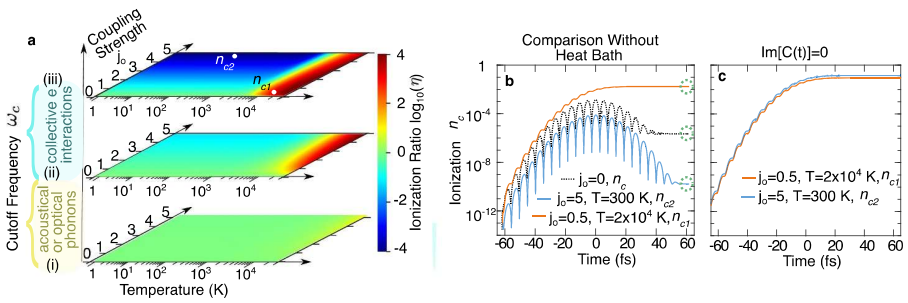

Figure 3. Panel (a) shows ionization ratio $\log_{10}(\eta)$ as a function of local temperature $T \in [1, 3\times10^4]$ K and coupling coefficient $j_o \in [0, 5]$. The three panels represent different cutoff frequencies, (i) $\omega_c = 0.01\omega_0$, (ii) $\omega_c = 0.1\omega_0$ and (iii) $\omega_c = 2.1\omega_0$. (b) Ionization versus time for two data points n_{c1} and n_{c2} in panel (iii) of (a); the black dotted curve shows ionization in the absence of a heat bath. The three data points marked by circles at the end of the time coordinate are related to discussions in figure 4. (c) same as plots for n_{c1} and n_{c2} in (b) only with setting the imaginary part of the heat bath response $C(t)$ (defined in equation (5)) to zero.

ionization at low temperatures, while all the other heat baths in figure 2(a) show negligible changes in ionization, as detected by experiments.

In figure 3(a), the ionization ratio $\log_{10}(\eta)$ is scanned over a wide range of T and j_o. Although electrons are fermions, their collective excitations can, to a good approximation, be treated as bosons [33, 35, 57]. As such, they can be directly modeled via the spin-boson Hamiltonian shown in equation (1). These different quasi-particle excitations are mainly distinguished by the choice of the cutoff frequencies ω_c. As a result, in figure 3(a) we chose three representative values of cutoff frequencies: (i) $\omega_c = 0.01\omega_0$ represents optical and acoustic phonons which lie in the terahertz range (ii) $\omega_c = 0.1\omega_0$ represents collective electron excitations, and (iii) $\omega_c = 2.1\omega_0$ represents the plasma frequencies that extend into the UV range. From panel (i), we infer that phonon effects on ionization are minimal, except under extreme conditions such as high-temperature laser machining. In contrast, panel (iii) indicates that environmental influences on ionization become more significant at large cutoff frequencies, even with moderate coupling strength. Additionally, ionization enhancement occurs only at the high temperature limit, whereas ionization suppression is observed exclusively at the low temperature limit. These two limits are represented by data points n_{c1}, n_{c2} in panel (iii), for which, the temporal evolution of ionization is plotted in figure 3(b). The black dotted curve represents ionization in the absence of a heat bath $n_c(j_o = 0)$. While all T and ω_c ranges can be realized in intense laser-driven ZnO, the shown j_o-dependence is not ZnO specific. We explore the typical range of j_o defined above.

The increase and decrease of ionization can be explained by the real and imaginary parts of the correlation function $C(t)$. With a given ω_c, at extremely high temperatures, the correlation function approaches a delta function (instantaneous) in time, leading to the Markovian limit [67]. In this limit, the real part of the correlation function dominates, and one may neglect the imaginary contribution. This is why the relaxation time approximation using T_2 as a purely real number remains

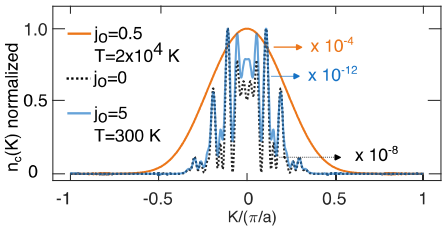

Figure 4. Ionization as a function of crystal momentum K. The ionization $n_c = \sum_i n_c(K_i)$ corresponds to the three data points marked by circles in figure 3(b).

a valid approximation at high temperatures. On the other hand, at low temperatures, the correlation function is non-Markovian with a wider distribution in time. In this case, the phase of the correlation function acts as a dynamic addition to the bandgap, increasing the original material bandgap, and thereby resulting in dephasing suppressed ionization. The importance of the heat bath phase becomes clear from a comparison of figures 3(b) and (c). In figure 3(c) the imaginary part of the $C(t)$ is set to zero, as a result of which ionization at $T = 300$ K changes from suppression into enhancement.

A possible experimental measurement of the n_c shown in figure 3 can be achieved via the angle-resolved photoemission spectroscopy (ARPES). Since ARPES typically presents the electron density as a function of the crystal momentum K, here in figure 4 we show n_c as a function of K after the driving field is gone. The curves are plotted using 800 evenly spaced mesh points. The ionization $n_c = \sum_i n_c(K_i)$ corresponds to three data points indicated by circles in figure 3(b). From figure 4, one can see that the dephasing ionization has a distinctive signature, markedly different from the optical ionization in the absence of an environment. On the other hand, dephasing suppressed ionization

Rep. Prog. Phys. **88** (2025) 070501 Letters

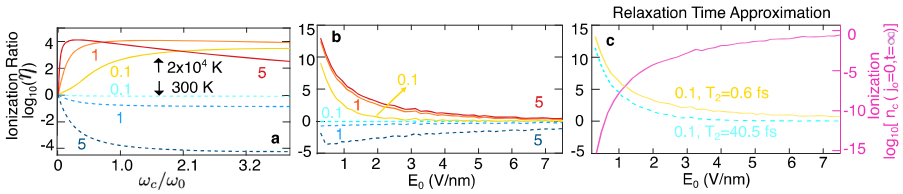

Figure 5. Ionization ratio as a function of cutoff frequency ω_c (panel (a)) and of peak electric field strength E_0 (panels (b) and (c)) are presented. We have chosen different values of $j_o \in \{0.1, 1, 5\}$ denoted by different colors beside each curve. The cold-colored dashed curves are for $T = 300$ K; warm-colored full curves refer to $T = 2 \times 10^4$ K. In (a), the ionization without the heat bath is $n_c(j_o = 0, t = \infty) = 2 \times 10^{-6}$. Panels (b) and (c) are calculated by $\omega_c = 0.4\omega_0$. The relaxation time used in panel (c) is calculated by $T_2 = \hbar/2\pi\, k_B j_o T$. The pink curve plotted on the right y axis shows the ionization $n_c(j_o = 0, t = \infty)$ in the absence of the heat bath.

behaves similarly to ionization without environmental influence.

This opens up the possibility of diagnostic measurements. For example, in a potential future experiment, the target material (ZnO) can be put in a cavity to modify the coupling to the environment. On the other hand, the ARPES results combined with our model can be used to retrieve the coupling coefficient j_o to the environment, which is otherwise nearly impossible to measure.

To further explore the parameter dependence, ionization ratios are plotted as functions of the cutoff frequency ω_c in figure 5(a) and as functions of the peak electric field strength E_0 in figures 5(b) and (c). Figure 5(c) presents the results calculated by relaxation time approximation. Two temperatures are considered: 300 K, shown by dashed curves in cool colors, and 2×10^4 K, shown by solid curves in warm colors. Each curve is color-coded according to the coupling strength j_o, with the corresponding j_o values labeled in matching colors.

Figure 5(a) confirms that dephasing ionization only occurs at high temperatures, while dephasing suppression ionization happens exclusively at low temperatures. Figure 5(b) indicates that the heat bath only plays a role at moderate electric field strengths. This can be explained by the multi-photon and tunneling ionization channels. When the electric field is strong, the Keldysh parameter $\gamma = \omega_0 \sqrt{m^* \mathcal{E}_g}/(eE_0)$ becomes smaller than 1, where m^* is the effective mass and $\mathcal{E}_g$ is the band gap energy, suggesting the tunneling effects dominate. With our choice of parameters, $\gamma = 1$ corresponds to $E_0 \approx 1.2$ V nm^{-1}. Since tunneling ($\gamma < 1$) occurs much more rapidly than multiphoton absorption [68, 69], the heat bath cannot follow the ionization process and thus has negligible influence at large E_0. In addition, while optical field ionization scales exponentially with E_0, dephasing ionization scales proportional to the laser intensity [14]. As a result, the relative importance of dephasing ionization drops for increasing laser fields. The multi-photon ionization ($\gamma > 1$) develops over an optical cycle and thus is more sensitive to the non-Markovian heat bath, making it more sensitive to heat bath influences.

In order to relate the relative ionization changes to absolute values, ionization in the absence of the heat bath $n_c(j_o = 0, t = \infty)$, is shown as a function of E_0 in figure 5(c). At the highest field strength, ionization is approaching saturation. Moreover, the ionization ratio calculated via the relaxation time approximation is also presented. Comparing figures 5(b) and (c), one can see that the relaxation time approximation predicts orders of magnitude higher ionization compared to that predicted by our model.

4. Discussion

So far, we have seen that the environment can modify ionization by orders of magnitude in the extreme limits of high T or strong coupling j_o. The environment in intense laser-solid interaction is difficult to control. There are various ways in which the environment can be engineered for more controlled experiments on dephasing and dephasing suppressed ionization.

First, light modes in high-quality micro and nano-cavities can be controlled to vary from sub-poissonian, super-poissonian, poissonian, and squeezed vacuum to thermal distributions; from weak to strong coupling with electrons [70, 71]. As such, they can serve as an artificial, strongly coupled environment in which the modification of strong field processes by ionization can be investigated.

Second, collective electron oscillations can be created in tailor-made experiments. The conduction band can be populated by doping semiconductors, or with a pump pulse in a pump-probe experiment. Ionization changes are probed with a second pulse or with transient absorption spectroscopy. As some of the effects observed here depend on strong coupling with the environment, control of the coupling strength is important. Coupling strength increases when going from bulk to 2D and 3D nano-scale materials, such as in nano-resonators and -cavities [72, 73].

Besides, in contrast to a simple two-level system, our two-band model incorporates electron momentum across the entire Brillouin zone. The theoretical framework we develop is general and can be extended to systems with any number of energy bands. To move beyond the basic two-band spin-boson model and address multi-band systems, one can refer to studies [74–76].

The possibility of engineering ionization has potential practical impacts. First, dephasing ionization increases ionization

Rep. Prog. Phys. **88** (2025) 070501 Letters

and thus, allows material micro-machining and -modification at lower laser intensities. This could be instrumental in generating highly charged ion states in high-density plasmas with lower pump pulse energy, contributing to the improvement of table-top x-ray sources. Second, the transition between perturbative nonlinear optics and strong field physics is marked by the onset of ionization. Dephasing suppressed ionization shifts this onset and permits probing dynamics in materials under excitation conditions previously unattainable.

5. Conclusion

The relaxation time approximation is frequently used in intense laser field physics to account for the many-body coupling between a single electron and its environment, which consists of lattice, impurities, and remaining electrons. This work aimed to understand the failure of the relaxation time approximation and to correctly describe ionization in an open quantum system. Ionization in the presence of the relaxation time approximation is enhanced by orders of magnitude over a wide range of parameters, which is termed dephasing ionization.

To decide whether dephasing ionization holds physical significance or is simply a failure of the relaxation time approximation, we have developed a more comprehensive model that captures more physics and still retains much of the simplicity of the relaxation time approximation.

Our results confirmed that ionization enhancement through dephasing ionization still persists, but only in fairly extreme parameter ranges. Very little enhancement is found for acoustical phonon frequencies. For optical phonons and collective electronic excitations dephasing ionization becomes dominant in the limit of high temperatures. Our analysis has also revealed the possibility that a heat bath can suppress ionization by orders of magnitude, which we have named dephasing-suppressed ionization.

We presented a novel framework here to model intense laser many-body processes in a low-cost, semi-phenomenological way. Future research will entail finding realistic environment descriptions beyond the heat bath. Though the SFSB presents a good approximation to a large class of collective excitations of electrons and lattice, it does not account for electron-electron scattering which requires an extended approach with a fermionic heat bath [77]. In particular, the scattering can be included via the Keldysh formalism [78]. Besides, time-dependent heat bath parameters, such as material temperature, are another aspect to be included during intense laser interactions. As such, the ionization dynamics investigated here present only approximate snapshots. For a full treatment of laser material interaction, a dynamically evolving heat bath will have to be considered.

Data availability statement

The data that support the findings of this study are available upon reasonable request from the authors. [redacted]

Acknowledgments

T B thanks NSERC for the support. L W thanks Fluffy B for being the motivation to complete this project.

References

[1] Krausz F and Ivanov M 2009 *Rev. Mod. Phys.* **81** 163–234
[2] Goulielmakis E and Brabec T 2022 *Nat. Photon.* **16** 411–21
[3] Haug H and Koch S W 2009 *Quantum Theory of the Optical and Electronic Properties of Semiconductors* (World Scientific)
[4] May V and Kühn O 2023 *Charge and Energy Transfer Dynamics in Molecular Systems* (Wiley)
[5] Jing J, Yu T, Lam C H, You J and Wu L A 2018 *Phys. Rev. A* **97** 012104
[6] Vampa G, McDonald C, Orlando G, Klug D, Corkum P and Brabec T 2014 *Phys. Rev. Lett.* **113** 073901
[7] Du T Y and Ma C 2022 *Phys. Rev. A* **105** 053125
[8] Witzel W M, Carroll M S, Morello A, Cywiński Ł and Das Sarma S 2010 *Phys. Rev. Lett.* **105** 187602
[9] Paz J P, Habib S and Zurek W H 1993 *Phys. Rev. D* **47** 488
[10] Yu T and Eberly J 2003 *Phys. Rev. B* **68** 165322
[11] Ladd T, Maryenko D, Yamamoto Y, Abe E and Itoh K 2005 *Phys. Rev. B* **71** 014401
[12] Kruchinin S Y 2019 *Phys. Rev. A* **100** 043839
[13] Brown G G, Jiménez-Galán A, Silva R E and Ivanov M 2024 *Phys. Rev. Res.* **6** 043005
[14] McDonald C, Taher A B and Brabec T 2017 *J. Opt.* **19** 114005
[15] Nakayama T 1983 *Surf. Sci.* **133** 101–13
[16] Stuart B C, Feit M D, Herman S, Rubenchik A, Shore B and Perry M 1996 *Phys. Rev. B* **53** 1749
[17] Özgür U, Alivov Y I, Liu C, Teke A, Reshchikov M A, Doğan S, Avrutin V, Cho S J and Morkoç H 2005 *J. Appl. Phys.* **98** 041301
[18] Hanif M, Salik M and Baig M 2013 *Plasma Chem. Plasma Process.* **33** 1167–78
[19] Cai X 2020 *Sci. Rep.* **10** 88
[20] Kilen I, Kolesik M, Hader J, Moloney J V, Huttner U, Hagen M K and Koch S W 2020 *Phys. Rev. Lett.* **125** 083901
[21] Brown G G, Jiménez-Galán A, Silva R E and Ivanov M 2024 *J. Opt. Soc. Am. B* **41** B40–B46
[22] Gattass R R and Mazur E 2008 *Nat. Photon.* **2** 219–25
[23] Yanik M F, Cinar H, Cinar H N, Chisholm A D, Jin Y and Ben-Yakar A 2004 *Nature* **432** 822–822
[24] Farsari M and Chichkov B N 2009 *Nat. Photon.* **3** 450–2
[25] Schiffrin A *et al* 2013 *Nature* **493** 70–74
[26] Boolakee T, Heide C, Garzón-Ramírez A, Weber H B, Franco I and Hommelhoff P 2022 *Nature* **605** 251–5
[27] Chlouba T, Shiloh R, Kraus S, Brückner L, Litzel J and Hommelhoff P 2023 *Nature* **622** 476–80
[28] Korolev V *et al* 2024 arXiv:2401.12929
[29] Segal D and Nitzan A 2005 *Phys. Rev. Lett.* **94** 034301
[30] Leggett A J, Chakravarty S, Dorsey A T, Fisher M P, Garg A and Zwerger W 1987 *Rev. Mod. Phys.* **59** 1
[31] Thorwart M, Paladino E and Grifoni M 2004 *Chem. Phys.* **296** 333–44
[32] Lee C K, Moix J and Cao J 2012 *J. Chem. Phys.* **136** 204120
[33] Lambert N, Ahmed S, Cirio M and Nori F 2019 *Nat. Commun.* **10** 3721
[34] Liu Z D, Lyyra H, Sun Y N, Liu B H, Li C F, Guo G C, Maniscalco S and Piilo J 2018 *Nat. Commun.* **9** 3453
[35] Caruso F and Giustino F 2016 *Phys. Rev. B* **94** 115208

[36] Li Z, Antonius G, Wu M, Da Jornada F H and Louie S G 2019 *Phys. Rev. Lett.* **122** 186402
[37] Wang L, Ciappina M F, Brabec T and Liu X 2024 *Phys. Rev. Lett.* **133** 113804
[38] Mahan G D 2013 *Many-Particle Physics* (Springer)
[39] Würger A 1998 *Phys. Rev. B* **57** 347
[40] Nicolin L and Segal D 2011 *J. Chem. Phys.* **135** 164106
[41] Morreau A and Muljarov E 2019 *Phys. Rev. B* **100** 115309
[42] Bundgaard-Nielsen M, Mørk J and Denning E V 2021 *Phys. Rev. B* **103** 235309
[43] Liu H, Zhu L, Bai S and Shi Q 2014 *J. Chem. Phys.* **140** 134106
[44] Thorpe A, Boroumand N, Parks A, Goulielmakis E and Brabec T 2023 *Phys. Rev. B* **107** 075135
[45] Meier C and Tannor D J 1999 *J. Chem. Phys.* **111** 3365–76
[46] Rouse D M, Gauger E M and Lovett B W 2022 *Phys. Rev. B* **105** 014302
[47] Tóth A, Borbély S, Zhou Y and Csehi A 2023 *Phys. Rev. A* **107** 053101
[48] Sussman B J 2011 *Am. J. Phys.* **79** 477–84
[49] Manzano D 2020 *AIP Adv.* **10** 025106
[50] Chen J, Tzou D and Beraun J 2006 *Int. J. Heat Mass Transfer* **49** 307–16
[51] Mozafarifard M, Liao Y, Nian Q and Wang Y 2023 *Int. J. Heat Mass Transfer* **202** 123759
[52] Carpene E 2006 *Phys. Rev. B* **74** 024301
[53] Yamamoto T, Tokura Y and Kato T 2022 *Phys. Rev. B* **106** 205419
[54] Anto-Sztrikacs N and Segal D 2021 *New J. Phys.* **23** 063036
[55] Franchini C, Reticcioli M, Setvin M and Diebold U 2021 *Nat. Rev. Mater.* **6** 560–86
[56] Magazzù L, Forn-Díaz P, Belyansky R, Orgiazzi J L, Yurtalan M, Otto M R, Lupascu A, Wilson C and Grifoni M 2018 *Nat. Commun.* **9** 1403
[57] Devreese J T and Alexandrov A S 2009 *Rep. Prog. Phys.* **72** 066501
[58] Chen C *et al* 2024 *Nature* **636** 342–7
[59] Lugovskoi A, Katsnelson M and Rudenko A 2019 *Phys. Rev. Lett.* **123** 176401
[60] Wu Y, Yu X, Hasaien J, Hong F, Shan P, Tian Z, Zhai Y, Hu J, Cheng J and Zhao J 2024 *Nat. Commun.* **15** 9683
[61] Errea I *et al* 2020 *Nature* **578** 66–69
[62] Goano M, Bertazzi F, Penna M and Bellotti E 2007 *J. Appl. Phys.* **102** 083709
[63] Vampa G, McDonald C, Orlando G, Corkum P and Brabec T 2015 *Phys. Rev. B* **91** 064302
[64] Vampa G, Hammond T, Thiré N, Schmidt B, Légaré F, McDonald C, Brabec T, Klug D and Corkum P 2015 *Phys. Rev. Lett.* **115** 193603
[65] Dufft D, Rosenfeld A, Das S, Grunwald R and Bonse J 2009 *J. Appl. Phys.* **105** 034908
[66] Mishchenko A, Prokof'Ev N, Sakamoto A and Svistunov B 2000 *Phys. Rev. B* **62** 6317
[67] Hofer P P, Perarnau-Llobet M, Miranda L D M, Haack G, Silva R, Brask J B and Brunner N 2017 *New J. Phys.* **19** 123037
[68] Landsman A S, Weger M, Maurer J, Boge R, Ludwig A, Heuser S, Cirelli C, Gallmann L and Keller U 2014 *Optica* **1** 343–9
[69] Klaiber M, Hatsagortsyan K Z and Keitel C H 2015 *Phys. Rev. Lett.* **114** 083001
[70] Wei Y, Liao Z and Wang X H 2024 *Phys. Lett. A* **526** 129965
[71] Najer D *et al* 2019 *Nature* **575** 622–7
[72] Di Giulio V, Akerboom E, Polman A and García de Abajo F J 2024 *ACS Nano* **18** 14255–75
[73] Akerboom E, Di Giulio V, Schilder N J, Garciía de Abajo F J and Polman A 2024 *ACS Nano* **18** 13560–7
[74] Chruściński D, Hesabi S and Lonigro D 2023 *Sci. Rep.* **13** 1518
[75] Merkli M, Berman G and Sayre R 2013 *J. Math. Chem.* **51** 890–913
[76] Reppert M, Reppert D, Pachon L A and Brumer P 2020 *Phys. Rev. A* **102** 012211
[77] Michishita Y and Peters R 2020 *Phys. Rev. Lett.* **124** 196401
[78] Keldysh L V 2024 Diagram technique for nonequilibrium processes *Selected Papers of Leonid V Keldysh* (World Scientific) pp 47–55

4.2 Supplementary for chapter 4

4.2.1 Classically driven two-level system in a heat bath

The total Hamiltonian consists of the Hamiltonian part of the two-level system, an interacting part for the interaction with the environment, and finally a classical external field part that is driving the system. For the interaction part, the independent boson model is used [145]. It is important to point out that the independent boson model in itself is an exactly solvable model [145]. Here, the point is that an additional time-dependent external field is driving the system.

Another approximation used in writing our Hamiltonian is the long wavelength regime approximation called dipole approximation. It is used where $k.r << 1$ or the vector potential $\mathbf{A}(\mathbf{r},\mathbf{t}) \approx \mathbf{A}(\mathbf{t})$ is only time-dependent [81]. Thus, the interaction of the system with the external field can be formulated using the Rabi frequency that is proportional to $\mathbf{dF}(t)$.

Finally, we can write our total Hamiltonian as follows

$$\hat{H} = E_2\hat{a}_2^\dagger\hat{a}_2 + E_1\hat{a}_1^\dagger\hat{a}_1 + \Omega^*(t)\hat{a}_2^\dagger\hat{a}_1 + \Omega(t)\hat{a}_1^\dagger\hat{a}_2 + \sum_q \omega_q\hat{b}_q^\dagger\hat{b}_q + \sum_j \hat{a}_j^\dagger\hat{a}_j \sum_q g_{q,j}(\hat{b}_q + \hat{b}_q^\dagger), \quad (4.1)$$

where $\hat{a}_j$ and $\hat{a}_j^\dagger$ are the creation and the destruction operators of electrons for state j, and $\Omega(t) = 2\mathbf{dF}(t)$ is the Rabi frequency. $\hat{b}_q$ and $\hat{b}_q^\dagger$ are phonon destruction and creation operators, respectively, and $g_{q,j}$ is the coupling coefficient between environmental bosons mode q and electron in state j. We want to bring the equation into the standard spin-boson Hamiltonian form. This is done by assuming that only the difference between $g_{q,j}$ (for different j states) is important for the dynamics [145].

We start with the relation

$$\hat{a}_j^\dagger\hat{a}_j \sum_q g_{q,j}(\hat{b}_q + \hat{b}_q^\dagger) = \hat{a}_j^\dagger\hat{a}_j \sum_q \left\{ g_{qj} - \frac{1}{2}\left(g_{q1} + g_{q2}\right) + \frac{1}{2}\left(g_{q1} + g_{q2}\right) \right\} (\hat{b}_q + \hat{b}_q^\dagger). \quad (4.2)$$

Therefore, we can write for each state

$$\hat{a}_1^\dagger\hat{a}_1 \sum_q g_{q,1}\left(\hat{b}_q + \hat{b}_q^\dagger\right) = \hat{a}_1^\dagger\hat{a}_1 \left\{ \sum_q \frac{1}{2}\left(g_{q,1} - g_{q,2}\right)\left(\hat{b}_q + \hat{b}_q^\dagger\right) + \frac{1}{2}\left(g_{q,1} + g_{q,2}\right)\left(\hat{b}_q + \hat{b}_q^\dagger\right) \right\}, \quad (4.3a)$$

$$\hat{a}_2^\dagger \hat{a}_2 \sum_q g_{q,2}\left(\hat{b}_q + \hat{b}_q^\dagger\right) = \hat{a}_2^\dagger \hat{a}_2 \left\{ \sum_q -\frac{1}{2}\left(g_{q,1} - g_{q,2}\right)\left(\hat{b}_q + \hat{b}_q^\dagger\right) + \frac{1}{2}\left(g_{q,1} + g_{q,2}\right)\left(\hat{b}_q + \hat{b}_q^\dagger\right) \right\}. \tag{4.3b}$$

We insert (4.3a) and (4.3b) in (4.1). We also define $g_q = \frac{1}{2}\left(g_{q,1} - g_{q,2}\right)$. Therefore, we get

$$\begin{aligned} \hat{H} = & \left\{ E_2 + \frac{1}{2}\sum_q \left(g_{q,1} + g_{q,2}\right)\left(\hat{b}_q + \hat{b}_q^\dagger\right) \right\} \hat{a}_2^\dagger \hat{a}_2 + \\ & \left\{ E_1 + \frac{1}{2}\sum_q \left(g_{q,1} + g_{q,2}\right)\left(\hat{b}_q + \hat{b}_q^\dagger\right) \right\} \hat{a}_2^\dagger \hat{a}_2 \\ & + \Omega^*(t)\hat{a}_2^\dagger \hat{a}_1 + \Omega(t)\hat{a}_1^\dagger \hat{a}_2 + \sum_q \omega_q \hat{b}_q^\dagger \hat{b}_q + \sum_q g_q \left(\hat{b}_q + \hat{b}_q^+\right)\left(\hat{a}_2^\dagger \hat{a}_2 - \hat{a}_1^\dagger \hat{a}_1\right). \end{aligned} \tag{4.4}$$

For now, we assume that $\Omega^*(t) = \Omega(t)$, without loss of generality. After shifting the zero energy point we reach the known spin-boson Hamiltonian as follows.

$$\hat{H} = \frac{\varepsilon}{2}\hat{\sigma}_z + \frac{1}{2}\Omega(t)\hat{\sigma}_x + \sum_q \omega_q \hat{b}_q^\dagger \hat{b}_q + \hat{\sigma}_z \sum_q g_q \left(\hat{b}_q + \hat{b}_q^\dagger\right). \tag{4.5}$$

We have $\hat{\sigma}_z = \hat{a}_2^\dagger \hat{a}_2 - \hat{a}_1^\dagger \hat{a}_1$ and $\hat{\sigma}_x = \hat{a}_2^\dagger \hat{a}_2 + \hat{a}_1^\dagger \hat{a}_1$. g_q is the coupling between the bath mode q and the two-level system. Spin-Boson model [61], Eq. (4.5), is one of the fundamental models which is suitable for describing many physical systems.

4.2.2 Polaron transformation of the spin-boson Hamiltonian

Starting from the spin-boson model Eq. (4.5), we perform a unitary transformation as follows

$$\hat{U}_P = e^{\hat{\sigma}_z \otimes \sum_q \frac{g_q}{\omega_q}(\hat{b}_q^\dagger - \hat{b}_q)}, \tag{4.6a}$$

$$\hat{U}_P^\dagger = e^{-\hat{\sigma}_z \otimes \sum_q \frac{g_q}{\omega_q}(\hat{b}_q^\dagger - \hat{b}_q)}. \tag{4.6b}$$

Unitary transformations of Eqs. (4.6) are non-local operators; thus, they couple the two-level system with the heat bath and create entanglement. They displace the bath oscillators in different directions depending on the state of the electron. As we will see, they also create an energy shift in both energy levels.

In transforming the spin-boson Hamiltonian, we have

$$\bar{\hat{H}} = \hat{U}_P \hat{H} \hat{U}_P^\dagger = \hat{U}_P \left\{ \frac{\varepsilon}{2}\hat{\sigma}_z + \frac{1}{2}\Omega(t)\hat{\sigma}_x + \sum_q \omega_q \hat{b}_q^\dagger \hat{b}_q + \hat{\sigma}_z \sum_q g_q \left(\hat{b}_q + \hat{b}_q^\dagger \right) \right\} \hat{U}_P^\dagger. \quad (4.7)$$

Transforming each term using the Baker-Campbell-Hausdorff (BCH) formula and Taylor expansion yields

$$\bar{\hat{\sigma}}_z = \hat{U}_P \hat{\sigma}_z \hat{U}_P^\dagger = \hat{\sigma}_z, \quad (4.8)$$

$$\bar{\hat{\sigma}}_x = \hat{U}_P \hat{\sigma}_x \hat{U}_P^\dagger = \frac{1}{2}\hat{\sigma}_x \left(\hat{D}_+^2 + \hat{D}_-^2 \right) + \frac{i}{2}\left(\hat{D}_+^2 - \hat{D}_-^2 \right), \quad (4.9)$$

$$\bar{\hat{b}}_q = \hat{U}_P \hat{b}_q \hat{U}_P^\dagger = e^{\hat{\sigma}_z \sum_q \frac{g_q}{\omega_q}(\hat{b}_q^\dagger - \hat{b}_q)} \hat{b}_q e^{-\hat{\sigma}_z \sum_q \frac{g_q}{\omega_q}(\hat{b}_q^\dagger - \hat{b}_q)} = \hat{b}_q - \hat{\sigma}_z \frac{g_q}{\omega_q}, \quad (4.10a)$$

$$\bar{\hat{b}}_q^\dagger = \hat{U}_P \hat{b}_q^\dagger \hat{U}_P^\dagger = e^{\hat{\sigma}_z \sum_q \frac{g_q}{\omega_q}(\hat{b}_q^\dagger - \hat{b}_q)} \hat{b}_q^\dagger e^{-\hat{\sigma}_z \sum_q \frac{g_q}{\omega_q}(\hat{b}_q^\dagger - \hat{b}_q)} = \hat{b}_q^\dagger - \hat{\sigma}_z \frac{g_q}{\omega_q}. \quad (4.10b)$$

The displacement operators $\hat{D}_\pm^2$ are defined as $\hat{D}_\pm^2 = e^{\pm \sum_q \frac{2g_q}{\omega_q}\left(\hat{b}_q^\dagger - \hat{b}_q\right)}$. For simplicity, we define

$$\hat{D} = \prod_q \hat{D}_q = e^{\sum_q \alpha_q^* \hat{b}_q^\dagger - \alpha_q \hat{b}_q}, \quad (4.11a)$$

$$\alpha_q = \frac{2g_q}{\omega_q}. \quad (4.11b)$$

The polaron transformed Hamiltonian is

$$\bar{\hat{H}} = \frac{\varepsilon}{2}\bar{\hat{\sigma}}_z + \frac{1}{2}\Omega(t)\bar{\hat{\sigma}}_x + \sum_q \omega_q \bar{\hat{b}}_q^\dagger \bar{\hat{b}}_q + \bar{\hat{\sigma}}_z \sum_q g_q \left(\bar{\hat{b}}_q + \bar{\hat{b}}_q^\dagger \right). \quad (4.12)$$

Substituting from Eqs. (4.10), and Eqs. (4.8, 4.9) in (4.12), one gets

$$\bar{\hat{H}} = \frac{\varepsilon}{2}\sigma_z - \sum_q \frac{g_q^2}{\omega_q} + \sum_q \omega_q \hat{b}_q^\dagger \hat{b}_q + \frac{1}{4}\Omega(t)\hat{\sigma}_x \left(\hat{D}_+^2 + \hat{D}_-^2 \right) + \frac{i}{4}\Omega(t)\hat{\sigma}_y \left(\hat{D}_+^2 - \hat{D}_-^2 \right). \quad (4.13)$$

It is convenient to to rewrite $\hat{\sigma}_x$ and $\hat{\sigma}_y$ in terms of $\hat{\sigma}_+$ and $\hat{\sigma}_-$ defined as following

$$\hat{\sigma}_\pm = \frac{1}{2}\left(\hat{\sigma}_x \pm i\hat{\sigma}_y \right). \quad (4.14)$$

Finally, the simplified polaron-transformed Hamiltonian is

$$\bar{\hat{H}} = \frac{\varepsilon}{2}\hat{\sigma}_z - \hat{\rho}^1 + \sum_q \omega_q \hat{b}_q^\dagger \hat{b}_q + \frac{1}{2}\Omega(t)\left\{\hat{\sigma}_+ \hat{D}_+^2 + \hat{\sigma}_- \hat{D}_-^2\right\}. \tag{4.15}$$

Note that ρ^1 is the phonon-induced energy shift in the system and can be removed by defining a new zero energy point. In Eq. (4.15), we have $\Omega(t = -\infty) = 0$. The total basis at the beginning can be chosen as the tensor product of the basis of the two-level system and the heat bath. To put it in the mathematical notation, the assumption of $\hat{\rho}_{total}(t = -\infty) = \hat{\rho}_S(t = -\infty) \otimes \hat{\rho}_B$ does not apply additional restrictions in this frame. This is in contrast to the original spin-boson Hamiltonian Eq. (4.5) where there is a coupling term between the two (the two level system and the heat bath) even at the beginning ($t = -\infty$). Thus, starting from the polaron-transformed Hamiltonian, one does not need to assume the non-physical unentanglement of the two-level system and the heat bath at the beginning.

To put it differently, one can compare the choosing of the total bases in these two different frames. The interaction part, the third term on the RHS of Eq. (4.15), acting on the total basis $|g\rangle|n\rangle$ gives $|e\rangle|2\alpha, n\rangle$, and acting on the $|e\rangle|n\rangle$ gives $|g\rangle|-2\alpha, n\rangle$. $|\pm 2\alpha, n\rangle$ are the displaced number states or the generalized coherent states [146, 147]. $|g\rangle$ and $|e\rangle$ are the ground and excited states of the two-level system, and α is the exponent part in the displacement operator, $\hat{D}_\pm(\alpha) = e^{\pm(\alpha\hat{b}^\dagger - \alpha^*\hat{b})}$.

In the polaron frame, if one starts with non-displaced bases in the heat bath, in the original frame these displaced number basis would be the starting point. This is what the non-local unitary operator in Eq. (4.6) does. An important point to note is that in the interaction picture, these displaced bases are time-dependent and difficult to work with. See the schematic (4.1).

Original frame	Polaron frame
$\|e\rangle\|n\rangle$	$\|e\rangle\|\alpha, n\rangle$
$\|e\rangle\|-\alpha, n\rangle$	$\|e\rangle\|n\rangle$ ⟵
$\|g\rangle\|n\rangle$	$\|g\rangle\|-\alpha, n\rangle$
$\|g\rangle\|\alpha, n\rangle$	$\|g\rangle\|n\rangle$ ⟵

Figure 4.1: Transforming from original to polaron frame and vice versa

We work in the interaction picture. We define $\hat{H}_I$ and $\hat{H}_0$ to be

$$\hat{H}_0 = \sum_q \omega_q \hat{b}_q^\dagger \hat{b}_q, \tag{4.16a}$$

$$\hat{H}_I = \frac{\varepsilon}{2}\hat{\sigma}_z + \frac{1}{2}\Omega(t)\left\{\hat{\sigma}_+ \hat{D}_+^2(t) + \hat{\sigma}_- \hat{D}_-^2(t)\right\}. \tag{4.16b}$$

By doing so, the creation and annihilation operators become time-dependent as follows

$$\hat{b}_q = \hat{b}_q e^{-i\omega_q t}, \tag{4.17a}$$

$$\hat{b}_q^+ = \hat{b}_q^+ e^{i\omega_q t}, \tag{4.17b}$$

$$\hat{\sigma}_{z,+,-}(t) = \hat{\sigma}_{z,+,-}. \tag{4.17c}$$

Writing $\hat{H}_I$ in the matrix form one gets

$$\hat{H}_I = \frac{1}{2}\begin{bmatrix} \varepsilon & \Omega(t)\hat{D}_+^2(t) \\ \Omega(t)\hat{D}_-^2(t) & -\varepsilon \end{bmatrix}. \tag{4.18}$$

Now, we can proceed with the procedures done in Chapter (3). The only difference is the additional $\hat{D}_\pm^2(t)$ in the off-diagonals. The first step was diagonalizing the Hamiltonian.

We find $\hat{V}$ and $\hat{V}^\dagger$ to be

$$\hat{V} = \frac{1}{\sqrt{2}} \begin{bmatrix} \frac{\sqrt{\lambda+\varepsilon}}{\sqrt{\lambda}} & -\frac{\Omega}{\sqrt{\lambda}\sqrt{\lambda+\varepsilon}}\hat{D}_+^2 \\ \frac{\Omega}{\sqrt{\lambda}\sqrt{\lambda+\varepsilon}}\hat{D}_-^2 & \frac{\sqrt{\lambda+\varepsilon}}{\sqrt{\lambda}} \end{bmatrix}, \tag{4.19a}$$

$$\hat{V}^\dagger = \frac{1}{\sqrt{2}} \begin{bmatrix} \frac{\sqrt{\lambda+\varepsilon}}{\sqrt{\lambda}} & \frac{\Omega}{\sqrt{\lambda}\sqrt{\lambda+\varepsilon}}\hat{D}_+^2 \\ -\frac{\Omega}{\sqrt{\lambda}\sqrt{\lambda+\varepsilon}}\hat{D}_-^2 & \frac{\sqrt{\lambda+\varepsilon}}{\sqrt{\lambda}} \end{bmatrix}. \tag{4.19b}$$

The time dependence of λ, Ω, and $\hat{D}_\pm^2$ is omitted for simplicity. Using Eqs. (4.19) we have

$$\hat{\tilde{H}}(t) = \hat{V}^\dagger \hat{H}_I \hat{V} = \frac{1}{2} \begin{bmatrix} \lambda(t) & 0 \\ 0 & -\lambda(t) \end{bmatrix}. \tag{4.20}$$

λ is defined as $\lambda(t) = \sqrt{\varepsilon^2 + \Omega(t)^2}$. Multiplying the Von Neumann equation with $\hat{V}^\dagger, \hat{V}$ from the left and right, inserting $\hat{V}\hat{V}^\dagger = \mathbb{1}$ and defining $\tilde{\hat{\rho}} = \hat{V}^\dagger \hat{\rho} \hat{V}$ we obtain a transformed but still exact equation. The rest is like what we did in chapter (3). The difference here is that matrices $\hat{V}$, Eq. (4.19a), and $\hat{V}^\dagger$, Eq. (4.19b), have displacement operators in them.

4.2.3 SFAF equations coupled to a heat bath

Starting from the polaron transformed Hamiltonian Eq. (4.15) we know that in the limit of laser frequency much smaller than the minimum bandgap, the electron dynamics follows dominantly the laser field and the adiabatic following approximation can be used. This is done by first diagonalizing the Hamiltonian. We use $\hat{V}$ and $\hat{V}^\dagger$ to transform the von Neumann equation. Staring from von Neumann equation we get

$$i\partial_t \hat{\rho} = \left[\hat{H}, \hat{\rho}\right]; \tag{4.21}$$

then, transforming using $\hat{V}$ and $\hat{V}^\dagger$ and using $\hat{V}^\dagger\hat{V} = \mathbb{1}$ yields

$$i\hat{V}^\dagger \partial_t \hat{\rho} \hat{V} = \hat{V}^\dagger \hat{H} \hat{V} \hat{V}^\dagger \hat{\rho} \hat{V} - \hat{V}^\dagger \hat{\rho} \hat{V} \hat{V}^\dagger \hat{H} \hat{V} = \left[\hat{\tilde{H}}, \hat{\tilde{\rho}}\right], \tag{4.22}$$

where $\hat{\hat{H}} = \hat{V}^\dagger \hat{H} \hat{V}, \hat{\hat{\rho}} = \hat{V}^\dagger \hat{\rho} \hat{V}$ we know that

$$\partial_t \left(\hat{V}^\dagger \hat{\rho} \hat{V} \right) = \left(\partial_t \hat{V}^\dagger \right) \hat{\rho} \hat{V} + \hat{V}^\dagger \left(\partial_t \hat{\rho} \right) \hat{V} + \hat{V}^\dagger \hat{\rho} \left(\partial_t \hat{V} \right), \tag{4.23a}$$

$$\hat{V}^+ \left(\partial_t \hat{\rho} \right) \hat{V} = \partial_t \hat{\hat{\rho}} - \left(\partial_t \hat{V}^\dagger \right) \hat{\rho} \hat{V} - \hat{V}^\dagger \hat{\rho} \left(\partial_t \hat{V} \right), \tag{4.23b}$$

Inserting $\hat{V}^\dagger \hat{V} = \mathbb{1}$

$$\hat{V}^+ \left(\partial_t \hat{\rho} \right) \hat{V} = \partial_t \hat{\hat{\rho}} - \left(\partial_t \hat{V}^\dagger \right) \hat{V} \hat{\hat{\rho}} - \hat{\hat{\rho}} \hat{V}^\dagger \left(\partial_t \hat{V} \right). \tag{4.24}$$

Finally, the transformed but still exact von Neumann equation have the form

$$i \partial_t \hat{\hat{\rho}} = \left[\hat{\hat{H}}, \hat{\hat{\rho}} \right] + i \left(\partial_t \hat{V}^+ \right) \hat{V} \hat{\hat{\rho}} + i \hat{\hat{\rho}} \hat{V}^\dagger \left(\partial_t \hat{V} \right). \tag{4.25}$$

Note that $\partial_t \hat{V}$ and $\partial_t \hat{V}^\dagger$ scale with ω_0 which is the laser frequency, and $\hat{\hat{H}}$ scales with ε. Since $\frac{\omega_0}{\varepsilon} << 1$ the last two terms of Eq. (4.25) can be neglected to obtain the zeroth order term. The zero order result gives the adiabatic following solution while considering noise terms as we will see later. It only contains virtual and no real excitation. In other words two-level adiabatic following in perturbative NLO in atomic systems is given by zeroth order which is dominated by virtual processes. We are interested in non-perturbative dynamics, where real transitions need to be accounted for as well. Therefore, including higher orders is essential. In order to go to higher orders in a Dyson series we use the ansatz

$$\hat{\hat{\rho}}(t) = e^{-i \int_{-\infty}^{t} \hat{\hat{H}} dt'} \hat{\hat{\rho}}'(t) e^{i \int_{-\infty}^{t} \hat{\hat{H}} dt'}. \tag{4.26}$$

Taking the derivative to construct the term on the LHS of Eq. (4.25) yeilds

$$\begin{aligned} i \partial_t \hat{\hat{\rho}} &= \hat{\hat{H}} e^{-i \int_{-\infty}^{t} \hat{\hat{H}} dt'} \hat{\hat{\rho}}' e^{i \int_{-\infty}^{t} \hat{\hat{H}} dt'} + i e^{-i \int_{-\infty}^{t} \hat{\hat{H}} dt'} \left(\partial_t \hat{\hat{\rho}}' \right) e^{i \int_{-\infty}^{t} \hat{\hat{H}} dt'} - e^{-i \int_{-\infty}^{t} \hat{\hat{H}} dt'} \hat{\hat{\rho}}' \hat{\hat{H}} e^{i \int_{-\infty}^{t} \hat{\hat{H}} dt'} \\ &= e^{-i \int_{-\infty}^{t} \hat{\hat{H}} dt'} \left[\hat{\hat{H}}, \hat{\hat{\rho}}' \right] e^{i \int_{-\infty}^{t} \hat{\hat{H}} dt'} + i e^{-i \int_{-\infty}^{t} \hat{\hat{H}} dt'} \left(\partial_t \hat{\hat{\rho}}' \right) e^{i \int_{-\infty}^{t} \hat{\hat{H}} dt'}. \end{aligned} \tag{4.27}$$

The first term on the RHS of Eq.(4.25) is

$$\begin{aligned} \left[\hat{\hat{H}}, \hat{\hat{\rho}} \right] &= \left[\hat{\hat{H}}, e^{-i \int_{-\infty}^{t} \hat{\hat{H}} dt'} \hat{\hat{\rho}}' e^{i \int_{-\infty}^{t} \hat{\hat{H}} dt'} \right] = \hat{\hat{H}} e^{-i \int_{-\infty}^{t} \hat{\hat{H}} dt'} \hat{\hat{\rho}}' e^{i \int_{-\infty}^{t} \hat{\hat{H}} dt'} - e^{-i \int_{-\infty}^{t} \hat{\hat{H}} dt'} \hat{\hat{\rho}}' e^{i \int_{-\infty}^{t} \hat{\hat{H}} dt'} \hat{\hat{H}} \\ &= e^{-i \int_{-\infty}^{t} \hat{\hat{H}} dt'} \left[\hat{\hat{H}}, \hat{\hat{\rho}}' \right] e^{i \int_{-\infty}^{t} \hat{\hat{H}} dt'}. \end{aligned} \tag{4.28}$$

Now, substituting the ansatz and Eqs.(4.27), (4.28) in the transformed von Neumann equation, Eq. (4.25) we get

$$\cancel{e^{-i\int_{-\infty}^{t}\hat{\hat{H}}dt'}\left[\hat{\hat{H}},\hat{\hat{\rho}}'\right]e^{i\int_{-\infty}^{t}\hat{\hat{H}}dt'}} + ie^{-i\int_{-\infty}^{t}\hat{\hat{H}}dt'}\left(\partial_t\hat{\hat{\rho}}'\right)e^{i\int_{-\infty}^{t}\hat{\hat{H}}dt'} =$$
$$\cancel{e^{-i\int_{-\infty}^{t}\hat{\hat{H}}dt'}\left[\hat{\hat{H}},\hat{\hat{\rho}}'\right]e^{i\int_{-\infty}^{t}\hat{\hat{H}}dt'}} + i\left(\partial_t\hat{V}^{\dagger}\right)\hat{V}e^{-i\int_{-\infty}^{t}\hat{\hat{H}}dt'}\hat{\hat{\rho}}'e^{i\int_{-\infty}^{t}\hat{\hat{H}}dt'} + ie^{-i\int_{-\infty}^{t}\hat{\hat{H}}dt'}\hat{\hat{\rho}}'e^{i\int_{-\infty}^{t}\hat{\hat{H}}dt'}\hat{V}^{\dagger}\left(\partial_t\hat{V}\right). \tag{4.29}$$

By simplifying we have

$$\partial_t\hat{\hat{\rho}}' = e^{i\int_{-\infty}^{t}\hat{\hat{H}}dt'}\left(\partial_t\hat{V}^{\dagger}\right)\hat{V}e^{-i\int_{-\infty}^{t}\hat{\hat{H}}dt'}\hat{\hat{\rho}}' + \hat{\hat{\rho}}'e^{i\int_{-\infty}^{t}\hat{\hat{H}}dt'}\hat{V}^{\dagger}\left(\partial_t\hat{V}\right)e^{-i\int_{-\infty}^{t}\hat{\hat{H}}dt'}. \tag{4.30}$$

One can rewrite this as

$$\partial_t\hat{\hat{\rho}}'(t) = \hat{\hat{W}}\hat{\hat{\rho}}'(t) + \hat{\hat{\rho}}'(t)\hat{\hat{W}}^{\dagger}. \tag{4.31}$$

Where $\hat{\hat{W}}$ is

$$\hat{\hat{W}} = e^{i\int_{-\infty}^{t}\hat{\hat{H}}dt'}\left(\partial_t\hat{V}^{\dagger}(t)\right)\hat{V}(t)e^{-i\int_{-\infty}^{t}\hat{\hat{H}}dt'}. \tag{4.32}$$

We can solve for $\hat{\hat{\rho}}'(t)$ using Eq. (4.31), where $\hat{T}$ is the time ordering operator

$$\hat{\hat{\rho}}' = \left(\hat{T}e^{\int_{-\infty}^{t}dt'\hat{\hat{W}}}\right)\hat{\hat{\rho}}'(t=-\infty)\left(\hat{T}e^{\int_{-\infty}^{t}dt'\hat{\hat{W}}}\right)^{\dagger}. \tag{4.33}$$

Transforming back to $\hat{\hat{\rho}}$ we get

$$\hat{\hat{\rho}} = \left(e^{-i\int_{-\infty}^{t}\hat{\hat{H}}dt'}\right)\left(\hat{T}e^{\int_{-\infty}^{t}dt'\hat{\hat{W}}}\right)\hat{\hat{\rho}}'(t=-\infty)\left(\hat{T}e^{\int_{-\infty}^{t}dt'\hat{\hat{W}}}\right)^{\dagger}\left(e^{i\int_{-\infty}^{t}\hat{\hat{H}}dt'}\right). \tag{4.34}$$

Going back to the polaron frame from $\hat{\hat{\rho}}$ to $\hat{\rho}$, yields

$$\hat{\rho}(t) = \hat{V}\left(e^{-i\int_{-\infty}^{t}\hat{\hat{H}}dt'}\right)\left(\hat{T}e^{\int_{-\infty}^{t}dt'\hat{\hat{W}}}\right)\hat{\hat{\rho}}(t=-\infty)\left(\hat{T}e^{\int_{-\infty}^{t}dt'\hat{\hat{W}}}\right)^{\dagger}\left(e^{i\int_{-\infty}^{t}\hat{\hat{H}}dt'}\right)V^{\dagger}. \tag{4.35}$$

Note that from Eq. (4.34), $\hat{\hat{\rho}}(t=-\infty) = \hat{\hat{\rho}}'(t=-\infty)$. Also using the fact that $V(t=-\infty)$ and $\hat{V}^{\dagger}(t=-\infty)$ are identity matrices yields

$$\hat{\rho}(t=-\infty) = \hat{\hat{\rho}}(t=-\infty) = \hat{\hat{\rho}}'(t=-\infty) = \begin{bmatrix} 0 & 0 \\ 0 & 1 \end{bmatrix} \bigotimes \hat{B}. \tag{4.36}$$

Note that $\hat{\rho}(t=-\infty) = \begin{bmatrix} 0 & 0 \\ 0 & \hat{B} \end{bmatrix}$ in the polaron frame means that in the polaron frame the heat bath is in equilibrium such that $\boldsymbol{B}$ is defined by the Gibbs state

$$\hat{B} = \frac{e^{-\hat{H}_0\beta}}{\mathrm{tr}_{bath}\left\{e^{-\hat{H}_0\beta}\right\}}, \tag{4.37}$$

and there is no correlation between the heat bath and the system since at time $t=-\infty$, $\Omega = 0$ in Eq. (4.15).

Eq. (4.35) is a unitary time evolution of the density matrix and it is still an exact form. In order to obtain an expansion series for this equation the time ordering operator can be written into Dyson series as follows. In the limit of step size $\Delta t \to 0$ we have until the first order

$$\hat{T}e^{\int_{-\infty}^{t}\hat{\tilde{W}}dt'} = \prod_{t_i=-\infty}^{t} e^{\hat{\tilde{W}}(t_i)\Delta t} \approx \prod_{t_i=-\infty}^{t} 1+\hat{\tilde{W}}(t_i)\Delta t \approx 1+\sum_{t_i=-\infty}^{t}\hat{\tilde{W}}(t_i)\Delta t = 1+\int_{-\infty}^{t}\hat{\tilde{W}}(t')dt'. \tag{4.38}$$

Note that higher order terms give n-times nested integrals. As stated before we will keep terms until the second order since we are interested in non-perturbative dynamics, where real transitions need to be accounted for. As such, inclusion of higher order Dyson terms is essential. Therefore, this yields [57, 5]

$$\hat{T}e^{\int_{-\infty}^{t}\hat{\tilde{W}}dt'} \approx 1+\int_{-\infty}^{t}dt'\hat{\tilde{W}}+\int_{-\infty}^{t}dt'\hat{\tilde{W}}(t')\int_{-\infty}^{t'}dt''\hat{\tilde{W}}(t'') \tag{4.39a}$$

$$\left\{\hat{T}e^{\int_{-\infty}^{t}\hat{\tilde{W}}dt'}\right\}^{+} \approx 1+\int_{-\infty}^{t}dt'\hat{\tilde{W}}^{+}+\int_{-\infty}^{t}dt'\left\{\int_{-\infty}^{t'}dt''\hat{\tilde{W}}^{\dagger}(t'')\right\}\hat{\tilde{W}}^{\dagger}(t') \tag{4.39b}$$

We now substitute this in Eq. (4.35) and define

$$\hat{W}(t,t') = e^{-i\int_{t'}^{t}\hat{\tilde{H}}dt''}\left(\partial_t\hat{V}^{\dagger}(t')\right)\hat{V}(t')e^{i\int_{t'}^{t}\hat{\tilde{H}}dt''}. \tag{4.40}$$

Note that, one time, $\hat{\tilde{W}}(t)$ was

$$\hat{\tilde{W}}(t) = e^{i\int_{-\infty}^{t}\hat{\tilde{H}}dt'}\left(\partial_t\hat{V}^{\dagger}(t)\right)\hat{V}(t)e^{-i\int_{-\infty}^{t}\hat{\tilde{H}}dt'} \tag{4.41}$$

So to be sure we have unitary transformations we have

$$\hat{W}(t,t') + \hat{W}^{\dagger}(t,t') = \int_{-\infty}^{t} e^{-i\int_{t'}^{t} dt'' \hat{\tilde{H}}} \left\{ \left(\partial_{t'} \hat{V}^{\dagger}(t')\right) \hat{V}(t') + \hat{V}^{\dagger}(t') \left(\partial_{t'} \hat{V}(t')\right) \right\} e^{i\int_{t'}^{t} dt'' \hat{\tilde{H}}} dt'. \tag{4.42}$$

We know that

$$\left(\partial_{t'} \hat{V}^{\dagger}(t')\right) \hat{V}(t') + \hat{V}^{\dagger}(t') \left(\partial_{t'} \hat{V}(t')\right) = \partial_{t'} \left(\hat{V}^{\dagger} \hat{V}\right) = \partial_{t'} 1. \tag{4.43}$$

Therefore, using Eq. (4.43) we have

$$\hat{W}(t,t') + \hat{W}^{+}(t,t') = \int_{-\infty}^{t} e^{-i\int_{t'}^{t} dt'' \hat{\tilde{H}}} \left\{ \partial_{t'} 1 \right\} e^{i\int_{t'}^{t} dt'' \hat{\tilde{H}}} dt' = 0. \tag{4.44}$$

Which also holds for $\tilde{W}(t)$ showing the anti-hermitian nature of $\hat{W}$. Finally, after some calculations to transform from $\hat{\tilde{W}}(t)$ to $\hat{W}(t,t')$ in Eq. (4.35) we reach

$$\begin{aligned} \hat{\rho}(t) = \hat{V} \left\{ 1 + \int_{-\infty}^{t} \hat{W}(t,t')dt' + \int_{-\infty}^{t} \hat{W}(t,t')dt' \int_{-\infty}^{t'} \hat{W}(t,t'')dt'' + ... \right\} \hat{V}^{\dagger} \hat{\rho}_0 \hat{V} \\ \left\{ 1 + \int_{-\infty}^{t} \hat{W}^{\dagger}(t,t')dt' + \int_{-\infty}^{t} \left(\int_{-\infty}^{t'} \hat{W}^{\dagger}(t,t'')dt'' \right) \hat{W}^{\dagger}(t,t')dt' \right\} \hat{V}^{\dagger} \end{aligned} \tag{4.45}$$

Where we have $\hat{\rho}_0 = \hat{V} e^{-i\int_{-\infty}^{t} \hat{\tilde{H}}} \hat{\rho}(t=-\infty) e^{i\int_{-\infty}^{t} \hat{\tilde{H}}} \hat{V}^{\dagger}$ is the zeroth order contribution. We know that $\hat{\tilde{\rho}}_0 = \hat{V}^{\dagger} \hat{\rho}_0 \hat{V}$; therefore, Eq. (4.45) yields

$$\begin{aligned} \hat{\tilde{\rho}}(t) = \hat{\tilde{\rho}}_0 + \int_{-\infty}^{t} \hat{W}(t,t')dt' \times \hat{\tilde{\rho}}_0 + \int_{-\infty}^{t} \hat{W}(t,t')dt' \int_{-\infty}^{t'} \hat{W}(t,t'')dt'' \times \hat{\tilde{\rho}}_0 \\ + \hat{\tilde{\rho}}_0 \times \int_{-\infty}^{t} \hat{W}^{\dagger}(t,t')dt' + \hat{\tilde{\rho}}_0 \times \int_{-\infty}^{t} \left(\int_{-\infty}^{t'} \hat{W}^{\dagger}(t,t'')dt'' \right) \hat{W}^{\dagger}(t,t')dt' \\ + \int_{-\infty}^{t} \hat{W}(t,t')dt' \times \hat{\tilde{\rho}}_0 \times \int_{-\infty}^{t} \hat{W}^{\dagger}(t,t')dt'. \end{aligned} \tag{4.46}$$

Final words for this section is that Hermiticity preservation, complete positivity preservation, and trace preservation should be checked for density matrix transformations. Our approach will preserve Hemiticity and trace; however, the positivity for any given field is conserved up to some specific order. According to Eq. (4.46) we need to calculate $\hat{W}(t,t')$ and $\hat{U}$, where we have $\hat{U} = \int_{-\infty}^{t} \hat{W}(t,t')$.

Calculating matrix $\hat{W}(t,t')$ elements

To calculate $\hat{W}(t,t')$ in Eq. (4.40), we need to first calculate $\frac{d}{dt}\hat{D}_{\pm}^2$. We have

$$\frac{d}{dt}\hat{D}_{\pm}^2 = \frac{d}{dt}e^{\pm\sum_q \frac{2g_q}{\omega_q}\left(\hat{b}_q^\dagger(t)-\hat{b}_q(t)\right)}. \tag{4.47}$$

We define $\alpha_q^* = \frac{2g_q}{\omega_q}e^{i\omega_q t}$ and $\alpha_q = \frac{2g_q}{\omega_q}e^{-i\omega_q t}$. Using the BCH formula, we have

$$\begin{aligned}
&\frac{d}{dt}\hat{D}_{\pm}^2 = \frac{d}{dt}e^{\pm\sum_q \alpha_q^*\hat{b}_q^\dagger(t)-\alpha_q\hat{b}_q(t)} = \frac{d}{dt}\left\{e^{\pm\sum_q \alpha_q^*\hat{b}_q^\dagger}e^{\mp\sum\alpha_q\hat{b}_q}e^{-\frac{1}{2}\sum_q|\alpha_q|^2[\pm\hat{b}_q^+,\mp\hat{b}_q]}\right\} = \\
&\left\{e^{\pm\sum_q\alpha_q^*\hat{b}_q^\dagger}\left\{(\pm i)\sum_q 2g_q\hat{b}_q^\dagger(t)\right\}e^{\mp\sum\alpha_q\hat{b}_q} + e^{\pm\sum_q\alpha_q^*\hat{b}_q^\dagger}e^{\mp\sum\alpha_q\hat{b}_q}\left\{(\pm i)\sum_q 2g_q\hat{b}_q(t)\right\}\right\}\times e^{-\frac{1}{2}\sum_q|\alpha_q|^2}.
\end{aligned} \tag{4.48}$$

For the commutation relations, we get

$$\left[\hat{b}_q, e^{\frac{2g_q}{\omega_q}\hat{b}_q^+}\right] = \frac{2g_q}{\omega_q}e^{\frac{2g_q}{\omega_q}\hat{b}_q^+}, \tag{4.49a}$$

$$\left[\hat{b}_q^+, e^{\frac{2g_q}{\omega_q}\hat{b}_q}\right] = -\frac{2g_q}{\omega_q}e^{\frac{2g_q}{\omega_q}\hat{b}_q}. \tag{4.49b}$$

Putting Eqs. (4.49) into Eq. (4.48), yields

$$\hat{D}_{\mp}^2\dot{\hat{D}}_{\pm}^2 = \sum_q \pm\left(2ig_q\right)\left(\hat{b}_q^\dagger(t)+\hat{b}_q(t)\right) + 4i\frac{g_q^2}{\omega_q}. \tag{4.50}$$

We define

$$\hat{D} = i\sum_q\left(2ig_q\right)\left(\hat{b}_q^\dagger(t)+\hat{b}_q(t)\right) = \sum_q i\omega_q\left(\alpha_q^*\hat{b}_q^\dagger+\alpha_q\hat{b}_q\right), \tag{4.51}$$

$$\hat{D}_0 = 4i\frac{g_q^2}{\omega_q} = i\omega_q|\alpha_q|^2. \tag{4.52}$$

Therefore, Eq. (4.50) becomes

$$\hat{D}_{\mp}^2\dot{\hat{D}}_{\pm}^2 = \pm\hat{D}+\hat{D}_0. \tag{4.53}$$

Now, we can calculate $\hat{W}^{\dagger}(t,t')$ defined as $\hat{W}^{\dagger}(t,t') = e^{-i\int_{t'}^{t}\hat{\hat{H}}dt''}\hat{V}^{\dagger}\left(\partial_t\hat{V}(t')\right)e^{i\int_{-\infty}^{t'}\hat{\hat{H}}dt''}$. We have a diagonalized Hamiltonian as

$$\hat{\hat{H}} = \frac{1}{2}\begin{bmatrix} \lambda & 0 \\ 0 & -\lambda \end{bmatrix} \tag{4.54}$$

Therefore, the corresponding operator matrices become

$$e^{-i\int_{t'}^{t}\hat{\hat{H}}dt''} = \begin{bmatrix} e^{-\frac{i}{2}\int_{t'}^{t}\lambda dt''} & 0 \\ 0 & e^{\frac{i}{2}\int_{t'}^{t}\lambda dt''} \end{bmatrix}, \tag{4.55}$$

$$e^{i\int_{t'}^{t}\hat{\hat{H}}dt''} = \begin{bmatrix} e^{\frac{i}{2}\int_{t'}^{t}\lambda dt''} & 0 \\ 0 & e^{-\frac{i}{2}\int_{t'}^{t}\lambda dt''} \end{bmatrix}. \tag{4.56}$$

In order to make calculations easier we define a_{11}, a_{12} in accordance with Eqs. (4.19a), (4.19b). Therefore, we have

$$a_{11} = \frac{\sqrt{\lambda+\varepsilon}}{\sqrt{\lambda}}, \tag{4.57a}$$

$$a_{12} = \frac{\Omega}{\sqrt{\lambda+\varepsilon}\sqrt{\lambda}}. \tag{4.57b}$$

Using the above definitions, we have for $\hat{V}$ and $\hat{V}^{\dagger}$

$$\partial_t\hat{V}(t) = \frac{1}{\sqrt{2}}\begin{bmatrix} \dot{a_{11}} & -\left(a_{12}\hat{\mathrm{D}}_{+}^{2}\right)' \\ \left(a_{12}\hat{\mathrm{D}}_{-}^{2}\right)' & \dot{a_{11}} \end{bmatrix}, \tag{4.58}$$

$$\hat{V}^{\dagger}(t) = \frac{1}{\sqrt{2}}\begin{bmatrix} a_{11} & a_{12}\hat{\mathrm{D}}_{+}^{2} \\ -a_{12}\hat{\mathrm{D}}_{-}^{2} & a_{11} \end{bmatrix}. \tag{4.59}$$

Now, that we have every piece we can write the operator matrix $\hat{W}^{\dagger}(t,t')$ as follows

$$\hat{W}^{\dagger}(t,t') = \frac{1}{2}\begin{bmatrix} e^{-\frac{i}{2}\int_{t'}^{t}\lambda dt''} & 0 \\ 0 & e^{\frac{i}{2}\int_{t'}^{t}\lambda dt''} \end{bmatrix}\times \begin{bmatrix} a_{11}\dot{a_{11}} + \left(a_{12}\hat{D}_{+}^{2}\right)\left(a_{12}\hat{D}_{-}^{2}\right)' & -a_{11}\left(a_{12}\hat{D}_{+}^{2}\right)' + a_{12}\dot{a_{11}}\hat{D}_{+}^{2} \\ a_{11}\left(a_{12}\hat{D}_{-}^{2}\right)' - a_{12}\dot{a_{11}}\hat{D}_{-}^{2} & a_{11}\dot{a_{11}} + \left(a_{12}\hat{D}_{-}^{2}\right)\left(a_{12}\hat{D}_{+}^{2}\right)' \end{bmatrix}\times \begin{bmatrix} e^{\frac{i}{2}\int_{t'}^{t}\lambda dt''} & 0 \\ 0 & e^{-\frac{i}{2}\int_{t'}^{t}\lambda dt''} \end{bmatrix}. \tag{4.60}$$

After simplification of Eq. (4.60), we get

$$\hat{W}^{\dagger}(t,t') = \frac{1}{2}\begin{bmatrix} a_{12}^{2}(-\hat{D}+\hat{D}_{0}) & -\left\{a_{11}\left(a_{12}\hat{D}_{+}^{2}\right)' - \dot{a_{11}}\left(a_{12}\hat{D}_{+}^{2}\right)\right\}e^{-i\int_{t'}^{t}\lambda dt''} \\ \left\{a_{11}\left(a_{12}\hat{D}_{-}^{2}\right)' - \dot{a_{11}}\left(a_{12}\hat{D}_{-}^{2}\right)\right\}e^{i\int_{t'}^{t}\lambda dt''} & a_{12}^{2}(\hat{D}+\hat{D}_{0}) \end{bmatrix}. \tag{4.61}$$

Using the definitions of a_{11} and a_{12} Eqs. (4.57a), (4.57b), we find for the diagonals

$$\hat{W}^{\dagger}(t,t') = \frac{1}{2}\begin{bmatrix} \left(1-\frac{\varepsilon}{\lambda}\right)(-\hat{D}+\hat{D}_{0}) & -\left\{a_{11}\left(a_{12}\hat{D}_{+}^{2}\right)' - \dot{a_{11}}\left(a_{12}\hat{D}_{+}^{2}\right)\right\}e^{-i\int_{t'}^{t}\lambda dt''} \\ \left\{a_{11}\left(a_{12}\hat{D}_{-}^{2}\right)' - \dot{a_{11}}\left(a_{12}\hat{D}_{-}^{2}\right)\right\}e^{i\int_{t'}^{t}\lambda dt''} & \left(1-\frac{\varepsilon}{\lambda}\right)(\hat{D}+\hat{D}_{0}) \end{bmatrix}. \tag{4.62}$$

For the off diagonals, we have

$$\begin{aligned} a_{11}\left(a_{12}\hat{D}_{-}^{2}\right)' - \dot{a_{11}}\left(a_{12}\hat{D}_{-}^{2}\right) &= \left(a_{11}a_{12}\hat{D}_{-}^{2}\right)' - 2\dot{a_{11}}a_{12}\hat{D}_{-}^{2} \\ &= \left(\frac{\Omega}{\lambda}\hat{D}_{-}^{2}\right)' - 2\frac{\Omega}{\sqrt{\lambda}\sqrt{\lambda+\varepsilon}}\frac{d}{dt}\left(\frac{\sqrt{\lambda+\varepsilon}}{\sqrt{\lambda}}\right)\hat{D}_{-}^{2} \\ &= \left(\frac{\Omega}{\lambda}\hat{D}_{-}^{2}\right)' - 2\frac{\sqrt{\lambda}}{\sqrt{\lambda+\varepsilon}}\frac{d}{dt}\left(\frac{\sqrt{\lambda+\varepsilon}}{\sqrt{\lambda}}\right)\left(\frac{\Omega}{\lambda}\hat{D}_{-}^{2}\right) \\ &= \left(\frac{\Omega}{\lambda}\hat{D}_{-}^{2}\right)' - \frac{d}{dt}\left[\ln\left(\frac{\lambda+\varepsilon}{\lambda}\right)\right]\left(\frac{\Omega}{\lambda}\hat{D}_{-}^{2}\right) = \left(\frac{\Omega}{\lambda}\hat{D}_{-}^{2}\right)' - \frac{\dot{\varepsilon}\lambda-\dot{\lambda}\varepsilon}{\lambda(\lambda+\varepsilon)}\left(\frac{\Omega}{\lambda}\hat{D}_{-}^{2}\right). \end{aligned} \tag{4.63}$$

We now evaluate the second term of Eq. (4.63) to determine its leading order contribution. This yields

$$\ln\left(\frac{\lambda+\varepsilon}{\lambda}\right)=\ln\left(\frac{\lambda^2-\varepsilon^2}{\lambda\left(\lambda-\varepsilon\right)}\right)=\ln\left(\frac{\Omega^2}{\varepsilon^2+\Omega^2-\varepsilon^2\sqrt{1+\frac{\Omega^2}{\varepsilon^2}}}\right)=\ln\left(\frac{\frac{\Omega^2}{\varepsilon^2}}{1+\frac{\Omega^2}{\varepsilon^2}-\sqrt{1+\frac{\Omega^2}{\varepsilon^2}}}\right). \tag{4.64}$$

We use the expansion

$$\sqrt{1+\frac{\Omega^2}{\varepsilon^2}}=1+\frac{1}{2}\left(\frac{\Omega}{\varepsilon}\right)^2-\frac{1}{8}\left(\frac{\Omega}{\varepsilon}\right)^4+\frac{1}{16}\left(\frac{\Omega}{\varepsilon}\right)^6-\frac{5}{128}\left(\frac{\Omega}{\varepsilon}\right)^8+\cdots. \tag{4.65}$$

Therefore, it yields

$$\begin{aligned}
&\ln\left(\frac{\frac{\Omega^2}{\varepsilon^2}}{1+\frac{\Omega^2}{\varepsilon^2}-\sqrt{1+\frac{\Omega^2}{\varepsilon^2}}}\right)=\ln\left(\frac{\frac{\Omega^2}{\varepsilon^2}}{1+\frac{\Omega^2}{\varepsilon^2}-1-\frac{1}{2}\left(\frac{\Omega}{\varepsilon}\right)^2+\frac{1}{8}\left(\frac{\Omega}{\varepsilon}\right)^4-\frac{1}{16}\left(\frac{\Omega}{\varepsilon}\right)^6+\frac{5}{128}\left(\frac{\Omega}{\varepsilon}\right)^8}\right)\\
&\ln 2-\ln\left(1+\frac{1}{4}\left(\frac{\Omega}{\varepsilon}\right)^2-\frac{1}{8}\left(\frac{\Omega}{\varepsilon}\right)^4+\frac{5}{64}\left(\frac{\Omega}{\varepsilon}\right)^6+\ldots\right)\\
&\approx\ln 2-\sum_{n=1}^{\infty}(-1)^{n+1}\frac{1}{n}\left(\frac{1}{4}\left(\frac{\Omega}{\varepsilon}\right)^2\right)^n\left(1-\frac{1}{2}\left(\frac{\Omega}{\varepsilon}\right)^2+\frac{5}{16}\left(\frac{\Omega}{\varepsilon}\right)^4+\ldots\right)^n\\
&=-\frac{1}{4}\frac{d}{dt}\left\{\left(\frac{\Omega}{\varepsilon}\right)^2-\frac{5}{8}\left(\frac{\Omega}{\varepsilon}\right)^4+\frac{11}{24}\left(\frac{\Omega}{\varepsilon}\right)^6+\ldots\right\}.
\end{aligned} \tag{4.66}$$

Therefore, the leading order is $\left(\frac{\Omega}{\varepsilon}\right)^2$ and this term will be neglected later. Thus, we have

$$\begin{aligned}
&\hat{W}^{\dagger}(t,t')=\\
&\frac{1}{2}\begin{bmatrix}\left(1-\frac{\varepsilon}{\lambda}\right)(-\hat{D}+\hat{D}_0) & -\left\{\left(\frac{\Omega}{\lambda}\hat{D}_+^2\right)'-\left(\frac{\Omega}{\lambda}\hat{D}_+^2\right)\left(\frac{\dot{\varepsilon}\lambda-\dot{\lambda}\varepsilon}{\lambda(\lambda+\varepsilon)}\right)\right\}e^{-i\int_{t'}^{t}\lambda d\tau}\\ \left\{\left(\frac{\Omega}{\lambda}\hat{D}_-^2\right)'-\left(\frac{\Omega}{\lambda}\hat{D}_-^2\right)\left(\frac{\dot{\varepsilon}\lambda-\dot{\lambda}\varepsilon}{\lambda(\lambda+\varepsilon)}\right)\right\}e^{i\int_{t'}^{t}\lambda d\tau} & \left(1-\frac{\varepsilon}{\lambda}\right)(\hat{D}+\hat{D}_0)\end{bmatrix}\\
&=\begin{bmatrix}-i\hat{w}_1+i\hat{w}_0 & i\hat{w}_{12}\\ -i\hat{w}_{12}^{+} & i\hat{w}_1+i\hat{w}_0\end{bmatrix}.
\end{aligned}$$

Calculating matrix $\hat{U}$ elements

Next step is to calculate matrix $\hat{U}^{\dagger}(t)$. We have

$$\hat{U}^{\dagger}(t)=\int_{-\infty}^{t}\hat{W}^{\dagger}(t,t')dt'=\frac{1}{2}\times$$
$$\begin{bmatrix} \int_{-\infty}^{t}\left(1-\frac{\varepsilon}{\lambda}\right)(-\hat{D}+\hat{D}_0)dt' & -\int_{-\infty}^{t}\left\{\left(\frac{\Omega}{\lambda}\hat{D}_{+}^{2}\right)'-\left(\frac{\Omega}{\lambda}\hat{D}_{+}^{2}\right)\left(\frac{\dot{\varepsilon}\lambda-\dot{\lambda}\varepsilon}{\lambda(\lambda+\varepsilon)}\right)\right\}e^{-i\int_{t'}^{t}\lambda d\tau}dt' \\ \int_{-\infty}^{t}\left\{\left(\frac{\Omega}{\lambda}\hat{D}_{-}^{2}\right)'-\left(\frac{\Omega}{\lambda}\hat{D}_{-}^{2}\right)\left(\frac{\dot{\varepsilon}\lambda-\dot{\lambda}\varepsilon}{\lambda(\lambda+\varepsilon)}\right)\right\}e^{i\int_{t'}^{t}\lambda d\tau}dt' & \int_{-\infty}^{t}\left(1-\frac{\varepsilon}{\lambda}\right)(\hat{D}+\hat{D}_0)dt' \end{bmatrix}$$
$$=\begin{bmatrix} -\hat{u}_1+\hat{u}_0 & \hat{u}_{12} \\ -\hat{u}_{12}^{+} & \hat{u}_1+\hat{u}_0 \end{bmatrix}. \tag{4.67}$$

Where we have

$$\begin{aligned}\hat{u}_{12}^{\dagger}(t)&=-\frac{1}{2}\int_{-\infty}^{t}dt'\left\{\left(\frac{\Omega}{\lambda}\hat{\mathrm{D}}_{-}^{2}\right)'-\frac{\Omega}{\lambda}\hat{\mathrm{D}}_{-}^{2}\left(\frac{\dot{\varepsilon}\lambda-\dot{\lambda}\varepsilon}{\lambda(\lambda+\varepsilon)}\right)\right\}e^{i\int_{t'}^{t}\lambda d\tau}\\&\approx-\frac{1}{2}\int_{-\infty}^{t}\left(\frac{\Omega}{\lambda}\hat{\mathrm{D}}_{-}^{2}\right)'e^{i\int_{t'}^{t}\lambda d\tau}dt'=-\frac{\Omega}{2\lambda}\hat{D}_{-}^{2}+\hat{\mathfrak{u}}^{\dagger}(t),\end{aligned} \tag{4.68a}$$

$$\hat{\mathfrak{u}}^{\dagger}(t)=-\frac{i}{2}\int_{-\infty}^{t}\Omega e^{i\int_{t'}^{t}\lambda d\tau}\hat{D}_{-}^{2}(t')dt'. \tag{4.68b}$$

On the other hand, $\hat{u}_{12}^{\dagger}(t,t')$ is

$$\begin{aligned}\hat{u}_{12}^{\dagger}(t,t')&=-\frac{1}{2}\int_{-\infty}^{t'}dt''\left\{\left(\frac{\Omega}{\lambda}\hat{D}_{-}^{2}\right)'-\frac{\Omega}{\lambda}\hat{D}_{-}^{2}\left(\frac{\dot{\varepsilon}\lambda-\dot{\lambda}\varepsilon}{\lambda(\lambda+\varepsilon)}\right)\right\}e^{i\int_{t''}^{t}\lambda d\tau}\\&\approx-\frac{1}{2}\int_{-\infty}^{t'}\left(\frac{\Omega}{\lambda}\hat{D}_{-}^{2}\right)'e^{i\int_{t''}^{t}\lambda d\tau}dt''=-\frac{\Omega}{2\lambda}\hat{D}_{-}^{2}e^{i\int_{t'}^{t}\lambda d\tau}+\hat{\mathfrak{u}}^{\dagger}(t,t'),\end{aligned} \tag{4.69a}$$

$$\hat{\mathfrak{u}}^{\dagger}(t,t')=-\frac{i}{2}\int_{-\infty}^{t'}\Omega e^{i\int_{t''}^{t}\lambda d\tau}\hat{D}_{-}^{2}(t'')dt''. \tag{4.69b}$$

The same can be done for $\hat{u}_{12}(t)$ and $\hat{u}_{12}(t,t')$ we have

$$\hat{u}_{12}(t)=-\frac{\Omega}{2\lambda}\hat{D}_{+}^{2}+\hat{\mathfrak{u}}(t), \tag{4.70a}$$

$$\hat{\mathfrak{u}}(t) = \frac{i}{2}\int_{-\infty}^{t} \Omega e^{-i\int_{t'}^{t}\lambda d\tau}\hat{D}_{+}^{2}(t')dt', \tag{4.70b}$$

$$\hat{u}_{12}(t,t') = -\frac{\Omega}{2\lambda}\hat{D}_{+}^{2}e^{-i\int_{t'}^{t}\lambda d\tau} + \hat{\mathfrak{u}}(t,t'), \tag{4.71a}$$

$$\hat{\mathfrak{u}}(t,t') = \frac{i}{2}\int_{-\infty}^{t'} \Omega e^{-i\int_{t''}^{t}\lambda d\tau}\hat{D}_{+}^{2}(t'')dt''. \tag{4.71b}$$

Starting again from Eqs. (4.45), (4.46) and substituting for $\hat{U}^{+}(t) = \int_{-\infty}^{t}\hat{W}^{\dagger}(t,t')dt'$ and $\hat{U}(t) = \int_{-\infty}^{t}\hat{W}(t,t')dt'$ we find

$$\begin{aligned}\hat{\tilde{\rho}}(t) = \hat{\tilde{\rho}}_0 + \hat{U}(t)\hat{\tilde{\rho}}_0 + \int_{-\infty}^{t}\hat{W}(t,t')dt'\int_{-\infty}^{t'}\hat{W}(t,t'')dt''\hat{\tilde{\rho}}_0 + \hat{\tilde{\rho}}_0\hat{U}^{\dagger}(t)\\ + \hat{\tilde{\rho}}_0\int_{-\infty}^{t}\left(\int_{-\infty}^{t'}\hat{W}^{\dagger}(t,t'')dt''\right)\hat{W}^{\dagger}(t,t')dt' + \hat{U}(t)\hat{\tilde{\rho}}_0\hat{U}^{\dagger}(t).\end{aligned} \tag{4.72}$$

Rewriting it yields

$$\begin{aligned}&\hat{\tilde{\rho}}(t) = \hat{\tilde{\rho}}_0 + \hat{\tilde{\rho}}_1 + \hat{\tilde{\rho}}_2 = \hat{\tilde{\rho}}_0 + \left\{\hat{U}(t)\hat{\tilde{\rho}}_0 + \hat{\tilde{\rho}}_0\hat{U}^{\dagger}(t)\right\} +\\ &\left\{\int_{-\infty}^{t}\hat{W}(t,t')dt'\int_{-\infty}^{t'}\hat{W}(t,t'')dt''\hat{\tilde{\rho}}_0 + \hat{\tilde{\rho}}_0\int_{-\infty}^{t}\left(\int_{-\infty}^{t'}\hat{W}^{\dagger}(t,t'')dt''\right)\hat{W}^{\dagger}(t,t')dt' + \hat{U}(t)\hat{\tilde{\rho}}_0\hat{U}^{\dagger}(t)\right\}.\end{aligned} \tag{4.73}$$

By doing the matrices multiplication, we get for different orders

$$\hat{\tilde{\rho}}_0(t) = \begin{bmatrix} 0 & 0 \\ 0 & \hat{B} \end{bmatrix}, \tag{4.74}$$

$$\hat{\tilde{\rho}}_1(t) = -\begin{bmatrix} 0 & \hat{u}_{12}\hat{B} \\ \hat{B}\hat{u}_{12}^{\dagger} & \left[\hat{u}_1, \hat{B}\right] \end{bmatrix}, \tag{4.75}$$

$$\hat{\tilde{\rho}}_2(t) = \begin{bmatrix} \hat{u}_{12}\hat{B}\hat{u}_{12}^{\dagger} & \\ \\ \hat{u}_{12}^{\dagger}\left[\hat{u}_1, \hat{B}\right] + \int_{-\infty}^{t} dt' \left\{\hat{u}_{12}(t,t')\hat{w}_1(t') + \hat{w}_1(t')\hat{u}_{12}(t,t')\right\}\hat{B} & \end{bmatrix}$$

$$\begin{bmatrix} \hat{u}_{12}\left[\hat{u}_1, \hat{B}\right] - \int_{-\infty}^{t} dt' \hat{u}_{12}(t,t')\hat{w}_1(t')\hat{B} + \int_{-\infty}^{t} \hat{w}_1(t')\hat{u}_{12}(t,t')\hat{B} \\ \\ -\int_{-\infty}^{t} dt' \hat{w}_{12}^{\dagger}(t,t')\hat{u}_{12}(t,t')\hat{B} + \hat{B}\int_{-\infty}^{t} dt' \hat{u}_{12}^{\dagger}(t,t')\hat{w}_{12}(t,t') - \hat{u}_1\hat{B}\hat{u}_1 \\ + \int_{-\infty}^{t} dt' \hat{w}_1(t')\hat{u}_1(t')\hat{B} + \hat{B}\int_{-\infty}^{t} dt' \hat{u}_1(t')\hat{w}_1(t') \end{bmatrix}. \tag{4.76}$$

Now, we have the zeroth, first and second order contributions. What remains is tracing out the heat bath degrees of freedom.

Slow and fast bath

In calculating matrix $\hat{W}$ and $\hat{U}$, we had terms which came from the derivatives of the displacement operator $\hat{D}_{\pm}^2$. These terms in the limits of adiabatic approximation with regards to noise terms can be considered to be zero. Therefore, terms such as $\hat{u}_1$ and $\hat{w}_1$ are zero in this thesis.

4.2.4 Ionization, intraband, and interband currents

We are in the polaron frame, and we know that the transformation between these two frames are given by a unitary transformation $\hat{U}_P, \hat{U}_P^{\dagger}$, Eqs. 4.6. We have

$$\hat{H}_{polaron} = \hat{U}_P \hat{H}_{original} \hat{U}_P^{\dagger} \tag{4.77}$$

$$\hat{\rho}_{polaron} = \hat{U}_P \hat{\rho}_{original} \hat{U}_P^{\dagger} \tag{4.78}$$

We have

$$\mathrm{tr}_{bath}\{\hat{\rho}_{polaron}\hat{j}_{polaron}\} = \mathrm{tr}_{bath}\{\hat{U}_P\hat{\rho}_{original}\hat{U}_P^{\dagger}\hat{U}_P\hat{j}_{original}\hat{U}_P^{\dagger}\} = \mathrm{tr}_{bath}\{\hat{\rho}_{original}\hat{j}_{original}\}, \tag{4.79}$$

where we have used the fact that $\hat{U}^\dagger \hat{U} = \mathbb{1}$ and also used the cyclic properties of the trace. We know that j in the original frame is given by

$$\hat{j} = \begin{bmatrix} j_{11} & j_{12} \\ j_{21} & j_{22} \end{bmatrix} = \frac{1}{2}\left(j_{11} - j_{22}\right)\hat{\sigma}_z + \frac{1}{2}\left(j_{11} + j_{22}\right)\mathbb{1} + \mathrm{Re}(j_{12})\hat{\sigma}_x - \cancel{\mathrm{Im}(j_{12})\hat{\sigma}_y} \tag{4.80}$$

Now, we transform $\hat{j}$ to the polaron frame. We know that

$$\begin{aligned} \hat{U}\hat{\sigma}_z\hat{U}^+ &= \hat{\sigma}_z \\ \hat{U}\mathbb{1}\hat{U}^+ &= \mathbb{1} \\ \hat{U}\hat{\sigma}_x\hat{U}^\dagger &= \hat{\sigma}_+\hat{D}_+^2 + \hat{\sigma}_-\hat{D}_-^2 \end{aligned} \tag{4.81}$$

. Therefore, $\hat{j}$ in the polaron frame would be

$$\hat{j}_{polaron} = \begin{bmatrix} j_{11} & j_{12}\hat{D}_+^2 \\ j_{21}\hat{D}_-^2 & j_{22} \end{bmatrix} \tag{4.82}$$

We need

$$\begin{aligned} \langle \hat{\rho}_{polaron}\hat{j}_{polaron}\rangle = \cancel{\mathrm{tr}_{bath}\{\mathbb{1}j_{11}\}} + \mathrm{tr}_{bath}\{\rho_{ee}\}\left(j_{11} - j_{22}\right) + \\ \mathrm{tr}_{bath}\{\rho_{eg}j_{21}\hat{D}_-^2 + \rho_{ge}j_{12}\hat{D}_+^2\}, \end{aligned} \tag{4.83}$$

where we can call the first term intraband contribution and the second term would be the interband contribution. The density matrix part consists of three different orders; therefore, for each order we have (Note that the next equations are written for the case of solids)

$$\langle \mathbf{j}_{er}\rangle \approx \frac{d}{dt}\int_{\overline{\mathrm{BZ}}} d^3K\, \mathbf{d}(\mathbf{K}_t)\,\rho_{eg}(\mathbf{K},t)\hat{D}_-^2 + \mathrm{c.c.}, \tag{4.84}$$

$$\langle \mathbf{j}_{ra}\rangle \approx \int_{\overline{\mathrm{BZ}}} d^3K\, \mathbf{v}(\mathbf{K}_t)n_c(\mathbf{K},t). \tag{4.85}$$

ρ_{eg} is the off diagonal matrix element for e meaning excited state, and g meaning ground state. In the following, we calculated the zeroth, first, and second order contributions.

Zeroth order SFAF contribution with noise

Neglecting the last two terms in Eq. (4.25) we reach

$$\hat{\rho}(t=-\infty)=\begin{bmatrix}0&0\\0&1\end{bmatrix}\bigotimes\hat{B}, \tag{4.86}$$

which shows that the population is in the ground state, and bath and system are uncorrelated in the polaron frame at the beginning since the interaction part of Hamiltonian goes to zero at the begining due to dependability to Ω. $\hat{B}$ is the Gibbs state. Finding the time dependent $\hat{\tilde{\rho}}(t)$ we get for the zeroth order

$$\hat{\tilde{\rho}}(t)=\begin{bmatrix}e^{-\frac{i}{2}\int_{-\infty}^{t}dt'\lambda(t')}&0\\0&e^{\frac{i}{2}\int_{-\infty}^{t}dt'\lambda(t')}\end{bmatrix}\begin{bmatrix}0&0\\0&\hat{B}\end{bmatrix}\begin{bmatrix}e^{\frac{i}{2}\int_{-\infty}^{t}dt'\lambda(t')}&0\\0&e^{-\frac{i}{2}\int_{-\infty}^{t}dt'\lambda(t')}\end{bmatrix}=\begin{bmatrix}0&0\\0&\hat{B}\end{bmatrix}. \tag{4.87}$$

Now, we need to transform back to the $\hat{\rho}_0(t)$ by using matrices $\hat{V}$ and $\hat{V}^\dagger$ we have

$$V(t)=\frac{1}{\sqrt{2}}\begin{bmatrix}a_{11}&-a_{12}\hat{D}_+^2\\a_{12}\hat{D}_-^2&a_{11}\end{bmatrix}, \tag{4.88}$$

$$\hat{V}^\dagger(t)=\frac{1}{\sqrt{2}}\begin{bmatrix}a_{11}&a_{12}\hat{D}_+^2\\-a_{12}\hat{D}_-^2&a_{11}\end{bmatrix}, \tag{4.89}$$

where $a_{11}=\frac{\sqrt{\lambda+\epsilon}}{\sqrt{\lambda}}$,and $a_{12}=\frac{\Omega}{\sqrt{\lambda}\sqrt{\lambda+\epsilon}}$ and we have $a_{11}^2=\frac{\lambda+\epsilon}{\lambda}$, $a_{12}^2=\frac{\lambda-\epsilon}{\lambda}$, $a_{11}a_{12}=\frac{\Omega}{\lambda}$; therefore, we get for $\hat{\rho}_0$

$$\hat{\rho}_0(t)=\hat{V}\hat{\tilde{\rho}}_0(t)\hat{V}^\dagger=\frac{1}{2}\begin{bmatrix}\frac{\lambda-\epsilon}{\lambda}\hat{D}_+^2\hat{B}\hat{D}_-^2&-\frac{\Omega}{\lambda}\hat{D}_+^2\hat{B}\\-\frac{\Omega}{\lambda}\hat{B}\hat{D}_-^2&\frac{\lambda+\epsilon}{\lambda}\hat{B}\end{bmatrix}. \tag{4.90}$$

The next step is tracing over the heat bath

$$\mathrm{tr}_{bath}\left\{\hat{\rho}_0(t)\right\}=\frac{1}{2}\begin{bmatrix}\frac{\lambda-\epsilon}{\lambda}\mathrm{tr}_{bath}\left\{\hat{D}_+^2\hat{B}\hat{D}_-^2\right\}&-\frac{\Omega}{\lambda}\mathrm{tr}_{bath}\left\{\hat{D}_+^2\hat{B}\right\}\\-\frac{\Omega}{\lambda}\mathrm{tr}_{bath}\left\{\hat{B}\hat{D}_-^2\right\}&\frac{\lambda+\epsilon}{\lambda}\mathrm{tr}_{bath}\{B\}\end{bmatrix}. \tag{4.91}$$

We need to calculate $\mathrm{tr}_{bath}\left\{\hat{B}\right\}$ and $\mathrm{tr}_{bath}\left\{\hat{D}_{+}^{2}\hat{B}\right\}$

$$\mathrm{tr}_{bath}\left\{\hat{B}\right\}=\mathrm{tr}_{bath}\left\{\frac{e^{-\hat{H}_0\beta}}{\mathrm{tr}_{bath}\left\{e^{-\hat{H}_0\beta}\right\}}\right\}=1, \tag{4.92}$$

$$\mathrm{tr}_{bath}\left\{\hat{D}_{+}^{2}\hat{B}\right\}=\frac{1}{\mathrm{tr}_{bath}\left\{e^{-\beta\sum_q\omega_q\left(\hat{b}_q^{+}\hat{b}_q+\frac{1}{2}\right)}\right\}}\mathrm{tr}_{bath}\left\{e^{2\sum_{q=q_1}^{q_n}\frac{g_q}{\omega_q}\left(\hat{b}_q^{+}(t)-\hat{b}_q(t)\right)}e^{-\beta\sum_{q=q_1}^{q_n}\omega_q\left(\hat{b}_q^{+}\hat{b}_q+\frac{1}{2}\right)}\right\}. \tag{4.93}$$

The partition function (denominator of the above equation) is

$$\begin{aligned}z&=\mathrm{tr}_{bath}\left\{e^{-\beta\sum_q\omega_q\left(\hat{b}_q^{+}\hat{b}_q+\frac{1}{2}\right)}\right\}=\prod_{q=q_1}^{q_n}\sum_{n_q=0}^{\infty}\left\langle n_q\right|e^{-\beta\sum_q\omega_q\left(\hat{b}_q^{\dagger}\hat{b}_q+\frac{1}{2}\right)}\left|n_q\right\rangle=\prod_{q=q_1}^{q_n}\frac{e^{-\beta\omega_q}}{1-e^{-\beta\omega_q}}\\&=\prod_{q=q_1}^{q_n}\frac{\sqrt{z_g}}{1-z_g}.\end{aligned} \tag{4.94}$$

Therefore, we obtain

$$\begin{aligned}\mathrm{tr}_{bath}\left\{\hat{D}_{+}^{2}\hat{B}\right\}&=\frac{\mathrm{tr}_{bath}\left\{\mathrm{e}^{\sum_{\mathrm{q}}\frac{2\mathrm{g_q}}{\omega_{\mathrm{q}}}\left(\hat{\mathrm{b}}_{\mathrm{q}}^{\dagger}(\mathrm{t})-\hat{\mathrm{b}}_{\mathrm{q}}(\mathrm{t})\right)}\mathrm{e}^{-\beta\sum_{\mathrm{q=q_1}}^{\mathrm{q_n}}\omega_{\mathrm{q}}\left(\hat{\mathrm{b}}_{\mathrm{q}}^{\dagger}\hat{\mathrm{b}}_{\mathrm{q}}+\frac{1}{2}\right)}\right\}}{\mathrm{tr}_{bath}\left\{e^{-\beta\sum_q\omega_q\left(\hat{b}_q^{\dagger}\hat{b}_q+\frac{1}{2}\right)}\right\}}\\&=\frac{\prod_q e^{-\frac{1}{2}|\alpha_q|^2}\sum_{n_q=0}^{\infty}e^{-\beta\left(\hat{n}_q+\frac{1}{2}\right)\omega_q}\left\langle n_q\right|e^{\alpha_q^{*}\hat{b}_q^{\dagger}-\alpha_q\hat{b}_q}\left|n_q\right\rangle}{\mathrm{tr}_{bath}\left\{e^{-\beta\sum_q\omega_q\left(\hat{b}_q^{\dagger}\hat{b}_q+\frac{1}{2}\right)}\right\}}\\&=\frac{\prod_q e^{-\frac{1}{2}|\alpha_q|^2}\sum_{n_q=0}^{\infty}e^{-\beta\left(n_q+\frac{1}{2}\right)\omega_q}\mathrm{L}_{\mathrm{n_q}}\left(\left|\alpha_{\mathrm{q}}\right|^2\right)}{\mathrm{tr}_{bath}\left\{e^{-\beta\sum_q\omega_q\left(\hat{b}_q^{\dagger}\hat{b}_q+\frac{1}{2}\right)}\right\}},\end{aligned} \tag{4.95}$$

where we have used the relation $L_{n_q}=\left\langle n_q\right|e^{\alpha_q^{*}b_q^{+}-\alpha_q b_q}\left|n_q\right\rangle$. L_{n_q} is the Laguerre function. Now, substituting from z_q we get

$$\mathrm{tr}_{bath}\left\{\hat{D}_{+}^{2}\hat{B}\right\}=\prod_q\frac{1-z_q}{\sqrt{z_q}}e^{-\frac{1}{2}|\alpha_q|^2}\sum_{n_q=0}^{\infty}L_{n_q}\left(\left|\alpha_q\right|^2\right)z_q^{n_q}\sqrt{z_q}. \tag{4.96}$$

Using the formula

$$\sum_{n=0}^{\infty} z^n \mathrm{L}_{\mathrm{n}}^{\alpha}(x) = \frac{1}{(1-z)^{\alpha+1}} e^{-\frac{zx}{1-z}}, \tag{4.97}$$

doing some simplification and substituting for $z_q = e^{-\beta\omega_q}$, we get

$$\mathrm{tr}_{bath}\left\{\hat{D}_+^2\hat{B}\right\} = \prod_q e^{-\frac{1}{2}|\alpha_q|^2 \frac{1+z_q}{1-z_q}} = \prod_q e^{-\frac{1}{2}|\alpha_q|^2 \coth\frac{\beta\omega_q}{2}}. \tag{4.98}$$

We have

$$\prod_q e^{-\frac{1}{2}|\alpha_q|^2 \coth\frac{\beta\omega_q}{2}} \Longrightarrow e^{-C_0/2}. \tag{4.99}$$

We know that

$$\mathrm{tr}_{bath}\left\{\hat{D}_+^2\hat{B}\right\} = \left\{\mathrm{tr}_{bath}\left\{\hat{B}\hat{D}_-^2\right\}\right\}^*. \tag{4.100}$$

Therefore

$$\mathrm{tr}_{bath}\left\{\hat{\rho}_0(t)\right\} = \frac{1}{2}\begin{bmatrix} \frac{\lambda-\varepsilon}{\lambda} & -\frac{\Omega}{\lambda}e^{-C_0/2} \\ -\frac{\Omega}{\lambda}e^{-C_0/2} & \frac{\lambda+\varepsilon}{\lambda} \end{bmatrix} \tag{4.101}$$

We see that the zeroth order contains only virtual population transfer to the excited state, and it goes to zero after the laser pulse. For the off-diagonals we start with

$$(1+x)^{\frac{-1}{2}} = 1 - \frac{1}{2}x + \frac{3}{8}x^2 - \frac{5}{16}x^3 + ... \tag{4.102}$$

Therefore, we have

$$\begin{aligned} \frac{\Omega}{\lambda} &= \frac{\frac{\Omega}{\varepsilon}}{\sqrt{1+\frac{\Omega^2}{\varepsilon^2}}} = \frac{\Omega}{\varepsilon}\left(1 - \frac{1}{2}\left(\frac{\Omega}{\varepsilon}\right)^2 + \frac{3}{8}\left(\frac{\Omega}{\varepsilon}\right)^4 - ...\right) \\ &= \frac{\Omega}{\varepsilon} - \frac{1}{2}\left(\frac{\Omega}{\varepsilon}\right)^3 + \frac{3}{8}\left(\frac{\Omega}{\varepsilon}\right)^5 - \cdots, \end{aligned} \tag{4.103}$$

where they can be used to calculate $\chi^{(3)}$ and higher order terms. Note that the density matrix calculated here is in the polaron frame. What we are interested in is the ionization which is given by the first element of density matrix either in polaron or original frame since both are the same. For the polarization or calculation of the interband currents we

need to use the matrix

$$\hat{\rho_0}(t) = \begin{bmatrix} \rho_{ee} & \rho_{eg}\hat{D}_-^2 \\ \rho_{ge}\hat{D}_+^2 & \rho_{gg} \end{bmatrix} \tag{4.104}$$

After tracing out the bath degrees of freedom and considering $\Omega/\varepsilon << 1$ we have

$$\hat{\rho}_0(t) = \begin{bmatrix} 0 & 0 \\ 0 & 1 \end{bmatrix} \tag{4.105}$$

First order SFAF contribution with noise

According to Eq. (4.46), the first order noise contribution would be $\hat{\tilde{\rho}}_1(t) = \hat{U}(t)\hat{\tilde{\rho}}_0(t) + \hat{\tilde{\rho}}_0(t)\hat{U}^\dagger$where

$$\hat{\tilde{\rho}}_0(t) = \begin{bmatrix} 0 & 0 \\ 0 & \hat{B} \end{bmatrix}, \tag{4.106}$$

we get

$$\hat{\tilde{\rho}}_1(t) = \hat{\tilde{\rho}}_{1S}(t) + \hat{\tilde{\rho}}_{1F}(t) = -\begin{bmatrix} 0 & \hat{u}_{12}\hat{B} \\ \hat{B}\hat{u}_{12}^\dagger & 0 \end{bmatrix} - \begin{bmatrix} 0 & 0 \\ 0 & [\hat{u}_1, \hat{B}] \end{bmatrix}. \tag{4.107}$$

Since we are in adiabatic approximation, where ω_0 is much smaller than the band gap, we can neglect the derivatives of displacement operators. These derivatives show themselves in the second term of the RHS of the Eq. (4.107). Now, we need to transform back to the $\hat{\rho}_1(t)$ by using matrices $\hat{V}$and $\hat{V}^\dagger$. The first part would be

$$\hat{\rho}_{1S}(t) = \frac{1}{2}\begin{bmatrix} \frac{\Omega}{\lambda}\left\{\hat{D}_+^2\hat{B}\hat{u}_{12}^\dagger + \hat{u}_{12}\dagger B\hat{D}_-^2\right\} & \frac{\lambda-\varepsilon}{\lambda}\hat{D}_+^2\hat{B}\hat{u}_{12}^\dagger\hat{D}_+^2 - \frac{\lambda+\varepsilon}{\lambda}\hat{u}_{12}\hat{B} \\ \frac{\lambda-\varepsilon}{\lambda}\hat{D}_-^2\hat{u}_{12}\hat{B}\hat{D}_-^2 - \frac{\lambda+\varepsilon}{\lambda}\hat{B}\hat{u}_{12}^+ & -\frac{\Omega}{\lambda}\left\{\hat{B}\hat{u}_{12}^\dagger\hat{D}_+^2 + \hat{D}_-^2\hat{u}_{12}\hat{B}\right\} \end{bmatrix}, \tag{4.108}$$

and the second part is

$$\hat{\rho}_{1F}(t) = -\frac{1}{2}\begin{bmatrix} \frac{\lambda-\varepsilon}{\lambda}\hat{D}_+^2[\hat{u}_1, \hat{B}]\hat{D}_-^2 & -\frac{\Omega}{\lambda}\hat{D}_+^2[\hat{u}_1, \hat{B}] \\ -\frac{\Omega}{\lambda}[\hat{u}_1, \hat{B}]\hat{D}_-^2 & \frac{\lambda+\varepsilon}{\lambda}[\hat{u}_1, \hat{B}] \end{bmatrix}. \tag{4.109}$$

We can split $\hat{\tilde{\rho}}_{1S}$ into two parts, the integral and non integral parts $\hat{\tilde{\rho}}_{1S} = \hat{\tilde{\rho}}'_{1S} + \hat{\tilde{\rho}}''_{1S}$. It yields

$$\hat{\tilde{\rho}}'_{1S} = \frac{1}{2}\begin{bmatrix} -\left(\frac{\Omega}{\lambda}\right)^2 & -\frac{\Omega\varepsilon}{\lambda^2} \\ -\frac{\Omega\varepsilon}{\lambda^2} & \left(\frac{\Omega}{\lambda}\right)^2 \end{bmatrix}, \tag{4.110}$$

$$\hat{\tilde{\rho}}''_{1S} = \frac{1}{2}\begin{bmatrix} \frac{\Omega}{\lambda}\mathrm{tr}_{bath}\left\{\hat{D}^2_{\dagger}\hat{B}\hat{\mathfrak{u}}^{\dagger} + h.c.\right\} & -\frac{\lambda+\varepsilon}{\lambda}\mathrm{tr}_{bath}\left\{\hat{\mathfrak{u}}\hat{B}\hat{D}^2_{-}\right\} + \frac{\lambda-\varepsilon}{\lambda}\mathrm{tr}_{bath}\left\{\hat{D}^2_{+}\hat{B}\hat{\mathfrak{u}}^{+}\right\} \\ -\frac{\lambda+\varepsilon}{\lambda}\mathrm{tr}_{bath}\left\{\hat{B}\hat{\mathfrak{u}}^{\dagger}\hat{D}^2_{+}\right\} + \frac{\lambda-\varepsilon}{\lambda}\mathrm{tr}_{bath}\left\{\hat{D}^2_{-}\hat{\mathfrak{u}}\hat{B}\right\} & -\frac{\Omega}{\lambda}\mathrm{tr}_{bath}\left\{\hat{D}^2_{+}\hat{B}\hat{\mathfrak{u}}^{\dagger} + h.c.\right\} \end{bmatrix}. \tag{4.111}$$

Now, the only step that remains is tracing over the heat bath degrees of freedom. We need to calculate $\mathrm{tr}_{bath}\left\{\hat{\mathfrak{u}}\hat{B}\hat{D}^2_{-}\right\}$, and its complex conjugate, $\mathrm{tr}_{bath}\left\{\hat{D}^2_{+}\hat{B}\hat{\mathfrak{u}}^{\dagger} + h.c.\right\}$.
Using the BCH formula for the displacement operator, we get

$$\hat{D}(\alpha)\,\hat{D}(\beta) = \hat{D}(\alpha+\beta)\,e^{\frac{1}{2}(\alpha\beta^* - \alpha^*\beta)}, \tag{4.112}$$

and using the fact that $\hat{\mathrm{D}}^2_{-}(\alpha) = \hat{\mathrm{D}}^2_{+}(-\alpha)$, in our case we have $\alpha \to \alpha e^{i\omega t}$.

Now, for calculating the diagonals, we have

$$\begin{aligned} \mathrm{tr}_{bath}\left\{\hat{D}^2_{+}\hat{B}\hat{u}^{\dagger}\right\} &= -i\int_{-\infty}^{t} dt'\Omega e^{i\int_{t'}^{t}\lambda d\tau}\mathrm{tr}_{bath}\left[\hat{D}^2_{+}(t)\hat{B}\hat{D}^2_{-}(t')\right] \\ &= -i\int_{-\infty}^{t} dt'\Omega e^{i\int_{t'}^{t}\lambda d\tau}\mathrm{tr}_{bath}\left[\hat{D}^2_{-}(t')\hat{D}^2_{+}(t)\hat{B}\right]. \end{aligned} \tag{4.113}$$

Where we also know that

$$\hat{D}^2_{-}(t')\hat{D}^2_{+}(t) = \prod_q \hat{D}^2_{+q}\left(-\alpha_q e^{i\omega_q t'} + \alpha_q e^{i\omega_q t}\right) e^{i\sum_q |\alpha_q|^2 \sin(\omega_q t)}, \tag{4.114}$$

and

$$\frac{\left|-\alpha_q e^{i\omega_q t'} + \alpha_q e^{i\omega_q t}\right|^2}{2} = \frac{2|\alpha_q|^2 - 2\cos\omega_q(t-t')}{2}. \tag{4.115}$$

Therefore, we obtain

$$\mathrm{tr}_{bath}\left\{\hat{D}_-^2(t')\hat{D}_+^2(t)\hat{B}\right\} = e^{-C_0}e^{iC_i(t-t')}e^{C_\beta(t-t')}, \tag{4.116}$$

$$\mathrm{tr}_{bath}\left\{\hat{D}_+^2\hat{B}\hat{u}^\dagger\right\} = -\frac{i}{2}e^{-C_0}\int_{-\infty}^{t} dt'\Omega e^{i\int_{t'}^{t}\lambda d\tau}e^{iC_i(t-t')}e^{C_\beta(t-t')}, \tag{4.117}$$

$$\mathrm{tr}_{bath}\left\{\hat{D}_+^2\hat{B}\hat{u}^\dagger + h.c.\right\} = e^{-C_0}\int_{-\infty}^{t} dt'\Omega e^{C_\beta(t-t')}\mathrm{Im}\left\{e^{i\int_{t'}^{t}\lambda d\tau}e^{iC_i(t-t')}\right\}. \tag{4.118}$$

Substituting all terms we get for the intergral parts

$$\begin{aligned}\hat{\tilde{\rho}}''_{1S} &= \frac{1}{2}\begin{bmatrix} \frac{\Omega}{\lambda}\mathrm{tr}_{bath}\left\{\hat{D}_+^2\hat{B}\hat{u}^\dagger + h.c.\right\} & -\frac{\lambda+\varepsilon}{\lambda}\mathrm{tr}_{bath}\left\{\hat{u}\hat{B}\hat{D}_-^2\right\} + \frac{\lambda-\varepsilon}{\lambda}\mathrm{tr}_{bath}\left\{\hat{D}_+^2\hat{B}\hat{u}^\dagger\right\} \\ -\frac{\lambda+\varepsilon}{\lambda}\mathrm{tr}_{bath}\left\{\hat{B}\hat{u}^\dagger\hat{D}_+^2\right\} + \frac{\lambda-\varepsilon}{\lambda}\mathrm{tr}_{bath}\left\{\hat{D}_-^2\hat{u}\hat{B}\right\} & -\frac{\Omega}{\lambda}\mathrm{tr}_{bath}\left\{\hat{D}_+^2\hat{B}\hat{u}^\dagger + h.c.\right\} \end{bmatrix} \\ &= \frac{1}{4}\begin{bmatrix} \frac{2\Omega}{\lambda}e^{-C_0}\int_{-\infty}^{t} dt'\Omega e^{C_\beta(t-t')}\mathrm{Im}\left\{e^{i\int_{t'}^{t}\lambda d\tau}e^{iC_i(t-t')}\right\} & -2i\mathrm{Im}\theta - 2\frac{\varepsilon}{\lambda}\mathrm{Re}\theta \\ 2i\mathrm{Im}\theta - 2\frac{\varepsilon}{\lambda}\mathrm{Re}\theta & -\frac{2\Omega}{\lambda}e^{-C_0}\int_{-\infty}^{t} dt'\Omega e^{C_\beta(t-t')}\mathrm{Im}\left\{e^{i\int_{t'}^{t}\lambda d\tau}e^{iC_i(t-t')}\right\} \end{bmatrix},\end{aligned} \tag{4.119}$$

where θ is

$$\theta = ie^{-C_0}\int_{-\infty}^{t} dt'\Omega e^{-i\int_{t'}^{t}\lambda d\tau}e^{-iC_i(t-t')}e^{C_\beta(t-t')}. \tag{4.120}$$

The total first order contribution becomes

$$\begin{aligned}\hat{\tilde{\rho}}_{1S} &= \hat{\tilde{\rho}}'_{1S} + \hat{\tilde{\rho}}''_{1S} = \frac{1}{2}\begin{bmatrix} -\left(\frac{\Omega}{\lambda}\right)^2 & \frac{\Omega\varepsilon}{\lambda^2} \\ \frac{\Omega\varepsilon}{\lambda^2} & \left(\frac{\Omega}{\lambda}\right)^2 \end{bmatrix} \\ &\frac{1}{4}\begin{bmatrix} \frac{2\Omega}{\lambda}e^{-C_0}\int_{-\infty}^{t} dt'\Omega e^{C_\beta(t-t')}\mathrm{Im}\left\{e^{i\int_{t'}^{t}\lambda d\tau}e^{iC_i(t-t')}\right\} & -2i\mathrm{Im}\theta - 2\frac{\varepsilon}{\lambda}\mathrm{Re}\theta \\ 2i\mathrm{Im}\theta - 2\frac{\varepsilon}{\lambda}\mathrm{Re}\theta & -\frac{2\Omega}{\lambda}e^{-C_0}\int_{-\infty}^{t} dt'\Omega e^{C_\beta(t-t')}\mathrm{Im}\left\{e^{i\int_{t'}^{t}\lambda d\tau}e^{iC_i(t-t')}\right\} \end{bmatrix}.\end{aligned} \tag{4.121}$$

Considering $\Omega/\varepsilon << 1$, we have

$$\hat{\rho}_{1S}(t) = \begin{bmatrix} 0 & \frac{-i}{2}e^{-C_0}\int_{-\infty}^{t} dt'\Omega(t')e^{C_\beta(t-t')}e^{-i\int_{t'}^{t}\lambda d\tau}e^{iC_i(t-t')} \\ \frac{i}{2}e^{-C_0}\int_{-\infty}^{t} dt'\Omega(t')e^{C_\beta(t-t')}e^{i\int_{t'}^{t}\lambda d\tau}e^{-iC_i(t-t')} & 0 \end{bmatrix}. \tag{4.122}$$

We have C_0, $C_i(t)$, and $C_\beta(t)$ as follows

$$e^{-\sum_q |\alpha_q|^2 \coth\left(\frac{\beta\omega_q}{2}\right)} \Longrightarrow e^{-4\int_0^\infty J(\omega)\coth\left(\frac{\beta\omega}{2}\right)d\omega} = e^{-C_0}, \tag{4.123a}$$

$$e^{i\sum_q |\alpha_q|^2 \sin(\omega_q t)} \Longrightarrow e^{4i\int_0^\infty J(\omega)\sin(\omega t)d\omega} = e^{iC_i(t)}, \tag{4.123b}$$

$$e^{\sum_q |\alpha_q|^2 \cos(\omega_q t)\coth\left(\frac{\beta\omega_q}{2}\right)} \Longrightarrow e^{4\int_0^\infty J(\omega)\cos(\omega t)\coth\left(\frac{\beta\omega}{2}\right)d\omega} = e^{C_\beta(t)}. \tag{4.123c}$$

In order to calculate g_q, material dependent many body calculations are needed. This can be avoided by introducing the continuum limit; meaning that we change the sum to integral $\sum_q \frac{g_q^2}{\omega_q^2} \to \int_0^\infty J(\omega)d\omega$.

Second order SFAF contribution with noise:

The second order contribution is constructed using the last terms of Eq. (4.73). We have

$$\tilde{\rho}_0(t) = \begin{bmatrix} 0 & 0 \\ 0 & \hat{B} \end{bmatrix}. \tag{4.124}$$

We get

$$\begin{aligned}
&\hat{\tilde{\rho}}_2(t) = \hat{\tilde{\rho}}_{2S}(t) + \hat{\tilde{\rho}}_{2F}(t) \\
&= \begin{bmatrix} \hat{u}_{12}\hat{B}\hat{u}_{12}^\dagger & 0 \\ 0 & -\int_{-\infty}^t dt' \hat{w}_{12}^\dagger(t,t')\hat{u}_{12}(t,t')\hat{B} + \hat{B}\int_{-\infty}^t dt' \hat{u}_{12}^\dagger(t,t')\hat{w}_{12}(t,t') \end{bmatrix} \\
&+ \begin{bmatrix} 0 & \int_{-\infty}^t \left[\hat{w}_{12}(t,t')\hat{u}_1(t') + \hat{u}_1(t')\hat{w}_{12}(t,t')\right]\hat{B} \\ -\int_{-\infty}^t \left[\hat{w}_{12}^\dagger(t,t')\hat{u}_1(t') - \hat{u}_1(t')\hat{w}_{12}^\dagger(t,t')\right]\hat{B} & -\hat{u}_1\hat{B}]\hat{u}_1 + \int_{-\infty}^t dt' \hat{w}_1(t')\hat{u}_1(t')\hat{B} + \\ & \hat{B}\int_{-\infty}^t dt' \hat{u}_1(t')\hat{w}_1(t') \end{bmatrix}.
\end{aligned} \tag{4.125}$$

Now, we need to transform back to the $\hat{\rho}_0(t)$ and $\hat{\rho}_1(t)$ and $\hat{\rho}_2(t)$ by using matrices $\hat{V}$and $\hat{V}^\dagger$. We have (For the slow bath part where the F contribution is zero)

$$\hat{\tilde{\rho}}_{2S}(t) = \begin{bmatrix} \hat{u}_{12}\hat{B}\hat{u}_{12}^\dagger & 0 \\ 0 & -\int_{-\infty}^{t} dt' \hat{w}_{12}^\dagger(t,t')\hat{u}_{12}(t,t')\hat{B} - \hat{B}\int_{-\infty}^{t} dt' \hat{u}_{12}^\dagger(t,t')\hat{w}_{12}(t,t') \end{bmatrix}. \tag{4.126}$$

Multiplying by $\hat{V}$ and $\hat{V}^\dagger$we get

$$\begin{aligned} \hat{\rho}_{2S}(t) &= \frac{1}{2}\hat{V}\hat{\tilde{\rho}}_{2S}(t)\hat{V}^\dagger \\ &= \frac{1}{2}\begin{bmatrix} a_{11} & -a_{12}\hat{D}_+^2 \\ a_{12}\hat{D}_-^2 & a_{11} \end{bmatrix}\begin{bmatrix} x_{11} & 0 \\ 0 & x_{22} \end{bmatrix}\begin{bmatrix} a_{11} & a_{12}\hat{D}_+^2 \\ -a_{12}\hat{D}_-^2 & a_{11} \end{bmatrix} \\ &= \frac{1}{2}\begin{bmatrix} a_{11}^2 x_{11} + a_{12}^2 x_{22}\hat{D}_+^2\hat{D}_-^2 & a_{11}a_{12}\left(x_{11}\hat{D}_+^2 - \hat{D}_+^2\hat{x}_{22}\right) \\ a_{11}a_{12}\left(\hat{D}_-^2\hat{x}_{11} - \hat{x}_{22}\hat{D}_-^2\right) & a_{12}^2\hat{D}_-^2\hat{x}_{11}\hat{D}_+^2 + a_{11}^2\hat{x}_{22} \end{bmatrix} \end{aligned} \tag{4.127}$$

Thus, the density matrix in the original frame would be

$$\begin{aligned} \hat{\rho}_{2S}(t) &= \frac{1}{2}\hat{V}\hat{\tilde{\rho}}_{2S}(t)\hat{V}^\dagger \\ &= \frac{1}{2}\begin{bmatrix} a_{11} & -a_{12}\hat{D}_+^2 \\ a_{12}\hat{D}_-^2 & a_{11} \end{bmatrix}\begin{bmatrix} \hat{x}_{11} & 0 \\ 0 & \hat{x}_{22} \end{bmatrix}\begin{bmatrix} a_{11} & a_{12}\hat{D}_+^2 \\ -a_{12}\hat{D}_-^2 & a_{11} \end{bmatrix} \\ &= \frac{1}{2}\begin{bmatrix} a_{11}^2\hat{x}_{11} + a_{12}^2\hat{x}_{22}\hat{D}_+^2\hat{D}_-^2 & a_{11}a_{12}\left(\hat{x}_{11}\hat{D}_+^2\hat{D}_-^2 - \hat{D}_+^2\hat{x}_{22}\hat{D}_-^2\right) \\ a_{11}a_{12}\left(\hat{D}_-^2\hat{x}_{11}\hat{D}_+^2 - \hat{x}_{22}\hat{D}_-^2\hat{D}_+^2\right) & a_{12}^2\hat{D}_-^2\hat{x}_{11}\hat{D}_+^2 + a_{11}^2\hat{x}_{22} \end{bmatrix}. \end{aligned} \tag{4.128}$$

Now, we need to trace over the heat bath the terms that we need are $\mathrm{tr}_{bath}\left\{\hat{x}_{11}\right\}, \mathrm{tr}_{bath}\left\{\hat{x}_{22}\right\}$. In the other combinations we have $\hat{D}_-^2\hat{D}_+^2 = \mathbb{1}$.

$$\begin{aligned} &\mathrm{tr}_{bath}\left\{\hat{x}_{11}\right\} = \mathrm{tr}_{bath}\left\{\hat{u}_{12}\hat{B}\hat{u}_{12}^+\right\} = \left(\frac{\Omega}{2\lambda}\right)^2 \mathrm{tr}_{bath}\{\hat{D}_+^2\hat{B}\hat{D}_-^2\} - \frac{\Omega}{2\lambda}\mathrm{tr}_{bath}\left\{\hat{u}\hat{B}\hat{D}_-^2\right\} - \frac{\Omega}{2\lambda}\mathrm{tr}_{bath}\left\{\hat{D}_+^2\hat{B}\hat{u}^\dagger\right\} \\ &+ \mathrm{tr}_{bath}\left\{\hat{u}\hat{B}\hat{u}^\dagger\right\} = \left(\frac{\Omega}{2\lambda}\right)^2 - \frac{\Omega}{2\lambda}\mathrm{tr}_{bath}\left\{\hat{D}_+^2\hat{B}\hat{u}^\dagger + h.c.\right\} + \mathrm{tr}_{bath}\left\{\hat{u}^+\hat{B}\hat{u}\right\} = -\mathrm{tr}_{bath}\left\{\hat{x}_{22}\right\}. \end{aligned} \tag{4.129}$$

We have

$$a_{11}^2 \mathrm{tr}_{bath}\left\{\hat{x}_{11}\right\} + a_{12}^2 \mathrm{tr}_{bath}\left\{\hat{x}_{22}\right\} = \frac{2\varepsilon}{\lambda}\left\{\left(\frac{\Omega}{2\lambda}\right)^2 - \frac{\Omega}{2\lambda}\mathrm{tr}_{bath}\left\{\hat{D}_+^2\hat{B}\hat{u}^\dagger + h.c.\right\} + \mathrm{tr}_{bath}\left\{\hat{u}^+\hat{B}\hat{u}\right\}\right\}$$
$$- \left\{a_{12}^2 \mathrm{tr}_{bath}\left\{\hat{x}_{11}\right\} + a_{11}^2 \mathrm{tr}_{bath}\left\{\hat{x}_{22}\right\}\right\}. \tag{4.130}$$

We also have

$$\mathrm{tr}_{bath}\left\{\hat{D}_+^2\hat{B}\hat{u}^\dagger + h.c.\right\} = e^{-C_0}\mathrm{Im}\left\{\int_{-\infty}^{t} dt'\Omega(t')e^{i\int_{t'}^{t}\lambda d\tau}e^{iC_i(t-t')}e^{C_\beta(t-t')}\right\}, \tag{4.131}$$

and

$$\mathrm{tr}_{bath}\left\{\hat{u}\hat{B}\hat{u}^\dagger\right\} = \frac{e^{-C_0}}{4}\int_{-\infty}^{t}\int_{-\infty}^{t} dt'dt''\Omega(t')\Omega(t'')e^{i\int_{t''}^{t'}\lambda d\tau}e^{iC_i(t'-t'')}e^{C_\beta(t'-t'')}. \tag{4.132}$$

In the limits of $\frac{\Omega}{\varepsilon} << 1$, we find the reduced density matrix in the original frame to be

$$\tilde{\rho}_{2S}(t) = \begin{bmatrix} \frac{e^{-C_0}}{4}\int_{-\infty}^{t}\int_{-\infty}^{t} dt'dt''\Omega(t')\Omega(t'')\times & 0 \\ e^{i\int_{t''}^{t'}\lambda d\tau}e^{iC_i(t'-t'')}e^{C_\beta(t'-t'')} & \\ 0 & -\frac{e^{-C_0}}{4}\int_{-\infty}^{t}\int_{-\infty}^{t} dt'dt''\Omega(t')\Omega(t'')\times \\ & e^{i\int_{t''}^{t'}\lambda d\tau}e^{iC_i(t'-t'')}e^{C_\beta(t'-t'')} \end{bmatrix}. \tag{4.133}$$

which gives the ionization and with that, we can also calculate the intraband currents in the solid case as follows

$$\langle \mathbf{j}_{ra}\rangle \approx \int_{\overline{\mathrm{BZ}}} d^3K\,\mathbf{v}(\mathbf{K}_t)n_c(\mathbf{K},t). \tag{4.134}$$

Again, we have C_0, $C_i(t)$, and $C_\beta(t)$ as follows

$$e^{-\sum_q|\alpha_q|^2\coth\left(\frac{\beta\omega_q}{2}\right)} \Longrightarrow e^{-4\int_0^\infty J(\omega)\coth\left(\frac{\beta\omega}{2}\right)d\omega} = e^{-C_0}, \tag{4.135a}$$

$$e^{i\sum_q|\alpha_q|^2\sin(\omega_q t)} \Longrightarrow e^{4i\int_0^\infty J(\omega)\sin(\omega t)d\omega} = e^{iC_i(t)} \tag{4.135b}$$

$$, e^{\sum_q|\alpha_q|^2\cos(\omega_q t)\coth\left(\frac{\beta\omega_q}{2}\right)} \Longrightarrow e^{4\int_0^\infty J(\omega)\cos(\omega t)\coth\left(\frac{\beta\omega}{2}\right)d\omega} = e^{C_\beta(t)}. \tag{4.135c}$$

We see that in the limit of $\frac{\Omega}{\varepsilon} << 1$; the first order contribution gives the interband current and second order gives the ionization or intraband currents.

Summary of all contributions

We calculate, here, ionization and interband currents for the zeroth order, first order and second order contributions. Ionization terms from zeroth order to second order are

$$\begin{aligned}
I^{(0)} &= \frac{1}{2}\frac{\lambda-\varepsilon}{\lambda}, \\
I^{(1)} &= -\frac{\Omega^2}{2\lambda^2} + \frac{\Omega}{2\lambda}e^{-C_0}\mathrm{Im}\int_{-\infty}^{t} dt'\Omega(t')e^{i\int_{t'}^{t}\lambda d\tau}e^{iC_i(t-t')}e^{C_\beta(t-t')}, \\
I^{(2)} &= \frac{\varepsilon\Omega^2}{4\lambda^3} - \frac{\varepsilon\Omega}{2\lambda^2}e^{-C_0}\mathrm{Im}\int_{-\infty}^{t} dt'\Omega(t')e^{i\int_{t'}^{t}\lambda d\tau}e^{iC_i(t-t')}e^{C_\beta(t-t')} \\
&+ \frac{\varepsilon}{4\lambda}e^{-C_0}\int_{-\infty}^{t}dt'\int_{-\infty}^{t}dt''\Omega(t')\Omega(t'')e^{i\int_{t''}^{t'}\lambda d\tau}e^{iC_i(t'-t'')}e^{C_\beta(t'-t'')}.
\end{aligned} \tag{4.136}$$

The off diagonal elements which give the interband contributions are

$$\begin{aligned}
J_{er}^{(0)} &= -\frac{\Omega}{\lambda}j_{12}, \\
J_{er}^{(1)} &= -\frac{\Omega\varepsilon}{\lambda^2}j_{12} - \frac{\varepsilon}{\lambda}e^{-C_0}\mathrm{Im}\int_{-\infty}^{t} dt'\Omega(t')e^{i\int_{t'}^{t}\lambda d\tau}e^{iC_i(t-t')}e^{C_\beta(t-t')}j_{12}, \\
J_{er}^{(2)} &= \frac{\Omega^3}{2\lambda^3}j_{12} - \frac{\Omega^2}{\lambda^2}e^{-C_0}\mathrm{Im}\int_{-\infty}^{t} dt'\Omega(t')e^{i\int_{t'}^{t}\lambda d\tau}e^{iC_i(t-t')}e^{C_\beta(t-t')}j_{12} \\
&+ \frac{\Omega}{2\lambda}e^{-C_0}\int_{-\infty}^{t}dt'\int_{-\infty}^{t}dt''\Omega(t')\Omega(t'')e^{i\int_{t''}^{t'}\lambda d\tau}e^{iC_i(t'-t'')}e^{C_\beta(t'-t'')}j_{12}.
\end{aligned} \tag{4.137}$$

Note that $j_{12} = j_{21}$ because we chose dipole to be real. Note that in the two time integral terms the convolution function couples the two time integrals which is inconvenient to evaluate. Thus, we do an integration by parts and write it as

$$\begin{aligned}
&\int_{-\infty}^{t}dt'\int_{-\infty}^{t}dt''\Omega(t')\Omega(t'')e^{i\int_{t''}^{t'}\lambda d\tau}e^{iC_i(t'-t'')}e^{C_\beta(t'-t'')} = \\
&2\int_{-\infty}^{t}dt'\int_{-\infty}^{t'}dt''\Omega(t')\Omega(t'')\mathrm{Re}\left\{e^{i\int_{t''}^{t'}\lambda d\tau}e^{iC_i(t'-t'')}\right\}e^{C_\beta(t'-t'')}.
\end{aligned} \tag{4.138}$$

In the paper [66], we only calculated the ionization terms which are the second order contribution and in the limits of $\Omega/\varepsilon \ll 1$.

In sum, the ionization would be given through the following equation

$$I^{(2)} = \frac{1}{2}\int_{-\infty}^{t} dt' \int_{-\infty}^{t'} dt'' \Omega(t')\Omega(t'')\mathrm{Re}\left\{ e^{i\int_{t''}^{t'} \lambda d\tau} e^{iC_i(t'-t'')} \right\} e^{C_\beta(t'-t'')}, \tag{4.139}$$

which is the last term in Eq. (4.136) when $\Omega/\varepsilon \ll 1$.

Chapter 5

Quantum Light Perturbation in Strong Field Physics

This chapter is based on the preprint [97] and it overlaps with its text.

5.1 Introduction

The goal of this chapter is to develop the theory of quantum sideband high harmonic generation (QSHHG) in atoms and solids and to identify methods by which to transfer quantum properties from the perturbative BSV onto the harmonic sidebands. The theoretical framework is a quantum generalization of the semi-classical Lewenstein model of HHG [28] and yields closed-form solutions for the HHG and QSHHG wavefunctions. Knowledge of the wavefunction enables identification of the quantum properties of QSHHG. The additional photons absorbed and emitted from the quantum perturbation, such as a BSV, create entanglement between individual harmonic sidebands and between the harmonic sidebands and the BSV. We show how this entanglement can be harnessed to create a variety of non-classical states commonly used in quantum information science, such as high purity single photon states, Schrödinger cat states, and photon added squeezed vacuum states. In this way, quantum properties of the BSV can be transferred onto QSHHG, opening a path towards engineering the quantum properties of ultrashort XUV high harmonics. While we primarily focus on single-mode properties, a qualitative discussion of two- and multi-mode entanglement is given in the following text. A more quantitative analysis is subject to future research.

In addition to revealing quantum properties of QSHHG, the theory offers an order of magnitude predictive power regarding the number of photons in the harmonics and

sidebands and compares very favorably with experiments [112]. This facilitates the optimization of QSHHG, thereby relaxing the requirements on the BSV power.

5.2 Theory summary

We use a strong field quantum optical model that generalizes the semi-classical approach of Lewenstein [31, 28]. Although the derivation is quite general, results and conclusions are derived for a BSV quantum perturbation at twice the frequency of the classical driving field which results in even harmonic sidebands. For a detailed derivation see the supplement 5.5. In the quantum optical description, HHG is modeled as a one photon process: N classical photons are emitted as a single high harmonic (HH) photon. QSHHG is, to lowest order, a two-photon process, wherein the emission of a harmonic photon is perturbed by the emission or absorption of a quantum photon, resulting in the effective emission of a QSHH photon. The international system of (SI) units is used, unless otherwise noted.

5.2.1 Wavefunction

HHG and QSHHG are described by the photon wavefunction

$$\left|\varphi_0(t)\right\rangle \approx \left|\varphi_h(t)\right\rangle \left|\varphi_m(t)\right\rangle = \hat{D}_h \hat{S}_m \left|\varphi_0(t_0)\right\rangle \tag{5.1}$$

with $|\varphi_0(t_0)\rangle$ the wavefunction at initial time t_0. We assume that HHG and QSHHG take place in different modes κ. The wavefunction can therefore be written as an independent product of these two processes. For example, coupling between QSHHG and HHG occurs for three-photon processes, when the frequency of the perturbing quantum field is twice that of the classical one [148, 149]. It can also occur in a first order process when the perturbing and driving fields have the same frequency. Both cases are subject to future research. A generalization of our approach is outlined in the supplement 5.5. HHG and QSHHG are determined in the limit $\left|\varphi_{h,m}\right\rangle = \left|\varphi_{h,m}(t \to \infty)\right\rangle$.

The HHG wavefunction $\left|\varphi_h\right\rangle$ is generated by the displacement operator

$$\hat{D}_h = \exp\left(\sum_\kappa h_\kappa \hat{a}_\kappa^\dagger - h_\kappa^* \hat{a}_\kappa\right), \tag{5.2}$$

where $\kappa \equiv (\mathbf{k}s)$ is a multi-index with photon wavevector $\mathbf{k}$, polarization index $s = 1, 2$.

The HHG coefficient h_κ is defined in the next section; it contains a sum over an ensemble of emitters at positions $\mathbf{x}_j$. The position dependence is not written explicitly.

The QSHHG wavefunction $\left|\varphi_m(t)\right\rangle$ is generated by a mixed-mode squeezed vacuum state operator between harmonic modes κ and perturbative quantum modes q,

$$\hat{S}_m = \exp\left(\sum_\kappa \left(f_\kappa \hat{a}_q^\dagger + g_\kappa \hat{a}_q\right)\hat{a}_\kappa^\dagger - \left(g_\kappa^* \hat{a}_q^\dagger + f_\kappa^* \hat{a}_q\right)\hat{a}_\kappa\right). \tag{5.3}$$

Our analysis is confined to a single perturbative mode q. The coefficients f_κ, g_κ represent HHG in the presence of emission and absorption of an additional perturbative quantum photon, respectively. In perturbative nonlinear optics, the former is referred to as difference (DFG) and the latter as sum frequency (SFG) generation. QSHHG coefficients f_κ, g_κ are defined in the next subsection.

In order to fully define Eq. (5.1), a particular initial state needs to be chosen; $|\varphi_0(t_0)\rangle = |\upsilon\xi_q\rangle$ consists of a multi-mode vacuum state, $|\upsilon\rangle = \prod_\kappa |\upsilon_\kappa\rangle$, for the harmonics, and a single squeezed vacuum state for the perturbative mode,

$$\left|\xi_q\right\rangle = \hat{S}_q \left|\upsilon_q\right\rangle = e^{\frac{1}{2}(\xi \hat{a}_q^2 - \xi^* \hat{a}_q^{\dagger 2})} \left|\upsilon_q\right\rangle \tag{5.4}$$

with $\xi \approx re^{i\theta}$. Normal ordering of $\left|\varphi_m\right\rangle = \hat{S}_m \left|\upsilon\xi_q\right\rangle$ yields

$$\left|\varphi_m\right\rangle = \frac{\overline{\mathfrak{N}}}{\sqrt{\cosh(r)}} \exp\left(\sum_\kappa Z_\kappa \hat{a}_\kappa^\dagger \hat{a}_q^\dagger\right) \exp\left(-\overline{\beta}\hat{a}_q^{\dagger 2}\right) \left|\upsilon\upsilon_q\right\rangle \tag{5.5}$$

with $\beta = (1/2)\tanh(r)e^{-i\theta}$, and $\overline{\beta} = \beta/(1 + \sum_\kappa |Z_\kappa|^2)$. Further,

$$\begin{aligned} Z_\kappa &= f_\kappa - g_\kappa \tanh(r)e^{i\theta} \\ \overline{\mathfrak{N}} &= \frac{1}{\sqrt{1 + \sum_\kappa |Z_\kappa|^2}}. \end{aligned} \tag{5.6}$$

Eq. (5.5) is a multi-mode harmonics wavefunction in the basis of electromagnetic plane wave modes, and can be used to calculate two or more correlated mode properties. The normal-ordered wavefunction has been derived in the limit of an intense squeezed vacuum beam with $r > 1$ and $|Z_\kappa|^2 \ll 1$.

5.2.2 HHG and QSHHG coefficients for atomic and molecular gases

The HHG coefficient of a single atom j is given by

$$h_\kappa = -e^{-i\mathbf{k}\mathbf{x}_j}\int_{-\infty}^{\infty} dt e^{i\omega_k t} H_k(t) = \tilde{H}_k e^{-i\mathbf{k}\mathbf{x}_j} \tag{5.7}$$
$$H_k = \frac{|e|E_v}{\hbar}\left\{ \mathbf{e}_\kappa \mathbf{x}(t) + \int d^3p\, \overline{\sigma}_\kappa(t)\left(\Gamma_{\mathbf{p}}(t) + \text{c.c}\right)\right\}$$

with

$$\mathbf{x}(t) = \int d^3p\, \mathbf{d}^*(\mathbf{p}_t)\, b_{\mathbf{p}}(t) + \text{c.c.} \tag{5.8}$$
$$b_{\mathbf{p}}(t) = \int_{t_0}^{t} dt'\, \Omega(t') \exp\left(iS(t',t) - \xi(t-t')\right).$$

The polarization of HHG is assumed to be parallel to the laser pulse; additionally, H_k does not depend on the direction of the wavevector. Both facts are reflected in the change of the lower index from κ to $k = \omega_k/c$. Note that H_k depends on the position $\mathbf{x}_j$ of the atom via the space dependence of the laser field, which is not explicitly stated. Frequency and polarization of the harmonic are given by ω_k and $\mathbf{e}_\kappa$, $\mathbf{d}(\mathbf{p}) = \langle \mathbf{p}|\mathbf{x}|0\rangle = d_0\mathbf{p}/(\mathbf{p}^2/(2m) + E_0)^3$ is the transition dipole moment between ground $|0\rangle$ and continuum plane wave state $|\mathbf{p}\rangle$ with $\mathbf{p}$ in the canonical momentum frame [28], E_0 is the binding energy, and $d_0 = 3.37 \times 10^{-4}\,[\mathrm{kg}^{1/2}\mathrm{m}^{9/2}\mathrm{s}^{-7/2}]$. Further, $\Omega(t) = (|e|/\hbar)\mathbf{d}(\mathbf{p}_t)\boldsymbol{\mathcal{F}}(t)$ is a generalized Rabi frequency, $\boldsymbol{\mathcal{F}}$ represents the classical intense laser field, $\mathbf{p}_t = \mathbf{p} + |e|\boldsymbol{\mathcal{A}}(t)$ is defined in the moving momentum frame, and $-\partial_t \boldsymbol{\mathcal{A}}(t) = \boldsymbol{\mathcal{F}}(t)$ defines the vector potential. Note that the electric field consists of a classical part $\boldsymbol{\mathcal{F}}$ with frequency ω_0 and field strength F_0, and of a quantum part $\hat{\mathbf{F}}$ which accounts for the emission of harmonic photons in Eqs. (5.2) and (5.3). Moreover, $E_v = \sqrt{\hbar\omega_k/2\varepsilon_0 V}$ is the vacuum electric field, V the quantization volume, and ε_0 the vacuum permittivity. We use a filter $\xi(t-t')$ that leaves HHG from the first recollision unchanged and extinguishes all higher returns. The dipole $\mathbf{x}(t)$ corresponds with the semiclassical Lewenstein dipole defined in Eq. (6) of Ref. [28] with

$$S(t) = \frac{1}{\hbar}\int_{t_0}^{t}\left(\frac{1}{2m}\mathbf{p}_\tau^2 + E_0\right) d\tau \tag{5.9}$$

the classical action, and $S(t',t) = S(t) - S(t')$. Further,

$$\Gamma_{\mathbf{p}}(t) = \Omega^*(t) b_{\mathbf{p}}(t) \tag{5.10}$$

is related to the optical field ionization rate $2\mathrm{Re}[\gamma]$ with $\gamma(t) = \int d^3p\, \Gamma_{\mathbf{p}}(t)$, see Eq. (52) of [28]. Finally, during ionization an electron is promoted into a laser driven continuum state, dressed with a displacement operator with coefficient

$$\begin{aligned}\sigma_\kappa(t) &= \frac{|e|E_v}{\hbar}\overline{\sigma}_\kappa(t) e^{i\omega_k t} \\ \overline{\sigma}_\kappa(t) &= -\frac{i}{\omega_k}\int_{t_0}^{t} dt' \left(\mathbf{e}_\kappa \mathbf{v}_{t'}\right) e^{-i\omega_k(t-t')}.\end{aligned} \tag{5.11}$$

Here, $\mathbf{v} = \mathbf{p}/m$ is the electron velocity. HHG, as described by H_k in Eq. (5.7), contains two contributions. The first term represents HHG via ionization, continuum evolution, and recollision [31, 28]. The second term describes HHG via the ionization nonlinearity [150].

The QSHHG coefficients f_κ, g_κ for a single atom j are given by

$$\begin{aligned}f_\kappa &= e^{-i(\mathbf{k}+\mathbf{q})\mathbf{x}_j}\int_{-\infty}^{\infty} dt e^{i(\omega_k+\omega_q)t} F_k(t) = \tilde{F}_k e^{-i(\mathbf{k}+\mathbf{q})\mathbf{x}_j} \\ F_k &= \left(\frac{|e|E_v}{\hbar}\right)^2 \int d^3p\, \overline{\sigma}_q(t)\left\{ \mathbf{e}_\kappa \mathbf{x}_{\mathbf{p}}(t) + i\overline{\sigma}_\kappa(t)\mathrm{Im}\left[\Gamma_{\mathbf{p}}(t)\right]\right\}\end{aligned} \tag{5.12}$$

and

$$\begin{aligned}g_\kappa &= e^{-i(\mathbf{k}-\mathbf{q})\mathbf{x}_j}\int_{-\infty}^{\infty} dt e^{i(\omega_k-\omega_q)t} G_k(t) = \tilde{G}_k e^{-i(\mathbf{k}-\mathbf{q})\mathbf{x}_j} \\ G_k &= \left(\frac{|e|E_v}{\hbar}\right)^2 \int d^3p\, \overline{\sigma}_q^*(t)\left\{ \mathbf{e}_\kappa \mathbf{x}_{\mathbf{p}}(t) + i\overline{\sigma}_\kappa(t)\mathrm{Im}\left[\Gamma_{\mathbf{p}}(t)\right]\right\},\end{aligned} \tag{5.13}$$

where ω_q and $\mathbf{q}$ are frequency and wavevector of the quantum light mode q, and

$$\mathbf{x}_{\mathbf{p}}(t) = \mathbf{d}^*(\mathbf{p}_t)\, b_{\mathbf{p}}(t) - \text{c.c.} \tag{5.14}$$

is the imaginary part of the transition dipole for a given $\mathbf{p}$. Again, the index of F, G has been changed from κ to k. Both, conventional HHG and QSHHG coefficients are very similar to the semi-classical coefficients [149], except for powers of the quantum

vacuum field term $|e|E_v/\hbar$. In the quasi-classical approach the coefficient $\overline{\sigma}_q(t)$ is within the time integral of $\mathbf{x}_\mathbf{p}(t)$. The same is initially the case for the quantum optical equations. However, in order to obtain a unitary QSHHG operator, $\overline{\sigma}_q$ needs to be pulled out of the inner time integral by integration by parts. The remaining non-unitary term is small and can be neglected.

5.2.3 HHG and QSHHG coefficients for solids

The results for atomic and molecular gases can be easily translated into HHG in two-band solids by replacing

$$\mathbf{p} \to \mathbf{k}, \quad \mathbf{k} \in \mathrm{BZ} \tag{5.15a}$$

$$E_0 + \frac{\mathbf{p}^2}{2m} \to \varepsilon(\mathbf{k}) \approx E_g + \frac{\mathbf{p}^2}{2m_*} = \varepsilon(\mathbf{p}) \tag{5.15b}$$

$$\frac{\mathbf{p}}{m} \to \frac{1}{\hbar^2}\nabla_\mathbf{k}\varepsilon = \mathbf{v}(\mathbf{k}) \approx \frac{\mathbf{p}}{m_*} \tag{5.15c}$$

$$\mathbf{d}(\mathbf{p}) \to \mathbf{d}(\mathbf{k}) = i\langle u_c(\mathbf{k})|\nabla_\mathbf{k}|u_v(\mathbf{k})\rangle \approx \frac{d_0 E_g}{\varepsilon(\mathbf{p})} \tag{5.15d}$$

where $\mathbf{k}$ represents the crystal momentum defined in the first Brillouin zone (BZ), and $\varepsilon(\mathbf{k})$ and $\mathbf{v}(\mathbf{k})$ represent relative band gap and band velocity, i.e. the difference between conduction and valence bands. The minimum band gap is $E_g = E_0$, m_* is the effective electron mass at the band gap minimum defined by $\partial_{k_i}\partial_{k_j}\varepsilon|_{\mathbf{k}=0} = \hbar^2/m_*$. For simplicity, we have replaced the inverse effective mass tensor by a scalar quantity. Finally, the atomic transition dipole needs to be replaced with the dipole moment between valence and conduction bands. The last term is the approximate dipole moment in $\mathbf{kp}$ perturbation theory [45]. Within the effective mass approximation, the atomic equations remain applicable to solids and are represented by the last terms in Eqs. (5.15a)-(5.15d).

5.2.4 Phase matching

In order to compare and characterize HHG and QSHHG, operator expectation values with regard to the macroscopic wavefunction need to be known. Here, we focus on $\hat{n} = \sum_\kappa \hat{n}_\kappa$,

$$\begin{aligned}\langle\varphi_h|\hat{n}|\varphi_h\rangle &= \sum_\kappa \left(\sum_j h_\kappa^*\right)\left(\sum_j h_\kappa\right) \\ &= \frac{VN_0^2}{(2\pi)^3}\int d^3k \left(\int d^3x\, h_\kappa^*\right)\left(\int d^3x\, h_\kappa\right). \end{aligned} \tag{5.16}$$

In the continuum limit, the sum over atoms $\sum_i \to N_0 \int d^3x$, with N_0 representing the number density of the material and $\sum_\kappa \to V/(2\pi)^3 \int d^3k$, with V as the quantization volume. Polarization and wavevector of intense laser, quantum field, HHG, and QSHHG are fixed along x and z, respectively. The space integrals and the transverse k_x- and k_y-integrals can be worked out approximately (see supplement). At this point, the only remaining integral is the one over $dk_z \approx dk = d\omega_k/c$. The $d\omega_k$ integral drops out upon examination of the differential expectation value of the number operator,

$$\begin{aligned}\frac{d\langle\hat{n}\rangle}{d\omega_k} &= \frac{d}{d\omega_k}\langle\varphi_h|\hat{n}|\varphi_h\rangle = c_k^2\,|\tilde{H}_k(\omega_k)|^2 \\ c_k^2 &= \frac{\left(N_0 \mathrm{w}_k l_i\right)^2}{2c}V, \end{aligned} \tag{5.17}$$

where $\mathrm{w}_k = \mathrm{w}(\omega_k)$ represents the transverse $1/e^2$ radius of the HH mode with frequency ω_k. Here, $\tilde{H}_k = \tilde{H}_k(\mathbf{x} = 0)$, since the space dependence has been integrated over, and the interaction length is l_i. HHG scales as l_i^2, as long as l_i is shorter than the dephasing length. Finally, the quantization volume cancels out due to the fact that the single atom response $\tilde{H}_k \propto 1/\sqrt{V}$.

We are mainly interested in the number of photons emitted in all spatial modes with frequencies in the band $(N - \frac{1}{2})\omega_0 \le \omega_k \le (N + \frac{1}{2})\omega_0$ which is given by

$$\langle\hat{n}\rangle_N = c_k^2 \int_{(N-\frac{1}{2})\omega_0}^{(N+\frac{1}{2})\omega_0} d\omega_k |\tilde{H}_k(\omega_k)|^2 = |h_N|^2, \tag{5.18}$$

with h_N being a dimensionless quantity.

Similarly, the number of QSHHG photons emitted into one harmonic interval ω_0 about

harmonic order N is found to be

$$\langle \hat{n} \rangle_N = c_q^2 \cosh^2(r) \int_{(N-\frac{1}{2})\omega_0}^{(N+\frac{1}{2})\omega_0} d\omega_k \left|\zeta_k\right|^2 = \cosh^2(r) \left|\zeta_N\right|^2 \tag{5.19}$$

with

$$\begin{aligned} |\zeta_k|^2 &= \left|\tilde{F}_k - \tilde{G}_k \tanh(r) e^{i\theta}\right|^2, \\ c_q^2 &= \frac{\left(N_0 \mathrm{w}_k l_i\right)^2}{2c} V^2 \frac{(\Delta q)^3}{(2\pi)^3}, \end{aligned} \tag{5.20}$$

and $(\Delta q)^3$ is the mode volume of the perturbative quantum field. It should be noted that we have approximated the temporally and spatially finite BSV field by a plane wave. This is being corrected for by replacing the plane wave mode volume by the experimentally measured BSV mode volume [112]. The parameter ζ_k emerges from Z_κ in Eq. (5.6) after performing the phase matching integrals. The quantization volume again drops out. Similar to the case for HHG, $\zeta_N = \zeta_N(\mathbf{x} = 0)$.

5.2.5 Effective QSHH mode

In experiments [112], the photons contained in one QSHH are measured and they are not in the individual plane wave modes. To that end, the connection between calculations and experiment is greatly facilitated by introducing an effective mode operator [151]

$$\hat{a}_N = \frac{1}{|\zeta_N|} \sum_{\kappa \in N} Z_\kappa^* \hat{a}_\kappa \tag{5.21}$$

that encompasses all plane wave modes of a quantum sideband. This operator fulfills the usual harmonic oscillator commutation relations $[\hat{a}_N, \hat{a}_M^\dagger] = \delta_{NM}$. The vacuum state of a QSHH mode is $\prod_{\kappa \in N} |v_\kappa\rangle = |v\rangle_N$, so that a number state

$$|n\rangle_N = \frac{1}{\sqrt{n!}} \left(\hat{a}_N^\dagger\right)^n |v_N\rangle, \tag{5.22}$$

corresponds to a sum over all combinations that have n photons in the plane wave modes of the quantum sideband N. With these definitions the wavefunction (5.5) becomes

$$\begin{aligned}
|\varphi_m\rangle &\approx \prod_N \frac{\mathfrak{N}_N}{\sqrt{\cosh(r)}} \exp\left(|\zeta_N| \hat{a}_N^\dagger \hat{a}_q^\dagger\right) \exp\left(-\beta_N \hat{a}_q^{\dagger 2}\right) \left|v_N v_q\right\rangle, \\
\beta_N &= \frac{\beta}{1+\sum_{\kappa\in N}|Z_\kappa|^2} = \frac{\beta}{1+|\zeta_N|^2}, \\
\mathfrak{N}_N &= \frac{1}{\sqrt{1+\sum_{\kappa\in N}|Z_\kappa|^2}} = \frac{1}{\sqrt{1+|\zeta_N|^2}}.
\end{aligned} \tag{5.23}$$

This wavefunction will be used throughout the remaining text.

5.3 Results

The following section begins with the calculation of the macroscopic photon numbers emitted by HHG and QSHHG and an associated discussion. This is followed by plotting the two-mode distribution function, which resembles a two-mode squeezed state and is entangled. Some entanglement features are briefly discussed. The rest of the chapter focuses mainly on single-mode properties. From the two-mode distribution function, the QSHHG distribution function is calculated. This reveals why the non-classical properties of the BSV perturbation are not carried over onto the QSHH state. Finally, projective measurements are discussed, where the photon number of the QSHH (N) or perturbative (q) mode is measured, resulting in a wavefunction in the other mode which carries interesting non-classical properties, such as squeezing and a Wigner function with negative values.

5.3.1 QSHHG: gases versus solids

In Fig. 5.1 QSHHG in solids (a-c) and in atoms (d) is compared. We utilize Eq. (5.15) to model the ZnO band structure. The parameters used are $m_* \approx 0.25m$, $E_g = 3.4$ eV, and $d_0 = 7 \times 10^{25}\ \left[\mathrm{s}^2/(\mathrm{kg}^3 \cdot \mathrm{m})\right]^{1/2}$, the last of which is converted from $d_0 = 4$ atomic units in Ref. [45]. The laser parameters are those which were used in recent experiments [112]: wavelength $\lambda_0 = 3.2$ µm and peak electric field strength $F_0 = 1.3 \times 10^9$ V/m, corresponding to peak intensity $I_0 = 5 \times 10^{11}$ W/cm^2. The electric field consists of a sine-carrier and a Gaussian envelope with pulse durations $\tau = 6T_0$, where oscillation period $T_0 = 2\pi/\omega_0 \approx 10$fs. The macroscopic propagation parameters are $N_0 = 4 \times 10^{22}$

cm^{-3}, $w_k = 40$ μm (assumed to be approximately half of the laser beam width due to the HHG nonlinearity), and $l_i = 5$ nm as determined by the absorption length. This results in the macroscopic HHG factor $(N_0 w_k l_i)^2/(2c) \approx 10^{23}$ s/m^3; $\omega_q = 2\omega_0$ is used for the squeezed vacuum field. From the pulse energy of 10 nJ, [112] one obtains $r = 13.6$ and $\sinh^2(r) \approx \cosh^2(r) = 10^{11}$ via the relation $\hbar\omega_q \langle \hat{n}_q \rangle = \hbar\omega_q \sinh^2 r = 10^{-8}$ J. The mode volume of the perturbative quantum beam must also be known for macroscopic QSHHG . In accordance with experiments [112], we choose a transverse width $w_q = 100$ μm and bandwidth $\Delta\lambda_q = 50$ nm. Inserting these values into the expression for the inverse of mode volume gives $\Delta\lambda_q/(w_q \lambda_q)^2 = 2 \times 10^{12}$ m^3.

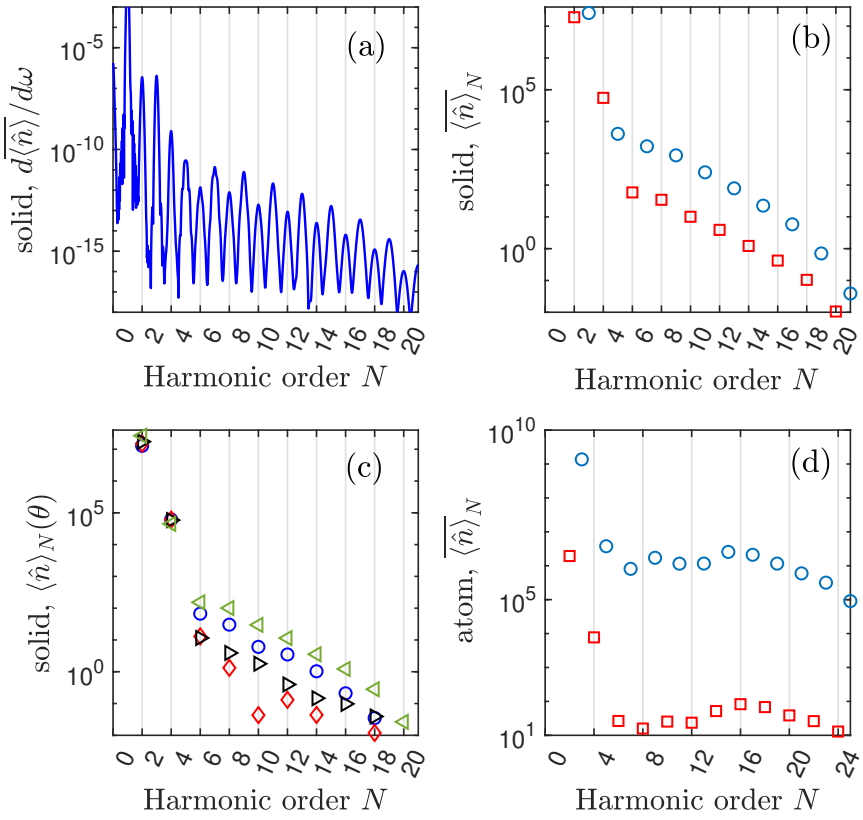

Figure 5.1: (a-c) HHG (odd) and QSHHG (even) spectrum in ZnO versus harmonic order N; (a) differential number of HH photons $d\overline{\langle\hat{n}\rangle}/d\omega$; (b) number of photons in the effective mode $\overline{\langle\hat{n}\rangle}_N$; HHG (blue circles), QSHHG (red circles). (a)-(b) average over squeezed vacuum phase θ. (c) $\langle\hat{n}\rangle_N(\theta)$: blue circles, red diamonds, black right-pointing triangles, green left-pointing triangles correspond to $\theta = 0, \pi/4, 3\pi/8, 7\pi/4$, respectively. (d) $\overline{\langle\hat{n}\rangle}_N$ averaged over θ for an atomic gas; HHG (blue circles), QSHHG (red squares). For parameters see text.

The atomic gas parameters for Fig. 5.1(d) are: hydrogen atom, $E_0 = 13.6$ eV, for dipole moment see subsection 5.2.2; laser: $\lambda_0 = 800$ nm, $I_0 = 10^{14}$ W/cm^2, $\tau = 6T_0 \approx 15$ fs. The macroscopic propagation parameters are: gas nozzle, $N_0 = 10^{18}$ cm^{-3}, $w_k = 100$ µm, and $l_i = 250$ µm, which result again in $(N_0 w_k l_i)^2/(2c) \approx 10^{23}$ s/m^3. The squeezed vacuum parameters are $\omega_q = 2\omega_0$, and the rest is the same as in Fig. 5.1(a-c).

The differential number of HH photons averaged over the BSV angle θ, $d\overline{\langle\hat{n}\rangle}/d\omega$, is plotted for ZnO in Fig. 5.1(a); (b) shows number of photons in one effective harmonic mode N averaged over θ, $\overline{\langle\hat{n}\rangle}_N$. The parameters are similar to recent experiments [112] and

agree well with the ratio of HHG to QSHHG which is roughly an order of magnitude. Fig. 5.1(c) reveals a sensitive dependence of QSHHG on θ; variation of θ changes QSHHG by up to 3 orders of magnitude. The modulation is not only a feature of a quantum perturbation and is also found in coherent control experiments with bi-chromatic coherent fields [152, 36].

Fig. 5.1(d) shows $\langle \hat{n} \rangle_N$ for gaseous atomic hydrogen to be compared with (b) for ZnO. In contrast to (b), the difference between QSHHG and HHG in the gas is six orders of magnitude. This can be understood by looking at the different scaling of HHG and QSHHG in Eqs. (5.7) and (5.12), (5.13). The main difference comes from the additional $\overline{\sigma}_q$ dependence outside the curled brackets in Eqs. (5.12) and (5.13). By denoting the ratio of QSHHG and HHG as R – a measure of the susceptibility to the quantum perturbation – we see that

$$R \propto |\sigma_q|^2 \propto \frac{I_0}{\omega_0^2} \frac{1}{\omega_q^3 m_*^2} \propto \frac{I_0}{8\omega_0^5 m_*^2}. \tag{5.24}$$

The first factor originates from $\mathbf{p}_t^2$. Note that $E_v^2 \propto \omega_q$, so that the frequency scaling of the second factor is $1/\omega_q^3$ and not $1/\omega_q^4$, as semiclassical theory would predict. The last proportionality stems from $\omega_q = 2\omega_0$.

The parameters corresponding to Fig. 5.1 include a factor of 4 reduction of both laser frequency and effective mass in the case of the solid. This contributes an overall factor of $4^7 = 16384$, which is uncompensated by the 200 times increase of intensity in the gas, and results in R increasing by a factor of ≈ 100. The difference of the solid:gas ratio in Fig. 5.1 is slightly less than 1000. This demonstrates that the simple estimate (5.24) presents a lower limit to the scaling of the solid:gas ratio.

Although solids are more susceptible to the quantum perturbation, the higher efficiency of HHG in atoms results in similar $\hat{n}_N$ for QSHHG in solids and atoms in Figs. 5.1(b) and (d). What is unique to solids is that the factor R, and thus the conversion efficiency, can be further increased by selecting materials with low effective mass. Choosing lasers with longer wavelengths is equally favorable for atoms and solids. For example, Bi related materials have $m_*/m \approx 0.002$ [153] with m being the free electron mass. Driving such a material with $\lambda_0 = 10\mu$m and leaving F_0 unchanged increases QSHHG by a factor of 5×10^6 over Fig. 5.1(b). Taking $N = 8$ in Fig. 5.1(b) as an example, QSHHG converts 10^{11} squeezed vacuum photons into 10^2 photons: a conversion efficiency of 10^{-9}. Selecting the above material and laser wavelength therefore enables an increase of the conversion

efficiency to ≈ 0.005. Further optimizations of the pump laser parameters, such as an increased beam radius, and through the use of nanostructures to enhance the density of states [154, 155, 156], bring a conversion efficiency approaching unity within reach.

The limit of near-unity conversion efficiency can be quite beneficial, as it would enable the frequency conversion of weak quantum optical states, such as Fock and entangled states (i.e. Bell states, etc...), to short wavelengths. Additionally, high conversion efficiency can be used to create potentially useful correlations and squeezing in the VUV to XUV wavelength regime. For example, if the SFG pathway for a single QSHH mode can be preferentially selected, Eq. (5.3) transitions into a two-mode sum-frequency operator. The resulting QSHH mode would be squeezed and highly efficient, as all photon pairs in the perturbation beam would get converted to that particular sideband [157]. Sideband selection can potentially be obtained through resonances of a material [158, 159] or a meta-surface, or through phase matching.

Finally, the number of HH photons in solids and atomic gases is within the range observed in experiments [112]. Thus, our simple closed-form approach, despite its approximations, exhibits an order of magnitude predictive power for conventional HHG. The accuracy can be further improved by adding absorption, more accurate models for the phase mismatch between laser and harmonics, by performing the phase matching integrals exactly, and by accounting for the effect of the Coulomb potential in the Schrödinger equation.

5.3.2 QSHH probability distribution

In this section the single effective mode QSHH photon distribution probability is calculated. It is sufficient to use a two-mode wavefunction $|\varphi_m\rangle$ consisting of the quantum perturbation and a single harmonic sideband. Tracing out the other harmonic sidebands yields higher order corrections.

The two-mode probability distribution is obtained from the wavefunction (5.23) as

$$P(m,n) = \left|\langle m,n|\varphi_m\rangle\right|^2, \tag{5.25}$$

where m, n refer to the photon number of the QSHH, and perturbative quantum mode, respectively. By summing over n, $P(m) = \sum_n P(m,n)$, and assuming an intense squeezed

vacuum field $r \gg 1$, one obtains the QSHHG photon distribution,

$$P(m) \approx \frac{(2m-1)!!}{(2m)!!} \frac{\left(2\langle\hat{n}\rangle_N \tanh^2(r)\right)^m}{(1+2\langle\hat{n}\rangle_N)^{m+1/2}}. \tag{5.26}$$

The distribution (5.26) is approximately normalized, $\sum_m P(m) = 1/\sqrt{1+2|\zeta_N|^2} \approx 1$, as $|\zeta_N|^2 \ll 1$. The approximate expression and exact numerical result are found to be in excellent agreement.

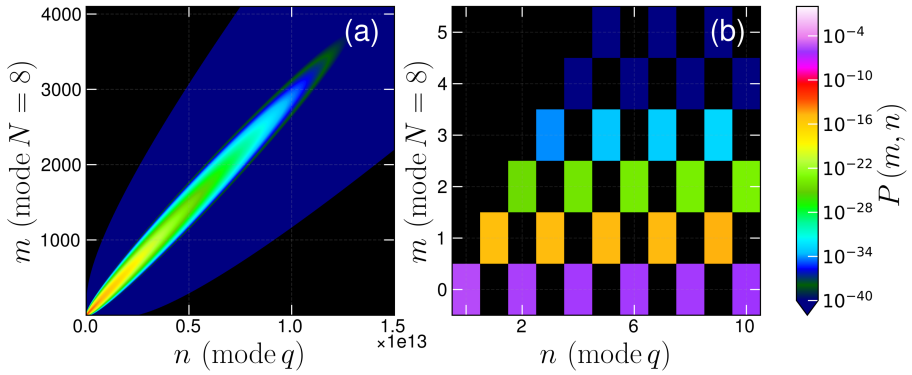

Figure 5.2: (a) Two-mode probability of QSHHG versus photon number n of the perturbative quantum mode and harmonic photon number m for $N = 8$; all parameters and $\langle\hat{n}\rangle_N(\theta = 0)$ are from Fig. 5.1(c). (b) Close-up for photon numbers close to zero.

The two-mode distribution (5.25) is plotted in Fig. 5.2(a) for harmonic order $N = 8$, see Fig. 5.1(c) for $\langle\hat{n}\rangle_N(\theta = 0)$; (b) shows a close-up for photon numbers close to zero. The distribution has been calculated numerically from Eqs. (5.25) and (5.23). Clearly, harmonic and quantum modes are entangled, as only even-even or odd-odd states are populated. Due to the large value of r, the probability extends to very high photon numbers in the quantum mode. The states $m > n$ are approximately zero, accurate to first order in $|\zeta_N|^2$.

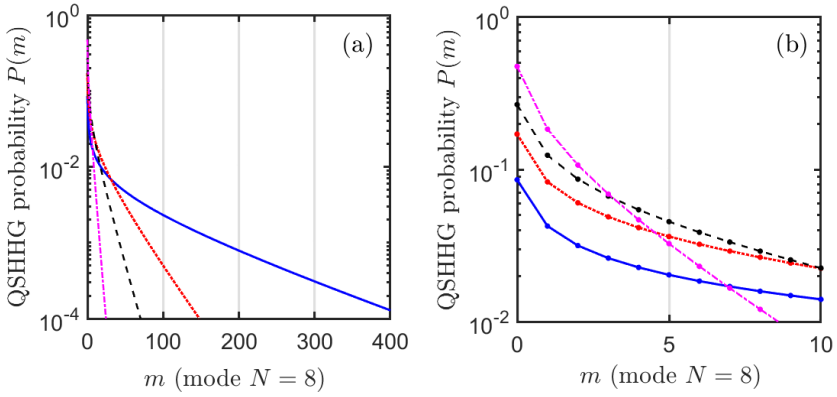

Figure 5.3: (a) Probability of QSHHG versus harmonic photon number m for $N = 8$ (full blue line), $N = 10$ (red dotted line), $N = 12$ (black dashed line), $N = 14$ (magenta dash-dotted line); m refers to number of photons in the QSHH mode N; all parameters and $\langle \hat{n} \rangle_N(\theta = 0)$ are from Fig. 5.1(c). (b) close-up for photon numbers close to zero.

In Fig. 5.3(a) the QSHHG probability $P(m)$ is plotted with a closeup in (b). The probability (5.26) agrees with the probability of a squeezed vacuum state, with the distinction that every photon state is populated and not only the even states. This is a consequence of the two-mode even-even, odd-odd probability distribution. When traced over one of the modes, all number states of the remaining mode are populated and the non-classical features are washed out. Following the above approach, $g^{(2)}(0)$ and the quadrature are obtained, which indicate a super-Poissonian distribution and photon bunching. However no non-classical features, such as squeezing, sub-Poissonian statistics, or a negative Wigner distribution [112] are indicated. In other words, for low conversion efficiency, all combinations of number states are populated and the non-classical features are traced out. However, in the case of unity conversion efficiency, where every BSV photon creates a QSHH photon, and for a single QSHH mode, only even QSHH number states are populated, thereby preserving the non-classical features [157].

For more than one QSHH mode, the entanglement between modes gets more complicated. For example, with three modes, Taylor expansion of Eq. (5.23) yields operator terms $\sum_{mnj} (\hat{a}_N^\dagger)^{2n+\eta_n} (\hat{a}_{N'}^\dagger)^{2m+\eta_m} (\hat{a}_q^\dagger)^j$, where $\eta_n, \eta_m = 0, 1$ for even, odd harmonic photon number states, respectively. The expansion coefficient of the squeezed vacuum operator is denoted by j and the photon number of the quantum mode is given by $l = 2j + 2n + 2m + \eta_n + \eta_m$. As a result, l can only be odd when only one of the harmonic modes is odd: $\eta_n = 0, 1$

and $\eta_m = 1, 0$. When both harmonic modes are odd or even, then l is even. While l can be any positive integer, n and m consist of only even or odd integers for a given l, thus resulting in a higher-dimensional checker board pattern similar to Fig. 5.2. Exploring multi-mode correlation presents an interesting avenue for future work. When the quantum mode is traced over in this three-mode case, all (even-even, odd-odd, and even-odd) states of the two harmonic modes will be populated. It is expected that this will also suppress non-classical properties and entanglement between harmonic modes, for low conversion efficiency.

The focus of the rest of the chapter is on single-mode properties of QSHHG. In the following, we demonstrate how non-classical light can be obtained from QSHHG by projective measurements. This relies on the entanglement between quantum and harmonic modes. Projective measurements of entangled wavefunctions generally result in non-classical behavior [4].

5.3.3 Projective measurement on perturbative quantum mode q

Multi-mode entanglement requires measuring all sidebands simultaneously, or limiting emission to select sidebands only; otherwise, when entangled sidebands are not measured and traced out, mixed states are generated and quantum properties destroyed [4]. Here we discuss the case of one and two sidebands. Our analysis starts with a single sideband, so that the wavefunction is limited to two modes. The number state of the perturbative quantum mode is determined as $|l\rangle_q$ by a projective measurement. Determination of the resulting wavefunction starts with a Taylor expansion of the effective two-mode wavefunction (5.23) followed by a projection on $|l\rangle_q$. The projected wavefunction, $|\varphi_N\rangle = {}_q\langle l|\varphi_m\rangle$, is found to be,

$$
\begin{aligned}
|\varphi_N\rangle &= N_\eta(-e^{i\theta})^{l/2}\sum_{m=0}^{l_\eta/2}(-1)^m\frac{\sqrt{\alpha_N}^{2m+\eta}}{\sqrt{(2m+\eta)!}}\,|2m+\eta\rangle_N \\
\alpha_N &= \frac{l_\eta|\zeta_N|^2}{2\beta_N}, \quad l_\eta = l-\eta, \quad \eta = 0, 1 \text{ for even, odd } l \\
N_{\eta=0} &\approx \frac{1}{\sqrt{\cosh(|\alpha_N|)}} \quad N_{\eta=1} \approx \frac{1}{\sqrt{\sinh(|\alpha_N|)}}.
\end{aligned}
\tag{5.27}
$$

As seen in Fig. 5.2, the product $\hat{S}_m\hat{S}_q$ produces either even-even or odd-odd number states. As such, when the projected quantum number l is even ($\eta = 0$) or odd ($\eta = 1$), the

resulting harmonic wavefunction contains only even or odd states, respectively.

From Eq. (5.27), second order coherence and quadrature of the QSHH modes are calculated. They are a function of the projected quantum mode photon number l_η. Definitions and details on the calculation are given in the supplement; we find

$$\begin{aligned} g_N^{(2)} &= \frac{1}{\tanh^2(|\alpha_N|)} \quad \text{for } \eta = 0 \\ g_N^{(2)} &= \tanh^2(|\alpha_N|) \quad \text{for } \eta = 1 \end{aligned} \tag{5.28}$$

with the second order coherence $g^{(2)} = (\langle \hat{n}^2 \rangle - \langle \hat{n} \rangle)/\langle \hat{n} \rangle^2$, and

$$\begin{aligned} \Delta X_{jN}^2 &= \frac{1}{4}\left(1+2\left(|\alpha_N|\tanh(|\alpha_N|)+(-1)^j \mathrm{Re}[\alpha_N]\right)\right), \ \eta = 0 \\ \Delta X_{jN}^2 &= \frac{1}{4}\left(1+2\left(\frac{|\alpha_N|}{\tanh(|\alpha_N|)}+(-1)^j \mathrm{Re}[\alpha_N]\right)\right), \quad \eta = 1, \end{aligned} \tag{5.29}$$

where $j = 1, 2$, the quadratures are $\hat{X}_j = 1/(2i^{j-1})(\hat{a} - (-1)^j \hat{a}^\dagger)$, and the variances $\Delta X_j^2 = \langle \hat{X}_j^2 \rangle - \langle \hat{X}_j \rangle^2$. All of the above equations were derived for $r \gg 1$, and $l_\eta \gg 1$, and give excellent agreement with exact, numerical results in this limit. Even for small l_η, the agreement is surprisingly decent.

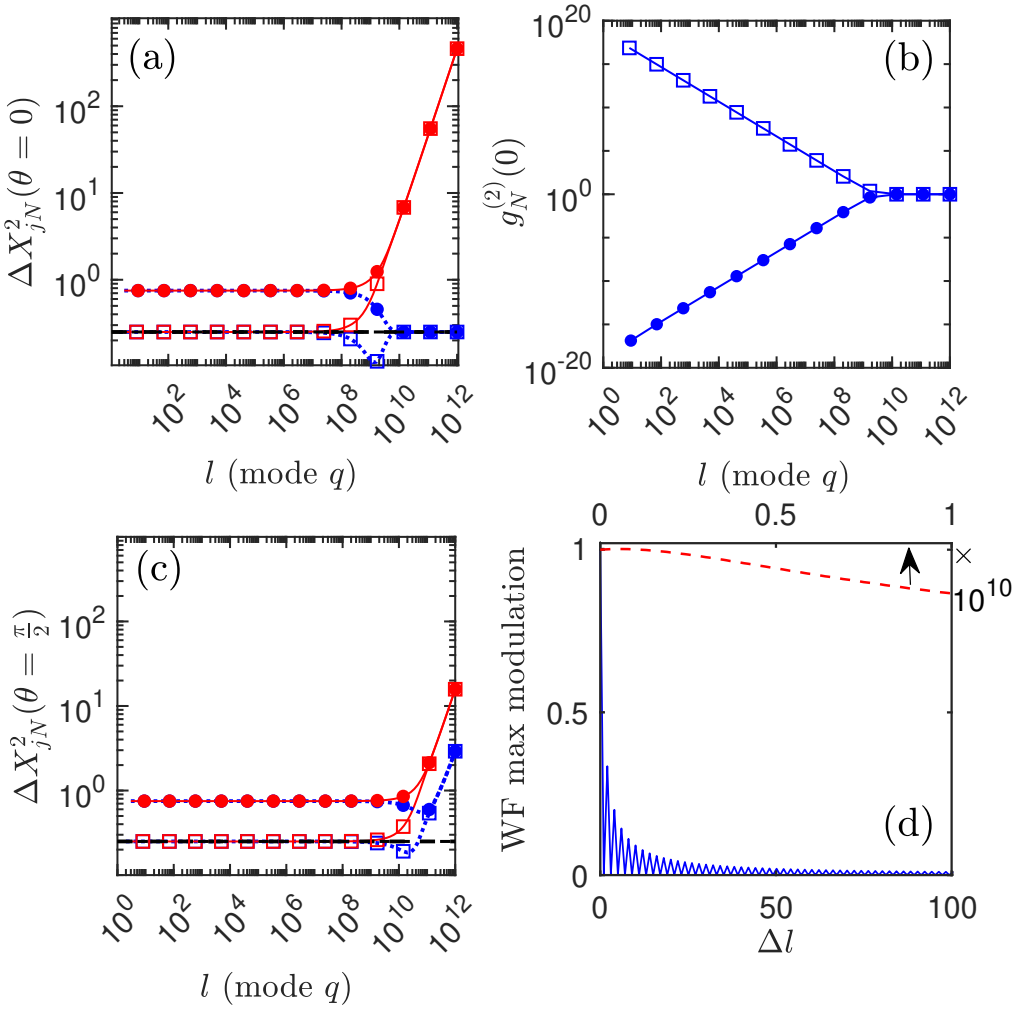

Figure 5.4: Parameters are the same as in Fig.5.1; (a-d) $|\zeta_N|^2(\theta=0)$ taken from $\langle\hat{n}\rangle_N$ for $N=8$ in 5.1(c), respectively. (a),(c) $\Delta X^2_{jN}(\theta=0,\pi/2)$ versus quantum photon number l, respectively; blue dotted, red full lines show ΔX^2_{jN} for $j=1,2$ respectively; symbols: in (a-c) squares and dots represent $\eta=0,1$ (even, odd states), respectively; symbol spacing follows a log distribution; black dashed lines indicate quadrature variance of vacuum. (b) second order correlation function $g^{(2)}(0,\theta=0)$ versus l. (d) Maximum modulation of Wigner function versus $l+\Delta l$, with $l=10^{10}$ and Δl the number state resolution; curves are normalized to the modulation at $\Delta l=0$; blue solid line is for Δl even and odd numbers, whereas red dashed line is for Δl only even numbers.

The quadrature variances and the second order correlation function are plotted for $N=8$ as a function of quantum mode photon number l in Figs. 5.4(a),(c) and (b), respectively. The parameter $|\alpha_N(\theta)|$ varies with θ for a given l. As such, quadrature variance and second order coherence are θ-dependent. Panels (a,b) are for $\theta=0$ and (c)

is for $\theta = \pi/2$. The second order correlation function for $\theta = \pi/2$ is not shown, as it is only quantitatively slightly different.

Note that the sum in the wavefunction (5.27) has a finite limit l_η. As a result, it goes over into a Schrödinger cat state [4] in the limit $l_\eta \to \infty$, i.e. coherent states with only odd or even number states populated. In the opposite limit $l_\eta \to 0$ it behaves like a heralded number state which through projection is collapsed into a single photon state of the QSHH mode.

The states with only even ($\eta = 0$ squares) or only odd ($\eta = 1$ dots) photon numbers l behave fundamentally different. In addition, in Figs. 5.4(a) and (c), blue and red represents the variances $j = 1, 2$. In the limit of even $l_{\eta=0} \to 0$, the QSHH distribution has the characteristics of a vacuum number state which has a quadrature variance of $1/4$, see blue and red open squares in Fig. 5.4(a), and $g^{(2)}(0) \to \infty$, see open squares in 5.4(b). The odd states are dominated by a one photon number state which has a quadrature variance of $3/4$, see blue and red dots in Fig. 5.4(a) and $g^{(2)}(0) \to 0$, see dots in Fig. 5.4(b). As such, the odd states, primarily composed of a one photon number state, follow a sub-Poissonian statistics and are highly non-classical. In the intermediate regime, $l \sim 10^9 - 10^{10}$ for (a), moderate squeezing does occur for the even numbered states. In the high l_η limit, even and odd states merge. All states have the $g^{(2)}(0) = 1$ of a coherent state which is typical for Schrödinger cat states. For $\theta = 0$, the quadrature $\Delta X_1^2 \to 1/4$, whereas ΔX_2^2 grows as a power function. For $\theta = \pi/2$, both quadrature variances grow as power functions.

For the three-mode case, projecting on quantum mode q, will separate even-even and odd-odd number state populations for even l from even-odd two-mode states for odd l. This results in an entangled two-harmonic mode state which will be subject to future research. However, measuring only one of the two sidebands traces out the other and this likely results in a mixed state, i.e. no quantum features, since the sidebands are entangled [4]. Therefore, all emitted sidebands ought to be measured.

The fact that the projected odd number state ranges from a single photon state to a Schrödinger cat state in dependence on l_η opens the possibility of quantum engineering QSHHG. Experimental realization is complicated by two facts. (i) The probability of the single photon state is low. (ii) The wavefunction contains even and odd number states; due to the wide range of l_η, it is difficult to resolve number states into single photons. As a result, even and odd states will mix and average out squeezing and the $g_N^{(2)}(0)$; for example, amplitude squeezing of the single photon state for low l will be lost.

(i) We find from Fig. 5.2(b) that the probability of the small $n = l_\eta$ odd photon

states is dominated by $m = 1$ with a probability of $\approx 10^{-15}$. The probability scales as $\propto (|\zeta_N|^2)^{2m+\eta}/\cosh(r)$, and therefore drops fast with increasing $2m + \eta$. As the two-mode probability in Fig. 5.2(b) is approximately triangular, the one photon number state is essentially pure. Few photon number states m offer less of an advantage; they consist of a superposition of even or odd number states from $n = 0$ or $n = 1$ up to $n = m$, respectively. Their purity is comparable to that of a finite Schrödinger cat state.

We recall from our discussion of increasing the conversion efficiency of QSHHG below Eq. (5.24) that it can be increased by more than six orders of magnitude by optimizing material and laser parameters. We decrease r so that the average number of photons, $\hat{n}_N = |\zeta_N|^2 \cosh^2(r)$ remains constant. As a result $\cosh(r)$ decreases by three orders of magnitude, and the probability of creation of a one photon state increases by nine orders of magnitude to 10^{-6}. If in addition other parameters are optimized, by for example using a wider pump beam radius, adding another 2 orders of magnitude, a probability for generating a single photon state of about 10^{-4} appears achievable. For a MHz laser system, this would mean the generation of a single photon state every 10ms.

(ii) Techniques for resolving the number of photons are limited to $l \sim 10$ [160]. This gives experimental access to single-photon and few odd-photon states and presents a path to shift the generation of pure heralded single-photon states towards the XUV. In the opposite limit of Schrödinger cat states, $l \gg 1$, projecting on the number state with large l presents a considerable problem for existing technologies. Schrödinger cat states exhibit characteristic interferences near the zeros of the quadratures, with opposite phase shifts for odd- and even-parity states and with varying fringe spacing for different average number of photons. With increasing uncertainty in the photon number resolution, these fringes will be washed out, see Fig. 5.4(d), where $l = 10^{10}$, Δl represents the photon number resolution, and the Wigner function is averaged over Δl. Snapshots of the Wigner function for various Δl are shown in the supplement. We show two cases, one with Δl running over even and odd numbers (blue full line), and one assuming that parity measurement is possible with Δl only extending over even numbers. Without parity measurement, the fringes average out over 100 number states, for even Δl and they vanish immediately for odd Δl, as even (l) and the next odd state ($l + 1$) are phase shifted by π. On the other hand, with the parity measurement, averaging over 10^{10} (even only) number states is possible with small losses in the fringe visibility. However, preserving the parity of the quantum mode for such large l is practically impossible, as loosing one photon in $\sim 10^{10}$ would suffice to toggle the parity of the state. The conversion efficiency would have to be

increased to levels higher than the typical optical losses of an experiment ($\sim 1\%$) for the parity to be maintained and for the cat state to be measurable. Even without knowledge of parity, a measurement of $g^{(2)}(0) \to 1$ and of the quadratures' excess noise by projecting over a range of photon numbers would provide an indication of the generation of the cat states. The quadratures's noise can be measured in the (few photons) quantum sidebands with homodyne interferometry [161] or, potentially, by extending *in-situ* techniques to the single shot [152].

5.3.4 Projective measurement on QSHH mode N

The analysis is performed for Eq. (5.23) with one QSHH mode, i.e. under the assumption that only one sideband is generated. Tracing out the other sidebands in a multi-mode scenario will modify the parameters ζ_N and β_N, but will leave the two-mode wavefunction unchanged otherwise. In a projective measurement, the number of photons m in the effective QSHH mode N is measured. The resulting wavefunction for the quantum mode q depends on m and is calculated by projecting an effective number state on the wavefunction (5.23) limited to two modes, $|\varphi_q\rangle = {}_N\langle m|\varphi_m\rangle$. This yields

$$|\varphi_q\rangle = N_m \sum_{l=0}^{\infty} (-1)^l \frac{\sqrt{(2l+m)!}}{l!} \beta_N^l \, |2l+m\rangle_q \,. \tag{5.30}$$

The norm is given by

$$\begin{aligned} \frac{1}{N_m^2} \approx \frac{\cosh(r)}{\sqrt{1+2\langle\hat{n}\rangle_N}} \Bigg[(2m-1)!! \left(\frac{\sinh(r)}{1+2\langle\hat{n}\rangle_N} \right)^m \\ + \frac{l}{2}(3m-1)(2m-3)!! \left(\frac{\sinh(r)}{1+2\langle\hat{n}\rangle_N} \right)^{m-1} \Bigg]. \end{aligned} \tag{5.31}$$

With the above wavefunction second order coherence and quadrature variances are calculated; for definitions and details see the supplement. We obtain for the second order coherence

$$g_N^{(2)}(0) \approx 1 + \frac{2}{2m+1}. \tag{5.32}$$

The quadratures ($j = 1, 2$) are found to be

$$\Delta X_{jN}^2 \approx \frac{m(m-1)}{2(2m-1)}\left(1 + (-1)^j \cos(\theta)\frac{1+|\zeta_N|^2}{\tanh r}\right) + \frac{(2m+1)}{4}\frac{A_j(r,\theta) + |\zeta_N|^2(1+\langle\hat{n}\rangle_N)}{1+2\langle\hat{n}\rangle_N} \tag{5.33}$$

with $A_j(r,\theta) = \cosh^2 r + \sinh^2 r + 2(-1)^j \cosh r \sinh r \cos(\theta)$ and $\langle\hat{n}\rangle_N = \cosh^2 r|\zeta_N|^2$. For the case $\theta = 0$, $\tanh r \approx 1$, $\langle\hat{n}\rangle_N \gg 1$ one obtains

$$\Delta X_{jN}^2 \approx \frac{2m+1}{4}\frac{(\cosh(r)+(-1)^j\sinh(r))^2}{1+2\langle\hat{n}\rangle_N} + \frac{|\zeta_N|^2}{4}\left(1+\frac{1}{2(2m-1)}\right). \tag{5.34}$$

We see that the quadrature consists of two contributions; the first term contains the quadrature of a squeezed vacuum state, but has a prefactor that depends on m and $\langle\hat{n}\rangle_N$. The second term is commonly not part of BSV states. Both modifications come from the mode mixing term $\hat{a}_N^\dagger \hat{a}_q^\dagger$ in Eq. (5.23). Finally, all of the above equations give excellent agreement with the exact, numerical results.

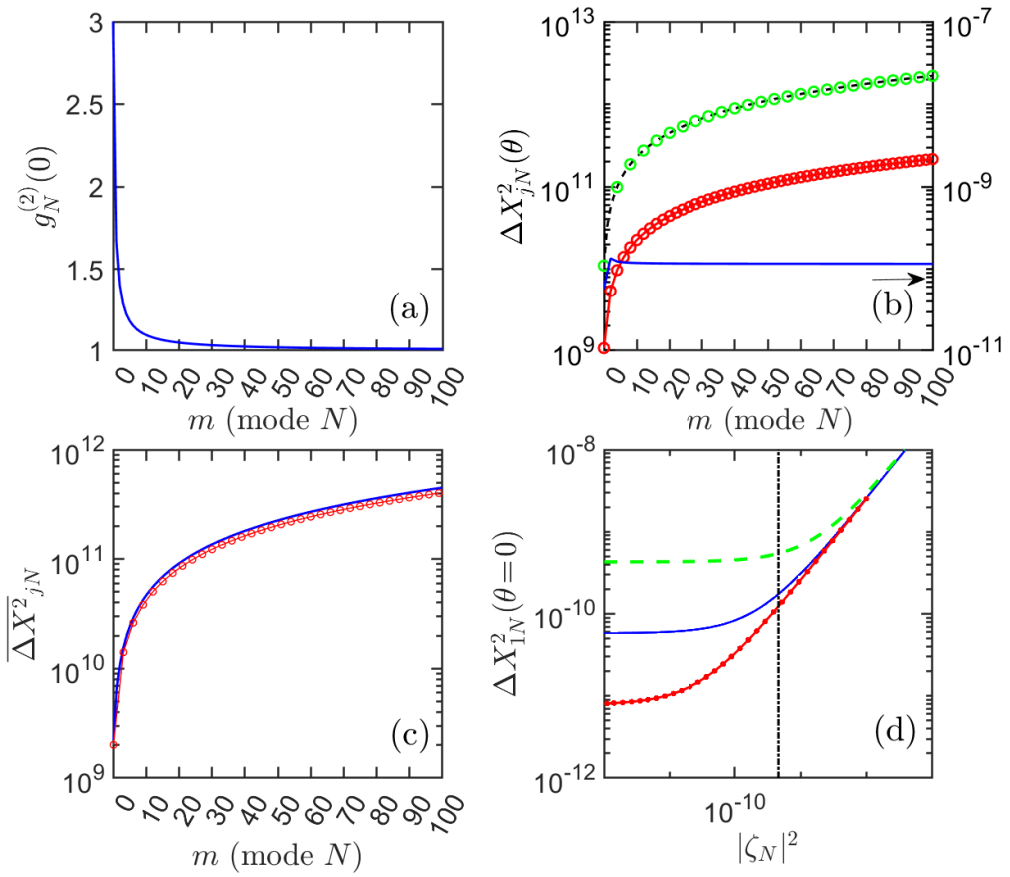

Figure 5.5: (a) second order correlation $g_N^{(2)}(0)$ versus m; independent of all other parameters. (b) Quadrature variances $\Delta X_{jN}^2(\theta)$ ($j = 1, 2$) for squeezed vacuum angle θ versus harmonic photon number m; evaluated for the effective QSHH order $N = 8$; parameters from Fig. 5.1(b); blue line, red circles for $\theta = 0$, $j = 1, 2$, respectively; black dashed line, green circles (on top) for $\theta = \pi/2$, $j = 1, 2$, respectively. (c) same as (b), but angle (θ) averaged quadrature variances for $N = 8$; blue line, red line with open circles for $j = 1, 2$, respectively. (d) $\Delta X_1^2(\theta = 0)$ evaluated from Eq. (5.34) versus $|\zeta_N|^2$ for $m = 50$ and for $r = 12.4$ (green dashed), $r = 13.4$ (full blue), $r = 14.4$ (red line with dots); dash-dotted line indicates $|\overline{\zeta}_N|^2$ of (b) for $N = 8$.

The wavefunction in Eq. (5.30) represents an m-photon added squeezed vacuum state [162]. For $m = 0$, $g_N^{(2)}(0) = 3$ takes the value of a squeezed vacuum state, see Fig. 5.5(a). Further, the product of quadrature variances in Fig. 5.5(b) for $m = 0$ and $\theta = 0$ gives $1/16$, the minimum uncertainty. However, the maximum degree of squeezing, occurring for $m = 0$ is reduced from that of the input state, which is $\Delta X_1^2 = \frac{1}{4}e^{-2r} \simeq 5 \times 10^{-13}$.

This can be understood from the fact that mixing between harmonic and quantum modes in QSHHG changes $\beta \to \beta_N$, so that in Eq. (5.34) a residual term $\propto |\zeta_N|^2$ remains, even for $m = 0$. This term is positive and reduces squeezing, although minimum uncertainty is sustained. Finally, due to mode mixing, the quadrature variances for $m \neq 0$ are different from a regular squeezed state, see blue line and red dots in Fig. 5.5(b) for $\Delta X^2_{jN}(\theta = 0)$ with $j = 1, 2$, respectively. Both quadratures increase with m, making the state larger than a minimum uncertainty state.

For $\theta = \pi/2$ squeezing disappears, like for a squeezed vacuum beam, see the black dashed line and green circles in Fig. 5.5(b) for $j = 1, 2$, respectively. The angle averaged quadrature variance also shows no squeezing, in agreement with a regular squeezed vacuum beam; however $\overline{\Delta X^2_{jN}}$ with $j = 1, 2$ need not necessarily be the same, as $|\zeta_N(\theta)|^2$ is not the same for θ and $\theta + \pi$, see Fig. 5.1(c). Finally, Eq. (5.34) is evaluated for a range of $|\zeta_N|^2$ for three values of r and for $m = 50$; the quadrature variance $\Delta X^2_{1N}(\theta = 0)$ is plotted versus $|\zeta_N|^2$ in Fig. 5.5(d). The black dash-dotted line indicates the value of $|\zeta_N|^2$ in 5.5(b). The squeezed vacuum parameter exerts large influence for small $|\zeta_N|^2$ for which the first term in Eq. (5.34) is dominant. This influence disappears for larger $|\zeta_N|^2$, where the second term in Eq. (5.34) dominates. The linear growth highlights that high conversion efficiency compromises the potential for squeezing.

Photon-added squeezed vacuum states have demonstrated an ability to measure phase closer to the Heisenberg limit than other quantum states, such as squeezed vacuum states [163]. Thus, measuring such states during QSHHG seems important. As the projection is done on the (weak) QSHH mode, photon number resolution is less of an issue than in the previous section. The photon added squeezed vacuum state remains a macroscopic state whose quadratures can be measured with conventional homodyne detection [161] or an extension of attosecond techniques such as TIPTOE [164] and nonlinear photoconductive field sampling [165] of quantum fields. Examples of Wigner functions for this state are shown in supplement 5.5. balanced detectors at the high photon fluxes in the quantum mode. However, as discussed above the efficiency of QSHHG can be substantially increased, which allows the use of quantum beams with a much smaller amount of photons. Aside from these technical challenges, an indication of photon added squeezed vacuum states could be obtained experimentally, by measuring the increase of the variance of the quadratures and decrease of $g^{(2)}_N(0)$ with increasing m.

5.4 Conclusion

High-harmonic generation is a process that can emit coherent XUV radiation, when driven by sufficiently intense lasers. For classical driving lasers, commonly classical XUV radiation is emitted. When the classical pump laser as perturbation is replaced by a quantum field, such as a bright squeezed vacuum, properties of high-harmonic generation, such as cutoff and photon statistics (bunching), are modified, however non-classical properties have not been demonstrated yet. In addition, scaling quantum HHG into the XUV regime appears to be challenging.

Quantum sideband high harmonic generation serves as an alternative approach that leverages the strength of readily available intense classical fields to generate the short-wavelength high harmonics, and the quantum properties of a weak perturbing beam to engineer the quantum-optical properties of the harmonics. This imposes less stringent restrictions on the brightness of the quantum perturbation and as such, widens the range of suitable quantum sources.

In this work, a comprehensive theoretical framework of quantum sideband high-harmonic generation has been introduced. It serves as a foundation for designing and developing quantum sideband high-harmonic generation as a short-wavelength attosecond source for quantum light generation. Our theoretical analysis has revealed that quantum sideband high harmonic generation creates entanglement between the harmonic sideband modes and between the harmonic sidebands and the quantum perturbation. The entangling allows to quantum engineer high harmonic generation via projective measurements. As a result, a variety of states commonly used in quantum information theory can be generated, such as heralded number states, Schrödinger cat states, and photon added squeezed vacuum states. These states will find applications in extending quantum sensing, quantum imaging, and quantum information science to the XUV regime.

Challenges to realize theses states experimentally and potential pathways to overcome them have been discussed. The biggest challenges are (i) the many-mode entanglement between all the sidebands and the BSV and (ii) the low conversion efficiency, which requires BSV beams with a large number of photons; however, still significantly less than what needed to drive high harmonic emission with the BVS field alone.

(i) Multi-mode entanglement requires measuring all sidebands simultaneously to avoid generating a mixed state, when projecting on the BSV. Strategies to monochromatize the emission spectrum were discussed, such as through the use of resonances or phase

matching. On the other hand, multi-mode entanglement provides an avenue for creating multi-mode correlations, an interesting avenue for future work.

(ii) The great disparity in photon numbers between sidebands and quantum mode limits the ability to generate, preserve and measure the quantum-optical states, whether generated by direct upconversion or by a projective measurement. This is a common issue when dealing with bright quantum-optical states, and an active area of research. Our simulations reveal that the conversion efficiency scales very favorably with the laser parameters (intensity, wavelength), and the effective mass of the electron, and that near-unity conversion efficiency can potentially be achieved with the help of resonant metasurfaces and optimized phase matching conditions. This boost in efficiency would unlock the potential of high-order sideband generation for the creation of the quantum-optical states predicted in this work.

5.5 Supplementary for chapter 5

5.5.1 Photon wavefunction

The semiclassical model of intense laser atom interaction treats high harmonic generation (HHG) and intense pump laser as a classical electric field [28]. Here, the model is generalized to treat high harmonic (HH) modes and quantum sideband (QSHH) modes quantum optically. Quantum sideband high harmonic generation (QSHHG) represents the generation of HH sidebands through mixing of a quantum field, such as bright squeezed vacuum (BSV), with HHG. The intense pump laser modes are treated classically, and back-action of high harmonic (HH) modes on laser modes is neglected. Our analysis starts from the Schrödinger equation in length gauge,

$$i\hbar\partial_t\Psi = \hat{H}\Psi = \left(\hat{H}_m + \hat{H}_f + \hat{H}_i\right)\Psi, \tag{5.35}$$

where $\hat{H}_m = \hat{\mathbf{p}}^2/(2m) + V(\mathbf{r})$ is the matter Hamiltonian, $\mathbf{p} = -i\hbar\boldsymbol{\nabla}_{\mathbf{r}}$ is the momentum operator, $\hat{H}_f = \sum_\kappa \hbar\omega_k \left(\hat{a}^\dagger_\kappa \hat{a}_\kappa\right)$ is the field Hamiltonian, and $\hat{H}_i = \sum_j \mathbf{r}|e|\hat{\mathbf{F}}(\mathbf{x}_j)$ is the interaction Hamiltonian. Electron charge and mass are denoted by e, m, and $\mathbf{r}, \mathbf{x}_j$ represent the relative and center of mass coordinates of atom j. The atom index is not important for the microscopic part of the derivation and will not be given explicitly. It will be used for macroscopic HHG and QSHHG taking into account propagation effects. Further, $\hat{a}^\dagger_\kappa, \hat{a}_\kappa$ are the creation and annihilation operators of a light mode with polarization $\mathbf{e}_\kappa$ and

wavevector $\mathbf{k} = k\mathbf{n}$; $k = \omega_k/c$, and $\mathbf{n}$ is the unit vector along propagation direction. For brevity, we use the multi-index $\kappa \equiv \mathbf{k}s$, where $s = 1, 2$ is the polarization index. Finally, the electric field and vector potential operators in dipole approximation,

$$\hat{\mathbf{F}}(\mathbf{x}) = i \sum_{\kappa} \eta_k \omega_k \mathbf{e}_\kappa \left(\hat{a}_\kappa e^{i\mathbf{kx}} - \hat{a}_\kappa^\dagger e^{-i\mathbf{kx}} \right) \tag{5.36a}$$

$$\hat{\mathbf{A}}(\mathbf{x}) = \sum_{\kappa} \eta_k \mathbf{e}_\kappa \left(\hat{a}_\kappa e^{i\mathbf{kx}} + \hat{a}_\kappa^\dagger e^{-i\mathbf{kx}} \right) \tag{5.36b}$$

do not depend on $\mathbf{r}$. Here, $\eta_k^2 = \hbar/(2\omega_k \varepsilon_0 V)$, ε_0 is the vacuum permittivity, and V the quantization volume.

Eq. (5.35) is solved by inserting the Ansatz

$$|\Psi\rangle = |0\rangle \otimes |\phi_0(t)\rangle + \int d^3p \, |\mathbf{p}\rangle \otimes |\phi_\mathbf{p}(t)\rangle, \tag{5.37}$$

where $|0(\mathbf{r})\rangle$ is the matter ground state with binding energy E_0; continuum states are approximated by plane wave states $|\mathbf{p}\rangle = 1/(2\pi\hbar)^{3/2} \exp((i/\hbar)\mathbf{pr})$, and $\phi_l(t)$ $(l = 0, p)$ are the corresponding ground and continuum state photon wavefunctions. The strong field approximation is used which is based on two assumptions. First, the effect of the Coulomb potential on the continuum states is neglected [28]. Second, ground state and continuum states are assumed to be approximately orthogonal, $\langle \mathbf{p}|0\rangle \approx 0$.

The matter wavefunctions are integrated out by projecting the functionals $\langle 0|$, $\langle \mathbf{p}|$ on Eq. (5.35). This results in two coupled equations for the photon wavefunctions $\phi_0(t), \phi_\mathbf{p}(t)$. These equations are transformed by using the Ansatz $|\phi_l\rangle = \hat{U}_i \hat{U}_v \hat{D}_\alpha |\varphi_l\rangle$ $(l = 0, \mathbf{p})$ [96]. The first operator $\hat{D}_\alpha = \prod_\kappa \hat{D}(\alpha_\kappa)$ removes the strong laser field from the photon wavefunctions. Here, κ runs over the modes of the classical pump field, and

$$\hat{D}(\alpha_\kappa) = \exp(\alpha_\kappa(t)\hat{a}_\kappa^\dagger - \alpha_\kappa^*(t)\hat{a}_\kappa) \tag{5.38}$$

is the coherent state operator of mode κ with $\alpha_\kappa(t) = \alpha_\kappa \exp(-i\omega_k t)$. The second operator $\hat{U}_v = \exp(i|e|/\hbar \mathbf{r}\hat{\mathbf{A}})$ transforms the Schrödinger equation from length to velocity gauge. Finally, the third (interaction representation) operator $\hat{U}_i = \exp(-i/\hbar \hat{H}_f t)$ eliminates the field Hamiltonian and makes the photon operators time dependent. Working out the

transformed equations of motion yields

$$i\hbar\partial_t|\varphi_0\rangle = E_0|\varphi_0\rangle + \int d^3p\, \mathbf{d}^*(\mathbf{p}_t)\,|e|\tilde{\mathbf{F}}(t)\,|\varphi_\mathbf{p}\rangle \tag{5.39a}$$

$$i\hbar\partial_t|\varphi_\mathbf{p}\rangle = \left(\frac{\mathbf{p}_t^2}{2m} + \frac{|e|}{m}\mathbf{p}_t\hat{\mathbf{A}}(t)\right)|\varphi_\mathbf{p}\rangle + \mathbf{d}(\mathbf{p}_t)\,|e|\tilde{\mathbf{F}}(t)\,|\varphi_0\rangle, \tag{5.39b}$$

where $\mathbf{p}_t = \mathbf{p} + |e|\boldsymbol{\mathcal{A}}(t)$. Further, $\mathbf{d}(\mathbf{p}) = \langle\mathbf{p}|\mathbf{x}|0\rangle = d_0\mathbf{p}/(\mathbf{p}^2/(2m) + E_0)^3$ is the transition dipole moment between ground and continuum plane wave states [28] with d_0 specified in the main part of the chapter. Note that $\hat{D}_\alpha$ and $\hat{U}_i$ transform the electric field and vector potential operators into $(\hat{D}_\alpha(t)\hat{U}_i)^\dagger\hat{\mathbf{F}}\hat{D}_\alpha(t)\hat{U}_i = \tilde{\mathbf{F}}(t) = \boldsymbol{\mathcal{F}}(t) + \hat{\mathbf{F}}(t)$ and $(\hat{D}_\alpha(t)\hat{U}_i)^\dagger\hat{\mathbf{A}}\hat{D}_\alpha(t)\hat{U}_i = \boldsymbol{\mathcal{A}}(t) + \hat{\mathbf{A}}(t)$; $\boldsymbol{\mathcal{F}}(t)$ and $\boldsymbol{\mathcal{A}}(t)$ are the classical intense laser electric field and vector potential with center frequency ω_0 and wavevector $\mathbf{k}_0$. All fields are time dependent in the interaction picture. Further, as the classical fields are much stronger than the quantum fields, $\boldsymbol{\mathcal{A}}^2$ is retained in Eq. (5.39), while $\hat{\mathbf{A}}^2$ is neglected. Although Eq. (5.39) still contains the quantum operators of the classical pump field modes, they are disregarded in the following derivation. Finally, all fields depend on the position of atom $\mathbf{x}_j$ at which HHG is taking place; this is not explicitly stated.

For integration of Eq. (5.39b) the following relation is useful, $\partial_t\exp(\hat{B}(t)) = (\partial_t\hat{B} + (1/2)[\hat{B}(t), \partial_t\hat{B}])\exp(\hat{B}(t))$, which is valid as long as the commutator gives a c-number. Here, the commutator results in a small phase term which is neglected. We obtain

$$\begin{aligned}|\varphi_\mathbf{p}(t)\rangle &= -i\int_{t_0}^{t} dt'\,\hat{c}_\mathbf{p}(t')\left|\varphi_0(t')\right\rangle \\ \hat{c}_\mathbf{p}(t) &= \tilde{\Omega}(t)\hat{D}_\sigma^\dagger(t)\exp\left(iS(t)\right).\end{aligned} \tag{5.40}$$

where t_0 is some initial time. Further, $\tilde{\Omega}(t) = \Omega(t) + \hat{\Omega}(t) = (|e|/\hbar)\mathbf{d}(\mathbf{p}_t)\tilde{\mathbf{F}}(t)$ is a generalized Rabi frequency that consists of a classical part $\Omega(t) = (|e|/\hbar)\mathbf{d}(\mathbf{p}_t)\boldsymbol{\mathcal{F}}(t)$, and an operator part $\hat{\Omega}(t) = \sum_\kappa\hat{\Omega}_\kappa(t)$ with

$$\hat{\Omega}_\kappa(t) = -i\Omega_\kappa(t)\left(\hat{a}_\kappa^\dagger e^{i\omega_k\tau} - \hat{a}_\kappa e^{-i\omega_k\tau}\right). \tag{5.41}$$

Here, $\Omega_\kappa(t) = (|e|/\hbar)\eta_k\omega_k(\mathbf{e}_\kappa\mathbf{d}(\mathbf{p}_t))$, and $\tau = t - (\mathbf{n}\mathbf{x}_j)/c$. The classical action integral is

given by

$$S(t) = \frac{1}{\hbar}\int_{t_0}^{t}\left(\frac{1}{2m}\mathbf{p}_\tau^2 + E_0\right)d\tau. \tag{5.42}$$

Finally, the continuum electron is dressed with a displacement operator $\hat{D}_\sigma^\dagger(t) = \prod_\kappa \hat{D}^\dagger(\sigma_\kappa(t))$; for a definition of $\hat{D}$ see Eq. (5.38). Here, $\hat{D}^\dagger\left(\sigma_\kappa(t)\right) = \exp(-\hat{\sigma}_\kappa)$ with $\hat{\sigma}_\kappa = \sigma_\kappa(t)\hat{a}_\kappa^\dagger - \sigma_\kappa^*(t)\hat{a}_\kappa$ and

$$\begin{aligned}\sigma_\kappa(t) &= \frac{|e|E_\upsilon}{\hbar}\overline{\sigma}_\kappa(t)e^{i\omega_k\tau},\\ \overline{\sigma}_\kappa(t) &= -\frac{i}{\omega_k}\int_{t_0}^{t}dt'\left(\mathbf{e}_\kappa\mathbf{v}_{t'}\right)e^{-i\omega_k(t-t')}.\end{aligned} \tag{5.43}$$

For $\omega_k \gg \omega_0$, $\overline{\sigma}_\kappa \approx (\mathbf{e}_\kappa\mathbf{v}_t)/\omega_k^2$ where $\mathbf{v} = \mathbf{p}/m$ is the electron velocity. This assumes that the contribution of the integral at time t_0 can be neglected.

Inserting Eq. (5.40) into Eq. (5.39a) results in an integro-differential equation for $|\varphi_0\rangle$,

$$\partial_t|\varphi_0(t)\rangle = -\int d^3p\,\hat{c}_\mathbf{p}^\dagger(t)\int_{t_0}^{t}dt'\,\hat{c}_\mathbf{p}(t')\,|\varphi_0(t')\rangle. \tag{5.44}$$

In the weak depletion limit, $|\varphi_0\rangle$ can be pulled out of the integral on the right hand side of Eq. (5.44) by integration by parts; higher order terms are neglected. The resulting differential equation of motion is

$$\partial_t|\varphi_0(t)\rangle \approx \left(\partial_t\hat{\mathfrak{h}}(t)\right)|\varphi_0(t)\rangle. \tag{5.45}$$

Integration of Eq. (5.45) by the method of Magnus and Fer [166] results to lowest order in

$$\begin{aligned}|\varphi_0(t)\rangle &\approx \exp\left(\hat{\mathfrak{h}}(t)\right)|\varphi_0(t_0)\rangle\\ \hat{\mathfrak{h}} &= -\int d^3p\int_{t_0}^{t}dt'\,\hat{c}_\mathbf{p}^\dagger(t')\int_{t_0}^{t'}dt''\,\hat{c}_\mathbf{p}(t'').\end{aligned} \tag{5.46}$$

The next order term in the Magnus Fer expansion,

$$\exp\left(\int_{t_0}^{t}dt'\int_{t_0}^{t}dt''\left[\partial_{t'}\hat{\mathfrak{h}},\partial_{t''}\hat{\mathfrak{h}}\right]\right), \tag{5.47}$$

is small and is neglected, see the discussion of the one- and two-photon operator terms in the next section.

Zero- one- and two-photon operator terms

The operator $\exp(\hat{\mathfrak{h}}(t))$ is not unitary due to the coupling between ground state and continuum photon wavefunction. In order to isolate the unitary part of the wavefunction, $\hat{\mathfrak{h}}(t)$ is split into an anti-Hermitian part plus small remainder. This is done here for zero-, one- and two-operator terms $\hat{\mathfrak{h}} \approx \mathfrak{h}^{(0)} + \hat{\mathfrak{h}}^{(1)} + \hat{\mathfrak{h}}^{(2)}$, respectively; higher order contributions and a phase term associated with the quantum statistics force [108, 167] are not considered here.

The expansion of $\hat{\mathfrak{h}}$ is done, by first expanding $\hat{c}_{\mathbf{p}}$ in Eq. (5.40) up to two-photon operator terms, $\hat{c}_{\mathbf{p}} \approx \hat{c}^{(0)}_{\mathbf{p}} + \hat{c}^{(1)}_{\mathbf{p}} + \hat{c}^{(2)}_{\mathbf{p}}$ with

$$\begin{aligned}
\hat{c}^{(0)}_{\mathbf{p}}(t) &= \Omega(t) e^{iS(t)} \\
\hat{c}^{(1)}_{\mathbf{p}}(t) &= \sum_{\kappa} \left(\hat{\Omega}_{\kappa}(t) - \Omega(t)\hat{\sigma}_{\kappa}(t) \right) e^{iS(t)} \\
\hat{c}^{(2)}_{\mathbf{p}}(t) &= \sum_{\kappa,\kappa'} \left(\frac{1}{2}\hat{\sigma}_{\kappa}(t)\hat{\sigma}_{\kappa'}(t) - \hat{\Omega}_{\kappa}(t)\hat{\sigma}_{\kappa'}(t) \right) e^{iS(t)}.
\end{aligned} \tag{5.48}$$

From this, $\hat{\mathfrak{h}} = \hat{\mathfrak{h}}^{(0)} + \hat{\mathfrak{h}}^{(1)} + \hat{\mathfrak{h}}^{(2)}$ in relation (5.46) is determined up to second order with

$$\hat{\mathfrak{h}}^{(0)} = -\int d^3p \int_{t_0}^{t} dt' \left(\hat{c}^{(0)*}_{\mathbf{p}} \hat{C}^{(0)}_{\mathbf{p}} \right)(t') \tag{5.49a}$$

$$\hat{\mathfrak{h}}^{(1)} = -\int d^3p \int_{t_0}^{t} dt' \left(\hat{c}^{(0)*}_{\mathbf{p}} \hat{C}^{(1)}_{\mathbf{p}} + \hat{c}^{(1)\dagger}_{\mathbf{p}} \hat{C}^{(0)}_{\mathbf{p}} \right)(t') \tag{5.49b}$$

$$\hat{\mathfrak{h}}^{(2)} = -\int d^3p \int_{t_0}^{t} dt' \left(\hat{c}^{(0)*}_{\mathbf{p}} \hat{C}^{(2)}_{\mathbf{p}} + \hat{c}^{(2)\dagger}_{\mathbf{p}} \hat{C}^{(0)}_{\mathbf{p}} + \hat{c}^{(1)\dagger}_{\mathbf{p}} \hat{C}^{(1)}_{\mathbf{p}} \right)(t'). \tag{5.49c}$$

Here, we have introduced $\hat{C}^{(j)}_{\mathbf{p}}(t) = \int_{-\infty}^{t} dt' \hat{c}^{(j)}_{\mathbf{p}}(t')$ $(j = 0, 1, 2)$ for the inner time integral. Note that HHG terms should have the photon operator term outside of the inner time integral, i.e. they should all be represented by small letter terms $\hat{c}^{(1,2)}_{\mathbf{p}}$. This is also required to obtain unitary operators for HHG and QSHHG. To achieve this, we perform integration by parts of the terms in Eqs. (5.49b) and (5.49c) containing $\hat{C}^{(1,2)}_{\mathbf{p}}$. For example, $\int^t dt' \hat{c}^{(0)*}_{\mathbf{p}} \hat{C}^{(1)}_{\mathbf{p}} = -\int^t dt' \hat{c}^{(1)}_{\mathbf{p}} \hat{C}^{(0)*}_{\mathbf{p}} + R$, where R is a small residual term. Finally the last

term in Eq. (5.49c) has a one-photon operator in the ionization and emission part; as we are not interested in two color ionization, this term is neglected from hereon.

Applying the above steps to Eq. (5.49) yields

$$\hat{\mathfrak{h}}^{(0)} = -\int d^3p \int_{t_0}^{t} dt' \left(\hat{c}_{\mathbf{p}}^{(0)*}\hat{C}_{\mathbf{p}}^{(0)}\right)(t') \tag{5.50a}$$

$$\hat{\mathfrak{h}}^{(1)} \approx \int d^3p \int_{t_0}^{\infty} dt' \left(\hat{c}_{\mathbf{p}}^{(1)}\hat{C}_{\mathbf{p}}^{(0)*} - \hat{c}_{\mathbf{p}}^{(1)\dagger}\hat{C}_{\mathbf{p}}^{(0)}\right)(t') \tag{5.50b}$$

$$\hat{\mathfrak{h}}^{(2)} \approx \int d^3p \int_{t_0}^{\infty} dt' \left(\hat{c}_{\mathbf{p}}^{(2)}\hat{C}_{\mathbf{p}}^{(0)*} - \hat{c}_{\mathbf{p}}^{(2)\dagger}\hat{C}_{\mathbf{p}}^{(0)}\right)(t'), \tag{5.50c}$$

where we also have let $t \to \infty$ in the HH and QSHH terms (5.50b) and (5.50c).

Next, we evaluate the individual terms in Eq. (5.50) by inserting Eq. (5.48). For Eq. (5.50a) one obtains

$$\begin{aligned}\mathfrak{h}^{(0)}(t) &= -\int_{t_0}^{t} dt' \gamma(t') = -\int_{t_0}^{t} dt' \int d^3p\, \Gamma_{\mathbf{p}}(t') \\ \Gamma_{\mathbf{p}}(t) &= \Omega^*(t) e^{-iS(t)} \int_{t_0}^{t} dt'\, \Omega(t')\, e^{iS(t')}.\end{aligned} \tag{5.51}$$

Here, $\gamma(t)$ is a complex rate, and $\gamma + \gamma^*$ gives the optical field ionization rate from ground state to continuum.

The one photon operator contribution (5.50b) is worked out to be $\hat{\mathfrak{h}}^{(1)} = \sum_\kappa \hat{\mathfrak{h}}_\kappa^{(1)}$ with

$$\hat{\mathfrak{h}}_\kappa^{(1)} = h_\kappa \hat{a}_\kappa^\dagger - h_\kappa^* \hat{a}_\kappa. \tag{5.52}$$

The next order term in the Magnus Fer expansion (5.47) is a small phase term that does not contribute to HHG and can be neglected. Therefore, Eq. (5.46) for HHG gives a coherent state with the HHG coefficient given by

$$h_\kappa = -e^{-i\mathbf{k}\mathbf{x}_j} \int_{-\infty}^{\infty} dt' e^{i\omega_k t'} H_k(t') = \tilde{H}_k e^{-i\mathbf{k}\mathbf{x}_j} \tag{5.53}$$

$$H_k = \frac{|e|E_v}{\hbar} \left\{ \left(\mathbf{e}_\kappa \mathbf{x}(t')\right) + \int d^3p\, \overline{\sigma}_\kappa(t') \left(\Gamma_{\mathbf{p}}(t') + \text{c.c}\right) \right\}$$

with

$$\mathbf{x}(t) = \int d^3p\, \mathbf{d}^*(\mathbf{p}_t)\, b_{\mathbf{p}}(t) + \text{c.c.},$$
$$b_{\mathbf{p}}(t) = \int_{t_0}^{t} dt' \Omega(t') \exp\left(iS(t',t) - \xi(t-t')\right), \tag{5.54}$$

and $E_v = \sqrt{\hbar\omega_k/2\varepsilon_0 V}$ the vacuum electric field. The first term in Eq. (5.53) agrees with previous work [28], where $\mathbf{x}(t)$ is the expectation value of the dipole moment driving HHG. Note that the subscript in H_k is chosen k to indicate that it does not depend on the HHG wavevector, but only on the frequency. It is also assumed that harmonic and laser polarization vectors are parallel, so that the polarization index can be neglected as well.

Usually dephasing is accounted for by a term $\xi(t-t') = (t-t')/T_2$ with T_2 the dephasing time. Suppression of HHG grows with increasingly higher order electron returns. We use here a different filter which leaves the first return unfiltered and extinguishes all higher returns,

$$\begin{aligned}
&\xi(t-t') = 0 && \text{for } t-t' \leq \frac{T_0}{2} \\
&\xi(t-t') = 10(t-t')/T_0 && \text{for } \frac{T_0}{2} \leq t-t' \leq T_0 \\
&\xi(t-t') = \infty && \text{for } t-t' > T_0
\end{aligned}$$

with optical period $T_0 = 2\pi/\omega_0$ and ω_0 the laser frequency. The filter is confined to one optical cycle, as the associated convolution operation is numerically expensive.

The QSHHG coefficients are determined from Eq. (5.50c) as

$$\hat{\mathfrak{H}}^{(2)} = \sum_{\kappa\kappa'} f_{\kappa\kappa'}\hat{a}^\dagger_\kappa \hat{a}^\dagger_{\kappa'} - f^*_{\kappa\kappa'}\hat{a}_\kappa \hat{a}_{\kappa'} + g_{\kappa\kappa'}\hat{a}^\dagger_\kappa \hat{a}_{\kappa'} - g^*_{\kappa\kappa'}\hat{a}_\kappa \hat{a}^\dagger_{\kappa'}, \tag{5.55}$$

where $f_{\kappa\kappa'}$ is the coefficient for emission or absorption of two photons,

$$\begin{aligned}
f_{\kappa\kappa'} = e^{-i(\mathbf{k}+\mathbf{k}')\mathbf{x}_j} \int_{-\infty}^{\infty} dt' e^{i(\omega_k+\omega_{k'})t'} \int d^3p\, \overline{\sigma}_{\kappa'}(t') \times \\
\left\{ \frac{|e|E_v}{\hbar}(\mathbf{e}_\kappa \mathbf{x}_{\mathbf{p}}(t')) + \frac{1}{2}\overline{\sigma}_\kappa(t') \left[\Gamma_{\mathbf{p}}(t') - \text{c.c.}\right] \right\}.
\end{aligned} \tag{5.56}$$

Emission of one and absorption of another photon is represented by

$$g_{\kappa\kappa'} = e^{-i(\mathbf{k}-\mathbf{k}')\mathbf{x}_j}\int_{-\infty}^{\infty} dt' e^{i(\omega_k-\omega_{k'})t'}\int d^3p\,\overline{\sigma}^*_{\kappa'}(t')\times \left\{\frac{|e|E_v}{\hbar}(\mathbf{e}_\kappa\mathbf{x}_\mathbf{p}(t')) + \frac{1}{2}\overline{\sigma}_\kappa(t')\left[\Gamma_\mathbf{p}(t') - \text{c.c.}\right]\right\}, \tag{5.57}$$

where

$$\mathbf{x}_\mathbf{p}(t) = \mathbf{d}^*(\mathbf{p}_t)b_\mathbf{p}(t) - \text{c.c.} \tag{5.58}$$

is the imaginary part of the ground state continuum transition dipole operator for a given $\mathbf{p}$. Here we have let $t \to \infty$.

For the second order expansion term in Eq. (5.47) one has to keep finite t; it is worked out to be

$$\begin{aligned}
&\int_{t_0}^{t} dt' \int_{t_0}^{t} dt'' \left[\partial_{t'}\hat{\mathfrak{H}}^{(2)}, \partial_{t''}\hat{\mathfrak{H}}^{(2)}\right] = \\
&= \left(\partial_{t'} f_{\kappa\kappa'}\,\partial_{t''} f^*_{\kappa\kappa'} - \text{c.c.}\right)\left(1 + \hat{n}_\kappa + \hat{n}_{\kappa'}\right) \\
&+ \left(\partial_{t'} g_{\kappa\kappa'}\,\partial_{t''} g^*_{\kappa\kappa'} - \text{c.c.}\right)\left(\hat{n}_{\kappa'} - \hat{n}_\kappa\right) \\
&+ \left(\partial_{t'} g_{\kappa\kappa'}\,\partial_{t''} f_{\kappa\kappa'} - \partial_{t'} f_{\kappa\kappa'}\,\partial_{t''} g_{\kappa\kappa'}\right)\hat{a}^{\dagger 2}_\kappa + \text{h.c.} \\
&+ \left(\partial_{t'} f_{\kappa\kappa'}\,\partial_{t''} g^*_{\kappa\kappa'} - \partial_{t'} g^*_{\kappa\kappa'}\,\partial_{t''} f_{\kappa\kappa'}\right)\hat{a}^{\dagger 2}_{\kappa'} + \text{h.c.}
\end{aligned} \tag{5.59}$$

It only contains one-mode, two-photon terms and no mixed mode terms; all terms are second order in f, g; as $|f, g| \ll 1$, all terms in Eq. (5.59) are neglected.

In the limit of a single perturbative mode, $\kappa' = q$, the κ' sum can be dropped. Further, we write $f_\kappa = f_{\kappa q} + f_{q\kappa} \approx f_{\kappa q}$, and $g_\kappa = g_{\kappa q} + g_{q\kappa} \approx g_{\kappa q}$, as only the term $\kappa' = q$ contributes significantly to QSHHG. This yields

$$\begin{aligned}
f_\kappa &= e^{-i(\mathbf{k}+\mathbf{q})\mathbf{x}_j}\int_{-\infty}^{\infty} dt' e^{i(\omega_k+\omega_q)t'} F_k(t') = \tilde{F}_k e^{-i(\mathbf{k}+\mathbf{q})\mathbf{x}_j} \\
F_k &= \left(\frac{|e|E_v}{\hbar}\right)^2 \int d^3p\,\overline{\sigma}_q(t')\left\{(\mathbf{e}_\kappa\mathbf{x}_\mathbf{p}(t')) + i\overline{\sigma}_\kappa(t')\text{Im}\left[\Gamma_\mathbf{p}(t')\right]\right\}
\end{aligned} \tag{5.60}$$

and

$$g_\kappa = e^{-i(\mathbf{k}-\mathbf{q})\mathbf{x}_j}\int_{-\infty}^{\infty} dt' e^{i(\omega_k-\omega_q)t'} G_k(t') = \tilde{G}_k e^{-i(\mathbf{k}-\mathbf{q})\mathbf{x}_j}$$
$$G_k = \left(\frac{|e|E_v}{\hbar}\right)^2 \int d^3p\, \overline{\sigma}_q^*(t') \left\{ (\mathbf{e}_\kappa \mathbf{x}_\mathbf{p}(t')) + i\overline{\sigma}_\kappa(t') \mathrm{Im}\left[\Gamma_\mathbf{p}(t')\right] \right\}, \tag{5.61}$$

where ω_q and $\mathbf{q}$ are frequency and wavevector of the perturbative quantum light mode q. Frequencies ω_k and wavevector $\mathbf{k}$ continue to characterize the HHG and QSHHG modes. Again, like for HHG, the subscripts for F_k and G_k are chosen k to indicate that they depend only on the QSHHG frequency or wavenumber.

Combining all the results, we obtain the wavefuntion

$$|\varphi_0\rangle \approx |\varphi_h\rangle\,|\varphi_m\rangle = \hat{D}_h \hat{S}_m\,|\varphi_0(t_0)\rangle\,, \tag{5.62}$$

where t_0 is the initial time, and the final time $t \to \infty$. The coherent state HHG operator is given by

$$\hat{D}_h = \exp\left(\sum_\kappa h_\kappa \hat{a}_\kappa^\dagger - h_\kappa^* \hat{a}_\kappa\right), \tag{5.63}$$

and the mixed mode, two-photon QSHHG operator is found to be

$$\hat{S}_m = \exp\left(\sum_\kappa \left(f_\kappa \hat{a}_q^\dagger + g_\kappa \hat{a}_q\right)\hat{a}_\kappa^\dagger - \left(g_\kappa^* \hat{a}_q^\dagger + f_\kappa^* \hat{a}_q\right)\hat{a}_\kappa\right). \tag{5.64}$$

Here, we have assumed that HH and QSHH modes do not overlap. As a result, the wavefunction can be written as a product of the HH and QSHH time evolution operators. In case of mode overlap, the commutators between HH and QSHH operators need to be considered.

In order to proceed, the above operators need to be applied to an initial state. Here, we use $\varphi_0(t_0) = |v\xi_q\rangle$ which consists of multi-mode vacuum states $|v\rangle = \prod_\kappa |v_\kappa\rangle$ for the harmonics, and a single BSV state for the perturbative mode,

$$\left|\xi_q\right\rangle = \hat{S}_q \left|v_q\right\rangle = e^{\frac{1}{2}(\xi \hat{a}_q^2 - \xi^* \hat{a}_q^{\dagger 2})} \left|v_q\right\rangle \tag{5.65}$$

with $\xi = re^{i\theta}$. The normal ordered form of the squeezed state operator is given by [168]

$$\hat{S}_q = \frac{1}{\sqrt{\cosh(r)}} e^{-\beta \hat{a}_q^{\dagger 2}} \, :e^{(\mathrm{sech}(r)-1)\hat{a}_q^\dagger \hat{a}_q}: \, e^{\beta^* \hat{a}_q^2} \tag{5.66}$$

with $\beta = (1/2)\tanh(r)e^{-i\theta}$. Expressions written between colons are normal ordered.

Finally, expectation values are dominantly determined by the ground state photon wavefunction; contributions of the continuum photon wavefunctions are negligible. As such, the expectation value of a general function of photon operators $\hat{O}(\ldots, \hat{a}_\kappa, \hat{a}_\kappa^\dagger, \ldots)$ is

$$\begin{aligned} \langle \phi_0 | \hat{O} | \phi_0 \rangle &= \langle \varphi_0 | \hat{D}_\alpha^\dagger \hat{U}_v^\dagger \hat{U}_i^\dagger \hat{O} \hat{U}_i \hat{U}_v \hat{D}_\alpha | \varphi_0 \rangle \\ &= \langle \varphi_0 | \hat{O}(\ldots, \hat{a}_\kappa e^{-i\omega_k \tau}, \hat{a}_\kappa^\dagger e^{i\omega_k \tau}, \ldots) | \varphi_0 \rangle. \end{aligned} \tag{5.67}$$

The U_v operator commutes with the other operators and cancels with its adjoint; the operator D_α adds the classical intense laser modes to the operators. As we are only interested in HH modes this is not explicitly written out. Finally, the operator U_i makes the mode operators time dependent with $\tau = t - (\mathbf{n}\mathbf{x}_j)/c$.

5.5.2 Phase matching

High harmonic generation

So far we have developed the microscopic theory of HHG and QSHHG for a single atom. There is also a macroscopic aspect; when the radiation is summed over all atoms, propagation effects come into play. We first look at regular HHG and determine the macroscopic expectation value of the number operator $\hat{n} = \sum_\kappa \hat{n}_\kappa$,

$$\langle \varphi_h | \hat{n} | \varphi_h \rangle = \sum_\kappa \left(\sum_j h_\kappa^* \right) \left(\sum_j h_\kappa \right) = \frac{V N_0}{(2\pi)^3} \int d^3k \left(\int d^3x \, h_\kappa^* \right) \left(\int d^3x \, h_\kappa \right), \tag{5.68}$$

While the integrals in Eq. (5.68) can be evaluated numerically, we give here an order of magnitude estimate. We assume that all dominant laser and harmonic modes propagate predominantly along z and are polarized along x. Also, it is assumed that the transverse profile of the pump laser remains approximately unchanged, i.e. independent of z. As a result, $\tilde{H}_k$ can be factorized in transverse (x, y) and longitudinal (z) parts.

First, the integral of each h_κ over the transverse spatial coordinates is performed; in the spirit of saddle point integration, the exponent of h_κ is expanded up to second order in

x, y, and x, y are set to zero in the pre-exponential terms. Then,

$$\int_{-\infty}^{\infty} d^3\mathbf{x}\, h_\kappa(\omega,\mathbf{x}) \approx \int_0^{l_i} dz h_\kappa(\omega,z) \int_{-\infty}^{\infty} dx dy\, e^{-\frac{x^2+y^2}{2\mathrm{w}_k^2}} e^{-i(k_x x + k_y y)}$$
$$= 2\pi \mathrm{w}_k^2 e^{-\frac{\mathrm{w}_k^2}{2}(k_x^2+k_y^2)} \int_0^{l_i} dz h_\kappa(\omega,z), \tag{5.69}$$

where l_i is the interaction length and $\mathrm{w}_k = \mathrm{w}(\omega_k)$ is the width of the transverse beam profile of harmonic mode κ. Note that due to the nonlinearity of the ionization process $\mathrm{w}_k/\mathrm{w}_0 < 1$ with $\mathrm{w}_0 = \mathrm{w}(\omega_0)$.

Second, the integral over $dk_x dk_y$ is performed. As harmonic emission is mainly directed along the laser propagation direction, one can approximate k_z in the plane wave of Eq. (5.53) by $k_z^2 = k^2 - (k_x^2 + k_y^2) \approx k^2$ with $k = \omega_k/c$; consequently also $dk_z \approx dk$ in Eq. (5.68). This corresponds to neglecting the z-dependent evolution of the transverse Gaussian profile of the harmonic pulse. Thus, the $dk_x dk_y$ integral in Eq. (5.68) can be performed separately as well,

$$\int_{-\infty}^{\infty} dk_x dk_y e^{-\mathrm{w}_k^2(k_x^2+k_y^2)} = \frac{\pi}{\mathrm{w}_k^2} \tag{5.70}$$

Third, the z-integral in Eq. (5.69) is $\int_0^{l_i} dz \exp(-i(k - Nk_0)z) = \int_0^{l_i} dz \exp(-i\Delta k z)$, where Δk is the difference between the harmonic wavevector and N times the fundamental wavevector. Here, we have taken κ as the mode with frequency $\omega_k = N\omega_0$. There are several sources that change k_0 and result in dephasing; beam geometry, gas refractive index, and the refractive index of the free electrons. The absolute square of the integral has a maximum at $\Delta k l_i = \pi$ [169]. We assume that $l_i < \pi/\Delta k$, so that $\int_0^{l_i} dz \exp(-i\Delta k z) \approx l_i$.

Finally, the $d\omega_k$ integral drops out, when looking at the differential expectation value of the number operator. Inserting the above results in Eq. (5.68) yields

$$\frac{d\langle\hat{n}\rangle}{d\omega_k} = \frac{\langle\varphi_h|\hat{n}|\varphi_h\rangle}{d\omega_k} = c_k^2 |\tilde{H}_k(\omega_k)|^2$$
$$c_k^2 = \frac{\left(N_0 \mathrm{w}_k l_i\right)^2}{2c} V, \tag{5.71}$$

where the atomic position coordinate is now set to $\mathbf{x} = 0$ in $\tilde{H}_k$. The quantization volume cancels out, as the single atom response $\tilde{H}_k \propto 1/\sqrt{V}$. As the transverse wavevector modes have been integrated over, the modes are counted only by frequency ω_k or wavenumber k.

We also define the number of photons emitted into a single mode with wavenumber k,

$$\langle \hat{n} \rangle_k = \frac{d\langle \hat{n} \rangle}{d\omega_k} \Delta\omega \tag{5.72}$$

with $\Delta\omega$ the harmonic mode width. The number of photons emitted into one harmonic interval ω_0 about harmonic order N is given by

$$\langle \hat{n} \rangle_N = c_k^2 \int_{(N-\frac{1}{2})\omega_0}^{(N+\frac{1}{2})\omega_0} d\omega_k |\tilde{H}_k(\omega_k)|^2 = |h_N|^2, \tag{5.73}$$

In summary, $|h_N|^2$ determines the macroscopic emission of HH photons in all transverse spatial modes in the frequency interval $(N - \frac{1}{2})\omega_0 \leq \omega_k \leq (N + \frac{1}{2})\omega_0$.

Quantum sideband high harmonic generation

Next we look at phase matching of QSHHG. First the expecation value of the number operator needs to be evaluated by using the Bogoliubov transformation [4],

$$\langle \varphi_m | \hat{n}_\kappa | \varphi_m \rangle = \left\langle \xi_q v_\kappa \right| \hat{S}_m^\dagger \hat{a}_\kappa^\dagger \hat{S}_m \hat{S}_m^\dagger \hat{a}_\kappa \hat{S}_m \left| v_\kappa \xi_q \right\rangle . \tag{5.74}$$

The transformation of the annihilation operator is found to be

$$\hat{S}_m^\dagger \hat{a}_\kappa \hat{S}_m = \cosh(M_\kappa)\hat{a}_\kappa + \frac{\sinh(M_\kappa)}{M_\kappa} \left(f_\kappa a_q^\dagger + g_\kappa \hat{a}_q \right) \tag{5.75}$$

with $M_\kappa^2 = |f_\kappa|^2 - |g_\kappa|^2$. Using Eqs. (5.75) in (5.74), followed by another Bogoliubov transformation in $\hat{S}_q$, yields

$$\begin{aligned} \langle \varphi_m | \hat{n}_\kappa | \varphi_m \rangle &\approx \cosh^2(r) \left| Z_\kappa \right|^2 \\ Z_\kappa &= f_\kappa - g_\kappa \tanh(r) e^{i\theta}. \end{aligned} \tag{5.76}$$

Here, $M_\kappa \ll 1$ and $r \gg 1$ has been used.

To obtain the macroscopic expectation value, the same procedure is followed as for

HHG,

$$\begin{aligned}\langle \varphi_m \left|\hat{n}\right| \varphi_m \rangle &= N_0^2 \cosh^2(r) \sum_{\kappa q} \left| \int_V d^3x \, Z_\kappa \right|^2 \\ &\approx \frac{V^2 N_0^2 (\Delta q)^3 \cosh^2(r)}{(2\pi)^6} \int d^3k \left| \int_V d^3x \, Z_\kappa \right|^2, \end{aligned} \tag{5.77}$$

where we have converted the sum over κ into an integral as before. Further, the mode volume of the perturbative mode q is introduced as $(\Delta q)^3 = \Delta q_x \Delta q_y \Delta q_z = (2\pi)^3/V$. Like before, the exponent is Taylor expanded with regard to the transverse space variables, and x, y is set to zero in the preexponent; the factured out $dxdy$ integrals for f_κ and g_κ are

$$\int_{-\infty}^{\infty} dxdy \, e^{-\frac{x^2+y^2}{2w_k^2}} e^{-i((k_x \pm q_x)x + (k_y \pm q_y)y)} = 2\pi w_k^2 e^{-\frac{w_k^2}{2}((k_x \pm q_x)^2 + (k_y \pm q_y)^2)}. \tag{5.78}$$

As harmonic emission is mainly directed along the laser propagation direction, again $k_z \approx k = \omega_k/c$ and $dk_z \approx dk = d\omega_k/c$. As before, the $dk_x dk_y$ integral over (5.78) squared can be separated out and performed as well to give

$$\int_{-\infty}^{\infty} dk_x dk_y e^{-w_k^2((k_x \pm q_x)^2 + (k_y \pm q_y)^2)} = \frac{\pi}{w_k^2}; \tag{5.79}$$

the q_x, q_y dependence vanishes. Assuming that the interaction length is shorter than the dephasing length, the integral over dz gives a factor l_i^2, as before.

After the transverse wavevectors have been integrated out, the modes are identified by the QSHHG frequency (wavenumber) alone. Inserting the above results in Eq. (5.77) determines the number of photons emitted in all modes. The number of photons emitted into a single mode k is

$$\begin{aligned}\langle \hat{n} \rangle_k &= c_q^2 \cosh^2(r) \left|\zeta_k\right|^2 \Delta\omega \\ |\zeta_k|^2 &= \left|\tilde{F}_k - \tilde{G}_k \tanh(r) e^{i\theta}\right|^2 \end{aligned} \tag{5.80}$$

with

$$c_q^2 = \frac{\left(N_0 w_k l_i\right)^2}{2c} V^2 \frac{(\Delta q)^3}{(2\pi)^3}. \tag{5.81}$$

The steps leading from Eq. (5.76) to (5.80) are summarized in the following. In the

transition from Z_κ to ζ_k the identity $V^2/(2\pi)^6\Delta^3 k\Delta^3 q = 1$ is used and the limit from discrete to continuous modes is performed. Whereas, Z_κ contains the sum over all atoms and represents a single mode $\kappa = (\mathbf{k}, s)$, ζ_k stands for a single mode k, as the transverse QSHHG wavevectors have been integrated out. Further, the sum over all atoms has been evaluated so that ζ_κ does no longer depend on $\mathbf{x}_j$. Finally, the factor $V^2\left|\zeta_\kappa\right|^2$ is independent of the quantization volume.

Comparison of Eq. (5.80) with (5.72) shows that the ratio of propagation related pre-factors of QSHHG to HHG is $1/(2\pi)^3(\Delta q)^3$. The mode volume is determined by the beam parameters of the quantum field spectral width $\Delta\lambda_q$ and transverse beam width w_q, from which one obtains $\Delta q_x = \Delta q_y \approx (2\pi)/\mathrm{w}_q$ and $\Delta q_z = 2\pi\Delta\lambda_q/\lambda_q^2$. As a result, $(\Delta q)^3/(2\pi)^3 = \Delta\lambda_q/(\mathrm{w}_q^2\lambda_q^2)$. This is an approximation. In reality the single BSV mode is composed of a number of plane wave modes. This fact has been accounted for by replacing the mode volume of a single plane wave mode with the mode volume of the BSV mode. The quality of this assumption is corroborated by the good agreement between experiment and theory with regard to the number of emitted sideband photons, see the manuscript.

Finally, like before we define QSHHG in the frequency interval $(N-\frac{1}{2})\omega_0 \leq \omega_k \leq (N+\frac{1}{2})\omega_0$ and in all spatial modes as

$$\langle\hat{n}\rangle_N = c_q^2\cosh^2(r)\int_{(N-\frac{1}{2})\omega_0}^{(N+\frac{1}{2})\omega_0} d\omega_k\left|\zeta_k\right|^2 = \cosh^2(r)\left|\zeta_N\right|^2. \tag{5.82}$$

5.5.3 Properties of QSHHG

Normal ordered wavefunction

To characterize the quantum properties of QSHHG we need a simpler expression for the wavefunction. This can be achieved in the limit of intense quantum fields perturbing HHG. We proceed by swapping the order of operators in Eq. (5.62),

$$\left|\varphi_m(t)\right\rangle = \hat{S}_m\left|v_\kappa\xi_q\right\rangle = \hat{S}_q\hat{S}_q^\dagger\hat{S}_m\hat{S}_q\left|v_\kappa v_q\right\rangle = \hat{S}_q\hat{S}'_m\left|vv_q\right\rangle. \tag{5.83}$$

The transformed operator $\hat{S}'_m$ is evaluated by Taylor expansion of $\hat{S}_m$ and by calculating the Bogoliubov transformation with regard to $\hat{S}_q$; this amounts to

$$\hat{S}'_m = \exp\left(\sum_\kappa \left(f'_\kappa \hat{a}^\dagger_q + g'_\kappa \hat{a}_q\right)\hat{a}^\dagger_\kappa - \left(g'^*_\kappa \hat{a}^\dagger_q + f'^*_\kappa \hat{a}_q\right)\hat{a}_\kappa\right) \tag{5.84}$$

with

$$\begin{aligned} f'_\kappa &= f_\kappa \cosh(r) - g_\kappa \sinh(r) e^{i\theta} = \cosh(r) Z_\kappa \\ g'_\kappa &= -f_\kappa \sinh(r) e^{-i\theta} + g_\kappa \cosh(r). \end{aligned} \tag{5.85}$$

The swap in Eq. (5.83) is important, as $f_\kappa, g_\kappa \ll 1$ are small and r is big. As such, an exponential operator of the order of unity acts on a very large exponential operator in the original expression. This would make it difficult to isolate the leading order terms in $\hat{S}_m$, and important terms can be easily lost.

Next, the exponent of the sum over κ modes in Eq. (5.84) is split into a product of single mode exponents by using the Baker-Campbell-Haussdorff (BCH) formula, $e^{\hat{A}+\hat{B}} = e^{\hat{A}} e^{\hat{B}} e^{-(1/2)[\hat{A},\hat{B}]} \cdots$; we only evaluate the lowest order commutator. Defining $\hat{J}^\dagger_{\kappa q} = f'_\kappa \hat{a}^\dagger_q + g'_\kappa \hat{a}_q$ and assuming two modes $j = \kappa, \kappa'$ yields

$$e^{\sum_{j=\kappa,\kappa'} \hat{J}^\dagger_{jq}\hat{a}^\dagger_j - \hat{J}_{jq}\hat{a}_j} = \hat{B} \prod_{j=\kappa,\kappa'} \exp\left(\hat{J}^\dagger_{jq}\hat{a}^\dagger_j - \hat{J}_{jq}\hat{a}_j\right), \tag{5.86}$$

where

$$\begin{aligned} \hat{B} &= \exp\left(-(1/2)\left[\hat{J}^\dagger_{\kappa q}\hat{a}^\dagger_\kappa - \hat{J}_{\kappa q}\hat{a}_\kappa, \hat{J}^\dagger_{\kappa' q}\hat{a}^\dagger_{\kappa'} - \hat{J}_{\kappa' q}\hat{a}_{\kappa'}\right]\right) \\ &= \exp\Big(-(1/2)\Big\{\hat{a}^\dagger_\kappa \hat{a}^\dagger_{\kappa'}\left[\hat{J}^\dagger_{\kappa q}, \hat{J}^\dagger_{\kappa' q}\right] + \hat{a}_\kappa \hat{a}_{\kappa'}\left[\hat{J}_{\kappa q}, \hat{J}_{\kappa' q}\right] \\ &+ \left(\hat{a}^\dagger_\kappa \hat{a}_{\kappa'} - \hat{a}^\dagger_{\kappa'}\hat{a}_\kappa\right)\left[\hat{J}^\dagger_{\kappa q}, \hat{J}_{\kappa' q}\right]\Big\}\Big) \end{aligned} \tag{5.87}$$

As

$$\begin{aligned} \left[\hat{J}^\dagger_{\kappa q}, \hat{J}_{\kappa' q}\right] &= -\left(f'_\kappa f'^*_{\kappa'} - g'_\kappa g'^*_{\kappa'}\right) = -\left(f_\kappa f^*_{\kappa'} - g_\kappa g^*_{\kappa'}\right) \ll 1 \\ \left[\hat{J}^\dagger_{\kappa q}, \hat{J}^\dagger_{\kappa' q}\right] &= -\left(f'_\kappa g'_{\kappa'} - f'_{\kappa'} g'_\kappa\right) = -\left(f_\kappa g_{\kappa'} - f_{\kappa'} g_\kappa\right) \ll 1 \\ \left[\hat{J}_{\kappa q}, \hat{J}_{\kappa' q}\right] &= \left(f'^*_\kappa g'^*_{\kappa'} - f'^*_{\kappa'} g'^*_\kappa\right) = \left(f^*_\kappa g^*_{\kappa'} - f^*_{\kappa'} g^*_\kappa\right) \ll 1, \end{aligned} \tag{5.88}$$

the commutator $\hat{B} \approx 1$ is negligible; and so are all higher order commutator terms.

In order to simplify $\hat{S}'_m$, it is normal ordered, i.e. all destruction operators are moved to the right of the creation operators. As a result, the destruction operators act directly on the vacuum states and drop out. Normal ordering results in [170]

$$\begin{aligned}\hat{S}'_m = &\prod_\kappa \mathcal{N}_\kappa \exp\left(\frac{1}{2} q_\kappa f'_\kappa \left(g'_\kappa \hat{a}^{\dagger 2}_\kappa - g'^{*}_\kappa \hat{a}^{\dagger 2}_q\right) + q''_\kappa f'_\kappa \hat{a}^\dagger_\kappa \hat{a}^\dagger_q\right) \\ &: \exp\left(-2q'_\kappa \left(\hat{a}^\dagger_\kappa \hat{a}_\kappa + \hat{a}^\dagger_q \hat{a}_q\right) + q'''_\kappa \left(g'_\kappa \hat{a}^\dagger_\kappa \hat{a}_q - g'^{*}_\kappa \hat{a}_\kappa \hat{a}^\dagger_q\right)\right) : \\ &\exp\left(\frac{1}{2} q_\kappa \left(f'^{*}_\kappa g'^{*}_\kappa \hat{a}^2_\kappa - f'^{*}_\kappa g'_\kappa \hat{a}^2_q\right) - q''_\kappa f'^{*}_\kappa \hat{a}_\kappa \hat{a}_q\right).\end{aligned} \tag{5.89}$$

The normalization factor is given by

$$\begin{aligned}\mathfrak{N}_\kappa &= \frac{1/\cosh^2(m_\kappa)}{\sqrt{1 + 2\left(|f'_\kappa|^2 + |g'_\kappa|^2\right)\left(\frac{\tanh(m_\kappa)}{m_\kappa}\right)^2 + \tanh^4(m_\kappa)}} \\ &\approx \frac{1}{\sqrt{1 + |f'_\kappa|^2}},\end{aligned} \tag{5.90}$$

where $4m^2_\kappa = |f'_\kappa|^2 - |g'_\kappa|^2 = |f_\kappa|^2 - |g_\kappa|^2 \ll 1$. The other parameters are

$$\begin{aligned}q_\kappa &= \frac{\tanh^2(m_\kappa)}{m^2_\kappa \left(1 + \tanh^2(m_\kappa)\right)^2 + |g'_\kappa|^2 \tanh^2(m_\kappa)} \approx \frac{1}{1 + |f'_\kappa|^2} \\ q'_\kappa &= q_\kappa \left(\frac{1}{4}\left(|f'_\kappa|^2 + |g'_\kappa|^2\right) + m^2_\kappa \tanh^2(m^2_\kappa)\right) \\ q''_\kappa &= \frac{m_\kappa \tanh(m_\kappa)\left(1 + \tanh^2(m_\kappa)\right)}{m^2_\kappa \left(1 + \tanh^2(m_\kappa)\right)^2 + |g'_\kappa|^2 \tanh^2(m_\kappa)} \approx \frac{1}{1 + |f'_\kappa|^2} \\ q'''_\kappa &= \frac{m_\kappa \tanh(m_\kappa)\left(1 - \tanh^2(m_\kappa)\right)}{m^2_\kappa \left(1 + \tanh^2(m_\kappa)\right)^2 + |g'_\kappa|^2 \tanh^2(m_\kappa)}\end{aligned} \tag{5.91}$$

The second line of Eq. (5.90) and the last, approximate expressions in the first and third line of Eq. (5.91) are valid for $r \gg 1$ and $f_\kappa, g_\kappa \ll 1$.

We first proceed with a single harmonic mode and then generalize the result to multi harmonic modes. Inserting Eq. (5.89) in (5.83), keeping only a single harmonic mode,

and using the normal ordered form (5.66) of $\hat{S}_q$ yields the simpler expression

$$\left|\varphi_m\right\rangle_\kappa = \frac{\mathfrak{N}_\kappa}{\sqrt{\cosh(r)}} e^{\frac{1}{2}q_\kappa f'_\kappa g'_\kappa \hat{a}_\kappa^{\dagger 2}} e^{-\beta \hat{a}_q^{\dagger 2}} : e^{(\mathrm{sech}(r)-1)\hat{a}_q^\dagger \hat{a}_q} : \; e^{\beta^* \hat{a}_q^2} e^{-\frac{1}{2}q_\kappa f'_\kappa g'^*_\kappa \hat{a}_q^{\dagger 2}} e^{q''_\kappa f'_\kappa \hat{a}_\kappa^\dagger \hat{a}_q^\dagger} \left|v_\kappa v_q\right\rangle, \tag{5.92}$$

where all exponents containing annihilation operators act on the vacuum and have become unity. The operators from $\hat{S}_q$ still need to be normal ordered. This is done using the IWOP method [171, 168] and yields

$$\left|\varphi_m\right\rangle_\kappa = \frac{\mathfrak{N}_\kappa e^{Q_1 \hat{a}_\kappa^{\dagger 2}} e^{-Q_2 \hat{a}_q^{\dagger 2}} e^{Q_m \hat{a}_\kappa^\dagger \hat{a}_q^\dagger}}{\sqrt{\cosh(r)}\sqrt{1+2\beta^* q_\kappa f'_\kappa g'^*_\kappa}} \left|v_\kappa v_q\right\rangle, \tag{5.93}$$

where

$$\begin{aligned} Q_1 &= \frac{1}{2}q_\kappa f'_\kappa g'_\kappa + \frac{\beta^* \left(q''_\kappa f'_\kappa\right)^2}{1+2\beta^* q_\kappa f'_\kappa g'^*_\kappa} \approx 0 \\ Q_2 &= \beta + \frac{\mathrm{sech}^2(r) q_\kappa f'_\kappa g'^*_\kappa}{2\left(1+2\beta^* q_\kappa f'_\kappa g'^*_\kappa\right)} \approx \frac{\beta}{1+|Z_\kappa|^2} \\ Q_m &= \frac{\mathrm{sech}(r) q''_\kappa f'_\kappa}{1+2\beta^* q_\kappa f'_\kappa g'^*_\kappa} \approx Z_\kappa. \end{aligned} \tag{5.94}$$

The approximate expressions were obtained by using $r \gg 1$ and $f_\kappa, g_\kappa \ll 1$, $\tanh(r) \approx 1$, Eq. (5.91), and

$$1 + 2\beta^* q_\kappa f'_\kappa g'^*_\kappa \approx \frac{1+|Z_\kappa|^2}{1+|f'_\kappa|^2}. \tag{5.95}$$

The last relation is also used in the evaluation of the pre-exponential factor in Eq. (5.93). Inserting the above approximations in Eq. (5.93) yields the final expression for the QSHHG wavefunction in the limit of a bright quantum perturbation,

$$\begin{aligned} \left|\varphi_m\right\rangle_\kappa &= \frac{\mathfrak{N}_\kappa}{\sqrt{\cosh(r)}} \exp\left(Z_\kappa \hat{a}_\kappa^\dagger \hat{a}_q^\dagger\right) \exp\left(-\beta_\kappa \hat{a}_q^{\dagger 2}\right) \left|v_\kappa v_2\right\rangle \\ \beta_\kappa &= \beta/(1+|Z_\kappa|^2) \quad \mathfrak{N}_\kappa \approx \frac{1}{\sqrt{1+|Z_\kappa|^2}}. \end{aligned} \tag{5.96}$$

The approximate wavefunction (5.96) can be shown to be normalized, accurate to first

order in $|Z_\kappa|^2 \ll 1$.

In the multi harmonic mode case we start again from Eq. (5.89); each κ, q mixed exponent in $\hat{S}_m$ contains $\hat{a}_q^\dagger$, $\hat{a}_q$ terms that need to be normal ordered. The $\hat{a}_\kappa^\dagger$ and $\hat{a}_\kappa$ operators of different harmonic modes commute; therefore all terms containing only harmonic operators with $\hat{a}_\kappa$ in it commute to the vauum state and drop out. Inserting Eq. (5.89) in (5.83) yields

$$\begin{aligned}|\varphi_m\rangle = \prod_\kappa & \frac{\mathfrak{N}_\kappa}{\sqrt{\cosh(r)}} e^{\frac{1}{2}q_\kappa f'_\kappa g'_\kappa \hat{a}_\kappa^{\dagger 2}} e^{-\beta \hat{a}_q^{\dagger 2}} : e^{(\mathrm{sech}(r)-1)\hat{a}_q^\dagger \hat{a}_q} : \\ & \times e^{\beta^* \hat{a}_q^2} e^{-\frac{1}{2}q_\kappa f'_\kappa g'^*_\kappa \hat{a}_q^{\dagger 2}} e^{q''_\kappa f'_\kappa \hat{a}_\kappa^\dagger \hat{a}_q^\dagger} : e^{-2q'_\kappa \hat{a}_q^\dagger \hat{a}_q} : e^{q'''_\kappa g'_\kappa \hat{a}_\kappa^\dagger \hat{a}_q} \\ & \times e^{-\frac{1}{2}q_\kappa f'^*_\kappa g'_\kappa \hat{a}_q^2} \left| v_\kappa v_q \right\rangle, \end{aligned} \tag{5.97}$$

where in addition to the single mode case above, the last three terms containing $\hat{a}_q$ in Eq. (5.97) appear in each harmonic mode and need to be normal ordered. Luckily, normal ordering of these terms gives contributions of higher order which can be neglected. Therefore, the multi-mode expression looks similar to the single mode one,

$$\begin{aligned}|\varphi_m\rangle &= \prod_\kappa \frac{\overline{\mathfrak{N}}}{\sqrt{\cosh(r)}} \exp\left(Z_\kappa \hat{a}_\kappa^\dagger \hat{a}_q^\dagger\right) \exp\left(-\overline{\beta} \hat{a}_q^{\dagger 2}\right) \left| v_\kappa v_q \right\rangle \\ \overline{\beta} &\approx \frac{\beta}{1+\sum_\kappa |Z_\kappa|^2}, \quad \overline{\mathfrak{N}} \approx \frac{1}{\sqrt{1+\sum_\kappa |Z_\kappa|^2}}. \end{aligned} \tag{5.98}$$

In the last equation, $\prod_\kappa 1/(1+|Z_\kappa|^2) \approx 1/(1+\sum_\kappa |Z_\kappa|^2)$ has been used. The sum in the denominator can be evaluated following the approach used in the phase matching section 5.5.2. In the manuscript all results are presented for QSHHG in the band $(N-1/2)\omega_0 \leq \omega_k \leq (N+1/2)\omega_0$. Summation over this frequency band and transverse modes yields

$$\overline{\beta} \to \beta_N \approx \frac{\beta}{1+|\zeta_N|^2}, \quad \overline{\mathfrak{N}} \to \mathfrak{N}_N \approx \frac{1}{\sqrt{1+|\zeta_N|^2}}, \tag{5.99}$$

where $\beta_N, \mathfrak{N}_N$ refer specifically to summing over the modes in the band ω_0 about harmonic N.

The multi-mode harmonic wavefunction (5.98) can be used to calculate correlation between two or more modes. Here we focus on calculating various one-mode properties of QSHHG. To that end we group the spatial and spectral plane-wave modes of a harmonic sideband into a single QSHH mode.

From plane wave modes to a single effective QSHH mode

Experimental measurements have been made on all photons contained in single QSHH mode which is composed of many plane wave modes, as discussed above. Therefore it is advantageous to define operators that create or destroy photons in a QSHH mode. We define the operator [151]

$$\hat{a}_N = \frac{1}{|\zeta_N|} \sum_{\kappa \in N} Z_\kappa^* \hat{a}_\kappa \tag{5.100}$$

that encompasses all plane wave modes of a single quantum sideband. The operator fulfills the usual harmonic oscillator commutation relations $[\hat{a}_N, \hat{a}_M^\dagger] = \delta_{NM}$. The quadrature operators

$$X_{jN} = 1/(2i^{j-1})(\hat{a}_N + (-1)^{j-1}\hat{a}_N^\dagger) \;\; (j = 1, 2). \tag{5.101}$$

also fulfill the usual bosonic commutator relations $[X_{1N}, X_{2N}] = i/2$.

A number state of the effective harmonic mode is determined by

$$|n\rangle_N = \frac{1}{\sqrt{n!}} \left(\hat{a}_N^\dagger\right)^n |v\rangle_N, \tag{5.102}$$

where $|v\rangle_N$ is the vacuum state of the quantum sideband. Translated back into the plane wave basis, this corresponds to a sum over all combinations that have n photons in the plane wave modes of the quantum sideband N. In the new basis, the wavefunction (5.98) of QSHH N becomes

$$\left|\varphi_m\right\rangle = \prod_N \frac{\mathfrak{N}_N}{\sqrt{\cosh(r)}} \exp\left(|\zeta_N| \hat{a}_N^\dagger \hat{a}_q^\dagger\right) \exp\left(-\beta_N \hat{a}_q^{\dagger 2}\right) \left| v_N v_q \right\rangle. \tag{5.103}$$

This wavefunction will be used throughout the remaining supplement.

We will focus on calculating the second order coherence

$$g_N^{(2)}(0) = \frac{\langle \varphi_m | \hat{n}_N^2 - \hat{n}_N | \varphi_m \rangle}{\langle \varphi_m | \hat{n}_N | \varphi_m \rangle^2} \tag{5.104}$$

and the quadrature variances ($j = 1, 2$),

$$\begin{aligned}\Delta X_{jN}^2 &= \langle\varphi_m|X_{jN}^2|\varphi_m\rangle - \langle\varphi_m|X_{jN}|\varphi_m\rangle^2 \\ &= \frac{1}{4}\left(1 + \langle\varphi_m|\hat{a}_N^2 + \hat{a}_N^{\dagger 2} + (-1)^{j-1}2\hat{n}_N|\varphi_m\rangle\right),\end{aligned} \tag{5.105}$$

determined by using Eq. (5.101) and $\langle X_{jN}\rangle = 0$.

Probability distribution of one QSHH-mode

In this section, the QSHH photon probability distribution in a single effective mode is calculated. This applies to experiments in which the perturbative quantum field is not measured / traced out. It is sufficient to use a two-mode wavefunction $|\varphi_m\rangle$ consisting of the quantum perturbation and a single harmonic sideband. For the full multi-mode wavefunction, when the other harmonic sideband modes need to be traced out, the calculation proceeds in a similar manner, however the two-mode coefficients will be modified to higher orders in $|\zeta_N|^2$.

The QSHHG photon number distribution is determined by $P_N(m) = \sum_n \left|\langle mn|\varphi_m\rangle\right|^2$ with $|\varphi_m\rangle$ defined in Eq. (5.103); m, n are the photon numbers of QSHH mode (N) and perturbative quantum mode (q), respectively. Using a Taylor expansion of Eq. (5.103) one finds

$$P_N(m) = \frac{\mathfrak{N}_N^2}{\cosh(r)}\frac{|\zeta_N|^{2m}}{m!}\sum_n \frac{|\beta_N|^{2n}}{(n!)^2}(2n+m)!\,. \tag{5.106}$$

The sum in Eq. (5.106) can be evaluated by using the following relation. First we set $x = |\beta_N|$. From squeezed vacuum states [4] it is known that $\sum_n x^{2n}(2n)!/(n!)^2 = 1/\sqrt{1-x^2}$. As a result, we can write the sum in Eq. (5.106) as

$$\begin{aligned}&\sum_n \frac{x^{2n}}{(n!)^2}(2n+m)! = \frac{d^m}{dx^m}\sum_n \frac{x^{2n+m}}{(n!)^2}(2n)! \\ &= \frac{d^m}{dx^m}\frac{x^m}{\sqrt{1-x^2}} \approx \frac{(2m-1)!!}{\sqrt{1-x^2}}\left(\frac{x^2}{(1-x^2)}\right)^m + \\ &+ \frac{m}{2}(3m-1)\frac{(2m-3)!!}{\sqrt{1-x^2}}\left(\frac{x^2}{(1-x^2)}\right)^{m-1} + \cdots .\end{aligned} \tag{5.107}$$

Note that we have used $r \gg 1$ so that $x \to 1$; in this limit, the leading order term comes

from applying the m-th order derivative just to the denominator. In Eq. (5.107) the leading and next order term have been included. For now we use only the leading order term; the next order is needed further below. By changing x back to the original variables, the sum in Eq. (5.106) can be expressed as

$$\sum_n \frac{|\beta_N|^{2n}}{(n!)^2}(2n+m)! \approx \frac{(2m-1)!!\cosh(r)\sinh^{2m}(r)}{(1+2|\zeta_N|^2\cosh^2(r))^{m+1/2}}. \tag{5.108}$$

Inserting Eq. (5.108) in (5.106) results in

$$P_N(m) = \frac{(2m-1)!!}{(2m)!!}\frac{\left(2|\zeta_N|^2\sinh^2(r)\right)^m}{(1+2|\zeta_N|^2\cosh^2(r))^{m+1/2}}, \tag{5.109}$$

where $(2m)!! = 2^m m!$ has been used.

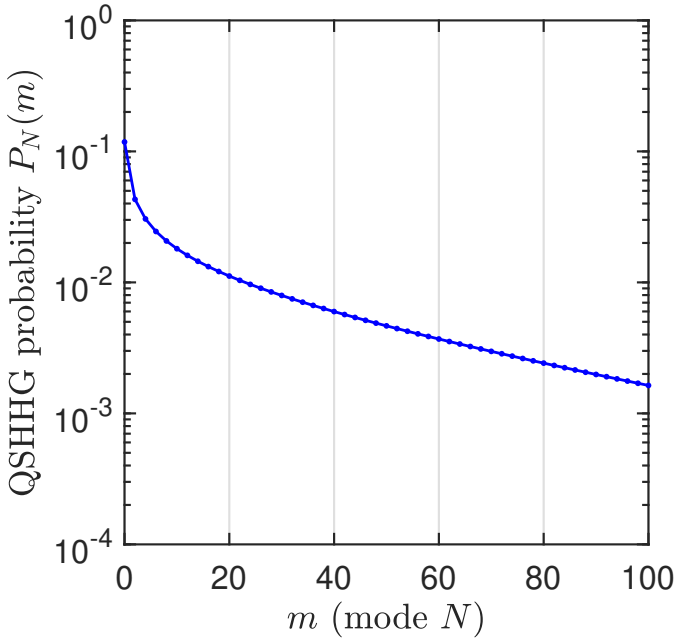

Figure 5.6: QSHHG probability versus effective harmonic photon number m; exact numerical evaluation of Eq. (5.103) (blue line), compared to analytical result (5.109) (dots); every m is populated, although dots are displayed only every second m for visibility. Analytical result is valid for $r \gg 1$. Parameters: $r = 10$, $\theta = 0$, and $\zeta_N = 5.4 \times 10^{-4}$. Smaller r and larger ζ_N are used compared to the manuscript, to demonstrate validity for less intense quantum modes.

To test the accuracy of the analytical result, the numerical evaluation of $P_N(m)$ with Eq.

(5.103) is compared with the analytical result (5.109) in Fig. (5.6). Excellent agreement between the numerical (full line) and the analytical (dots) result is obtained.

Second order coherence and quadrature variance have been calculated before by using a Bogoliubov transformation [112]. The same results can be obtained by using wavefunction (5.103) which is not shown here.

Projective measurement on quantum mode q

We assume a measurement in which the wavefunction is projected on a number state of the quantum mode, $|l\rangle_q$; m and n again refer to general number states of the QSHH mode N and perturbative quantum mode q. The analysis is limited to the two modes. We start from a Taylor expansion of the wavefunction (5.103) limited to two modes,

$$\left|\varphi_m\right\rangle = N_\eta \sum_m \frac{|\zeta_N|^{2m}}{(2m)!}\hat{a}_N^{\dagger 2m}\hat{a}_q^{\dagger 2m} + \frac{|\zeta_N|^{2m+1}}{(2m+1)!}\hat{a}_N^{\dagger 2m+1}\hat{a}_q^{\dagger 2m+1}\sum_n \frac{(-\beta_N)^n}{n!}\hat{a}_q^{\dagger 2n}\left|v_N v_q\right\rangle . \quad (5.110)$$

Here N_η is a normalization factor to be determined.

There are two conditions that give a fixed photon number l in mode q: $2m+2n+\eta = l$, where $\eta = 0, 1$ for even, odd l, respectively. As such, $n = l_\eta/2 - m$ with $l_\eta = l - \eta$ even, and the sum over n can be eliminated to give

$$|\varphi_m\rangle = N_\eta(-\beta_N)^{l/2}\sqrt{l!}\sum_{m=0}^{l_\eta/2}(-1)^m\left(\frac{|\zeta_N|^2}{\beta_N}\right)^{m+\eta/2}\frac{1}{\sqrt{(2m+\eta)!}\,(l_\eta/2-m)!}\,|2m+\eta\rangle_N\,|l\rangle_q. \quad (5.111)$$

Projecting on a number state of the quantum mode gives the wavefunction $|\varphi_N\rangle = {}_q\langle l|\varphi_m(t)\rangle$,

$$|\varphi_N\rangle = N_\eta(-e^{-i\theta})^{l/2}\sum_{m=0}^{l_\eta/2}(-1)^m\left(\frac{|\zeta_N|^2}{\beta_N}\right)^{m+\eta/2}\frac{1}{\sqrt{(2m+\eta)!}\,(l_\eta/2-m)!}\,|2m+\eta\rangle_N . \quad (5.112)$$

where l-dependent absolute value factors have been dropped, as they will disappear during normalization.

The normalization factor N_η is determined from $\sum_m P_N(2m+\eta) = 1$ for $\eta = 0, 1$ with

$$P_N(2m+\eta) = \frac{N_\eta^2 |\beta_N|^\eta}{(2m+\eta)!((l_\eta/2-m)!)^2} \left(\frac{|\zeta_N|^2}{|\beta_N|}\right)^{2m+\eta}. \tag{5.113}$$

To proceed with the analytical derivation, the approximation

$$\frac{1}{(l_\eta/2-m)!} \approx \frac{1}{(l_\eta/2)!}(l_\eta/2)^m \left(1 - \frac{m(m+1)}{l_\eta}\right) \tag{5.114}$$

is used. For intense quantum fields l_η ranges to $> 10^{12}$ and $m \sim 100-1000$. As $m/l_\eta \ll 1$, the zero order approximation in m/l_η is sufficient, and the second term in the bracket of Eq. (5.114) is neglected. Although this approximation is not expected to hold for very small m, it still gives decent results, as will be demonstrated in Fig. 5.7. Further, for the same reason the sum over m can be extended to infinity in the large l_η limit. The approximate wavefunction is obtained as

$$\begin{aligned} |\varphi_N\rangle &= N_\eta(-e^{-i\theta})^{l/2} \sum_{m=0}^{\infty} (-1)^m \frac{\sqrt{\alpha_N}^{2m+\eta}}{\sqrt{(2m+\eta)!}} |2m+\eta\rangle_N \\ N_0 &\approx \frac{1}{\sqrt{\cosh(|\alpha_N|)}} \qquad \alpha_N = \frac{l_\eta |\zeta_N|^2}{2\beta_N} \\ N_1 &\approx \frac{1}{\sqrt{\sinh(|\alpha_N|)}} \end{aligned} \tag{5.115}$$

To leading order, N_η is determined by using the relations

$$\begin{aligned} \sum_m \frac{|\alpha_N|^{2m}}{(2m)!} &= \cosh(|\alpha_N|) \\ \sum_m \frac{|\alpha_N|^{2m+1}}{(2m+1)!} &= \sinh(|\alpha_N|). \end{aligned}$$

Using the projected wavefunction (5.115) and the same approximations as above, we find

$$\begin{aligned} g_N^{(2)} &\approx \frac{1}{\tanh^2(|\alpha_N|)} \qquad \text{for } \eta = 0 \\ g_N^{(2)} &\approx \tanh^2(|\alpha_N|) \qquad \text{for } \eta = 1 \end{aligned} \tag{5.116}$$

and for the quadratures ($j = 1, 2$)

$$\Delta X^2_{jN} \approx \frac{1}{4}\left[1+2\left(|\alpha_N|\tanh(|\alpha_N|)+(-1)^j \mathrm{Re}[\alpha_N]\right)\right],\ \eta = 0$$
$$\Delta X^2_{jN} \approx \frac{1}{4}\left[1+2\left(\frac{|\alpha_N|}{\tanh(|\alpha_N|)}+(-1)^j \mathrm{Re}[\alpha_N]\right)\right],\quad \eta = 1. \tag{5.117}$$

In Fig. (5.7) the exact numerical results for $g^{(2)}_N(0)$ and ΔX^2_{jN} (full lines), obtained from the wavefunction (5.103), are compared with the analytical results (5.116) and (5.117) (markers). The agreement is excellent, validating the analytical derivation.

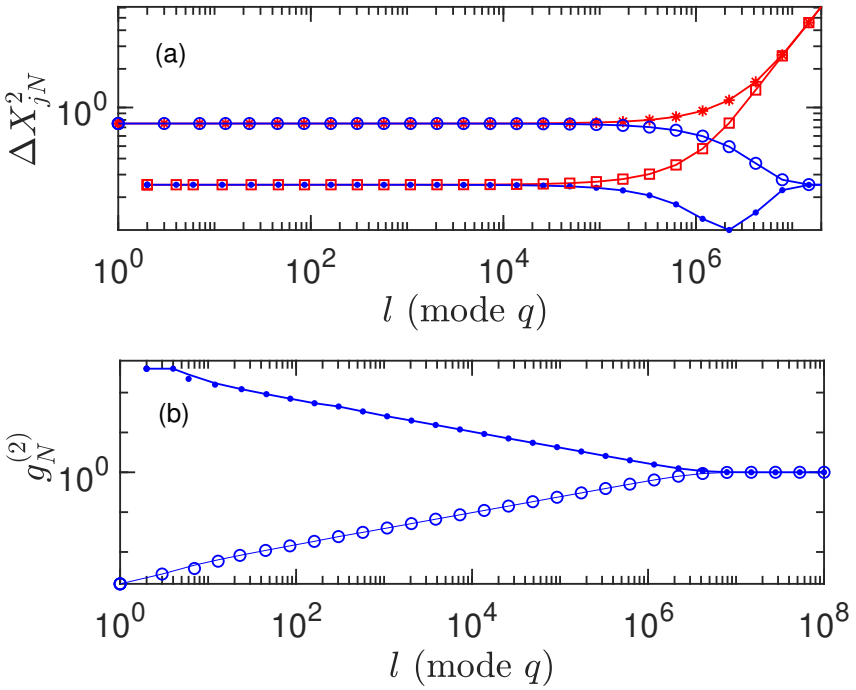

Figure 5.7: After a projective measurement on quantum mode q the wavefunction (5.112) of the QSHH mode N is obtained; with this wavefunction ΔX^2_{jN} ($j = 1, 2$) and $g^{(2)}_N(0)$ are evaluated and plotted in (a), (b), respectively versus photon number l of the perturbative quantum mode. Parameters: $r = 10$, $\theta = 0$ and $|\zeta_N|^2 = 5.4 \times 10^{-4}$. (a), (b) exact numerical results (full lines) are compared with analytical results (markers). (a) even l ($\eta = 0$, full dots and open squares) and odd l ($\eta = 1$, open circles and stars). The blue, red plots represent $\Delta X^2_{1N}, \Delta X^2_{2N}$, respectively. (b) even ($\eta = 0$, dot), odd ($\eta = 1$, circle) photon number l of mode q.

In Fig. 5.8(a)-(c) the Wigner function of the projected wavefunction (5.115) is plotted for quantum photon number $l = 10^{10}$. The parameters are taken from Fig. 1(c) of the

manuscript for harmonic sideband $N = 8$ and $\theta = 0$; $r = 13.6$ and $\langle \hat{n} \rangle_N = 67.2$. Here we study the effect of limited photon number resolution. It is extremely challenging to resolve such high photon numbers down to a single photon. The uncertainty of photon number resolution is referred to as Δl. A clear modulation of the Wigner function with negative and positive parts can be seen in Fig. 5.8(a) for a projective measurement with single-photon resolution, $\Delta l = 0$. The modulation is completely averaged out in Fig. 5.8(b) for a photon resolution $\Delta l = 100$. This is due to the phase oscillation of π between even and odd l states. When the parity is known, i.e. only even or odd states are measured, then the non-classical structure remains for the most part preserved, even for poor photon number resolution, see Fig. 5.8(c) for $\Delta l = 5 \times 10^9$.

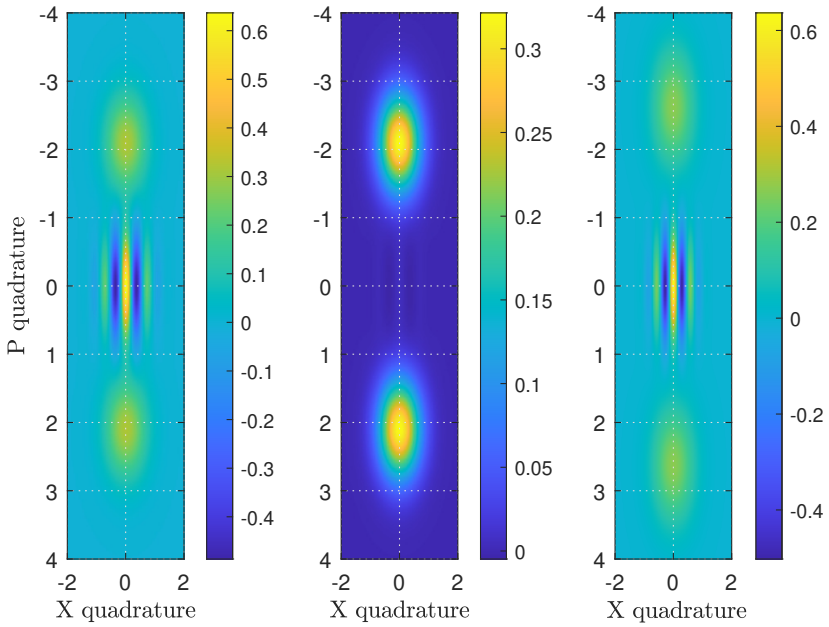

Figure 5.8: The Wigner function of the wavefunction (5.115) is plotted versus X, P which are the quadratures. Parameters are taken from Fig. 1(c) of the manuscript for harmonic sideband $N = 8$ and $\theta = 0$; $r = 13.6$ and $\langle \hat{n} \rangle_N = 67.2$; projected, perturbative quantum photon number $l = 10^{10}$; photon number resolution $\Delta l = 0, 100, 5 \times 10^9$ for (a), (b), (c), respectively; in (c) parity measurement is assumed so that the Wigner function is only averaged over even states.

Projective measurement on harmonic modes N

In a projective measurement m photons in the QSHH mode N are obtained. The resulting wavefunction of quantum mode q, ${}_N\langle m|\varphi_m\rangle = |\varphi_q\rangle$, is obtained from Eq. (5.103) limited to two modes. Taylor expansion of the wavefunction followed by the projection on the QSHH number state gives

$$\left|\varphi_q\right\rangle = N_m \sum_{n=0}^{\infty} (-1)^n \frac{\sqrt{(2n+m)!}}{n!} \beta_N^n \left|2n+m\right\rangle_q , \tag{5.118}$$

where factors that do not depend on n have been dropped, as they will fall away during normalization anyway. The normalization factor is determined by

$$\begin{aligned} \left\langle \varphi_q|\varphi_q \right\rangle &= \sum_n P_q(n) = N_m^2 B_m = 1 \\ B_m &= \sum_{n=0}^{\infty} |\beta_N|^{2n} \frac{(2n+m)!}{(n!)^2}, \end{aligned} \tag{5.119}$$

which has the same form as Eq. (5.106) and thus, can be evaluated with the same method as in Eq. (5.108). This gives

$$B_m \approx \frac{(2m-1)!!\cosh(r)}{\sqrt{1+2|\zeta_N|^2\cosh^2(r)}} \left[\left(\frac{\sinh(r)}{1+2|\zeta_N|^2\cosh^2(r)} \right)^m + \frac{m}{2}\frac{3m-1}{2m-1} \left(\frac{\sinh(r)}{1+2|\zeta_N|^2\cosh^2(r)} \right)^{m-1} \right] \tag{5.120}$$

For $g_N^{(2)}(0)$ we need the expectation values of $\hat{n}_q$ and $\hat{n}_q^2$; For the calculation it is sufficient to limit Eq. (5.120) to the leading order term; we have

$$\left\langle \varphi_q \left| \hat{n}_q \right| \varphi_q \right\rangle = N_m^2 \sum_{n=0}^{\infty} (-1)^n \frac{(2n+m)!}{(n!)^2} \beta_N^n (2n+m). \tag{5.121}$$

By rewriting the last term $2n+m = (2n+m+1)-1$ we can use the same procedure as was used above for the normalization, and obtain

$$\left\langle \varphi_q \left| \hat{n}_q \right| \varphi_q \right\rangle = N_m^2 B_{m+1} - 1 \approx (2m+1) \frac{\sinh^2(r)}{1+2|\zeta_N|^2\cosh^2(r)}. \tag{5.122}$$

Further,

$$\left\langle \varphi_q \left| \hat{n}_q^2 \right| \varphi_q \right\rangle = N_m^2 \sum_{n=0}^{\infty} (-1)^n \frac{(2n+m)!}{(n!)^2} \beta_N^n (2n+m)^2. \tag{5.123}$$

Again, the last term is reexpressed as $(2n+m)^2 = (2n+m+2)(2n+m+1) - 3(2n+m+1) + 1 \approx (2n+m+2)(2n+m+1)$ which gives the leading order term in the $r \gg 1$ limit, $N_m^2 B_{m+2}$; this results in

$$\left\langle \varphi_q \left| \hat{n}_q^2 \right| \varphi_q \right\rangle \approx (2m+3)(2m+1) \left(\frac{\sinh^2(r)}{1 + 2|\zeta_N|^2 \cosh^2(r)} \right)^2. \tag{5.124}$$

Eqs. (5.122) and (5.124) determine $g_N^{(2)}(0)$ as

$$g_N^{(2)}(0) \approx \frac{(2m+3)(2m+1)\sinh^4(r)}{(2m+1)^2 \sinh^4(r)} = 1 + \frac{2}{2m+1}. \tag{5.125}$$

For the quadratures we still need to evaluate

$$\begin{aligned} \left\langle \varphi_q \left| \hat{a}_q^{\dagger 2} \right| \varphi_q \right\rangle &\approx \frac{-1}{2\beta_\kappa} \left(N_m^2 B_{m+1} - (m+1) \right) \\ \left\langle \varphi_q \left| \hat{a}_q^2 \right| \varphi_q \right\rangle_m &\approx \frac{-1}{2\beta_\kappa^*} \left(N_m^2 B_{m+1} - (m+1) \right). \end{aligned} \tag{5.126}$$

Inserting Eqs. (5.126) and (5.122) in Eq. (5.105) gives ($j = 1, 2$)

$$\Delta X_{jN}^2 = \frac{1}{4} \left(2N_m^2 B_{m+1} - 1 + (-1)^j \frac{1 + |\zeta_N|^2}{\tanh(r)} \cos(\theta) \left(2N_m^2 B_{m+1} - 2(m+1) \right) \right). \tag{5.127}$$

In order to evaluate Eq. (5.127) correctly, the next order term in Eq. (5.120) has to be carried along as well. We use $|\zeta_N|^2 \cosh^2(r) \gg 1$ and keep $|\zeta_N|^2 \ll 1$ only to leading order. This results in ($j = 1, 2$)

$$\begin{aligned} \Delta X_{jN}^2 \approx{}& \frac{A_j(r,\theta) + |\zeta_N|^2 (1 + |\zeta_N|^2 \cosh^2(r))}{1 + 2|\zeta_N|^2 \cosh^2(r)} \frac{(2m+1)}{4} \\ &+ \frac{m(m-1)}{2(2m-1)} \left(1 + (-1)^j \cos(\theta) \frac{1 + |\zeta_N|^2}{\tanh(r)} \right). \end{aligned} \tag{5.128}$$

with

$$A_j(r,\theta)=\cosh^2(r)+\sinh^2(r)+2(-1)^j\cosh(r)\sinh(r)\cos(\theta).$$

For the case $\theta = 0$ one obtains

$$\Delta X^2_{1N} \approx \frac{2m+1}{4}\frac{(\cosh(r)-\sinh(r))^2}{1+2|\zeta_N|^2\cosh^2(r)} + \frac{|\zeta_N|^2}{4}\left(1+\frac{1}{2(2m-1)}\right). \tag{5.129}$$

The first term is proportional to the quadrature variance of squeezed vacuum. The additional pre-factors in the first term and the second term come from the mixing between harmonic modes and perturbative quantum mode.

In Fig. (5.9) quadrature variances (a) and second order correlation function (b) of quantum mode q are shown versus photon number m in QSHH mode N. Numerical (full lines) and analytical results (dots) match well.

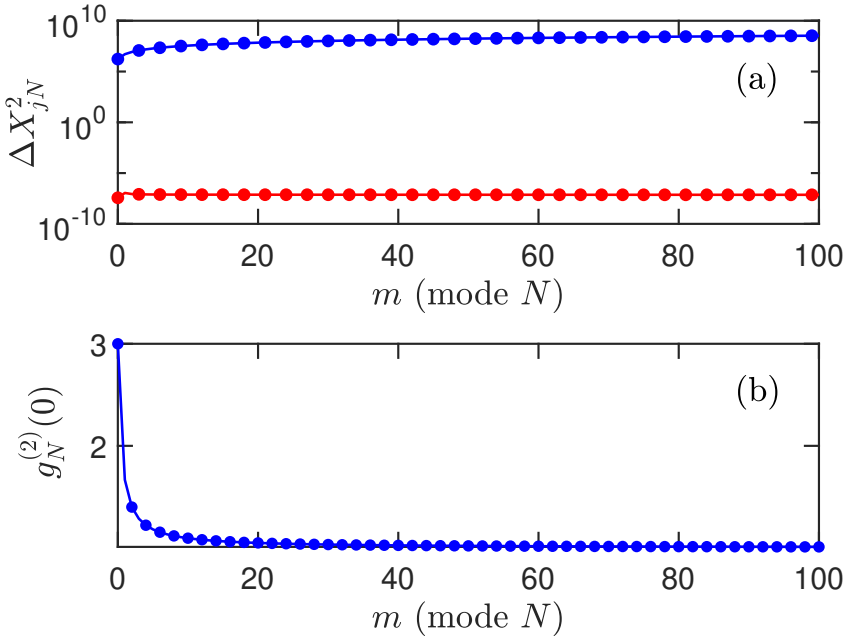

Figure 5.9: In a projective measurement m photons are measured in a QSHH mode. The resulting wavefunction depends on the perturbative quantum mode alone. Variance of quadratures ($j = 1$, blue), ($j = 2$, red) (a), and $g^{(2)}_N(0)$ of quantum mode q (b) versus QSHH photon number m are plotted. Parameters: $r = 10$, $\theta = 0$, and $\zeta_N = 5.4 \times 10^{-4}$. Numerical results from evaluation of Eqs. (5.103) (full lines) are compared with analytical results (dots).

Eq. (5.118) presents an m-photon added squeezed vacuum state [162]. Its Wigner function is plotted in Fig. 5.10 for m=1 (a), m=2 (b) and m=5 (c); parameters are r=13.6 and $\theta = 0$. The Wigner function becomes negative, a clear indication of nonclassicality, and features sub-shot noise oscillations in the squeezed quadrature. Also note the strongly elongated shape of the Wigner function along the X quadrature.

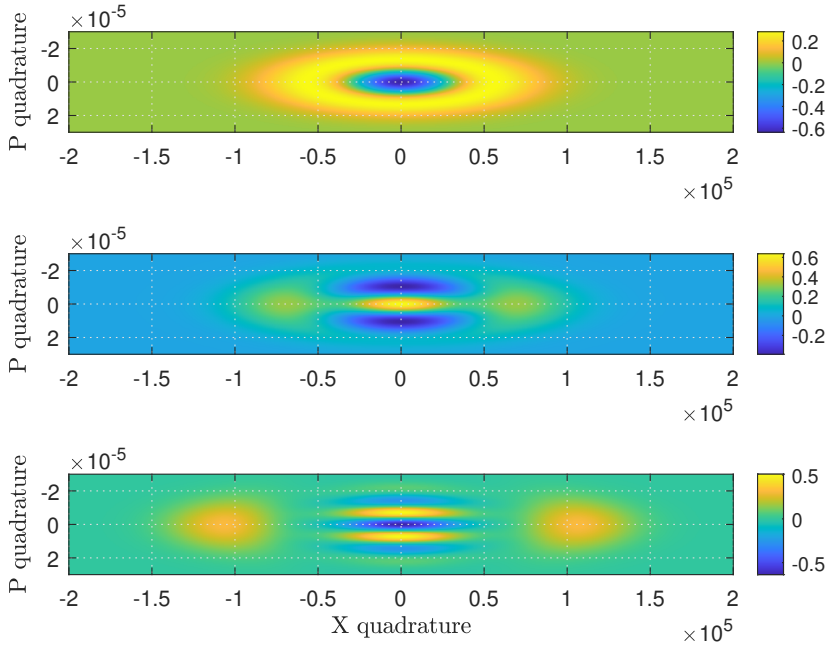

Figure 5.10: The Wigner functions of Eq. (5.115) plotted versus X, P, the quadratures, for (a) $m = 1$, (b) $m = 2$ and (c) m=5, with $r = 13.6$ and $\theta = 0$.

5.6 Appendix

Chapter 5 is the theoretical base for the experiment [113] reprinted here, in appendix.

5.6.1 Photon bunching in high harmonic emission controlled by quantum light

Aside from the papers that made the main body of this thesis, I have also contributed in this project. Chapter 5 is trying to formulate two-color HHG with quantum light which is the topic of the following paper. The paper is reproduced with permission from Springer

Nature. I helped in the experiment, and together with Giulio Vampa and Thomas Brabec developed the theory.

nature photonics

Article

https://doi.org/10.1038/s41566-025-01673-6

Photon bunching in high-harmonic emission controlled by quantum light

Received: 5 April 2024

Accepted: 31 March 2025

Published online: 13 May 2025

Check for updates

Samuel Lemieux [1], Sohail A. Jalil [1], David N. Purschke [1], Neda Boroumand [2], T. J. Hammond [3], David Villeneuve [1], Andrei Naumov [1], Thomas Brabec [2] & Giulio Vampa [1]

Attosecond spectroscopy comprises several techniques to probe matter using electrons and photons. One frontier of attosecond methods is to reveal complex phenomena arising from quantum-mechanical correlations in the matter system, in the photon fields and among them. Recent theories have laid the groundwork for understanding how quantum-optical properties affect high-field photonics, such as strong-field ionization and acceleration of electrons in quantum-optical fields, and how entanglement between the field modes arises during the interaction. Here we demonstrate a new experimental approach that transduces some properties of a quantum-optical state through a strong-field nonlinearity. We perturb high-harmonic emission from a semiconductor with a bright squeezed vacuum field, resulting in the emission of sidebands of the high harmonics with super-Poissonian statistics, indicating that the emitted photons are bunched. Our results suggest that perturbing strong-field dynamics with quantum-optical states is a viable way to coherently control the generation of these states at short wavelengths, such as extreme ultraviolet or soft X-rays. Quantum correlations will be instrumental to advance attosecond spectroscopy and imaging beyond the classical limits.

Quantum-optical states of light are finding numerous applications in fields such as computing, sensing and metrology[1], spectroscopy[2,3] and imaging[4]. Most of the technology relies on the manipulation and readout of photons at infrared or visible frequencies. Accessing quantum light at shorter wavelengths, such as extreme ultraviolet (XUV) or X-rays[5,6], may be quite beneficial: phase sensitivity increases, a feature particularly appealing for sensing applications, while detector noise decreases because the photon energy is much greater than thermal fluctuations. Yet, investigation of quantum-optical states at short wavelengths is still in its infancy[7,8]. Short-wavelength radiation can be produced in a laboratory via high-harmonic generation[9], an extremely nonlinear optical process that creates what is effectively an attosecond-lived oscillating quantum antenna composed of laser-accelerated electron–hole pairs in matter that radiates light at odd multiples of the driving laser frequency[10–12]. During the interaction, quantum-mechanical correlations arise within the matter system[13,14] and, as recently discovered, in the photon fields. Exploring high-harmonic emission from a quantum-optical perspective is poised to reveal new insights into strong light–matter interactions[15–20] and unlock new capabilities, such as the generation of cat or kitten states[21], squeezed XUV light[17,22] and entangled XUV photons[23].

Here we investigate experimentally how strongly driven electron–hole pairs responsible for high-harmonic emission from a semiconductor (ZnO) react to a quantum-optical perturbation, that is, a bright squeezed vacuum (BSV) beam. A BSV is a macroscopic quantum-optical state generated at the output of an unseeded high-gain optical parametric amplifier[24–26]. In the degenerate case considered here, it features amplitude fluctuations in one of the electric field quadratures below those of the vacuum (the squeezed quadrature) and for this reason is employed in precision metrology with sub-shot-noise

[1]Joint Attosecond Science Laboratory, National Research Council of Canada and University of Ottawa, Ottawa, Ontario, Canada. [2]Department of Physics, University of Ottawa, Ottawa, Ontario, Canada. [3]Department of Physics, University of Windsor, Windsor, Ontario, Canada. e-mail: [redacted]

Article https://doi.org/10.1038/s41566-025-01673-6

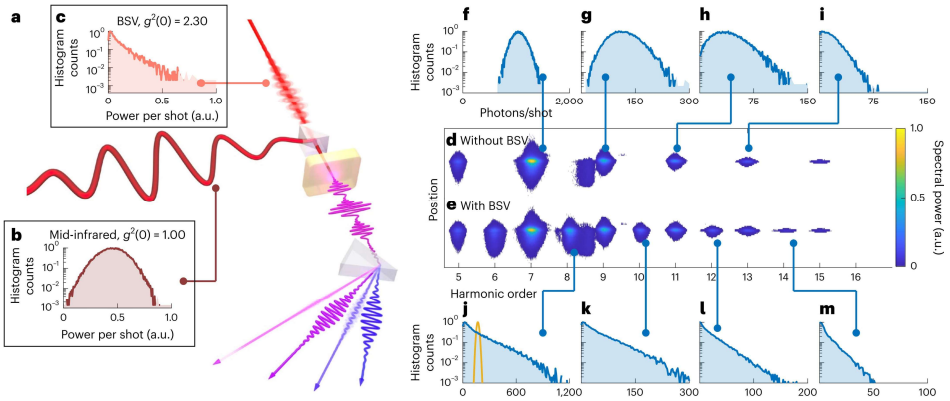

Fig. 1 | Generation of non-Poissonian sidebands. a, Intense coherent mid-infrared laser pulses (solid red line, wavelength $\lambda = 3{,}300$ nm, intensity $I \approx 1.2$ TW cm^{-2}, pulse duration $\tau_{FWHM} = 80$ fs, energy $u = 1.25$ µJ) are overlapped in space and time with BSV pulses (fuzzy orange line, $\lambda = 1{,}600$ nm, $\Delta\lambda = 50$ nm, $u = 1.5$ nJ) inside a 500-nm-thick ZnO (0001) crystal and generate a comb of high-order harmonics (purple lines). **b**, A histogram of the pulse energy of the coherent mid-infrared beam. The large non-zero average energy and shape of the distribution result in $g^{(2)}(0) = 1.00$, as expected for a coherent beam. **c**, Pulse energy statistics of the BSV beam, clearly showing the heavy-tail distribution expected from squeezed vacuum. The calculated $g^{(2)}(0)$ is 2.30. **d**,**f**–**i**, The high-harmonic spectrum without BSV perturbation (**d**) shows that only odd-order harmonics are measured, with statistics (**f**–**i**) like that of the mid-infrared beam. **e**,**j**–**m**, The BSV perturbation generates sidebands of the high-harmonic spectrum at nearly the even-order harmonics (**e**), with statistics closely resembling that of the BSV beam (**j**–**m**) and clearly deviating from Poisson statistics (the Poisson distribution with the mean number of photons measured for the eighth sideband is given in **j**, orange line). Statistics for the harmonics and sidebands are given in number of photons per shot.

sensitivity[1]. The BSV beam creates sidebands of the unperturbed odd-harmonic spectrum that exhibit shot-to-shot power fluctuations with super-Poissonian statistics, indicative of photon bunching and of the generation of a non-coherent state at the short high-harmonic wavelength. Furthermore, our simple theoretical model predicts that the variance of the field quadratures of the sidebands can be coherently controlled by using the relative phase between the BSV and the unperturbed spectrum, paving the way for the controlled generation of non-coherent quantum-optical attosecond states.

To perturb electron trajectories leading to high-harmonic emission, we mix a BSV beam at a wavelength of 1,600 nm with an intense coherent mid-infrared beam with a wavelength of 3,300 nm, inside a ZnO (0001) single crystal (Fig. 1a). The BSV beam is obtained by spontaneous parametric down-conversion in the high-gain regime of a 50-fs, 800-nm laser in two successive beta barium borate (BBO) crystals, a scheme that filters the number of spatial and spectral modes[27]. The statistics of the measured pulse energy of each shot in these two beams confirms that the mid-infrared pump is in a coherent state, with a normalized time-zero second-order correlation function $g^{(2)}(\tau = 0) = 1.00$ (Fig. 1b), where τ is the arrival delay of the photons, whereas the BSV beam exhibits a heavy-tail distribution with $g^{(2)}(0) = 2.30$ (Fig. 1c) typical of a femtosecond BSV[27–29]. A modal analysis suggests that the BSV beam is composed of one spatial mode and between one and two effective spectral modes (Methods), which explains the lower $g^{(2)}$ compared with the theoretical limit of 3. At an intensity of ~1.2 TW cm^{-2}, the mid-infrared driver generates only odd-order harmonics down to a wavelength of ~210 nm (photon energy of 5.9 eV) (Fig. 1d, spectrum). The addition of the BSV beam generates sidebands at nearly the even-order harmonics of the coherent pump (Fig. 1e). The emission of even-order sidebands indicates that the perturbation σ to the high-harmonic dipole obeys the following time-translation symmetry: $\sigma(t + \frac{\pi}{\omega}) = -\sigma(t)$ (refs. 30,31), that is, it changes sign between two adjacent laser half-cycles (where ω is the frequency of the driving field). Thus, even though the BSV field is not well defined at any instant, it retains the time-translation symmetry of a coherent field. In other words, it is first-order coherent[24] and repeats identically every cycle within the coherence length, with amplitude fluctuations only arising among different temporal modes (pulses).

The photon statistics of the generated ultraviolet light are strikingly different between sidebands and harmonics: whereas the unperturbed harmonics exhibit statistics resembling that of the coherent pump (Fig. 1f–i), the sidebands inherit the heavy-tailed distribution of the BSV beam (Fig. 1j–m). For comparison, the Poisson distribution with the mean number of photons in the eighth sideband is given in Fig. 1j (orange line). This split between harmonics and sidebands is even more apparent when comparing the $g^{(2)}(0)$. Figure 2 reports the $g^{(2)}(0)$ for 20 blocks of the data for each unperturbed harmonic and sideband, as a function of the measured average number of photons per shot. Whereas the harmonics maintain a $g^{(2)}(0) < 1.1$, the sidebands exhibit $g^{(2)}(0)$ between 1.8 and 2.6, on average comparable to that of the BSV ($g^{(2)}_{BSV}(0) = 2.3$; Fig. 2, dashed black line). Thus, the sidebands exhibit super-Poissonian statistics with fluctuations comparable to those of the BSV. Since the emission occurs within the femtosecond pulse duration, $g^{(2)}(\tau > 0) = 1$, thus $g^{(2)}(0) > g^{(2)}(\tau > 0)$, that is, the sidebands are likely photon bunched[24]. The photon number statistics of the perturbed odd-order harmonics also inherit the heavy-tail distribution of the BSV beam (Fig. 3a–d), and as a result, the $g^{(2)}(0)$ increases above 1 (Fig. 3e, filled circles).

Only ~1.5 nJ of BSV is needed to generate a broad comb of non-Poissonian light across the visible and deep-ultraviolet spectral regions (ZnO is known to generate high harmonics up to photon energies of 10 eV (ref. 32), thus the generation of sidebands in the vacuum-ultraviolet spectral region is plausible). The generation of sidebands across the whole high-harmonic spectrum indicates that high-harmonic generation gates the interaction with the BSV pulse to a fraction of the coherent mid-infrared cycle, periodically every

https://doi.org/10.1038/s41566-025-01673-6

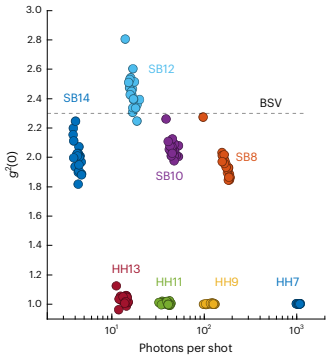

Fig. 2 | $g^{(2)}(0)$ of the sidebands. The $g^{(2)}(0)$ of the high harmonics (labelled 'HHx', where 'x' is the harmonic order) is close to 1.0 (as expected of coherent beams), while for the sidebands (labelled 'SBx', where 'x' is the sideband order), $1.8 < g^{(2)}(0) < 2.6$, comparable to that of the BSV beam (dashed black line). The data set comprises 40,000 shots divided into 20 blocks (one data point per block).

half cycle. The duration of the gate depends on the duration of the perturbed electron–hole pair trajectory[31], thus it can be as short as attoseconds. A temporal characterization of the sideband comb is likely to yield a train of attosecond to few-femtosecond bursts of non-classical light. In addition, each sideband has a spectral bandwidth comparable to the high harmonics, evidence of further temporal gating within the mid-infrared pulse envelope. Although the frequency detuning of the BSV beam from the perfect 2ω could broaden the spectrum of each sideband[33], the 6% detuning of the centre wavelength from 3,200 nm should yield a maximum sideband spectral width of ~0.12ω. The measured width is much larger, ~$0.25–0.30\omega$, thus corroborating the hypothesis of temporal gating. In contrast, direct up-conversion of the BSV beam, which is spectrally filtered with a 50 nm bandwidth at 1,600 nm (Extended Data Fig. 4c, blue spectrum), results in narrow low-order harmonics (Extended Data Fig. 1a) that are substantially weaker than the sidebands. Thus, our approach leverages the strength of the coherent mid-infrared driver to generate brighter non-coherent states at short wavelengths. Gating also occurs in space, which results in a filtering of the number of spatial sideband modes. In addition, Extended Data Fig. 1b shows harmonic generation with the broadband BSV beam (unfiltered; Extended Data Fig. 4c, orange spectrum) up to the seventh harmonic. Single-shot acquisitions of the harmonic spectra allow to retrieve $g^{(2)}(0) = 7.9$ and 4.9 for the fifth and seventh harmonic, respectively. Harmonic generation from BSV has also been recently demonstrated[34], though without reporting $g^{(2)}$ values.

The sideband power varies linearly with the BSV power (Extended Data Fig. 2), as expected from a wave-mixing picture of high-harmonic generation perturbed with classical fields[35,36]. Linear scaling in the perturbing field is interpreted as arising from one-photon addition/subtraction channels from the sub-laser-cycle high-harmonic polarization, as shown schematically in Fig. 4a. In the sum-frequency channel, one sideband photon of frequency ω_{sb} is created by absorption of one perturbing (BSV) photon of frequency ω_0 and one high-harmonic polarization photon of frequency $\omega_1 = \omega_{sb} - \omega_0$. In the difference-frequency channel, the sideband photon is created by emission of a perturbing photon from a high-harmonic polarization of frequency $\omega_2 = \omega_{sb} + \omega_0$. At the same time, perturbing the odd-order harmonics (Fig. 3) requires a minimum of two photons in the perturbation, as required by symmetry and demonstrated for coherent perturbations[35,36]. On the basis of this understanding, we model the generation of sidebands and perturbed high harmonics with the following interaction Hamiltonian for the radiation field:

$$H_{\mathrm{int}} = i\hbar\Gamma\left(\epsilon_1 \hat{a}_0 \hat{a}_{\mathrm{sb}}^{\dagger} + \epsilon_2 \hat{a}_0^{\dagger} \hat{a}_{\mathrm{sb}}^{\dagger}\right) + \mathrm{h.c.}, \qquad (1)$$

where the first two terms represent the sum-frequency and difference-frequency channels, respectively. Γ represents the interaction strength, $i\hbar = 2\pi\hbar$ is Planck constant, and h.c. stands for Hermite conjugate. For the quantized modes, $\hat{a}_{[\mathrm{sb},0]}$ and $\hat{a}_{[\mathrm{sb},0]}^{\dagger}$ represent the lowering and raising operators of the sideband and perturbation fields. This Hamiltonian accounts for interactions with the BSV mode to all orders in the perturbation, as evinced by expanding the associated unitary evolution operator in series (see Methods for the unitary operator). The unperturbed high-harmonic polarization states are considered coherent and undepleted and therefore treated classically, thus $\epsilon_1, \epsilon_2 \in \mathbb{C}$. The complex ϵ_1 and ϵ_2 account for the varying spectral phases θ_1 and θ_2 of the high harmonics (attochirp[12]). The perturbing field is assumed to be a squeezed vacuum state with squeezing parameter $\xi = re^{i\phi}$ ($r \in \Re$)[24]. This model predicts that the sidebands should have the same $g^{(2)}$ as the BSV perturbation (Methods), even in the presence of multiple BSV modes, in agreement with the measurements reported in Fig. 2. This is expected from one-photon (that is, linear) processes, where the photon number distribution of the perturbation is copied to that of the sidebands (with varying efficiencies, which however do not affect $g^{(2)}$, in the limit of large photon numbers). The mean sideband photon number, $\langle n \rangle$, and the variance of the two field quadratures, $\langle (\Delta X)^2 \rangle$ and $\langle (\Delta P)^2 \rangle$, are plotted in Fig. 4b, c and d, respectively, as functions of ϕ and $\theta_1 - \theta_2$. We find that $\langle n \rangle$ oscillates with ϕ because of interference between the degenerate sum- and difference-frequency pathways. This behaviour is analogous to that measured with classical fields[30,31]. The quadratures, on the other hand, reveal a more nuanced

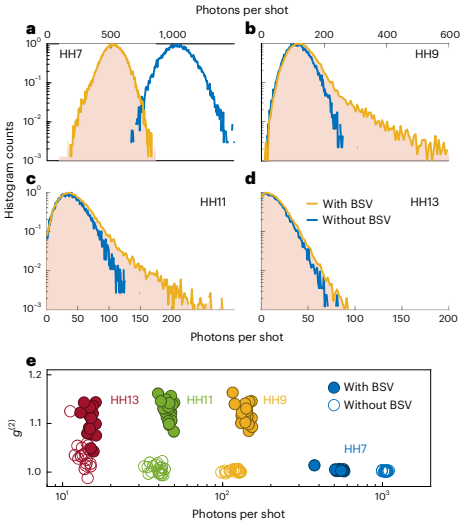

Fig. 3 | $g^{(2)}(0)$ of the perturbed odd harmonics. a–d, The BSV beam is sufficiently strong to also perturb the odd harmonics, whose photon number statistics pick up a heavy tail, as shown for harmonics 7 (**a**), 9 (**b**), 11 (**c**) and 13 (**d**). **e**, The $g^{(2)}(0)$ is thereby increased from the coherent-state value of 1.

 https://doi.org/10.1038/s41566-025-01673-6

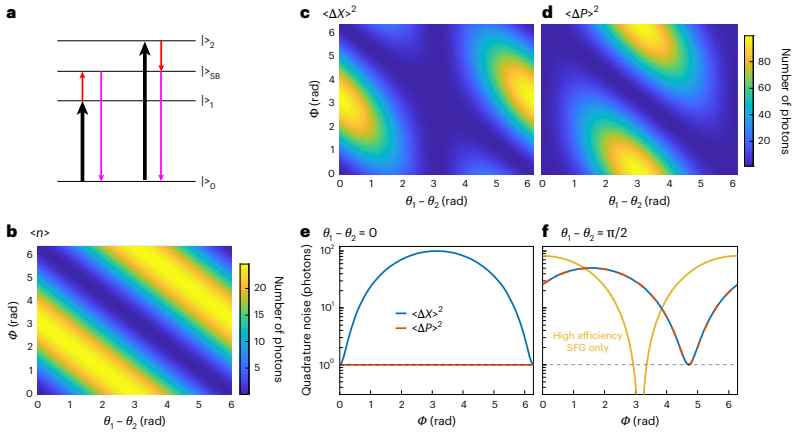

Fig. 4 | Wave-mixing model. a, The model accounts for emission of a sideband photon (purple arrows) by absorption of one lower-lying high-harmonic polarization photon ($|\rangle_0 \rightarrow |\rangle_1$ transition, black arrow) and one perturbing photon (red arrow) (left) and by absorption of one upper-lying high-harmonic polarization photon ($|\rangle_0 \rightarrow |\rangle_2$ transition) and emission of one perturbing photon (right). **b**, The average number of sideband photons $\langle n \rangle$ oscillates with the BSV phase ϕ and the relative phase between the un-perturbed high-harmonic states, $\theta_1 - \theta_2$, in agreement with classical models of coherent control. **c**,**d**, The X (**c**) and P (**d**) quadratures of the sideband field also modulate. **e**,**f**, Depending on $\theta_1 - \theta_2$, the quadratures can be different from one another (**e**, the case when the P quadrature retains minimum uncertainty) or equal (**f**), leading to either squashed or super-thermal states. The amplitude of the quadratures can be controlled by using ϕ. Squeezing can be achieved in the sum-frequency channel when all perturbation photons are up-converted (yellow line, obtained with $\epsilon_2 = 0$, $\Gamma t = \pi/2$, where t is the interaction time, $\langle n \rangle_0 (t = 0) = 20$).

modulation: depending on the relative phase between the initial high-harmonic states and the squeezed perturbation, the quadratures can be equal (Fig. 4f), leading to the generation of super-thermal sidebands[37,38], or unequal, resulting in squashed states[39] (Fig. 4e). In the case where $\theta_1 - \theta_2 = 0$ (Fig. 4e), that is, when the harmonics are in phase, one quadrature modulates with ϕ whereas the other retains minimum uncertainty ($4\langle(\Delta P)^2\rangle = 1$), resulting in a maximally squashed state. We note that the foci of the BSV and mid-infrared beams are displaced longitudinally in our experiment, which causes substantial transverse averaging of the relative phase between the two beams and suppresses any coherent oscillations (see Methods for an estimate of the phase averaging). Squashed and super-thermal states have found use in quantum-enhanced imaging[40] and quantum computation[39]. Additionally, the model predicts that the spent perturbing field and the emitted sideband are correlated since the latter requires absorption of a squeezed photon. A projective measurement on a sideband photon, therefore, may result in the generation of a coherently controlled cat or kitten state in the perturbing squeezed beam[21].

Can the sidebands be squeezed? It is commonly understood that the generation of a squeezed (that is, below shot noise) sum frequency is possible when nearly all photons of the initial, lower-frequency squeezed beam are up-converted[41]. This is also what our model predicts when the perturbing field is depleted (Fig. 4f, yellow line). In the spontaneous regime of parametric down-conversion, where squeezed vacuum photons are correlated in pairs, preserving squeezing at the sum frequency requires up-conversion of both correlated photons in a pair, a condition that is only reached when most photons are converted, if the conversion process does not preferentially select pairs. However, in the experiment, we estimate that ~10 photons per shot are emitted from the crystal at the 12th sideband, when the average pulse energy of the BSV is set to ~1.5 nJ, corresponding to ~1×10^{10} photons per shot. Thus, approximately 1 sideband photon is emitted per 10^9 BSV photons. This conversion efficiency is used for modelling. With this low conversion efficiency, squeezing gives way to the emission of squashed or thermal sidebands.

In summary, we experimentally demonstrated that perturbing high-harmonic generation with a quantum-optical perturbation, that is, bright squeezed vacuum, generates a comb of super-bunched high-order sidebands. Our results indicate that strong-field excitation, acceleration and recombination of electron–hole pairs responsible for high-harmonic emission gate a quantum-optical field with sub-cycle precision and establish an effective method to study the quantum-optical nature of strong-field interactions, eliciting questions regarding how quantumness is transferred to the accelerated pairs and how the theorized photon-statistics force emerges[18]. This sub-cycle gating can also potentially be harnessed to measure quantum-optical states and further our understanding of time-resolved quantum electrodynamics[42,43]. The same method can probably be applied to the generation of unusual coherently controlled attosecond currents[44,45] and terahertz radiation[46]. Finally, our method paves the way for coherently controlled emission of non-classical states with high photon energy, with potential benefits for quantum-enhanced metrology at short wavelengths, possibly even in the extreme ultraviolet, and in the attosecond temporal domain.

Online content

Any methods, additional references, Nature Portfolio reporting summaries, source data, extended data, supplementary information, acknowledgements, peer review information; details of author contributions and competing interests; and statements of data and code availability are available at https://doi.org/10.1038/s41566-025-01673-6.

References

1. Degen, C. L., Reinhard, F. & Cappellaro, P. Quantum sensing. *Rev. Mod. Phys.* **89**, 035002 (2017).

2. Mukamel, S. et al. Roadmap on quantum light spectroscopy. *J. Phys. B* **53**, 072002 (2020).
3. Kira, M. et al. Quantum spectroscopy with Schrödinger-cat states. *Nat. Phys.* **7**, 799–804 (2011).
4. Chrapkiewicz, R. et al. Hologram of a single photon. *Nat. Photonics* **10**, 576–579 (2016).
5. Adams, B. W. et al. X-ray quantum optics. *J. Mod. Opt.* **60**, 2–21 (2013).
6. Tamasaku, K. et al. Visualizing the local optical response to extreme-ultraviolet radiation with a resolution of λ/380. *Nat. Phys.* **7**, 705–708 (2011).
7. Eisenberger, P. & McCall, S. L. X-ray parametric conversion. *Phys. Rev. Lett.* **26**, 684 (1971).
8. Shwartz, S. et al. X-ray parametric down-conversion in the Langevin regime. *Phys. Rev. Lett.* **109**, 013602 (2012).
9. Ferray, M. et al. Multiple-harmonic conversion of 1064 nm radiation in rare gases. *J. Phys. B* **21**, L31 (1988).
10. Krausz, F. & Ivanov, M. Attosecond physics. *Rev. Mod. Phys.* **81**, 163 (2009).
11. Corkum, P. B. Plasma perspective on strong field multiphoton ionization. *Phys. Rev. Lett.* **71**, 1994 (1993).
12. Villeneuve, D. M. Attosecond science. *Contemp. Phys.* **59**, 47–61 (2018).
13. Koll, L.-M. et al. Experimental control of quantum-mechanical entanglement in an attosecond pump–probe experiment. *Phys. Rev. Lett.* **128**, 043201 (2022).
14. Shiner, A. D. et al. Probing collective multi-electron dynamics in xenon with high-harmonic spectroscopy. *Nat. Phys.* **7**, 464–467 (2011).
15. Stammer, P. et al. Quantum electrodynamics of intense laser-matter interactions: a tool for quantum state engineering. *PRX Quantum* **4**, 010201 (2023).
16. Gorlach, A. et al. High-harmonic generation driven by quantum light. *Nat. Phys.* **19**, 1689–1696 (2023).
17. Gorlach, A. et al. The quantum-optical nature of high harmonic generation. *Nat. Commun.* **11**, 4598 (2020).
18. Even Tzur, M. et al. Photon-statistics force in ultrafast electron dynamics. *Nat. Photonics* **17**, 501–509 (2023).
19. Tsatrafyllis, N. et al. High-order harmonics measured by the photon statistics of the infrared driving-field exiting the atomic medium. *Nat. Commun.* **8**, 15170 (2017).
20. Theidel, D. et al. Evidence of the quantum optical nature of high-harmonic generation. *PRX Quantum* **5**, 040319 (2024).
21. Lewenstein, M. et al. Generation of optical Schrödinger cat states in intense laser–matter interactions. *Nat. Phys.* **17**, 1104–1108 (2021).
22. Tzur, M. E. et al. Generation of squeezed high-order harmonics. *Phys. Rev. Res.* **6**, 033079 (2024).
23. Sloan, J. et al. Entangling extreme ultraviolet photons through strong field pair generation. Preprint at https://arxiv.org/abs/2309.16466 (2023).
24. Gerry, C. C. & Peter L. K. *Introductory Quantum Optics* (Cambridge Univ. Press, 2023).
25. Slusher, R. E. et al. Pulsed squeezed light. *Phys. Rev. Lett.* **59**, 2566 (1987).
26. Aytür, O. & Kumar, P. Pulsed twin beams of light. *Phys. Rev. Lett.* **65**, 1551 (1990).
27. Pérez, A. M. et al. Bright squeezed-vacuum source with 1.1 spatial mode. *Opt. Lett.* **39**, 2403–2406 (2014).
28. Sh. Iskhakov, T. et al. Superbunched bright squeezed vacuum state. *Opt. Lett.* **37**, 1919–1921 (2012).
29. Cutipa, P. & Chekhova, M. V. Bright squeezed vacuum for two-photon spectroscopy: simultaneously high resolution in time and frequency, space and wavevector. *Opt. Lett.* **47**, 465–468 (2022).
30. Dudovich, N. et al. Measuring and controlling the birth of attosecond XUV pulses. *Nat. Phys.* **2**, 781–786 (2006).
31. Vampa, G. et al. Linking high harmonics from gases and solids. *Nature* **522**, 462–464 (2015).
32. Ghimire, S. et al. Observation of high-order harmonic generation in a bulk crystal. *Nat. Phys.* **7**, 138–141 (2011).
33. Orenstein, G. et al. Shaping electron-hole trajectories for solid-state high harmonic generation control. *Opt. Express* **27**, 37835–37845 (2019).
34. Rasputnyi, A. et al. High-harmonic generation by a bright squeezed vacuum. *Nat. Phys.* **20**, 1960–1965 (2024).
35. Bertrand, J. B. et al. Ultrahigh-order wave mixing in noncollinear high harmonic generation. *Phys. Rev. Lett.* **106**, 023001 (2011).
36. Purschke, D. N. et al. Microscopic mechanisms of high-order wave mixing in solids. *Phys. Rev. A* **108**, L051103 (2023).
37. Manceau, M. et al. Indefinite-mean Pareto photon distribution from amplified quantum noise. *Phys. Rev. Lett.* **123**, 123606 (2019).
38. Lettau, T. et al. Superthermal photon bunching in terms of simple probability distributions. *Phys. Rev. A* **97**, 053835 (2018).
39. Jahangiri, S. et al. Point processes with Gaussian boson sampling. *Phys. Rev. E* **101**, 022134 (2020).
40. Allevi, A., Cassina, S. & Bondani, M. Super-thermal light for imaging applications. *Quantum Meas. Quantum Metrol.* **4**, 26–34 (2017).
41. Vollmer, C. E. et al. Quantum up-conversion of squeezed vacuum states from 1550 to 532 nm. *Phys. Rev. Lett.* **112**, 073602 (2014).
42. Kizmann, M. et al. Subcycle squeezing of light from a time flow perspective. *Nat. Phys.* **15**, 960–966 (2019).
43. Riek, C. et al. Subcycle quantum electrodynamics. *Nature* **541**, 376–379 (2017).
44. Dupont, E. et al. Phase-controlled currents in semiconductors. *Phys. Rev. Lett.* **74**, 3596 (1995).
45. Sederberg, S. et al. Vectorized optoelectronic control and metrology in a semiconductor. *Nat. Photonics* **14**, 680–685 (2020).
46. Jana, K. et al. Quantum control of flying doughnut terahertz pulses. *Sci. Adv.* **10**, eadl1803 (2024).

Article https://doi.org/10.1038/s41566-025-01673-6

Methods

Experimental layout

A sketch of the experimental layout is shown in Extended Data Fig. 3. A femtosecond amplified Ti:sapphire laser system (Coherent Legend) delivers 50-fs pulses with 1.8 mJ of energy at a repetition rate of 1 kHz. A white-light seeded optical parametric amplifier (LightConversion TOPAS-C) is pumped with 1.3 mJ. The signal and idler beams are set to wavelengths of 1.29 µm and 2.11 µm, respectively. They are spatially separated and recombined on a type II Silver Thiogallate (AGS) crystal tuned for difference-frequency generation at a wavelength of 3.30 µm. A long-pass filter with a cut-on wavelength of 2.4 µm (Edmund #68-653) removes signal and idler beams. About 5 µJ of energy is measured in the mid-infrared beam after this filter. The mid-infrared beam, the coherent pump in the experiment, is focused on a 500-nm-thick ZnO (0001) single crystal epitaxially grown on a 0.5-mm-thick sapphire substrate with an off-axis parabola with focal length $f = 25$ mm, generating odd-order high harmonics. The size of the high-harmonic beam at the ZnO exit surface is 40 µm ($1/e^2$ diameter), measured on the basis of the drop of harmonic power as a sharp Au electrode deposited on the ZnO surface is scanned over the beam. Using the high-harmonic spot size, the estimated mid-infrared pulse duration of 80 fs and the energy incident on the ZnO (1.25 µJ), we estimate the mid-infrared intensity to be comparable to or less than 1.2 TW cm^{-2}. The harmonic beam is split into two replicas by using a metallic beam splitter (Thorlabs NDUV03A), and both replicas are focused, vertically displaced, on the input slit of a commercial UV–vis spectrometer (Princeton Instruments Isoplane 320, equipped with a PI-MAX4 intensified camera with slow-gate UV photocathode). A typical image of the spectrum is shown in Extended Data Fig. 3 (top left).

The remaining 500 µJ from the laser system is utilized to generate a BSV beam in type I geometry in two 2-mm-thick, uncoated BBO crystals in tandem. The BBO separation is 19 cm. The pump beam is telescoped down to ~1 mm size before entering the BBO crystals, and a combination of wavelength and transmission polarizers serves as a power throttle. The input power on the BBOs is 48 mW. The serial combination of BBOs effectively filters a smaller selection of spatial (and frequency) modes emanating from the first crystal, as demonstrated in ref. 27. The BSV spectrum is subsequently filtered to a 50 nm bandwidth centred at about 1.6 µm (Edmund #87-872), and spurious visible light is further suppressed with an RG1000 filter. The BSV pulse energy after the filters is ~1.5 nJ. The BSV beam at the BBO output is re-imaged on the ZnO crystal with suitable demagnification to a spot size of 70–100 µm ($1/e^2$ diameter), as measured with an infrared objective lens (10× Mitutoyo Plan Apo NIR infinity corrected) and an InGaAs camera (Xenics Bobcat+ 320). Collinear combination of BSV and mid-infrared beams is performed with a custom dielectric mirror (S1 HR 1,600–2,000 nm HT 3,200–4,200 nm, S2 uncoated, CaF_2 substrate; Laseroptik GmbH). The spatial overlap at the ZnO crystal is measured by using the same imaging system utilized to measure the BSV focus size. Both beams have parallel polarizations.

The spectrometer camera is gated to record single shots of the ultraviolet spectrum at a refresh rate of ~60 Hz in three different region of interests (ROIs): ROI1 and ROI2 are vertically centred on either of the two harmonic beams, and ROI3 is along the vertical centre of the sensor to record the background of every shot (Extended Data Fig. 3, two-dimensional (2D) spectrum). The single-shot ROIs are then vertically fully integrated and horizontally integrated over a region of $[m - 0.3, m + 0.3]$, where m is the sideband/harmonic order. The resulting analog-to-digital units (ADUs) in the shot are then converted to photon number as

$$S_{\mathrm{out}}\{\mathrm{ph/shot}\} = \frac{S_{\mathrm{in}}\{\mathrm{ADU}\}}{\mathrm{QE}\{\mathrm{p.e./ph}\} \times \mathrm{sensitivity}\{\mathrm{ADU/p.e.}\}},$$

where the quantum efficiency (QE) of the photocathode in the intensifier (number of photoelectrons (p.e.) for incident photon) is 0.25 and the sensitivity of 92.6 accounts for both the micro-channel plate (MCP) gain in the intensifier and the camera specifications (factory calibrated). The measured photons per shot in each harmonic in ROI1 and ROI2 are then utilized to calculate the two-mode $g^{(2)}(0) = \langle n_1 n_2 \rangle / (\langle n_1 \rangle \langle n_2 \rangle)$. Correlating the two ROIs instead of calculating the $g^{(2)}(0)$ of either ROI alone removes the stochastic response of the intensifier, which tends to distort the photon number distributions and artificially increases the value of $g^{(2)}$.

The reflection of the mid-infrared pump off the surface of a CaF_2 window is measured with a PbSe amplified photodiode (Thorlabs PDA20H), a boxcar integrator and a 12-bit digital acquisition card (DAQ), simultaneously to the high-harmonic spectra. The reflection of the BSV off the RG1000 filter is measured with an InGaAs photodiode (Thorlabs DET10D). The signal is directly digitized with a 2-GHz oscilloscope and numerically integrated, asynchronously to the other beams. Given the high number of photons in the mid-infrared and BSV beams, the single-mode $g^{(2)}(0)$ is calculated with the scale-invariant form $g^{(2)}(0) = \langle n \rangle^2 / \langle n^2 \rangle$.

Estimate of transverse phase averaging

We measure a longitudinal displacement of the mid-infrared and BSV foci of 600 µm. We performed the experiment 100 µm away from the BSV focus and 500 µm away from the mid-infrared focus. Because of wavefront curvature away from the focus, the mid-infrared phase at a position one beam waist 'w_0' away from the axis is $\phi = \frac{\pi w_0^2}{\lambda R(z)} = z_r / R(z)$, where z_r is the Rayleigh range and $R(z) = z[1 + (z_r/z)^2]$ is the radius of curvature. Using $w_0 = 20$ µm and $z = 500$ µm, $z_r = 380$ µm, we obtain $\phi = 0.5$ rad, or 32% of a mid-infrared quarter cycle. Because the coherent modulation is periodic every quarter cycle of the mid-infrared field, phase averaging over just one-eighth of a cycle is sufficient to substantially quench the modulation.

Modal analysis of the BSV beam

To explain the measured value of $g^{(2)}$ of the BSV beam, we perform a spatio-spectral modal analysis using a singular value decomposition of the spatial profile and of the spectrum of the BSV source with the sklearn Python package. This is done on a set of several hundred single-shot beam profiles and spectra. The analysis of the spatial modes is presented in Extended Data Fig. 4a,b. Extended Data Fig. 4a shows the beam profile of the BSV beam averaged over all measured shots. Extended Data Fig. 4b shows the first principal component from the most prominent eigenvector of the covariance matrix of flattened single-shot images. They are nearly identical. In fact, the first principal component accounts for 98.5% of the variance of the data set. Thus, our BSV photons are nearly all in one spatial mode.

Extended Data Fig. 4c,d presents the spectral analysis. Extended Data Fig. 4c shows the average BSV spectrum before the 1.6-µm bandpass filter (orange line). Running a clustering algorithm on 10,000 single-shot spectra, we identify two distinct classes of spectra: one exhibiting a single peak centred at 1,600 nm (solid dotted line) and one exhibiting a two-peak structure with a node at 1,600 nm (dashed black line). A third cluster is composed of spectra that are in between the first two. All clusters are equally represented in the data set; that is, the associated spectra are all equally likely to be generated. We associate the single-peaked spectra with a degenerate squeezed vacuum mode and the two-peak spectra with a twin-beam squeezed mode. To estimate the $g^{(2)}$ that we expect to measure from this few-mode source, we perform a Monte Carlo sampling of each distribution, drawing from both a BSV and exponential distributions for the one-peak and two-peak modes, respectively. The number of photons in each shot is the sum of the number of photons sampled from each distribution. The two-mode distribution is shown in Extended Data Fig. 4d (orange line). With equal average occupancy in the two modes, we find $g^{(2)} = 1.7$, in agreement with our measurement of the BSV statistics before the bandpass filter.

Thus, our BSV seems to be composed of approximately two equal-amplitude spectral modes. Our method yields a slightly lower number of modes than predicted by the commonly used expression for the effective number of modes $m = (g^{(2)}_{sm} - 1)/(g^{(2)}_{meas} - 1)$, where $g^{(2)}_{sm}$ is the single-mode $g^{(2)}$ of BSV and $g^{(2)}_{meas}$ is the measured $g^{(2)}$ (refs. 28,47). For degenerate BSV, $g^{(2)}_{sm} = 3$ in the limit of large photon numbers, and for non-degenerate BSV, $g^{(2)}_{sm} = 2$, yielding $m = 2.8$ and $m = 1.4$, respectively. We note that this common expression accounts for m effective modes of the same type (all degenerate or all non-degenerate), despite the fact that $g^{(2)}$ decreases farther from degeneracy[28], a result that suggests that the admixture must be between degenerate and non-degenerate modes.

The average BSV spectrum after the 1.6-μm bandpass filter is shown in Extended Data Fig. 4c (blue line). The transmission of both representative spectra (single and double-peaked) through the filter is calculated to be ~40% and ~5% for the first and second modes, respectively. Thus, after the filter, the relative amplitude decreases to ~13% and the effective number of modes is reduced to nearly 1. Monte Carlo sampling with an occupancy ratio between the twin-beam and squeezed-vacuum modes of ~0.13 yields $g^{(2)} = 2.6$. The distribution is shown in Extended Data Fig. 4d (blue line). This value of $g^{(2)}$ is close to the measured value of 2.3.

Theoretical model

The initial photon state is considered to be $|\varphi_0(0)\rangle = |\mathcal{E}\rangle_0|0\rangle_{sb}$, where the subscripts '0' and 'sb' refer to the perturbation and the sideband modes. The perturbation is in a squeezed vacuum state with squeezing parameter $\xi = re^{i\phi}$ ($r \in \Re$); the sideband is initially in vacuum. The unperturbed harmonic polarization states ('1' and '2' in Fig. 4a) are assumed to be in coherent states with amplitudes $\epsilon_1 = |\epsilon_1|e^{i\theta_1}$ and $\epsilon_2 = |\epsilon_2|e^{i\theta_2}$, and we assume them to be undepleted. Therefore, they are treated classically with parameters ϵ_1 and ϵ_2 in the interaction Hamiltonian equation (1) and do not enter the initial photon state ansatz. The Hamiltonian in equation (1) leads to the final state

$$|\varphi_0(t)\rangle = e^{g a_0 a_{sb}^\dagger + f a_0^\dagger a_{sb}^\dagger - \text{h.c.}} |\mathcal{E}\rangle_0 |0\rangle_{sb} = \hat{S}|\mathcal{E}\rangle_0 |0\rangle_{sb}, \tag{2}$$

With $g = \Gamma t\epsilon_1$ and $f = \Gamma t\epsilon_2$, where t is the interaction time, representing the efficiencies of the sum-frequency and difference-frequency channels, respectively. The field quadratures are given by $\hat{X} = \hat{a} + \hat{a}^\dagger$ and $\hat{P} = -i(\hat{a} - \hat{a}^\dagger)$. The variances $\langle\varphi_0|(\Delta X_{sb})^2|\varphi_0\rangle = \langle(X_{sb} - \langle X_{sb}\rangle)^2\rangle$ ($\langle(\Delta P_{sb})^2\rangle$) and the mean photon number $\langle n_{sb}\rangle$ are calculated with the Bogoliubov transformation

$$\hat{S}^\dagger \hat{a}_{sb}{}^\dagger \hat{S} = \hat{a}_{sb}{}^\dagger \cosh N + \hat{p}_0^\dagger \frac{\sinh N}{N},$$

where $\hat{p}_0^\dagger = g^* \hat{a}_0^\dagger + f^* \hat{a}_0$ and $N^2 = |f|^2 - |g|^2$. These are

$$\left\langle\varphi_0\left|\hat{a}_{sb}{}^2\right|\varphi_0\right\rangle = M^2\left[fg\left(\sinh^2 r + \cosh^2 r\right) - \left(f^2 e^{-i\phi} + g^2 e^{i\phi}\right)\sinh r \cosh r\right],$$

$$\left\langle\varphi_0\left|\hat{a}_{sb}^{\dagger 2}\right|\varphi_0\right\rangle = M^2\left[f^* g^*\left(\sinh^2 r + \cosh^2 r\right) - \left(f^{*2} e^{i\phi} + g^{*2} e^{-i\phi}\right)\sinh r \cosh r\right]$$

$$\langle n_{sb}\rangle = \left\langle\varphi_0\left|\hat{a}_{sb}^\dagger \hat{a}_{sb}\right|\varphi_0\right\rangle = M^2\left|f\cosh r - g e^{i\phi}\sinh r\right|^2,$$

with $M^2 = \sinh^2 N/N$. The result for the quadratures is

$$\Delta^2_{X^2_\varphi} = 1 + 2M^2\left(\left|f\cosh r - g e^{i\phi}\sinh r\right|^2 \pm \Re\left[fg\right]\left(\sinh^2 r + \cosh^2 r\right) \mp \Re\left[f^2 e^{-i\phi} + g^2 e^{i\phi}\right]\sinh r\cosh r\right).$$

According to the definition of the quadratures, the vacuum state has $\Delta^2_{X^2_\varphi} = 1$. Figure 4 plots $\Delta^2_{X^2_\varphi}$ and $\langle n_{sb}\rangle$ for the parameter values $\sinh r = \sqrt{1\times 10^{11}}$, $\Gamma t = \pi/(4\times 10^5)$, $|\epsilon_1| = |\epsilon_2| = 1$, which results in a conversion efficiency of 2×10^{-10}, similar to that measured experimentally. To show the possibility of squeezing in the sum-frequency pathway alone, we set $|\epsilon_2| = 1$, $\Gamma t = \pi/2$, $\sinh r = \sqrt{20}$ (Fig. 4f, yellow line). Squeezing only occurs when the conversion efficiency from the squeezed perturbation approaches unity, in agreement with ref. 41. The difference-frequency pathway, instead, always results in excess quadrature noise because it is effectively a two-mode squeezing interaction, which is known to create states with thermal statistics in each mode[24].

To calculate the $g^{(2)}(0)$ of the sidebands, we assume the normally ordered operator in equation (2) to be approximately a two-mode squeezing operator

$$|\varphi_0(t)\rangle \simeq e^{\gamma a_{sb}^\dagger a_0^\dagger - \gamma^* a_{sb} a_0}|\xi'\rangle_0|0\rangle_{sb} = |\bar{\varphi}_0(t)\rangle, \tag{3}$$

where $\gamma = f - 2g\beta = |\gamma|e^{i\varphi}$ and $\xi' = r'e^{i\varphi}$ is an effective squeezing parameter. It is related to the original squeezing parameter ξ through the following relations: $\tilde{\beta} = \frac{1}{2}\tanh r' e^{i\phi}$, $\tilde{\beta} = \beta/(1+|\gamma|^2)$, $\beta = \frac{1}{2}\tanh r e^{i\phi}$. For the normal ordering derivation, we consider $|\gamma| \simeq \tanh|\gamma|$; that is, powers of $|\gamma|$ greater than 2 are neglected. Using the Bogoliubov transformation $S^\dagger a_{sb} S = a_{sb}\cosh|\gamma| + a_0^\dagger \sinh|\gamma|e^{i\varphi}$, we evaluate

$$\left\langle\bar{\varphi}_0(t)\right|a_{sb}^\dagger a_{sb}\left|\bar{\varphi}_0(t)\right\rangle = (\sinh|\gamma|)^2\left\langle a_0 a_0^\dagger\right\rangle,$$

$$\left\langle a_{sb}^\dagger a_{sb} a_{sb}^\dagger a_{sb}\right\rangle = (\sinh|\gamma|\cosh|\gamma|)^2\left\langle a_0 a_0^\dagger\right\rangle + (\sinh|\gamma|)^4\left\langle\left(a_0 a_0^\dagger\right)^2\right\rangle.$$

To evaluate the $g^{(2)}$ in the presence of K independent BSV modes, we assume the existence of K independent sideband modes paired to each of the BSV modes, that is, a collection of K independent two-mode (sideband, BSV) squeezers, as evinced from equation (3), each squeezer satisfying the Bogoliubov transformations above. The multi-mode $g^{(2)}_{sb}(0)$ is defined as[47]

$$g^{(2)}_{sb}(0) = \frac{\left\langle :\left(\sum_k a^\dagger_{sb,k} a_{sb,k}\right)^2 :\right\rangle}{\left\langle\sum_k a^\dagger_{sb,k} a_{sb,k}\right\rangle^2},$$

where $: \;:$ denotes normal ordering and $a_{sb,k}$ refers to sideband mode k. This evaluates to

$$g^{(2)}_{sb}(0) = \frac{\sum_k(\sinh|\gamma_k|)^4\left[\left\langle a_{0,k}a^\dagger_{0,k}\right\rangle + \left\langle\left(a_{0,k}a^\dagger_{0,k}\right)^2\right\rangle\right] + \sum_{k\neq k'}(\sinh|\gamma_k|\sinh|\gamma_{k'}|)^2\left\langle a_{0,k}a^\dagger_{0,k}\right\rangle\left\langle a_{0,k'}a^\dagger_{0,k'}\right\rangle}{\left[\sum_k(\sinh|\gamma_k|)^2\left\langle a_{0,k}a^\dagger_{0,k}\right\rangle\right]^2} =$$

$$= \frac{\sum_k(\sinh|\gamma_k|)^4\left[\langle n_{0,k}+1\rangle + \left\langle(n_{0,k}+1)^2\right\rangle\right] + \sum_{k\neq k'}(\sinh|\gamma_k|\sinh|\gamma_{k'}|)^2\langle n_{0,k}+1\rangle\langle n_{0,k'}+1\rangle}{\left[\sum_k(\sinh|\gamma_k|)^2\langle n_{0,k}+1\rangle\right]^2}$$

where we used $aa^\dagger - a^\dagger a = aa^\dagger - n = 1$. For a collection of equally populated, degenerate squeezed vacuum modes at the perturbation, $r_k = r$, $\gamma_k = \gamma$, $\langle n_{0,k}+1\rangle = (\cosh r')^2$, $\left\langle(n_{0,k}+1)^2\right\rangle = (\cosh r')^4[1 + 3(\sinh r')^2]$, and $g^{(2)}_{sb}(0)$ reduces to

$$g^{(2)}_{sb}(0) = \frac{K\left[3(\cosh r')^4 - (\cosh r')^2\right] + K(K-1)(\cosh r')^4}{K^2(\cosh r')^4}$$

$$= 1 + \frac{(3-1)}{K} - \frac{1}{K(\cosh r')^2} \approx 1 + \frac{(3-1)}{K} = g^{(2)}_0(0)$$

where $g^{(2)}_0(0)$ is the multi-mode $g^{(2)}$ of degenerate squeezed vacuum[28]. Thus, in agreement with experimental observations (Fig. 2), all sidebands are expected to have the same $g^{(2)}$ as the BSV perturbation, whether it is single-mode ($g^{(2)} = 3$) or multi-mode ($g^{(2)} < 3$).

Data availability

Data available on request from the authors. Correspondence and requests for materials should be addressed to the corresponding author.

Article https://doi.org/10.1038/s41566-025-01673-6

References

47. Christ, A. et al. Probing multimode squeezing with correlation functions. *New J. Phys.* **13**, 033027 (2011).

Acknowledgements

We acknowledge D. Crane and R. Kroeker for providing continuing technical support; B. Sussman, G. Thekkadath, F. Bouchard, J. Lundeen, D. Reis and P. Corkum for useful discussions; J. Upham for lending specialized equipment. G.V. and S.A.J. acknowledge financial support from the Joint Center for Extreme Photonics. G.V. acknowledges support from NSERC Discovery grant RGPIN-2021-04286. D.P. acknowledges support from the NSERC Postdoctoral fellowship programme. S.L. and G.V. acknowledge support from the NRC Quantum Sensing programme, project QSP-103.

Author contributions

G.V. conceived the experiment. S.L., S.A.J., D.N.P. and T.J.H. performed the experiment with help from N.B. and D.V. N.B. and T.B. developed the theoretical model. A.N. maintained the infrastructure. T.B. and G.V. supervised the project. G.V. wrote the manuscript with help from all co-authors.

Competing interests

The authors declare no competing interests.

Additional information

Extended data is available for this paper at https://doi.org/10.1038/s41566-025-01673-6.

Correspondence and requests for materials should be addressed to Giulio Vampa.

Peer review information *Nature Photonics* thanks Olga Kocharovskaya, Michael Krüger and the other, anonymous, reviewer(s) for their contribution to the peer review of this work.

Article https://doi.org/10.1038/s41566-025-01673-6

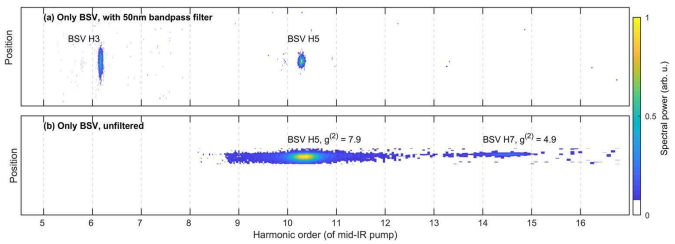

Extended Data Fig. 1 | Direct up-conversion of BSV. (a) When the BSV pulse energy is 30 nJ, the 3rd and 5th harmonics of the BSV frequency are measurable. Note that the spectral width is much narrower than the sidebands because the BSV bandwidth is limited to 50 nm, corresponding to a coherence time of 75 fs. **(b)** Without the bandpass filter on the BSV beam, up to the 7th harmonic is measured with a BSV energy of 37 nJ (the 3rd harmonic is not measured in this case as it is outside the detected range of the spectrometer). Single-shot measurements of this spectrum allow to retrieve the $g^{(2)}(0) = 7.9$ and 4.9 for the 5th and 7th harmonics of the BSV beam, respectively.

Article https://doi.org/10.1038/s41566-025-01673-6

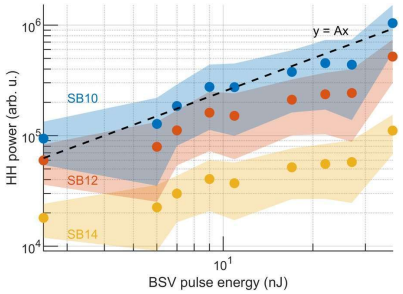

Extended Data Fig. 2 | Scaling of sidebands and harmonics with BSV power. The sidebands power scales linearly with the BSV pulse energy, in agreement with a wave-mixing interpretation of *in-situ* high-harmonic control, suggesting a one-photon mixing process in the BSV beam. The colored areas denote the uncertainty of one standard deviation of the set of single-shot spectra.

Article https://doi.org/10.1038/s41566-025-01673-6

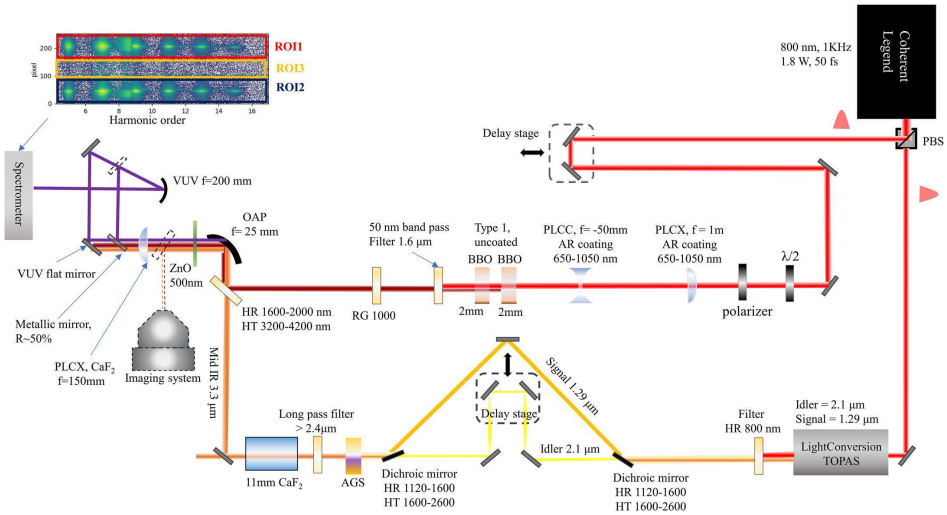

Extended Data Fig. 3 | Sketch of experimental layout. 'PBS': Polarizing beam splitter, a combination of half-wave plate and thin-film polarizer; 'Spectrometer': Princeton Instruments IsoPlane 320, equipped with PI-MAX4 intensified camera; 'OAP': Off-Axis Parabola, f = 25 mm (Thorlabs MPD119-M01); 'AGS': 400 µm-thick, θ = 39 deg, φ = 45 deg, AR coated 1–2.6 µm on the front surface, AR 2.6–11 µm on the back surface. 'Imaging system' includes an InGaAs camera (Xenics Bobcat+ 320). All mirrors after the ZnO crystal are Al-coated vacuum ultraviolet mirrors (Acton coating #1900). Monitoring photodiodes for the mid-infrared and BSV beams are not shown.

Article https://doi.org/10.1038/s41566-025-01673-6

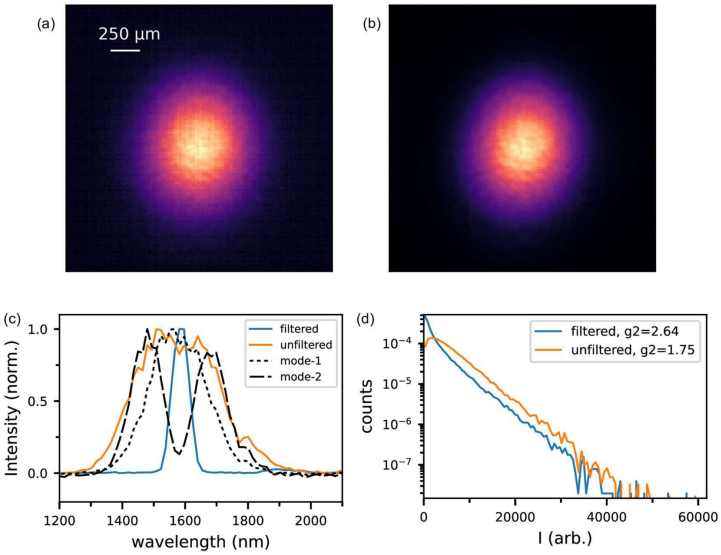

Extended Data Fig. 4 | Modal analysis of the BSV beam. (**a**) Spatial mode of the BSV averaged over 100 shots. (**b**) First principal component from the most prominent eigenvector of the covariance matrix of flattened single-shot images, displaying nearly identical structure to the average spatial mode. (**c**) Average spectrum before (orange) and after (blue) spectral filtering and representative single-shot spectra from the two distinct clusters (black lines). (**d**) Monte Carlo sampling of two uncorrelated distributions, one with thermal (exponential) statistics, representing the non-degenerate mode (dashed black line in panel **c**), and one with BSV statistics, representing the degenerate mode (dotted black line in panel **c**). The orange and blue curves represent the case where the two modes have equal intensity and where the non-degenerate mode has 10 percent of the intensity of the degenerate mode, respectively. These situations correspond approximately to the filtered and unfiltered spectra in (**c**).

5.6.2 A simple case of SFG and DFG

Here we consider a scenario where we have two different channels i.e. the sum frequency generation (SFG) and difference frequency generation (DFG). We consider a case where we have vacuum in one mode and squeezed light in the other mode. We want to see in which case we get squeezing in the vacuum mode. This part is useful in understanding the SFG and DFG channels of QSHHG later. We follow the derivation of the paper [157]. The Hamiltonian for these two cases is as follows

$$\hat{H}_{SFG} = i\hbar\xi\left(\hat{a}_1\hat{a}_2^\dagger - \hat{a}_1^\dagger\hat{a}_2\right), \tag{5.130}$$

$$\hat{H}_{DFG} = i\hbar\xi\left(\hat{a}_1^\dagger\hat{a}_2^\dagger - \hat{a}_1\hat{a}_2\right). \tag{5.131}$$

We have:

$$\begin{aligned} \hat{a}_1 &\rightarrow \text{Squeezed Light} \\ \hat{a}_2 &\rightarrow \text{Vacuum state} \\ \xi &\rightarrow \text{real.} \end{aligned} \tag{5.132}$$

We considered ξ to be real; the complex case can be easily derived.
The Heisenberg equation of motion is

$$\frac{d\hat{a}}{dt} = \frac{i}{\hbar}\left[\hat{H}, \hat{a}\right]. \tag{5.133}$$

- **SFG Hamiltonian**: In this case using Eq. (5.133) for mode 1, we have

$$\frac{d\hat{a}_1}{dt} = \xi\left[\hat{a}_1\hat{a}_2^\dagger - \hat{a}_1^\dagger\hat{a}_2, \hat{a}_1\right] = -\hat{a}_2\xi. \tag{5.134}$$

  Doing the same for $\hat{a}_2$, for the second derivative in mode 1, we have

$$\frac{d^2\hat{a}_1}{dt^2} = -\xi\frac{d\hat{a}_2}{dt} = -\xi^2\hat{a}_1. \tag{5.135}$$

  Integrating the above equation, we get

$$\begin{aligned} \hat{a}_1(t) &= \hat{a}_1(0)\cos(\xi t) - \hat{a}_2(0)\sin\xi t, \\ \hat{a}_2(t) &= \hat{a}_2(0)\cos(\xi t) + \hat{a}_1(0)\sin\xi t. \end{aligned} \tag{5.136}$$

What we need is to calculate the quadratures in mode 2. We have the following formula for the quadratures [4]

$$\langle \Delta \hat{X}^2 \rangle = 1 + 2\langle \hat{n} \rangle + 2\langle \hat{a} \rangle \langle \hat{a}^\dagger \rangle \pm \langle \Delta \hat{a}^2 \rangle \pm \langle \Delta \hat{a}^\dagger \rangle. \tag{5.137}$$

For mode 2 the expectation value of the number operator is

$$\begin{aligned} \langle \hat{n}_2 \rangle =& \langle \hat{a}_2^\dagger \hat{a}_2 \rangle = \langle \left(\hat{a}_2^\dagger(0) \cos(\xi t) + \hat{a}_1^\dagger(0) \sin \xi t \right) \times \left(\hat{a}_2(0) \cos(\xi t) + \hat{a}_1(0) \sin \xi t \right) \rangle \\ =& \sinh^2(\xi t) \langle \hat{a}_1^\dagger(0) \hat{a}_1(0) \rangle = \sinh^2(\xi t) \sinh^2(r). \end{aligned} \tag{5.138}$$

In the above, we have used the fact that expectation value of number operator is $\sinh^2 r$, where r is the squeezing parameter [4]. Furthermore, we have the following relations:

$$\langle \hat{a}_2 \rangle = \langle \hat{a}_2^\dagger \rangle = 0, \tag{5.139}$$

$$\langle \hat{a}_2^2 \rangle = \sinh^2(\xi t) \langle \hat{a}_1^2(0) \rangle = -\sinh r \cosh r e^{i\theta} \sinh^2(\xi t), \tag{5.140}$$

$$\langle \hat{a}_2^{2\dagger} \rangle = \sinh^2(\xi t) \langle \hat{a}_1^{2\dagger}(0) \rangle = -\sinh r \cosh r e^{-i\theta} \sinh^2(\xi t). \tag{5.141}$$

Again we have used the equations for the squeezed light from the book [4]. Putting everything together, for the quadratures we get

$$\begin{aligned} \langle \Delta \hat{X}^2 \rangle =& 1 + 2\sinh^2 r \sinh^2(\xi t) \pm \left(-\sinh r \cosh r e^{-i\theta} \sinh^2(\xi t) \right) \\ & \pm \left(-\sinh r \cosh r e^{i\theta} \sinh^2(\xi t) \right). \end{aligned} \tag{5.142}$$

At time $t = \frac{\pi}{2\xi}$, and for the case of $\theta = 0$, we have unity conversion efficiency. At this time we get

$$\langle \Delta \hat{X}^2 \rangle = (\sinh r \pm \cosh r)^2 = e^{\pm 2r}. \tag{5.143}$$

The above equation shows that we get squeezing in mode 2 with the condition of unity conversion effciency.

- **DFG Hamiltonian**: In this case we have

$$\frac{d\hat{a}_1}{dt} = \xi \left[\hat{a}_1^\dagger \hat{a}_2^\dagger - \hat{a}_1 \hat{a}_2, \hat{a}_1 \right] = \hat{a}_2^\dagger \xi. \tag{5.144}$$

For the second derivative, we have

$$\frac{d^2\hat{a}_1}{dt^2} = \xi\frac{d\hat{a}_2^\dagger}{dt} = \xi^2\hat{a}_1. \tag{5.145}$$

Integrating the above equation we get

$$\begin{aligned}\hat{a}_1(t) &= \hat{a}_1(0)\cosh(\xi t) + \hat{a}_2^\dagger(0)\sinh\xi t,\\ \hat{a}_2(t) &= \hat{a}_2(0)\cosh(\xi t) + \hat{a}_1^\dagger(0)\sinh\xi t.\end{aligned} \tag{5.146}$$

What we need is to calculate the quadratures in mode 2. For mode 2 the expectation value of the number operator is

$$\begin{aligned}\langle\hat{n}_2\rangle &= \langle\hat{a}_2^\dagger\hat{a}_2\rangle = \langle\left(\hat{a}_2^\dagger(0)\cos(\xi t) + \hat{a}_1(0)\sin\xi t\right)\times\left(\hat{a}_2^\dagger(0)\cos(\xi t) + \hat{a}_1(0)\sin\xi t\right)\rangle\\ &= \sinh^2(\xi t)\langle\hat{a}_1(0)\hat{a}_1^\dagger(0)\rangle = \sinh^2(\xi t)\cosh^2(r).\end{aligned} \tag{5.147}$$

In the above, we have used the fact that expectation value of number operator is $\sinh^2 r$, where r is the squeezing parameter. Furthermore, we have the following relations:

$$\langle\hat{a}_2\rangle = \langle\hat{a}_2^\dagger\rangle = 0, \tag{5.148}$$

$$\langle\hat{a}_2^2\rangle = \sinh^2(\xi t)\langle\hat{a}_1^{2\dagger}(0)\rangle = -\sinh r\cosh re^{-i\theta}\sinh^2(\xi t), \tag{5.149}$$

$$\langle\hat{a}_2^{2\dagger}\rangle = \sinh^2(\xi t)\langle\hat{a}_1^2(0)\rangle = -\sinh r\cosh re^{i\theta}\sinh^2(\xi t). \tag{5.150}$$

Putting everything together, for the quadratures we get

$$\begin{aligned}\langle\Delta\hat{X}^2\rangle &= 1 + 2\cosh^2 r\sinh^2(\xi t) \pm \left(-\sinh r\cosh re^{i\theta}\sinh^2(\xi t)\right)\\ &\pm\left(-\sinh r\cosh re^{-i\theta}\sinh^2(\xi t)\right).\end{aligned} \tag{5.151}$$

At time where $\sinh(\xi t)^2 = 1$, we do not have unity conversion efficiency. At this time we get

$$\langle\Delta\hat{X}^2\rangle = 2 + (\sinh r \pm \cosh r)^2 = 2 + e^{\pm 2r}. \tag{5.152}$$

The above equation shows that we do not get squeezing in mode 2 in the case of DFG.

Chapter 6

Conclusion and Outlook

In this thesis quantum aspects of strong field processes were investigated. While in strong field physics matter is treated quantum mechanically, light fields are usually described by the classical Maxwell equations. In my work additional quantum aspects come in through two avenues.

First, matter is a many-body system consisting of many ions and electrons. Strong field processes are usually treated in the single electron approximation. I have attempted to build in many-body dynamics via a heat bath approach, i.e. one electron is exposed to an intense field, and all the other particles present the environment. In a first work, we considered only a bosonic heat bath. Although the spin boson Hamiltonian is simple many interactions can be covered which allows to treat the heat bath as a harmonic oscillator with a linear coupling to the system. This is best done in the notation of second quantization and allows for an analytic integration of the electron heat bath interaction.

Second, quantum optical aspects of strong field physics have generated increasing interest. In difference to semiclassical theories that have been used so far, here fields are treated using the formalism of second quantization. These quantum optical properties, such as squeezing and entanglement and the negativity of the Wigner function, are of fundamental importance for the field of quantum information and quantum computation [114].

Chapter (2) reviews the derivation of the Keldysh ionization theory, and it is based on the publication [1]. In particular, we give a detailed account of the analytic continuation of the integration contour into the complex domain. Another point that we did was to show in detail how to evaluate a saddle point integral in the presence of a singularity. We also obtained a factor of 2 relative to Keldysh's original derivation in the atomic ionization rates. This creates the foundation for understanding strong field processes and acquiring

the necessary theoretical tools.

In chapter (3), a closed-form formalism for modeling high harmonic generation in solids was derived; using that a diagnostic tool to separate virtual and real transitions was developed. Comparing the results with experiments clarified the importance of often neglected processes, such as dephasing of the strong field dynamics from coupling to the many body environment of solids. At time of publication [66] there was no good method beyond the relaxation time approximation to deal with noise in strong field processes. Relaxation time approximation leads to unphysical excitation to the excited states [5].

In chapter (4), inspired by the previous chapter, we add noise to our strong field adiabatic following approximation (SFAF) formalism and compare the results with T_2 relaxation time approximation [66]. We model the many body effects as bosonics heat bath. The bosonic heat bath can account for a wide range of interactions including collective electronic interactions, such as phonons, excitons, and plasmons. However, it does not account for fermionic electron electron collisions. Developing a fermionic heat bath model for electron collisions is subject to future research. Here, our approach was focused on a heat bath in thermal equilibrium. Clearly during strong laser interaction the heat bath evolves dynamically which can also be treated with our formalism, and it is also subject to future research.

In chapter (5), we discuss the quantum sideband high harmonic generation (QSHHG). QSHHG are the even harmonics generated by adding the second harmonic to the fundamental laser; the word quantum comes from the fact that we used quantum light to generate them. A comprehensive theoretical framework of QSHH has been introduced. It serves as a foundation for designing and developing QSHHG as a short wavelength attosecond source for quantum light generation. Our theoretical analysis has revealed that QSHHG creates entanglement between the harmonic sideband modes and between the harmonic sidebands and the quantum perturbation. The entanglement allows to quantum engineer high harmonic generation via projective measurements. As a result, a variety of states commonly used in quantum information theory can be generated, such as Schrödinger cat states, and photon added squeezed vacuum states. These states will find applications in extending quantum sensing, quantum imaging, and quantum information science to the XUV regime [97]. One possible future work can be adding noise to QSHHG model. Another one can be using the formalism of density matrix and investigating the effect of loss, such as through reflections on optical elements.

Bibliography

[1] N. Boroumand, A. Thorpe, A. M. Parks, and T. Brabec, "Keldysh ionization theory of atoms: mathematical details," *Journal of Physics B: Atomic, Molecular and Optical Physics*, vol. 55, p. 213001, oct 2022.

[2] G. Vampa and T. Brabec, "Merge of high harmonic generation from gases and solids and its implications for attosecond science," *Journal of Physics B: Atomic, Molecular and Optical Physics*, vol. 50, no. 8, p. 083001, 2017.

[3] V. May and O. Kühn, *Charge and Energy Transfer Dynamics in Molecular Systems*. Wiley-VCH, 2011.

[4] C. Gerry and P. L. Knight, *Introductory Quantum Optics*. Cambridge: Cambridge University Press, 2005.

[5] A. Thorpe, N. Boroumand, A. M. Parks, E. Goulielmakis, and T. Brabec, "High harmonic generation in solids: Real versus virtual transition channels," *Phys. Rev. B*, vol. 107, p. 075135, Feb 2023.

[6] A. Einstein, "On the quantum theory of radiation," *Physikalische Zeitschrift*, vol. 18, pp. 121–128, 1917.

[7] T. H. Maiman, "Stimulated optical radiation in ruby," *Nature*, vol. 187, pp. 493–494, August 1960.

[8] J. Levesque and P. B. Corkum, "Attosecond science and technology," *Canadian Journal of Physics*, vol. 84, no. 1, pp. 1–18, 2006.

[9] N. Bloembergen, *Nonlinear Optics*. W. A. Benjamin, Inc., 1965.

[10] R. W. Boyd, *Nonlinear Optics*. San Diego: Academic Press, 2nd ed., 2003.

[11] P. A. Franken, A. E. Hill, C. W. Peters, and G. Weinreich, "Generation of optical harmonics," *Physical Review Letters*, vol. 7, no. 4, pp. 118–119, 1961.

[12] N. H. Burnett, H. A. Baldis, M. C. Richardson, and G. D. Enright, "Harmonic generation in co2 laser target interaction," *Appl. Phys. Lett.; (United States)*, vol. 31:3, 08 1977.

[13] A. McPherson, G. Gibson, H. Jara, U. Johann, T. S. Luk, I. A. McIntyre, K. Boyer, and C. K. Rhodes, "Studies of multiphoton production of vacuum-ultraviolet radiation in the rare gases," *J. Opt. Soc. Am. B*, vol. 4, pp. 595–601, Apr 1987.

[14] R. R. Gattass and E. Mazur, "Femtosecond laser micromachining in transparent materials," *Nature Photonics*, vol. 2, no. 4, pp. 219–225, 2008.

[15] E. Goulielmakis and T. Brabec, "High harmonic generation in condensed matter," *Nature Photonics*, vol. 16, no. 6, pp. 411–421, 2022.

[16] G. Vampa, T. J. Hammond, N. Thiré, B. E. Schmidt, F. Légaré, C. R. McDonald, T. Brabec, D. D. Klug, and P. B. Corkum, "All-optical reconstruction of crystal band structure," *Phys. Rev. Lett.*, vol. 115, p. 193603, Nov 2015.

[17] T. T. Luu, M. Garg, S. Y. Kruchinin, A. Moulet, M. T. Hassan, and E. Goulielmakis, "Extreme ultraviolet high-harmonic spectroscopy of solids," *Nature*, vol. 521, no. 7553, pp. 498–502, 2015.

[18] M. Garg, M. Zhan, T. T. Luu, H. Lakhotia, T. Klostermann, A. Guggenmos, and E. Goulielmakis, "Multi-petahertz electronic metrology," *Nature*, vol. 538, no. 7625, pp. 359–363, 2016.

[19] M. Garg, H. Y. Kim, and E. Goulielmakis, "Ultimate waveform reproducibility of extreme-ultraviolet pulses by high-harmonic generation in quartz," *Nature Photonics*, vol. 12, no. 5, pp. 291–296, 2018.

[20] A. A. Lanin, E. A. Stepanov, A. B. Fedotov, and A. M. Zheltikov, "Mapping the electron band structure by intraband high-harmonic generation in solids," *Optica*, vol. 4, pp. 516–519, May 2017.

[21] H. Liu, Y. Li, Y. S. You, S. Ghimire, T. F. Heinz, and D. A. Reis, "High-harmonic generation from an atomically thin semiconductor," *Nature Physics*, vol. 13, no. 3, pp. 262–265, 2017.

[22] T. T. Luu and H. J. Wörner, "Measurement of the berry curvature of solids using high-harmonic spectroscopy," *Nature Communications*, vol. 9, no. 1, p. 916, 2018.

[23] H. Lakhotia, H. Y. Kim, M. Zhan, S. Hu, S. Meng, and E. Goulielmakis, "Laser picoscopy of valence electrons in solids," *Nature*, vol. 583, no. 7814, pp. 55–59, 2020.

[24] F. Krausz and M. Ivanov, "Attosecond physics," *Rev. Mod. Phys.*, vol. 81, pp. 163–234, Feb 2009.

[25] L. V. Keldysh, "Ionization in the field of a strong electromagnetic wave," *Sov. Phys. JETP*, vol. 20, pp. 1307–1314, 1964.

[26] M. Y. Ivanov, M. Spanner, and O. S. and, "Anatomy of strong field ionization," *Journal of Modern Optics*, vol. 52, no. 2-3, pp. 165–184, 2005.

[27] M. Schultze, K. Ramasesha, C. Pemmaraju, S. Sato, D. Whitmore, A. Gandman, J. S. Prell, L. J. Borja, D. Prendergast, K. Yabana, D. M. Neumark, and S. R. Leone, "Attosecond band-gap dynamics in silicon," *Science*, vol. 346, no. 6215, pp. 1348–1352, 2014.

[28] M. Lewenstein, P. Balcou, M. Ivanov, A. L'Huillier, and P. B. Corkum, "Theory of high-harmonic generation by low-frequency laser fields," *Physical Review A*, vol. 49, pp. 2117–2132, 1994.

[29] M. Schultze, E. M. Bothschafter, A. Sommer, S. Holzner, W. Schweinberger, M. Fiess, M. Hofstetter, R. Kienberger, V. Apalkov, V. S. Yakovlev, M. I. Stockman, and F. Krausz, "Controlling dielectrics with the electric field of light," *Nature*, vol. 493, no. 7430, pp. 75–78, 2013.

[30] C. R. McDonald, G. Vampa, P. B. Corkum, and T. Brabec, "Intense-laser solid state physics: Unraveling the difference between semiconductors and dielectrics," *Phys. Rev. Lett.*, vol. 118, p. 173601, Apr 2017.

[31] P. B. Corkum, "Plasma perspective on strong field multiphoton ionization," *Phys. Rev. Lett.*, vol. 71, pp. 1994–1997, Sep 1993.

[32] S. Ghimire, A. D. DiChiara, E. Sistrunk, P. Agostini, L. F. DiMauro, and D. A. Reis, "Observation of high-order harmonic generation in a bulk crystal," *Nature Physics*, vol. 7, pp. 138–141, 2011.

[33] O. Schubert, M. Hohenleutner, F. Langer, B. Urbanek, C. Lange, U. Huttner, D. Golde, T. Meier, M. Kira, S. W. Koch, and R. Huber, "Sub-cycle control of terahertz high-harmonic generation by dynamical bloch oscillations," *Nature Photonics*, vol. 8, pp. 119–123, 2014.

[34] F. Langer, M. Hohenleutner, C. P. Schmid, C. Poellmann, P. Nagler, T. Korn, C. Schüller, M. S. Sherwin, U. Huttner, J. T. Steiner, S. W. Koch, M. Kira, and R. Huber, "Lightwave-driven quasiparticle collisions on a subcycle timescale," *Nature*, vol. 533, pp. 225–229, 2016.

[35] U. Huttner, M. Kira, and S. W. Koch, "Ultrahigh off-resonant field effects in semiconductors," *Laser & Photonics Reviews*, vol. 11, p. 1700049, 2017.

[36] G. Vampa, T. Hammond, N. Thiré, B. Schmidt, F. Légaré, C. McDonald, T. Brabec, and P. Corkum, "Linking high harmonics from gases and solids," *Nature*, vol. 522, no. 7557, pp. 462–464, 2015.

[37] N. Yoshikawa, K. Nagai, K. Uchida, Y. Takaguchi, S. Sasaki, Y. Miyata, and K. Tanaka, "Interband resonant high-harmonic generation by valley polarized electron–hole pairs," *Nature Communications*, vol. 10, p. 3709, 2019.

[38] A. J. Uzan, G. Orenstein, B. D. Bruner, Álvaro Jiménez-Galán, C. McDonald, R. E. F. Silva, N. D. Klimkin, V. Blanchet, T. Arusi-Parpar, M. Krüger, A. N. Rubtsov, O. Smirnova, M. Ivanov, B. Yan, T. Brabec, and N. Dudovich, "Attosecond spectral singularities in solid-state high-harmonic generation," *Nature Photonics*, vol. 14, pp. 183–187, 2020.

[39] M. Wu, Y. You, S. Ghimire, D. A. Reis, D. A. Browne, K. J. Schafer, and M. B. Gaarde, "Orientation dependence of temporal and spectral properties of high-order harmonics in solids," *Phys. Rev. A*, vol. 96, p. 063412, Dec 2017.

[40] D. Dimitrovski, T. G. Pedersen, and L. B. Madsen, "Floquet-bloch shifts in two-band semiconductors interacting with light," *Phys. Rev. A*, vol. 95, p. 063420, Jun 2017.

[41] N. Tancogne-Dejean, O. D. Mücke, F. X. Kärtner, and A. Rubio, "Ellipticity dependence of high-harmonic generation in solids originating from coupled intraband and interband dynamics," *Nature Communications*, vol. 8, p. 745, 2017.

[42] R. E. F. Silva, F. Martín, and M. Ivanov, "High harmonic generation in crystals using maximally localized wannier functions," *Phys. Rev. B*, vol. 100, p. 195201, Nov 2019.

[43] K. S. Virk and J. E. Sipe, "Semiconductor optics in length gauge: A general numerical approach," *Physical Review B*, vol. 76, no. 3, p. 035213, 2007.

[44] N. W. Ashcroft and N. D. Mermin, *Solid State Physics*. Philadelphia: Holt, Rinehart and Winston, 1976. See Appendix I for additional reference.

[45] G. Vampa, C. R. McDonald, G. Orlando, D. D. Klug, P. B. Corkum, and T. Brabec, "Theoretical analysis of high-harmonic generation in solids," *Phys. Rev. Lett.*, vol. 113, p. 073901, Aug 2014.

[46] G. Vampa, C. R. McDonald, G. Orlando, P. B. Corkum, and T. Brabec, "Semiclassical analysis of high harmonic generation in bulk crystals," *Phys. Rev. B*, vol. 91, p. 064302, Feb 2015.

[47] L. Li, P. Lan, X. Zhu, T. Huang, Q. Zhang, M. Lein, and P. Lu, "Reciprocal-space-trajectory perspective on high-harmonic generation in solids," *Phys. Rev. Lett.*, vol. 122, p. 193901, May 2019.

[48] L. Yue and M. B. Gaarde, "Imperfect recollisions in high-harmonic generation in solids," *Phys. Rev. Lett.*, vol. 124, p. 153204, Apr 2020.

[49] L. Yue and M. B. Gaarde, "Introduction to theory of high-harmonic generation in solids: tutorial," *J. Opt. Soc. Am. B*, vol. 39, pp. 535–555, Feb 2022.

[50] A. M. Parks, G. Ernotte, A. Thorpe, C. R. McDonald, P. B. Corkum, M. Taucer, and T. Brabec, "Wannier quasi-classical approach to high harmonic generation in semiconductors," *Optica*, vol. 7, pp. 1764–1772, Dec 2020.

[51] X. He, J. M. Dahlström, R. Rakowski, C. M. Heyl, A. Persson, J. Mauritsson, and A. L'Huillier, "Interference effects in two-color high-order harmonic generation," *Physical Review A*, vol. 82, no. 3, p. 033410, 2010.

[52] I. J. Kim, C. M. Kim, H. T. Kim, G. H. Lee, Y. S. Lee, J. Y. Park, D. J. Cho, and C. H. Nam, "Highly efficient high-harmonic generation in an orthogonally polarized two-color laser field," *Physical Review Letters*, vol. 94, no. 24, p. 243901, 2005.

[53] H. P. Breuer and F. Petruccione, *The Theory of Open Quantum Systems*. Oxford University Press, 2002.

[54] D. A. Micha and I. Burghardt, *Quantum Dynamics of Complex Molecular Systems*, vol. 83 of *Springer Series in Chemical Physics*. Springer Berlin Heidelberg, 2007.

[55] M. A. Nielsen and I. L. Chuang, *Quantum Computation and Quantum Information: 10th Anniversary Edition*. Cambridge: Cambridge University Press, 2010.

[56] A. Nitzen, *Chemical Dynamics in Condensed Phases: Relaxation, Transfer and Reactions in Condensed Molecular Systems*. Oxford University Press, 2020.

[57] J. J. Sakurai and J. Napolitano, *Modern Quantum Mechanics*. San Francisco: Addison-Wesley, 2nd ed., 2011.

[58] U. Shrikant and P. Mandayam, "Quantum non-markovianity: Overview and recent developments," *Frontiers in Quantum Science and Technology*, vol. 2, 2023.

[59] A. G. Redfield, "On the theory of relaxation processes," *IBM Journal of Research and Development*, vol. 1, no. 1, 1957.

[60] G. Lindblad, "On the generators of quantum dynamical semigroups," *Communications in Mathematical Physics*, vol. 48, no. 2, pp. 119–130, 1976.

[61] A. J. Leggett, S. Chakravarty, A. T. Dorsey, M. P. A. Fisher, A. Garg, and W. Zwerger, "Dynamics of the dissipative two-state system," *Reviews of Modern Physics*, vol. 59, no. 1, pp. 1–85, 1987.

[62] R. K. Pathria and P. D. Beale, *Statistical Mechanics*. New York: Academic Press, 4th ed., 2021.

[63] M. D. Levenson, *Introduction to Nonlinear Laser Spectroscopy*. Boston: Academic Press, 1982.

[64] P. J. Campagnola *et al.*, "Three-dimensional high-resolution second-harmonic generation imaging of endogenous structural proteins in biological tissues," *Biophysical Journal*, vol. 82, no. 1, pp. 493–508, 2002.

[65] C. R. McDonald, A. B. Taher, and T. Brabec, "Strong optical field ionisation of solids," *Journal of Optics*, vol. 19, no. 11, p. 114005, 2017.

[66] N. Boroumand, A. Thorpe, G. Bart, A. M. Parks, M. Toutounji, G. Vampa, T. Brabec, and L. Wang, "Strong field physics in open quantum systems," *Reports on Progress in Physics*, 2025. Accepted Manuscript, published online 11 July 2025.

[67] N. A. Kamar, D. A. Paz, and M. F. Maghrebi, "Spin-boson model under dephasing: Markovian versus non-markovian dynamics," *Phys. Rev. B*, vol. 110, p. 075126, Aug 2024.

[68] N. Lambert, S. Ahmed, M. Cirio, and F. Nori, "Modelling the ultra-strongly coupled spin-boson model with unphysical modes," *Nature Communications*, vol. 10, no. 1, p. 3721, 2019.

[69] P. Forn-Díaz, L. Lamata, E. Rico, J. Kono, and E. Solano, "Ultrastrong coupling regimes of light-matter interaction," *Rev. Mod. Phys.*, vol. 91, p. 025005, Jun 2019.

[70] U. Weiss, H. Grabert, and S. Linkwitz, "Influence of friction and temperature on coherent quantum tunneling," *Journal of Low Temperature Physics*, vol. 68, no. 3-4, pp. 213–244, 1987.

[71] J. Gilmore and R. H. McKenzie, "Spin boson models for quantum decoherence of electronic excitations of biomolecules and quantum dots in a solvent," *Journal of Physics: Condensed Matter*, vol. 17, no. 12, pp. 1735–1746, 2005.

[72] S. J. Jang and B. Mennucci, "Delocalized excitons in natural light-harvesting complexes," *Rev. Mod. Phys.*, vol. 90, p. 035003, Aug 2018.

[73] K. Sun, M. Kang, H. Nuomin, G. Schwartz, D. N. Beratan, K. R. Brown, and J. Kim, "Quantum simulation of spin-boson models with structured bath," *Nature Communications*, vol. 16, no. 1, p. 4042, 2025.

[74] A. Würger, "Strong-coupling theory for the spin-phonon model," *Phys. Rev. B*, vol. 57, pp. 347–361, Jan 1998.

[75] C. K. Lee, J. Moix, and J. Cao, "Accuracy of second order perturbation theory in the polaron and variational polaron frames," *The Journal of Chemical Physics*, vol. 136, p. 204120, 2012.

[76] T. Shi, Y. Chang, and J. J. García-Ripoll, "Ultrastrong coupling few-photon scattering theory," *Phys. Rev. Lett.*, vol. 120, p. 153602, Apr 2018.

[77] G. Díaz-Camacho, A. Bermudez, and J. J. García-Ripoll, "Dynamical polaron ansatz: A theoretical tool for the ultrastrong-coupling regime of circuit qed," *Phys. Rev. A*, vol. 93, p. 043843, Apr 2016.

[78] F. Mascherpa, A. Smirne, S. F. Huelga, and M. B. Plenio, "Open systems with error bounds: Spin-boson model with spectral density variations," *Phys. Rev. Lett.*, vol. 118, p. 100401, Mar 2017.

[79] A. Kell, X. Feng, M. Reppert, and R. Jankowiak, "On the shape of the phonon spectral density in photosynthetic complexes," *The Journal of Physical Chemistry B*, vol. 117, no. 24, pp. 7317–7323, 2013.

[80] R. Pässler, "Basic moments of phonon density of states spectra and characteristic phonon temperatures of group iv, iii–v, and ii–vi materials," *Journal of Applied Physics*, vol. 101, no. 9, p. 093513, 2007.

[81] M. O. Scully and S. M. Zubairy, *Quantum Optics*. Cambridge: Cambridge University Press, 1st ed., 1997.

[82] R. H. Brown and R. Q. Twiss, "Correlation between photons in two coherent beams of light," *Nature*, vol. 177, no. 4497, pp. 27–29, 1956.

[83] R. J. Glauber, "The quantum theory of optical coherence," *Phys. Rev.*, vol. 130, pp. 2529–2539, Jun 1963.

[84] U. L. Andersen, T. Gehring, C. Marquardt, and G. Leuchs, "30 years of squeezed light generation," *Physica Scripta*, vol. 91, p. 053001, apr 2016.

[85] M. Chekhova, G. Leuchs, and M. Żukowski, "Bright squeezed vacuum: Entanglement of macroscopic light beams," *Optics Communications*, vol. 337, pp. 27–43, 2015. Macroscopic quantumness: theory and applications in optical sciences.

[86] P. R. Sharapova, G. Frascella, M. Riabinin, A. M. Pérez, O. V. Tikhonova, S. Lemieux, R. W. Boyd, G. Leuchs, and M. V. Chekhova, "Properties of bright squeezed vacuum at increasing brightness," *Phys. Rev. Res.*, vol. 2, p. 013371, Mar 2020.

[87] A. M. Pérez, T. S. Iskhakov, P. Sharapova, S. Lemieux, O. V. Tikhonova, M. V. Chekhova, and G. Leuchs, "Bright squeezed-vacuum source with 1.1 spatial mode," *Optics Letters*, vol. 39, no. 8, pp. 2403–2406, 2014.

[88] V. Bužek, A. Vidiella-Barranco, and P. L. Knight, "Superpositions of coherent states: Squeezing and dissipation," *Phys. Rev. A*, vol. 45, pp. 6570–6585, May 1992.

[89] B. Yurke and D. Stoler, "Generating quantum mechanical superpositions of macroscopically distinguishable states via amplitude dispersion," *Phys. Rev. Lett.*, vol. 57, pp. 13–16, Jul 1986.

[90] S. Glancy and H. M. de Vasconcelos, "Methods for producing optical coherent state superpositions," *J. Opt. Soc. Am. B*, vol. 25, pp. 712–733, May 2008.

[91] A. Gilchrist, K. Nemoto, W. J. Munro, T. C. Ralph, S. Glancy, S. L. Braunstein, and G. J. Milburn, "Schrödinger cats and their power for quantum information processing," *Journal of Optics B: Quantum and Semiclassical Optics*, vol. 6, no. 8, pp. S828–S833, 2004.

[92] Z. Zhang and H. Fan, "Properties of states generated by excitations on a squeezed vacuum state," *Physics Letters A*, vol. 165, no. 1, pp. 14–18, 1992.

[93] A. Biswas and G. S. Agarwal, "Nonclassicality and decoherence of photon-subtracted squeezed states," *Phys. Rev. A*, vol. 75, p. 032104, Mar 2007.

[94] T. L. Curtright, D. B. Fairlie, and C. K. Zachos, *A Concise Treatise on Quantum Mechanics in Phase Space*. Singapore: World Scientific, 2013.

[95] I. Gonoskov, N. Tsatrafyllis, I. Kominis, and P. Tzallas, "Quantum optical signatures in strong-field laser physics: Infrared photon counting in high-order-harmonic generation," *Scientific Reports*, vol. 6, no. 1, p. 32821, 2016.

[96] A. Gorlach, O. Neufeld, N. Rivera, O. Cohen, and I. Kaminer, "The quantum-optical nature of high harmonic generation," *Nature Communications*, vol. 11, no. 1, p. 4598, 2020.

[97] N. Boroumand, A. Thorpe, G. Bart, L. Wang, D. N. Purschke, G. Vampa, and T. Brabec, "Quantum engineering of high harmonic generation," 2025. https://arxiv.org/abs/2505.22536.

[98] P. Földi, I. Magashegyi, Á. Gombköto, and S. Varró, "Describing high-order harmonic generation using quantum optical models," in *Photonics*, vol. 8, p. 263, MDPI, 2021.

[99] Á. Gombkötő, P. Földi, and S. Varró, "Quantum-optical description of photon statistics and cross correlations in high-order harmonic generation," *Physical Review A*, vol. 104, no. 3, p. 033703, 2021.

[100] N. Tsatrafyllis, S. Kühn, M. Dumergue, P. Foldi, S. Kahaly, E. Cormier, I. Gonoskov, B. Kiss, K. Varju, S. Varro, *et al.*, "Quantum optical signatures in a strong laser pulse after interaction with semiconductors," *Physical Review Letters*, vol. 122, no. 19, p. 193602, 2019.

[101] J. Rivera-Dean, P. Stammer, E. Pisanty, T. Lamprou, P. Tzallas, M. Lewenstein, and M. F. Ciappina, "New schemes for creating large optical schrödinger cat states using strong laser fields," *Journal of Computational Electronics*, vol. 20, pp. 2111–2123, 2021.

[102] M. Lewenstein, M. F. Ciappina, E. Pisanty, J. Rivera-Dean, P. Stammer, T. Lamprou, and P. Tzallas, "Generation of optical schrödinger cat states in intense laser–matter interactions," *Nature Physics*, vol. 17, no. 10, pp. 1104–1108, 2021.

[103] P. Stammer, J. Rivera-Dean, A. Maxwell, T. Lamprou, A. Ordóñez, M. F. Ciappina, P. Tzallas, and M. Lewenstein, "Quantum electrodynamics of intense laser-matter interactions: A tool for quantum state engineering," *PRX Quantum*, vol. 4, no. 1, p. 010201, 2023.

[104] J. Rivera-Dean, P. Stammer, A. S. Maxwell, T. Lamprou, P. Tzallas, M. Lewenstein, and M. F. Ciappina, "Light-matter entanglement after above-threshold ionization processes in atoms," *Physical Review A*, vol. 106, no. 6, p. 063705, 2022.

[105] J. Sloan, A. Gorlach, M. E. Tzur, N. Rivera, O. Cohen, I. Kaminer, and M. Soljačić, "Entangling extreme ultraviolet photons through strong field pair generation," *arXiv preprint arXiv:2309.16466*, 2023.

[106] S. Yi, N. D. Klimkin, G. G. Brown, O. Smirnova, S. Patchkovskii, I. Babushkin, and M. Ivanov, "Generation of massively entangled bright states of light during harmonic generation in resonant media," *Physical Review X*, vol. 15, no. 1, p. 011023, 2025.

[107] P. Stammer, J. Rivera-Dean, A. S. Maxwell, T. Lamprou, J. Argüello-Luengo, P. Tzallas, M. F. Ciappina, and M. Lewenstein, "Entanglement and squeezing of the optical field modes in high harmonic generation," *Physical Review Letters*, vol. 132, no. 14, p. 143603, 2024.

[108] M. Even Tzur, M. Birk, A. Gorlach, M. Krüger, I. Kaminer, and O. Cohen, "Photon-statistics force in ultrafast electron dynamics," *Nature Photonics*, vol. 17, no. 6, pp. 501–509, 2023.

[109] M. Even Tzur and O. Cohen, "Motion of charged particles in bright squeezed vacuum," *Light: Science & Applications*, vol. 13, no. 1, p. 41, 2024.

[110] A. Rasputnyi, Z. Chen, M. Birk, O. Cohen, I. Kaminer, M. Krüger, D. Seletskiy, M. Chekhova, and F. Tani, "High-harmonic generation by a bright squeezed vacuum," *Nature Physics*, vol. 20, no. 12, pp. 1960–1965, 2024.

[111] J. Heimerl, A. Mikhaylov, S. Meier, H. Höllerer, I. Kaminer, M. Chekhova, and P. Hommelhoff, "Multiphoton electron emission with non-classical light," *Nature Physics*, vol. 20, no. 6, pp. 945–950, 2024.

[112] S. Lemieux, S. A. Jalil, D. Purschke, N. Boroumand, D. Villeneuve, A. Naumov, T. Brabec, and G. Vampa, "Photon bunching in high-harmonic emission controlled by quantum light," *arXiv preprint arXiv:2404.05474*, 2024.

[113] S. Lemieux, S. A. Jalil, D. N. Purschke, N. Boroumand, T. J. Hammond, D. Villeneuve, A. Naumov, T. Brabec, and G. Vampa, "Photon bunching in high-harmonic emission controlled by quantum light," *Nature Photonics*, 2025.

[114] M. Walschaers, "Non-gaussian quantum states and where to find them," *PRX Quantum*, vol. 2, p. 030204, Sep 2021.

[115] J. R. Oppenheimer, "Three notes on the quantum theory of aperiodic effects," *Phys. Rev.*, vol. 31, pp. 66–81, Jan 1928.

[116] M. V. Ammosov, N. B. Delone, and V. P. Krainov, "Tunnel ionization of complex atoms and of atomic ions in an alternating electromagnetic field," *Soviet Physics JETP*, vol. 64, p. 1191, 1986.

[117] K. Amini, J. Biegert, F. Calegari, A. Chacón, M. F. Ciappina, A. Dauphin, D. K. Efimov, C. F. de Morisson Faria, K. Giergiel, P. Gniewek, A. S. Landsman, M. Lesiuk, M. Mandrysz, A. S. Maxwell, R. Moszyński, L. Ortmann, J. A. Pérez-Hernández, A. Picón, E. Pisanty, J. Prauzner-Bechcicki, and M. Lewenstein, "Symphony on strong field approximation," *Reports on Progress in Physics*, vol. 82, no. 11, p. 116001, 2019.

[118] F. H. M. Faisal, "Multiple absorption of laser photons by atoms," *Journal of Physics B: Atomic and Molecular Physics*, vol. 6, no. 4, p. L89, 1973.

[119] H. R. Reiss, "Effect of an intense electromagnetic field on a weakly bound system," *Phys. Rev. A*, vol. 22, pp. 1786–1813, Nov 1980.

[120] J. Bauer, "Low-frequency–high-intensity limit of the keldysh-faisal-reiss theory," *Phys. Rev. A*, vol. 73, p. 023421, Feb 2006.

[121] A. M. Perelomov, V. S. Popov, and M. V. Terent'ev, "Ionization of atoms in an alternating field," *Sov. Phys. JETP*, vol. 23, p. 924, 1966.

[122] G. F. Gribakin and M. Y. Kuchiev, "Multiphoton detachment of electrons from negative ions," *Phys. Rev. A*, vol. 55, pp. 3760–3771, May 1997.

[123] V. S. Popov, "Imaginary-time method in quantum mechanics and field theory," *Physics of Atomic Nuclei*, vol. 68, pp. 686–708, 2005.

[124] Y. V. Vanne and A. Saenz, "Exact keldysh theory of strong-field ionization: Residue method versus saddle-point approximation," *Physical Review A*, vol. 75, p. 033403, 2007.

[125] B. M. Karnakov, V. D. Mur, S. V. Popruzhenko, and V. S. Popov, "Current progress in developing the nonlinear ionization theory of atoms and ions," *Physics Uspekhi*, vol. 58, pp. 3–32, 2015.

[126] L. V. Fedorov, "Keldysh's "ionization in the field of a strong electromagnetic wave" and modern physics of atomic interaction with a strong laser field," *Journal of Experimental and Theoretical Physics*, vol. 122, pp. 449–455, 2016.

[127] V. S. Popov, "Tunnel and multiphoton ionization of atoms and ions in a strong laser field (keldysh theory)," *Physics Uspekhi*, vol. 47, pp. 855–885, 2004.

[128] Z. J. Long and W. K. Liu, "Keldysh theory of strong field ionization," *Canadian Journal of Physics*, vol. 88, pp. 227–245, 2010.

[129] V. N. Ostrovsky, T. K. Kjeldsen, and L. B. Madsen, "Comment on "generalization of keldysh's theory"," *Physical Review A*, vol. 75, p. 027401, 2007.

[130] T. Brabec and F. Krausz, "Intense few-cycle laser fields: Frontiers of nonlinear optics," *Reviews of Modern Physics*, vol. 72, pp. 545–591, 2000.

[131] P. B. Corkum and F. Krausz, "Attosecond science," *Nature Physics*, vol. 3, pp. 381–387, 2007.

[132] F. Krausz and M. Ivanov, "Attosecond physics," *Reviews of Modern Physics*, vol. 81, pp. 163–234, 2009.

[133] J. H. Eberly, J. Javanainen, and K. Rzążewski, "Above-threshold ionization," *Physics Reports*, vol. 204, pp. 331–383, 1991.

[134] D. B. Milošević, G. G. Paulus, D. Bauer, and W. Becker, "Above-threshold ionization by few-cycle pulses," *Journal of Physics B: Atomic, Molecular and Optical Physics*, vol. 39, pp. R203–R262, 2006.

[135] W. Becker, X. Liu, P. J. Ho, and J. H. Eberly, "Theories of photoelectron correlation in laser-driven multiple atomic ionization," *Reviews of Modern Physics*, vol. 84, pp. 1011–1043, 2012.

[136] H. A. Bethe and E. E. Salpeter, *Quantum Mechanics of One- and Two-Electron Atoms*. New York: Plenum Publishing, 1977.

[137] R. Loudon, *The Quantum Theory of Light*. Oxford: Oxford University Press, 2nd ed., 1983.

[138] M. J. Ablowitz and A. S. Fokas, *Complex Variables: Introduction and Applications*. Cambridge: Cambridge University Press, 2nd ed., 2003.

[139] W. Greiner and J. Reinhardt, *Quantum Electrodynamics*. New York: Springer, 4th ed., 2009.

[140] M. Crance, "Multiphoton detachment from negative ions of halogens, angular distributions and excess photon absorption," *Journal of Physics B: Atomic, Molecular and Optical Physics*, vol. 21, pp. 3559–3569, 1988.

[141] M. H. Mittleman, "Adiabatic theory of nonresonant multiphoton ionization," *Physical Review A*, vol. 40, pp. 463–472, 1989.

[142] F. Trombetta, S. Basile, and G. Ferrante, "Multiphoton-ionization transition amplitudes and the keldysh approximation," *Physical Review A*, vol. 40, pp. 2774–2777, 1989.

[143] Y. Sanari, H. Hirori, T. Aharen, H. Tahara, Y. Shinohara, K. L. Ishikawa, T. Otobe, P. Xia, N. Ishii, J. Itatani, S. A. Sato, and Y. Kanemitsu, "Role of virtual band population for high harmonic generation in solids," *Phys. Rev. B*, vol. 102, p. 041125, Jul 2020.

[144] T. Boolakee, C. Heide, A. Garzón-Ramírez, H. B. Weber, I. Franco, and P. Hommelhoff, "Light-field control of real and virtual charge carriers," *Nature*, vol. 605, no. 7909, pp. 251–255, 2022.

[145] G. D. Mahan, *Many Particle Physics*. New York: Plenum, 3rd ed., 2000.

[146] K. E. Cahill and R. J. Glauber, "Ordered expansions in boson amplitude operators," *Physical Review*, vol. 177, no. 5, pp. 1857–1881, 1969.

[147] F. A. M. de Oliveira, M. S. Kim, P. L. Knight, and V. Bužek, "Properties of displaced number states," *Phys. Rev. A*, vol. 41, pp. 2645–2652, Mar 1990.

[148] J. Bertrand, H. J. Wörner, H.-C. Bandulet, É. Bisson, M. Spanner, J.-C. Kieffer, D. Villeneuve, and P. B. Corkum, "Ultrahigh-order wave mixing in noncollinear high harmonic generation," *Physical review letters*, vol. 106, no. 2, p. 023001, 2011.

[149] D. N. Purschke, Á. Jiménez-Galán, T. Brabec, A. Y. Naumov, A. Staudte, D. M. Villeneuve, and G. Vampa, "Microscopic mechanisms of high-order wave mixing in solids," *Physical Review A*, vol. 108, no. 5, p. L051103, 2023.

[150] F. Brunel, "Harmonic generation due to plasma effects in a gas undergoing multiphoton ionization in the high-intensity limit," *Journal of the Optical Society of America B*, vol. 7, no. 4, pp. 521–526, 1990.

[151] P. P. Rohde, W. Mauerer, and C. Silberhorn, "Spectral structure and decompositions of optical states, and their applications," *New Journal of Physics*, vol. 9, no. 4, p. 91, 2007.

[152] N. Dudovich, O. Smirnova, J. Levesque, Y. Mairesse, M. Y. Ivanov, D. Villeneuve, and P. B. Corkum, "Measuring and controlling the birth of attosecond xuv pulses," *Nature physics*, vol. 2, no. 11, pp. 781–786, 2006.

[153] A. Reshak, Z. Alahmed, and S. Auluck, "A density functional study of the electronic properties of bismuth subcarbonate bi2o2co3," *Solid state sciences*, vol. 38, pp. 138–142, 2014.

[154] M. Sivis, M. Taucer, G. Vampa, K. Johnston, A. Staudte, A. Y. Naumov, D. Villeneuve, C. Ropers, and P. Corkum, "Tailored semiconductors for high-harmonic optoelectronics," *Science*, vol. 357, no. 6348, pp. 303–306, 2017.

[155] H. Liu, C. Guo, G. Vampa, J. L. Zhang, T. Sarmiento, M. Xiao, P. H. Bucksbaum, J. Vučković, S. Fan, and D. A. Reis, "Enhanced high-harmonic generation from an all-dielectric metasurface," *Nature Physics*, vol. 14, no. 10, pp. 1006–1010, 2018.

[156] G. Vampa, B. Ghamsari, S. Siadat Mousavi, T. Hammond, A. Olivieri, E. Lisicka-Skrek, A. Y. Naumov, D. Villeneuve, A. Staudte, P. Berini, *et al.*, "Plasmon-enhanced high-harmonic generation from silicon," *Nature Physics*, vol. 13, no. 7, pp. 659–662, 2017.

[157] C. E. Vollmer, C. Baune, A. Samblowski, T. Eberle, V. Händchen, J. Fiurášek, and R. Schnabel, "Quantum up-conversion of squeezed vacuum states from 1550 to 532 nm," *Phys. Rev. Lett.*, vol. 112, p. 073602, Feb 2014.

[158] O. Raz, O. Pedatzur, B. D. Bruner, and N. Dudovich, "Spectral caustics in attosecond science," *Nature Photonics*, vol. 6, no. 3, pp. 170–173, 2012.

[159] A. J. Uzan, G. Orenstein, Á. Jiménez-Galán, C. McDonald, R. E. Silva, B. D. Bruner, N. D. Klimkin, V. Blanchet, T. Arusi-Parpar, M. Krüger, *et al.*, "Attosecond spectral singularities in solid-state high-harmonic generation," *Nature Photonics*, vol. 14, no. 3, pp. 183–187, 2020.

[160] M. Schmidt, M. Von Helversen, M. López, F. Gericke, E. Schlottmann, T. Heindel, S. Kück, S. Reitzenstein, and J. Beyer, "Photon-number-resolving transition-edge sensors for the metrology of quantum light sources," *Journal of Low Temperature Physics*, vol. 193, pp. 1243–1250, 2018.

[161] A. I. Lvovsky, "Squeezed light," *Photonics: Scientific Foundations, Technology and Applications*, vol. 1, pp. 121–163, 2015.

[162] S. Kun, J. Xiao-Hui, and J. Huan-Yu, "Nonclassicality of photon-added squeezed vacuum states," *Chinese Physics B*, vol. 19, no. 6, p. 064205, 2010.

[163] L.-L. Guo, Y.-F. Yu, and Z.-M. Zhang, "Improving the phase sensitivity of an su (1, 1) interferometer with photon-added squeezed vacuum light," *Optics Express*, vol. 26, no. 22, pp. 29099–29109, 2018.

[164] S. B. Park, K. Kim, W. Cho, S. I. Hwang, I. Ivanov, C. H. Nam, and K. T. Kim, "Direct sampling of a light wave in air," *Optica*, vol. 5, no. 4, pp. 402–408, 2018.

[165] S. Sederberg, D. Zimin, S. Keiber, F. Siegrist, M. S. Wismer, V. S. Yakovlev, I. Floss, C. Lemell, J. Burgdörfer, M. Schultze, *et al.*, "Attosecond optoelectronic field measurement in solids," *Nature communications*, vol. 11, no. 1, p. 430, 2020.

[166] R. M. Wilcox, "Exponential operators and parameter differentiation in quantum physics," *Journal of Mathematical Physics*, vol. 8, no. 4, pp. 962–982, 1967.

[167] Z. Xie, Z. Chen, H. Li, Q. Yan, H. Chen, X. Lin, I. Kaminer, O. D. Miller, and Y. Yang, "Maximal quantum interaction between free electrons and photons," *Physical Review Letters*, vol. 134, no. 4, p. 043803, 2025.

[168] H.-Y. Fan, "Operator ordering in quantum optics theory and the development of dirac'ssymbolic method," *Journal of Optics B: Quantum and Semiclassical Optics*, vol. 5, no. 4, p. R147, 2003.

[169] R. W. Boyd, *Nonlinear optics*. Academic press, 2020.

[170] G. Agrawal and C. Mehta, "Ordering of the exponential of a quadratic in boson operators. ii. multimode case," *Journal of Mathematical Physics*, vol. 18, no. 3, pp. 408–412, 1977.

[171] X. Qiu, J. Huang, Z. Fu, and F. Jia, "Coherent state representation of squeezing operator and its applications," *Results in Physics*, vol. 43, p. 106100, 2022.